INFORMATION TO USERS

This manuscript has been reproduced from the microfilm master. UMI films the text directly from the original or copy submitted. Thus, some thesis and dissertation copies are in typewriter face, while others may be from any type of computer printer.

The quality of this reproduction is dependent upon the quality of the copy submitted. Broken or indistinct print, colored or poor quality illustrations and photographs, print bleedthrough, substandard margins, and improper alignment can adversely affect reproduction.

In the unlikely event that the author did not send UMI a complete manuscript and there are missing pages, these will be noted. Also, if unauthorized copyright material had to be removed, a note will indicate the deletion.

Oversize materials (e.g., maps, drawings, charts) are reproduced by sectioning the original, beginning at the upper left-hand corner and continuing from left to right in equal sections with small overlaps.

ProQuest Information and Learning
300 North Zeeb Road, Ann Arbor, MI 48106-1346 USA
800-521-0600

DISSERTATION

LIGHT FORCE MANIPULATION OF GALLIUM ATOMS

Submitted by

Steven James Rehse

Department of Physics

In partial fulfillment of the requirements

For the Degree of Doctor of Philosophy

Colorado State University

Fort Collins, Colorado

Fall 2002

COLORADO STATE UNIVERSITY

August 15, 2002

WE HEREBY RECOMMEND THAT THE DISSERTATION PREPARED UNDER OUR SUPERVISION BY STEVEN JAMES REHSE ENTITLED LIGHT FORCE MANIPULATION OF GALLIUM ATOMS BE ACCEPTED AS FULFILLING IN PART REQUIREMENTS FOR THE DEGREE OF DOCTOR OF PHILOSOPHY.

Committee on Graduate Work

Adviser

Department Head

ABSTRACT OF DISSERTATION

LIGHT FORCE MANIPULATION OF GALLIUM ATOMS

We have demonstrated the first one-dimensional laser cooling of neutral gallium atoms. We identified the $4p^2P_{3/2}(F=3) \rightarrow 4d^2D_{5/2}(F=4)$ transition at 294.45 nm as a cycling transition suitable for laser cooling. We developed a frequency stabilized tunable UV laser capable of generating over 90 mW for use at that wavelength. A careful spectroscopy of the hyperfine structure was performed on the 294.45 nm transition. This spectroscopy significantly improved the measurement of the Ga hyperfine constants and corrected existing errors in the literature.

Using the UV laser, a beam of Ga atoms was cooled in one-dimension utilizing the polarization gradient technique. With a cooling laser detuned by at least −14 MHz from the $4p^2P_{3/2}(F=3) \rightarrow 4d^2D_{5/2}(F=4)$ transition and a power of at least 60 mW ($I/I_0 \cong 12$) the transverse velocity of the atoms was reduced to <14 cm/s, which corresponds to a temperature of <165 μK. This is roughly one-half the Doppler cooling limit. Sub-Doppler cooling due to the polarization gradient was directly observed and the cooling efficiency as a function of cooling laser interaction length and power was investigated.

Optical pumping of atoms out of the F=3 state due to the UV laser was observed during cooling. Optical repumping with a second weaker UV laser beam was

investigated. A frequency shifted beam derived from the cooling beam was used for repumping and the populations of the hyperfine levels in the $4p^2P_{3/2}$ state were measured with a 417 nm probe laser. Two different frequency shifts for the repump beam were investigated: +334 MHz and +410 MHz. Both were found to repopulate the F=3 state, although they redistributed the atoms among the other hyperfine states in different ways.

Light force focusing of the cooled Ga atomic beam was attempted on the $4p^2P_{3/2}(F=3) \rightarrow 5s^2S_{1/2}(F=2)$ transition at 417.32 nm using 11 mW of laser light detuned 200 to 400 MHz from resonance. Self-organized islanding of the Ga atoms during deposition on silicon, gallium arsenide, and fused silica substrates precluded any observation of the light force focusing.

Steven James Rehse
Physics Department
Colorado State University
Fort Collins, CO 80523
Fall 2002

ACKNOWLEDGMENTS

No dissertation can be completed in isolation. The work presented in this thesis is the result of innumerable conversations, collaborations, and contributions from others. Without their help and assistance, none of it would have been possible. And so it is fitting that I acknowledge here the guidance and support from those that assisted me most along the way.

My advisor Dr. Siu Au Lee has supported me financially and intellectually for the past six years. She taught me much in and out of the lab and made me see the world in a different way. There is no doubt that this thesis is a direct result of her interest, involvement, and desire to see me succeed.

My Thesis Committee deserves special acknowledgment: Dr. Carmen Menoni, Dr. Stephen Lundeen, Dr. James Sites, and Dr. Chiao-Yao (Joe) She. I was fortunate to have a Committee that I consulted with frequently and felt comfortable coming to for guidance. Often times their advice pertained not merely to this thesis, but to issues both professional and personal. For that I thank them.

To the other faculty in the Department I owe a nod of thanks for assisting my development as a physicist. In particular, Dr. William Fairbank, Jr. and Dr. Hans Dieter Hochheimer will always be linked in my memory with my time spent in the CSU Department of Physics.

Probably the most significant contributors to the work in this thesis are the other students that worked with me in the laboratory. Their myriad accomplishments, both large and small, were all appreciated greatly. The level of work performed by the other graduate students in our lab was amazing. Karen Bockel was a steadfast friend and excellent lab partner who contributed more to this thesis then she will ever possibly know. Shannon Siefken was a constant joy to work and converse with and Anthony Glueck provided viewpoints and opinions that I would never have noticed on my own. The undergraduates who assisted me were: Henry Cook, III, Kristin Bjornsen, and Heather Michalak. Every summer was an adventure with them around. The local high-school students who assisted me were Julie Eaton and Janet Tsai. If ever I needed faith in the future, the attitude and ability of these young women reassured me that we have nothing to fear.

Two German interns worked with our group during my time spent on this project. Volker Bahn and Florian Denk both deserve my thanks for pitching in with their formidable abilities and talents.

I had the great fortune to work with two excellent machine shop coordinators during my years at CSU: Wally Akers and Bob Adame. They were both always patient, always considerate and always friendly. They were great machinists and great teachers. I can think of no higher compliment.

I thank my family for their unending patience during my years of graduate school. They were always supportive of my goals and never critical of the life choices I made along the way. And they were there for me at the very end when I really wanted them there.

I must acknowledge the love and support of my partner Genevieve. Without her, it is entirely possible that I would not be here right now writing this. She constantly bolstered my spirits, encouraged and supported me, and most importantly, she gave me a reason to finish here and move on to the next phase of my life.

Lastly, to my closest friends in the Department: Keir, Jenny, and Pam. What can I say? If they hadn't been here, I wouldn't have made it. There is no way I would have survived through the long years without their unconditional support, understanding and faith. I can only hope I did the same for them.

DEDICATION

This thesis is dedicated to my fellow CSU graduate students, without whom...

Because no man is an island.

TABLE OF CONTENTS

CHAPTER 1

Introduction

1.1 The Development of Laser Cooling

The use of lasers to manipulate neutral atoms has seen a remarkable growth in the past few decades with an ever increasing list of atomic species capable of being controlled and new techniques being introduced. The motion of a neutral atom, unlike an ion, is relatively unaffected by the application of a d.c. electric or magnetic field. However, a neutral atom can interact with the electromagnetic field of a laser beam due to the atom's well defined atomic energy levels. The atom's motion can be affected via the exchange of photons with the laser electromagnetic field and the subsequent excitation and de-excitation of the atom.

The idea of using lasers to exert a force on a neutral atom was introduced by Hänsch and Schawlow in 1975.[1] In their proposed experiment, a neutral atom's kinetic energy was reduced (effectively cooling the atom) via interaction with an isotropic laser field composed of six laser beams tuned slightly below an atomic resonance. This cooling relied on the Doppler shift to "tune" the lasers into resonance with only those atoms opposing their direction of propagation. Thus the laser field acted as a viscous medium, always exerting a force against the motion of the atoms. In time, this cooling scheme would be commonly called a Doppler molasses, due to its viscous nature.

Hänsch and Schawlow anticipated that an atom's velocity would be reduced by the ratio of the resonance line's Doppler width to the natural linewidth. For example, it was predicted that a cloud of magnesium atoms could be effectively cooled to 0.24 K by this Doppler cooling.

The first experimental laser cooling of neutral atoms was demonstrated in 1980 when a beam of sodium atoms was cooled using a single counter-propagating laser beam.[2] In this experiment, the atoms were cooled by 73 K (from an initial temperature of 523-623 K). The failure to cool the atoms to the predicted limit was attributed to optical pumping of the atoms to the incorrect ground state and laser frequency instabilities.

In 1985, two different research groups demonstrated the stopping of a beam of sodium atoms using a single counter-propagating resonant laser beam. In these experiments, an atom's deceleration shifted its resonance away from the frequency of the laser beam and the cooling process stopped. To compensate for the extremely rapid shift of atomic energy levels due to this deceleration, the groups pursued different techniques. At NIST, Prodan et al. utilized a spatially varying magnetic field (a "Zeeman slower") to tune the atomic levels along the beam path.[3] This effectively produced a stationary "gas" of atoms whose temperature was 100 mK. At JILA, Ertmer et al. utilized a counter-propagating laser beam that was frequency chirped with a high precision to keep the laser in resonance.[4] This technique produced a "gas" of atoms with a temperature below 50 mK.

Also in 1985, a beam of sodium atoms was collimated with laser light for the first time using a two-dimensional Doppler cooling scheme.[5] In this experiment, the

transverse temperature (i.e. the temperature resulting from an atom's velocity only along the axial dimensions of the atom beam) was reduced to 3.5 mK.

In 1985 the first true realization of the idea promulgated by Hänsch and Schawlow 10 years earlier was demonstrated. Chu et al. at AT&T Bell Laboratories reported the viscous confinement and cooling of neutral sodium atoms in three dimensions using only the radiation pressure of six counter-propagating laser beams.[6] Although these atoms were not trapped by the lasers, they were confined in the intersection of the six laser beams for a period of about 0.1 sec and cooled to ~240 μK, at the time thought to be the quantum limit of the experiment.

At this point, all was well in the AMO community as far as laser cooling was concerned. The technique was valid and so far every theoretical prediction had been borne out. This peace was not to last. Shortly after the first demonstration of the Doppler molasses, Lett et al. at NIST-Gaithersburg observed a cloud of sodium atoms laser cooled well below the Doppler limit.[7] Their cloud of atoms had a temperature as low as 43±20 μK as opposed to the 240 μK which was theoretically the Doppler cooling limit. This rather shocking result was quickly confirmed independently and virtually simultaneously by two separate groups at Stanford University and the E'cole Normale Superieure.[8,9] From the results of these experiments, it was clear that the previous theory and understanding of the laser cooling mechanism were incomplete.[10] The explanation for this sub-Doppler cooling was the presence of an additional cooling force originating from the Zeeman sublevels of the atoms and the shifting of these sublevels due to gradients in the polarization of the cooling lasers.[11] The discovery, explanation, and measurement of laser cooling led to the 1997 Nobel Prize in Physics being award jointly to Steven Chu,

Claude Cohen-Tannoudji and William Phillips "...for development of methods to cool and trap atoms with laser light."

The use of laser cooling techniques for the efficient generation of a very cold cloud of atoms (~100 μK) with an appreciable number of atoms (>10^7) was the first step on the path to the creation of a Bose-Einstein condensate (BEC) in a dilute atomic vapor. The demonstration of the BEC was experimentally realized by three different groups in 1995.[12,13,14] This research led to the 2001 Nobel Prize in Physics being awarded jointly to Eric Cornell, Wolfgang Ketterle and Carl Wieman "...for the achievement of Bose-Einstein condensation in dilute gases of alkali atoms, and for early fundamental studies of the properties of the condensates."

In the time since the creation of the first BEC, the cooling and trapping of Fermionic atoms has also been demonstrated.[15,16] When these trapped atoms were cooled below the Fermi limit, a degenerate Fermi gas was created.[17] It has also been recently demonstrated that it is possible to create an all-optical BEC in a trap formed by tightly focused laser beams without the magnetic field components.[18] Currently, the study of BEC and degenerate Fermi gases is a very active area of research.

1.2 The Use of Light Forces for Nanoscale Fabrication

While the slowing or cooling of neutral atoms with light forces was being investigated and perfected, many other experiments studying light forces on neutral atoms were being performed as well. As early as 1978, laser light forces were used to focus and deflect atomic beams.[19] Since that time, many experiments have been performed in which atoms have been diffracted from a standing wave laser, allowing the laser beams to function as mirrors, lenses, waveguides or variable intensity beamsplitters for a beam of

atoms.[20] This category of interaction is loosely referred to as "atom optics" due to the obvious analogy with standard light optics. A thorough review of the myriad other atom optics applications and experiments would be too extensive for this thesis and may be found in the literature.[21,22]

The combination of laser cooling and atom optics techniques opens up a very exciting and practical application: nanofabrication.[23] Nanolithography is the patterning of a substrate with nanoscale features via exposure to a beam of light or material particles. Due to diffraction effects, typically the smallest lithographic feature that can be written is proportional to the wavelength of the beam used for patterning. Even with deep UV light this still limits the ultimate feature size to ~100 nm. In contrast, an atom's deBroglie wavelength is on the order of 10 pm – four orders of magnitude less. Despite this tremendous decrease in beam diffraction, an atom beam's greatest advantage over traditional lithographic beams is that atoms possess electronic energy levels that can be accessed with lasers. This ability to "talk to" the atom beam suggests entirely new methods of nanolithography. Nanolithography utilizing beams of neutral atoms can be broadly put into two categories: direct deposition via standing wave laser focusing and resist patterning via exposure to an atom beam.

1.3 Direct Write Atom Lithography

Direct deposition via standing wave focusing is commonly called direct write optical lithography (DWOL). A schematic of this technique is shown in Figure 1.1. In this technique a near resonant standing wave laser beam is introduced perpendicular to an atom beam and parallel to a deposition substrate. The laser exerts a force on the atoms such that they are pushed into the nodes or anti-nodes of the standing wave. The standing

wave laser beam acts as an array of atom lenses, focusing the atoms into structures separated by one-half the wavelength of the light. This atom focusing technique can be used to fabricate very small (<100 nm) highly periodic structures if the atoms are deposited onto the substrate as they are focused by the laser. The force exerted on the atoms by the laser is quite small, however, and the atoms must be highly collimated perpendicular to the laser beam (usually by laser cooling techniques) to insure proper focusing.

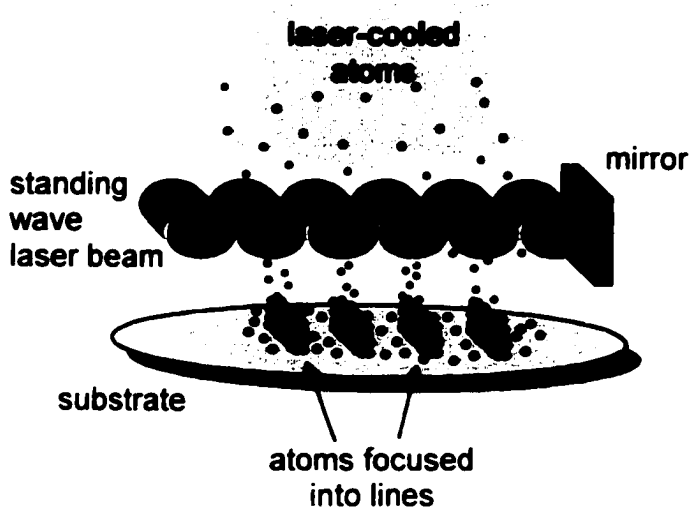

Figure 1.1 A schematic of the direct write optical lithography technique.

DWOL was first demonstrated in sodium in 1992 by Timp et al. at AT&T Bell Laboratories.[24] In this experiment, a standing wave at 589 nm was used as an array of cylindrical lenses to focus the sodium atom beam into a grating with a periodicity of 294.3 nm ($\lambda/2$). Since then several species of atoms have been focused and deposited in both one and two dimensions: chromium in 1993 and 1997,[25,26] aluminum in 1995,[27] and cesium in 1997.[28] The most recent DWOL efforts have concentrated on technologically

interesting atoms such as gallium at Colorado State University, indium at the University of Bonn,[29] and iron at the Eindhoven University of Technology.[30]

The main advantage that this technique has over other nanolithography techniques is that the atoms are patterned directly onto a substrate. No resist sensitive to the atoms is required, no post-deposition processing of the substrate is needed to transfer the pattern permanently to the substrate, and the patterns are formed from the atoms of interest themselves. When the atoms are technologically interesting, this can be quite important. Specifically, chromium and aluminum are excellent conductors and are interesting for this reason. The group III atoms such as aluminum, gallium, and indium are important because of their role in the III-V semiconductor system and iron is of interest for fabricating giant magneto resistance materials.

1.4 Metastable Atom Beam Lithography

A second example of neutral atom nanolithography is the use of a metastable atom beam to pattern a substrate sensitive to the impact of the atoms. A schematic of this technique is shown in Figure 1.2. Prior to exposure to the metastable beam, a resist - which is a thin layer of material sensitive to the lithographic beam - is pre-coated on the substrate. When a metastable atom impacts the resist, it decays to the ground state and imparts its internal energy to the resist. The release of this energy causes a chemical change in the resist. After exposure to the atom beam the substrate is etched and the resist areas chemically altered by the atoms will react differently to the etchant than the unexposed areas. Therefore to create a pattern, it is necessary only to control where the atoms hit the resist. A physical mask placed in close proximity to a substrate can be used to "shadow" the substrate. Those atoms making it through the mask will impact the

resist-coated substrate and transfer the pattern of the mask to the substrate. In Figure 1.2, the gap between the mask and the substrate is greatly exaggerated. Typically the mask would be in contact with the substrate. This is then called "contact lithography".

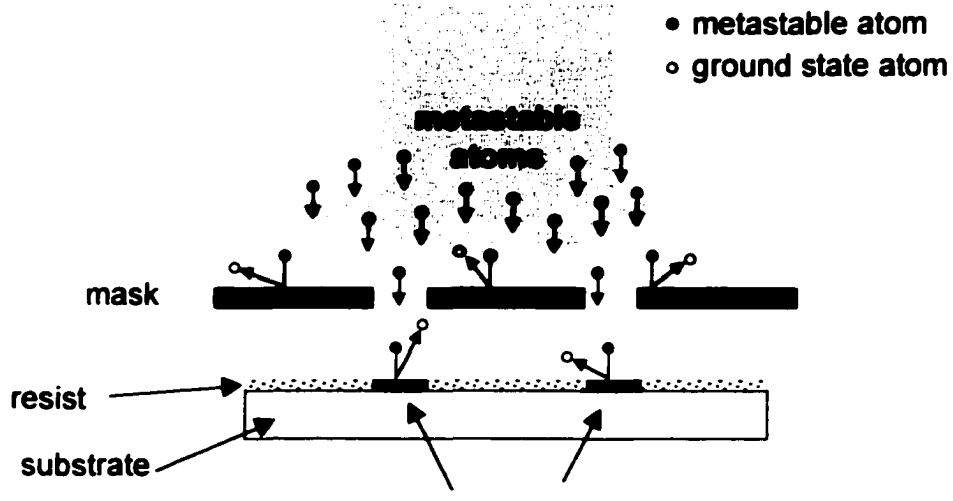

Figure 1.2 The metastable atom beam lithography technique.

Johnson et al. at Harvard demonstrated this technique using a metastable argon (Ar*) beam to transfer 80 nm features to substrates of silicon, silicon dioxide and gold.[31] At Colorado State, we later achieved an order of magnitude increase in efficiency using a metastable neon (Ne*) beam to transfer 50 nm and 500 nm features to a GaAs substrate.[32] Scanning electron microscope (SEM) micrographs of the GaAs nanostructures after etching are shown in Figure 1.3. The 50 nm pillars have an aspect ratio of greater than 2:1, which at the time was the highest aspect ratio features ever fabricated using neutral atom lithography. A thorough description of this metastable neon experiment is presented in Appendix one.

Some of the limitations of this technique were the requirement of a physical mask that was fragile (due to its physical size), hard to manufacture, and limited to one

configuration. The process was time consuming, with reasonable resist formation requiring at least 12 hours of exposure to the metastable beam. Despite our knowledge of the resist composition, the resist formation process was not very well understood. In addition, the transfer of the pattern to the substrate was highly dependent on the etching process and the nature of the substrate. After approximately a year of investigation into using a neutral metastable atom beam as a practical method for nanolithography, it was decided that DWOL offered a more attractive avenue of research.

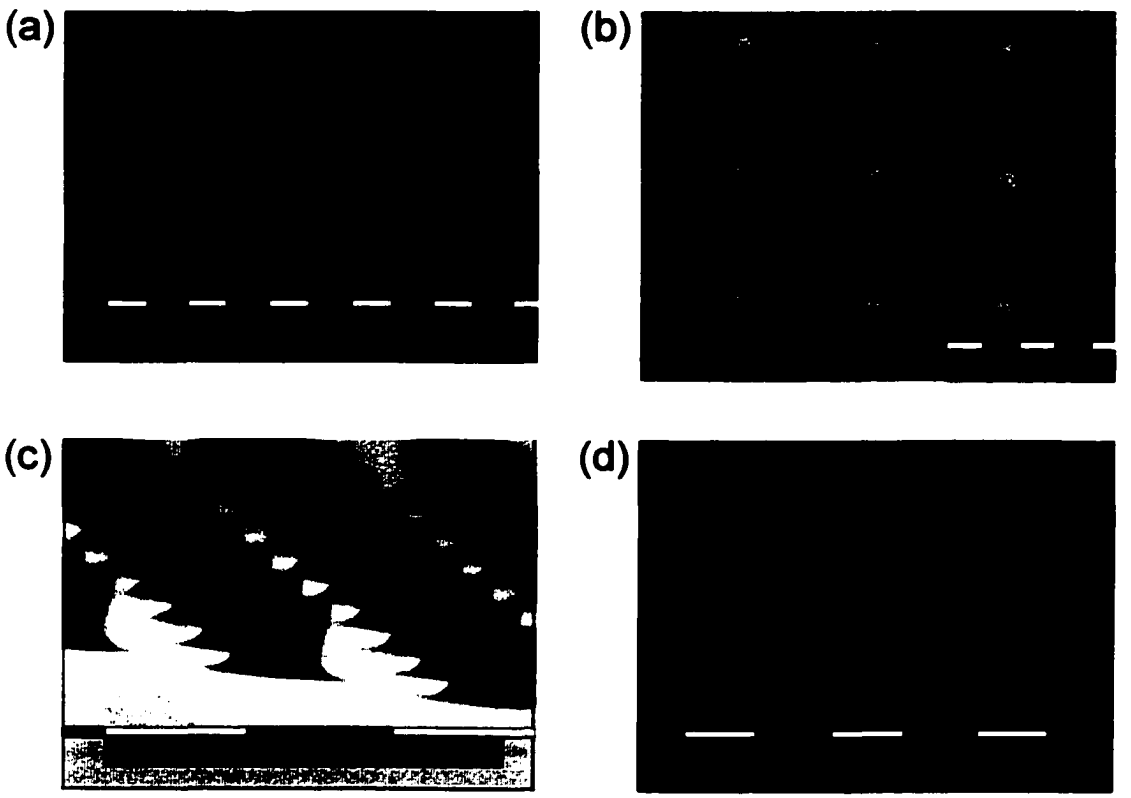

Figure 1.3 SEM images of GaAs nanostructures. (a) The 50 nm diameter pillars. The SEM view angle is 60°. (b) Same as (a) but viewed at 0°. (c), (d) The 500 nm squares viewed at 90° and at 60° respectively.

1.5 Statement of Thesis

We are interested in using the DWOL technique to fabricate Ga nanostructures. Ga is a group III element (along with the previously focused aluminum) making it interesting for useful technological applications as opposed to mere demonstrations.[33] Because Ga is one of the primary components of the modern III-V semiconductor systems (such as GaAs, GaN, etc.), the ability to optically focus Ga atoms could be an exciting step toward the growth of quantum wires or quantum dots in semiconductor heterostructures. Such heterostructures are used extensively to fabricate diode lasers. Currently, III-V heterostructures are grown in alternating layers of materials which act as regions of one dimensional charge carrier quantum confinement. A schematic of such a heterostructure is shown in Figure 1.4(a). If the laser focusing of Ga atoms could be accomplished during the growth of the heterostructure, periodic regions of alternating high and low Ga density would act as additional regions of charge carrier confinement. The Ga density variations could be written into the layers of the heterostructure. A schematic of this idea is shown in Figure 1.4(b). If focused in one dimension, quantum wires could be fabricated. If the Ga atoms were focused in two dimensions, quantum dots could be fabricated. The eventual extension of the laser focusing technique into a part of the MBE process was a major motivation for the experiments demonstrating light force manipulation of Ga.

This thesis describes my efforts to experimentally realize one dimensional laser manipulation of an atomic Ga beam. It is divided into eight chapters. Chapter two is an overview of the light forces utilized in this experiment for laser cooling and laser focusing. The experimental parameters anticipated for manipulating Ga are discussed.

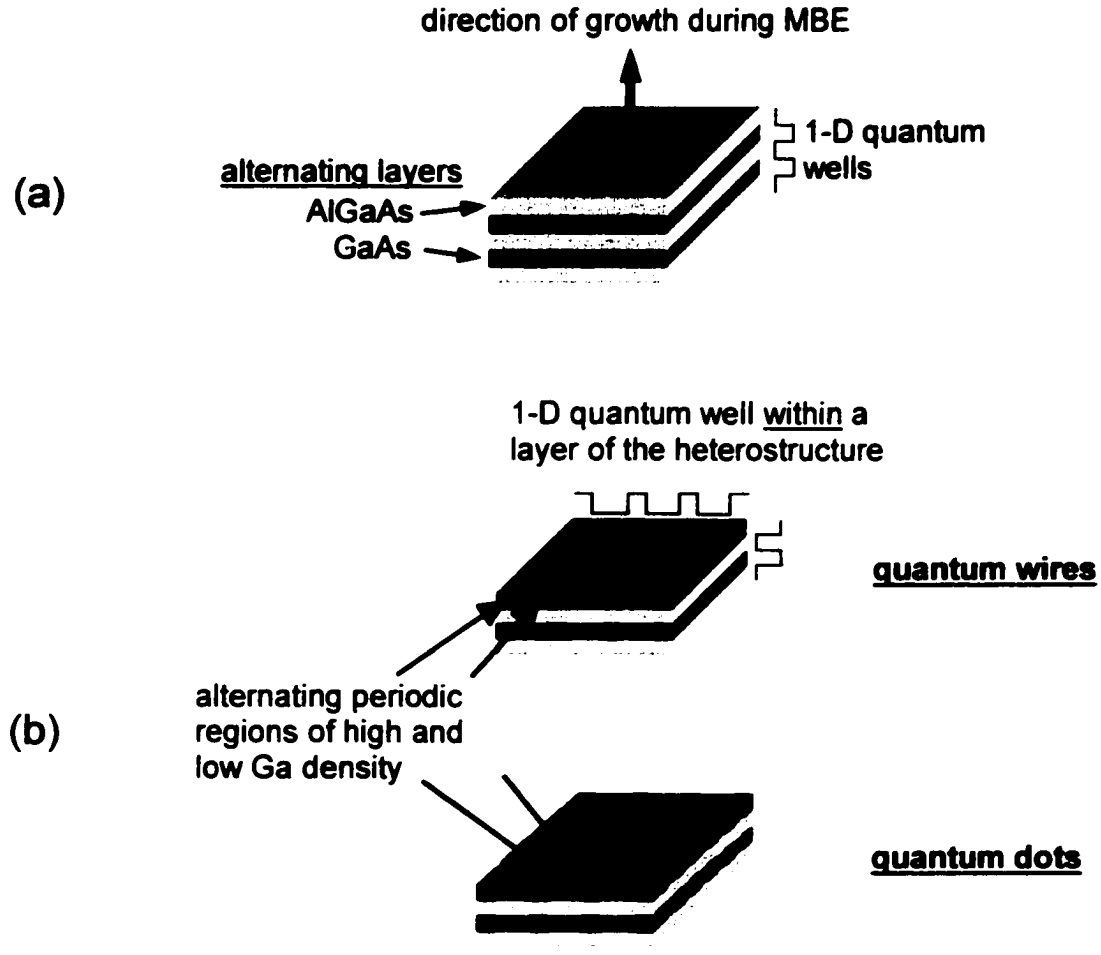

Figure 1.4 (a) Schematic of a III-V semiconductor heterostructure. (b) Schematic of the quantum confinement regions that could be created using the light force focusing technique.

Chapter three discusses the generation of a Ga beam suitable for demonstrating this light force manipulation. Chapter four covers the development of two single frequency lasers – one at 295 nm and one at 417 nm – required for laser spectroscopy and to demonstrate laser cooling and focusing. Understanding the hyperfine structure of the Ga atom is essential to both the laser cooling and focusing. Therefore, Chapter five describes hyperfine spectroscopy utilizing the two lasers given above. Chapters six and seven

cover the first demonstration of laser cooling in Ga atoms and my attempt to use the collimated beam obtained thereby to demonstrate direct write optical lithography.

Chapter eight summarizes the major results of this work, describes what improvements could be made for the next generation of experiments, and also comments on the future application of the techniques developed herein to growing quantum confinement structures (such as quantum dots or quantum wires) in III-V semiconductor heterostructures.

REFERENCES

[1] T.W. Hänsch and A.L. Schawlow, "Cooling of gases by laser radiation," Opt. Comm. **13**, 68 (1975)

[2] V.I. Balykin, V.S. Letokhov, and V.I. Mishin, "Cooling of sodium atoms by resonant laser emission," Sov. Phys. JETP **51**, 692 (1980)

[3] J. Prodan, A. Migdall, W.D. Phillips, I. So, H. Metcalf, and J. Dalibard, "Stopping atoms with laser light," Phys. Rev. Lett. **54**, 992 (1985)

[4] W. Ertmer, R. Blatt, J.L. Hall and M. Zhu, "Laser manipulation of atomic beam velocities: demonstration of stopped atoms and velocity reversal," Phys. Rev. Lett. **54**, 996 (1985)

[5] V.I. Balykin, V.S. Letokhov, and A.I. Sidorov, "Radiative collimation of an atomic beam by two-dimensional cooling by a laser beam," JETP Lett. **40**, 1026 (1985)

[6] S. Chu, L. Hollberg, J.E. Bjorkholm, A. Cable, and A. Ashkin, "Three-dimensional viscous confinement and cooling of atoms by resonance radiation pressure," Phys. Rev. Lett. **55**, 48 (1985)

[7] P.D. Lett, R.N. Watts, C.I. Westbrook, W.D. Phillips, P.L. Gould, and H.J. Metcalf, "Observation of atoms laser cooled below the Doppler limit," Phys. Rev. Lett. **61**, 169 (1988)

[8] J. Dalibard, C. Salomon, A. Aspect., E. Arimondo, R. Kaiser, N. Vansteenkiste, and C. Cohen-Tannoudji, "New schemes in laser cooling," in *Atomic Physics 11*, S. Haroche, J.C. Gay, and G. Grynberg, eds. (World Scientific, Singapore, 1989), p. 199

[9] S. Chu, Y. Shevy, D. Weiss, and P. Ungar, "Laser cooling due to atomic dipole orientation," in *Atomic Physics 11*, S. Haroche, J.C. Gay, and G. Grynberg, eds. (World Scientific, Singapore, 1989), p. 636

[10] A thorough description and review of these early laser cooling experiments can be found in P.D. Lett, W.D. Phillips, S.L. Rolston, C.E. Tanner, R.N. Watts, and C.I. Westbrook, "Optical molasses," J. Opt. Soc. Am. B **6**, 2084 (1989)

[11] J. Dalibard and C. Cohen-Tannoudji, "Laser cooling below the Doppler limit by polarization gradients: simple theoretical models," J. Opt. Soc. Am. B **6**, 2023 (1989)

[12] M.H. Anderson, J.R. Ensher, M.R. Matthews, C.E. Weiman and E.A. Cornell, "Observation of Bose-Einstein condensation in a dilute atomic vapor," Science **269**, 198 (1995)

[13] C.C. Bradley, C.A. Sackett, J.J. Tollett, and R.G. Hulet, "Evidence of Bose-Einstein condensation in an atomic gas with attractive interactions," Phys. Rev. Lett. **75**, 1687 (1995)

[14] K.B. Davis, M.-O. Mewes, M.R. Andrews, N.J. van Druten, D.S. Durfee, D.M. Kurn, and W. Ketterle, "Bose-Einstein condensation in a gas of sodium atoms," Phys. Rev. Lett. **75**, 3969 (1995)

[15] W.I. McAlexander, E.R.I. Abraham, N.W.M. Ritchie, C.J. Williams, H.T.C. Stoof, and R.G. Hulet, "Precise atomic radiative lifetime via photoassociative spectroscopy of ultracold lithium," Phys. Rev. A **51**, R871 (1995)

[16] F.S. Cataliotti, E.A. Cornell, C. Fort, M. Inguscio, F. Marin, M. Prevedelli, L. Ricci, and G.M. Tino, "Magneto-optical trapping of Fermionic potassium atoms," Phys. Rev. A **57**, 1136 (1998)

[17] B. DeMarco and D.S. Jin, "Onset of Fermi degeneracy in a trapped atomic gas," Science **285**, 1703 (1999)

[18] M.D. Barrett, J.A. Sauer, and M.S. Chapman, "All-optical formation of an atomic Bose-Einstein condensate, " Phys. Rev. Lett. **87**, 010404 (2001)

[19] J.E. Bjorkholm, R.R. Freeman, A. Ashkin, and D.B. Pearson, "Observation of focusing of neutral atoms by the dipole forces of resonance-radiation pressure," Phys. Rev. Lett. **41**, 1361 (1978)

[20] See, for example, D.M. Giltner, R.W. McGowan and S.A. Lee, "Atom interferometer based on Bragg scattering from standing light waves," Phys. Rev. Lett. **75**, 2638 (1995); D.M. Giltner, R.W. McGowan, and S.A. Lee, "Theoretical and experimental study of the Bragg scattering of atoms from a standing light wave," Phys. Rev. A **52**, 3966 (1995);

[21] C.S. Adams, M. Sigel, and J. Mlynek, "Atom Optics," Phys. Rep. **240**, 13 (1994)

[22] *Atom Optics*, M.G. Prentiss and W.D. Phillips, eds., Proc. SPIE **2995**, (1997)

[23] J.H. Thywissen, K.S. Johnson, R. Younkin, N.H. Dekker, K.K. Berggren, A.P. Chu, M. Prentiss, and S.A. Lee, "Nanofabrication using neutral atomic beams," J. Vac. Sci. Technol. B **15**, 2093 (1997)

[24] G. Timp, R.E. Behringer, D.M. Tennant, J.E. Cunningham, M. Prentiss, and K.K. Berggren, "Using light as a lens for submicron, neutral-atom lithography," Phys. Rev. Lett. **69**, 1636 (1992)

[25] J.J. McClelland, R.E. Scholten, E.C. Palm, and R.J. Celotta, "Laser-focused atomic deposition," Science **262**, 877 (1993)

[26] U. Drodofsky, J. Stuhler, B. Brezger, Th. Schulze, M. Drewsen, T. Pfau, and J. Mlynek, "Nanometerscale lithography with chromium atoms using light forces," Micro. Eng. **35**, 285 (1997)

[27] R.W. McGowan, D.M. Giltner, and S.A. Lee, "Light force cooling, focusing, and nanometer-scale deposition of aluminum atoms," Opt. Lett. **20**, 2535 (1995)

[28] F. Lison, H.-J. Adams, D. Haubrich, M. Kreis, S. Nowak, and D. Meschede, "Nanoscale atomic lithography with a cesium atomic beam," Appl. Phys. B **65**, 419 (1997)

[29] Dietmar Haubrich, IAP-University of Bonn, (personal communication)

[30] R. Bosch, *Ferromagnetic Nanostructures by Laser Manipulation*, Ph.D. Thesis (Eindhoven University of Technology, Eindhoven, Germany 2002)

[31] K.S. Johnson, K.K. Berggren, A. Black, C.T. Black, A.P. Chu, N.H. Dekker, D.C. Ralph, J.H. Thywissen, R. Younkin, M. Tinkham, M. Prentiss, and G.M. Whitesides, "Using neutral metastable argon atoms and contamination lithography to form nanostructures in silicon, silicon dioxide, and gold," Appl. Phys. Lett. **69**, 2773 (1996)

[32] S.J. Rehse, A.D. Glueck, S.A. Lee, A.B. Goulakov, C.S. Menoni, D.C. Ralph, K.S. Johnson, and M. Prentiss, "Nanolithography with metastable neon atoms enhanced rate of contamination resist formation for nanostructure fabrication," Appl. Phys. Lett. **71**, 1427 (1997)

[33] S.J. Rehse, R.W. McGowan and S.A. Lee, "Optical manipulation of group III atoms," Appl. Phys. B **70**, 657 (2000)

CHAPTER 2

Light Force Manipulation of Atoms: Laser Cooling and Laser Focusing

There are two primary mechanisms for exerting a force on an atom with laser light that are important for this work. The first mechanism relies on absorption and spontaneous emission of photons and exerts a non-conservative force on the atom. This is sometimes referred to as the spontaneous force or the scattering force and is very appropriate for cooling the atoms, since a removal of energy from the system is desired. The second mechanism relies on absorption and stimulated emission of photons back into the laser field. This force is conservative and is mediated by the interaction of the laser electric field and the induced electric dipole moment in the atom. Thus, it is referred to as the dipole force. The dipole force is a conservative force - the total atom kinetic energy and atom/laser interaction potential energy must remain constant. This makes this force an ideal candidate for use in atom optics experiments, including laser focusing. In this chapter I discuss the theoretical background for both the spontaneous force and the dipole force. I explain the applications of these forces as a means for laser cooling and laser focusing. I specifically discuss the particular parameters required for manipulation of gallium (Ga) atoms by means of these two forces.

2.1 The Spontaneous Force

The spontaneous force is due to the absorption and spontaneous emission of photons. To understand how the photons can exert a force on an atom, consider an atom at rest illuminated by a resonant laser beam propagating in the $\hat{x}$ direction. Such a situation is shown in Figure 2.1. Each photon in the laser beam carries a momentum $\vec{p}_{photon} = \hbar k \hat{x}$. The atom has no initial momentum, so $\vec{p}_{atom} = 0$. After absorption, the photon momentum is transferred to the atom ($\vec{p}_{atom} = \hbar k \hat{x}$) and the atom is left in an excited state. This is shown in Figure 2.1(a). Upon de-excitation of the atom by spontaneous emission a second photon is emitted. By conservation of momentum, this photon must impart a momentum kick to the atom. Unlike the absorbed photon however, the emitted photon has no preferred direction. Spontaneous emission is an isotropic process and the photon is emitted with equal probability into 4π steradians. After N spontaneous emissions the time averaged net momentum transfer to the atom from the spontaneous emission process is zero, $\langle \Delta \vec{p}_{atom} \rangle = 0$. This is shown in Figure 2.1(b). The total atom momentum change from N absorption/spontaneous emission cycles is shown in Figure 2.1(c). From the absorptions, the atom will have acquired N momentum kicks and have a new momentum $\vec{p}_{atom} = N\hbar k \hat{x}$. From the spontaneous emissions, the atom will have acquired no change in momentum. Thus, the net effect of N absorption and emission cycles is that the atom experiences an overall force pushing it in the direction of propagation of the laser. This is the spontaneous force.

2.2 Doppler Molasses

To understand how this spontaneous force can be used to cool or remove momentum from an atom, let us assume an atom with two energy levels separated by a

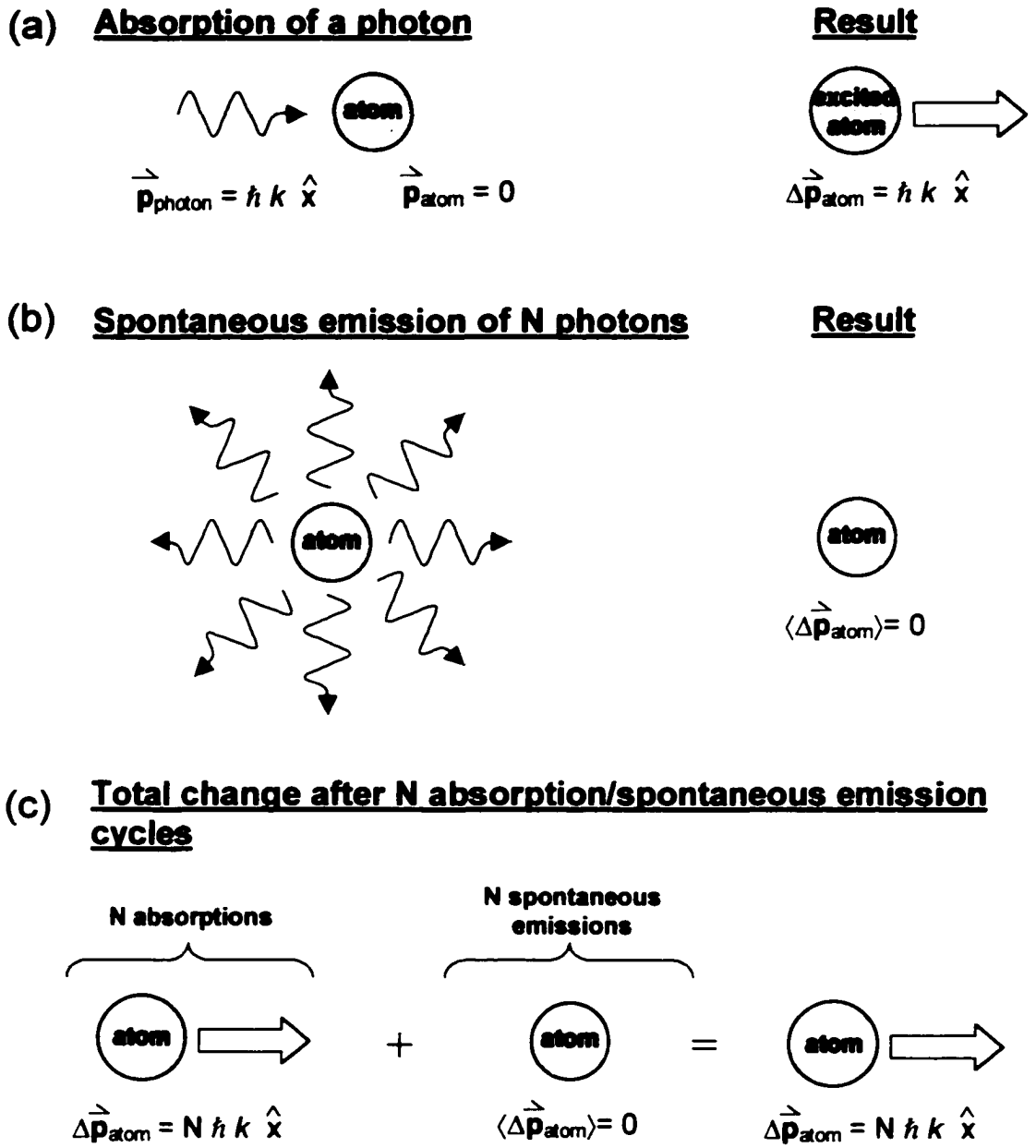

Figure 1.1 An atom exchanges momentum with photons in a laser field. (a) Photon absorption pushes atom in direction of laser. (b) Isotropic spontaneous emission imparts no net momentum to atom. (c) After N absorption/spontaneous emission cycles, the atom has net momentum in the direction of the laser.

frequency ω_0. This atom is irradiated by two counter-propagating laser beams with frequency ω and wavelength λ. The detuning of the laser - the difference between the laser frequency and the atom resonant frequency - is given by $\Delta = \omega - \omega_0$. This is shown in Figure 2.2 with the laser detuned to the red, or low frequency side, of the atom's resonance frequency.

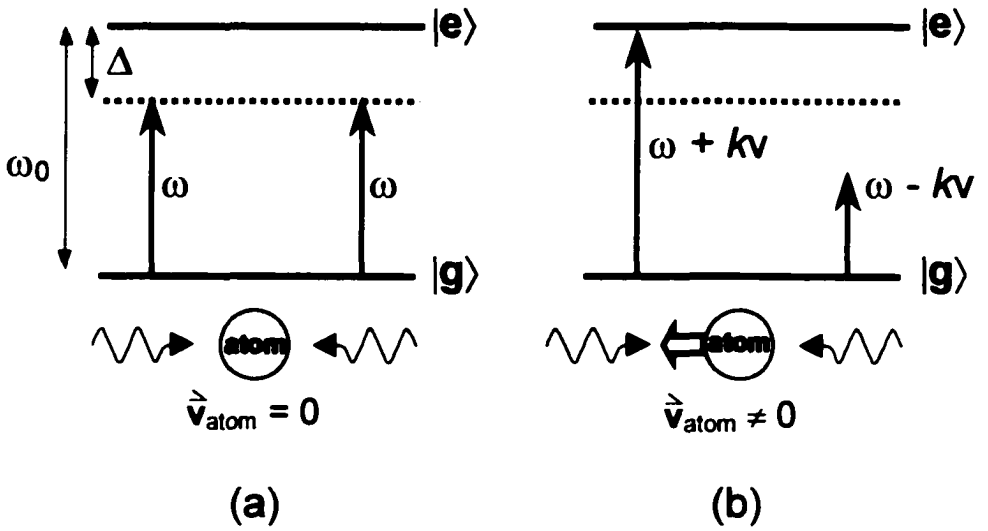

Figure 2.2 An atom illuminated by counter-propagating red-detuned lasers demonstrates Doppler cooling. (a) The atom has no velocity – both lasers equally detuned. (b) The atom has a nonzero velocity - the laser opposing the motion of the atom is tuned into resonance.

In Figure 2.2(a) the atom has no velocity along the axis of the lasers. It sees both lasers with frequency ω, detuned by an amount Δ. The atom will absorb photons from each laser beam with equal probability and the spontaneous forces will cancel out. Now, considering one-dimensional motion only, let us assume the atom has some velocity v as in Figure 2.2(b). The Doppler shift in the laser frequency that this atom experiences is $\pm 2\pi v/\lambda = \pm kv$. The laser opposing the atom's motion has a Doppler-shifted frequency $\omega + kv$, which for a red-detuned laser is closer to resonance. The laser travelling in the

same direction as the atom's motion has a Doppler-shifted frequency ω-kv, which is further from resonance. The atom will preferentially absorb photons and receive momentum kicks from the laser opposing its motion because it is tuned closer to resonance. The chance of photon absorption from the laser travelling in the same direction is decreased. Thus, the scattering rate of photons is always greater from the laser opposing the motion of the atom, and no matter which way the atom moves, it experiences a damping force. The damping force acts to cool or remove velocity from the atom. Because this force depends on the Doppler shift, this type of laser cooling is sometimes referred to as a Doppler molasses.

If the laser is detuned to the blue, or higher frequency side of the atom's resonance, the lasers will act to heat, or add velocity to the atom. This happens because the atom preferentially absorbs photons from the laser propagating in the same direction. This is an accelerating force rather than a viscous force. Thus a Doppler molasses must always utilize red detuned lasers.

2.3 Calculation of Force

The strength of the spontaneous force can be calculated.[1] Let us assume that the upper state of the transition has a lifetime τ such that the transition's natural linewidth $\Gamma = 1/\tau$. We must also assume that the irradiating laser has some intensity I. If each photon in the laser carries momentum $\hbar k$, then the average force on the atom from one laser beam is just the photon momentum times the average rate of photon absorption. This is given by

$$F = \frac{\Delta p}{\Delta t} = \hbar k \frac{\rho_{22}}{\tau} \qquad (2.1)$$

where ρ_{22} is the atomic density matrix element.[2] Writing this force in terms of the laser beam properties for an atom moving in the positive direction gives

$$F_{\pm} = \pm \hbar k \frac{\Gamma}{2} \frac{I/I_0}{1 + I/I_0 + [2(\Delta \mp kv)/\Gamma]^2} \tag{2.2}$$

where F_+ corresponds to the force from a laser propagating in the same direction as the atom and F_- is the force from a laser propagating in the opposite direction. I_0 is the saturation intensity and is the intensity at which the power broadening of the line is $\sqrt{2}$. If the atom is illuminated by two counter propagating laser beams as in the Doppler molasses, and if the lasers do not interact, then the total force on the atom is given by $F_+ + F_-$. Figure 2.3 shows the laser force vs. atom velocity for a moving Ga atom illuminated by two counter-propagating lasers. Figure 2.3(a) shows both F_+, F_- and the total force $F_+ + F_-$ for lasers with a red detuning $\Delta = -\Gamma/2$ and a normalized intensity of $I/I_0 = 1.0$. Note that for negative velocities the total force is always positive and for positive velocities the total force is always negative. The Doppler molasses acts as a viscous medium to the atom and the cooling will proceed most effectively in the linear regime around the origin. Figure 2.3(b) shows the total force vs. velocity curves for five different detunings. Note that the further from resonance the laser is detuned the wider the regime of linear slope near the origin. Therefore to cool faster atoms, the laser must be detuned further from resonance. The downside of this is that the when the laser is detuned further from resonance than $-\Gamma/2$, the cooling proceeds more slowly. This can be seen by the decrease in slope of the total force curves near the origin. Figure 2.3(c) shows the total force vs. velocity curves for three different normalized intensities with a red detuning $\Delta = -\Gamma/2$.

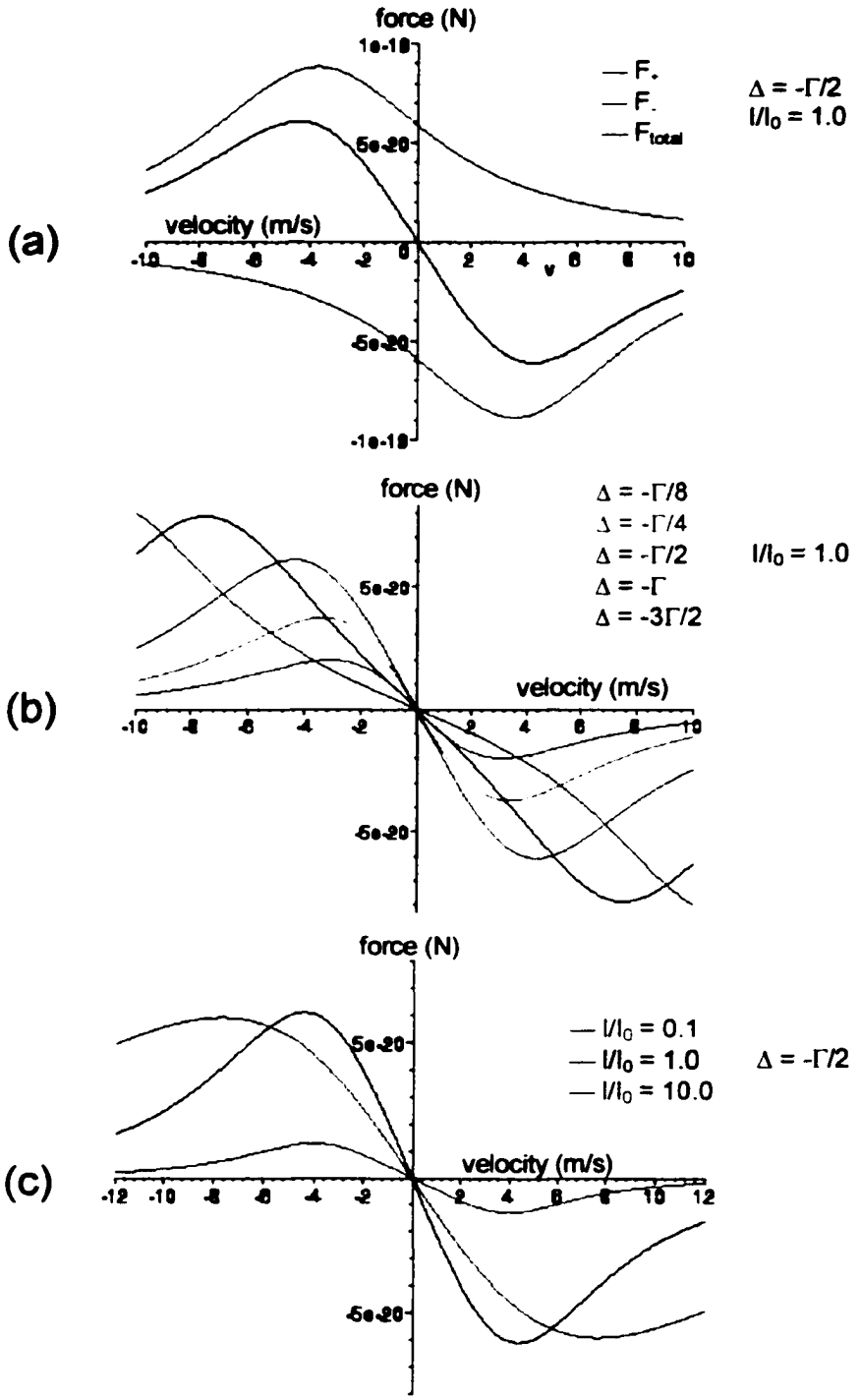

Figure 2.3 Force on an atom from counter-propagating laser beams vs. atomic velocity. (a) Total force on the atom. (b) Force for five different detunings. (c) Force for three different normalized intensities.

Knowing this force as a function of velocity, it is possible to iteratively calculate the damping using Newton's laws. Figure 2.4 shows the calculated velocity of Ga atoms as a function of the time spent in a one-dimensional molasses for four different initial velocities. For each initial velocity, the damping from two different molasses detunings is shown. Figure 2.4(a) shows the damping with a normalized intensity $I/I_0 = 0.10$ and Figure 2.4(b) shows the damping with a normalized intensity $I/I_0 = 1.00$. Note that at low velocities (< 4 m/s which was typical of atoms in our atomic beam), a smaller detuning is preferable. Again, a larger detuning is more efficient for cooling faster atoms, but will not cool the slow atoms very effectively.

2.4 The Doppler Limit

An atom being damped in such a way can not be cooled indefinitely. There is heating in the system caused by the random nature of the photon absorptions and spontaneous emissions. The cooling force we have described so far is an average force. Each individual photon interaction still imparts kinetic energy to the atoms and this acts as a heating source. In the cooling process $\langle v \rangle = 0$ but $\langle v^2 \rangle \neq 0$. The cooling of the atom will eventually stop and a minimum rms temperature will be reached when the cooling rate is equal to the heating rate, or the system is in thermodynamic equilibrium. In the limit of low intensity ($I/I_0 \ll 1$) and low velocity ($|kv| \ll \Gamma$) the minimum temperature that can be reached is given by

$$k_B T_{min} = \frac{\hbar\Gamma}{4} \frac{1 + (2\Delta/\Gamma)^2}{2|\Delta|/\Gamma} \tag{2.3}$$

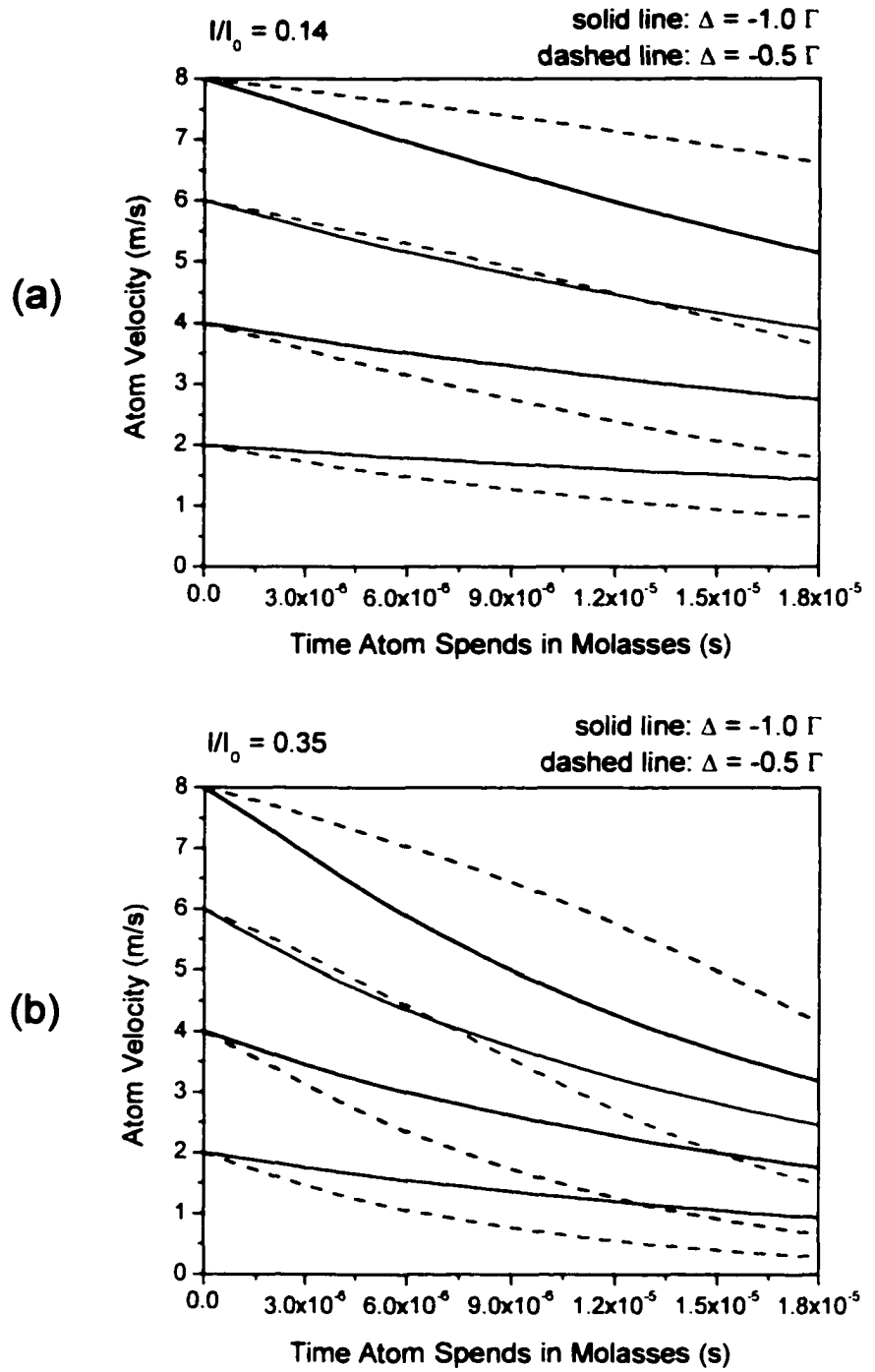

Figure 2.4 Gallium atom velocity as a function of time spent in a Doppler molasses for different initial velocities.

For any given Γ, this temperature reaches a minimum when the detuning is chosen to be $\Delta = -\Gamma/2$. This gives $k_B T_{min} = \hbar\Gamma/2$ which is called the "Doppler-cooling limit". This Doppler cooling limit corresponds to a minimum velocity, v_D, in one dimension.

$$\frac{1}{2} m v_D^2 = \frac{1}{2} k_B T_{min} \tag{2.4}$$

Figure 2.5 shows a graph of the time required to cool to the Doppler limit for atoms with an initial velocity of 4.5 m/s as a function of the normalized intensity and the detuning.

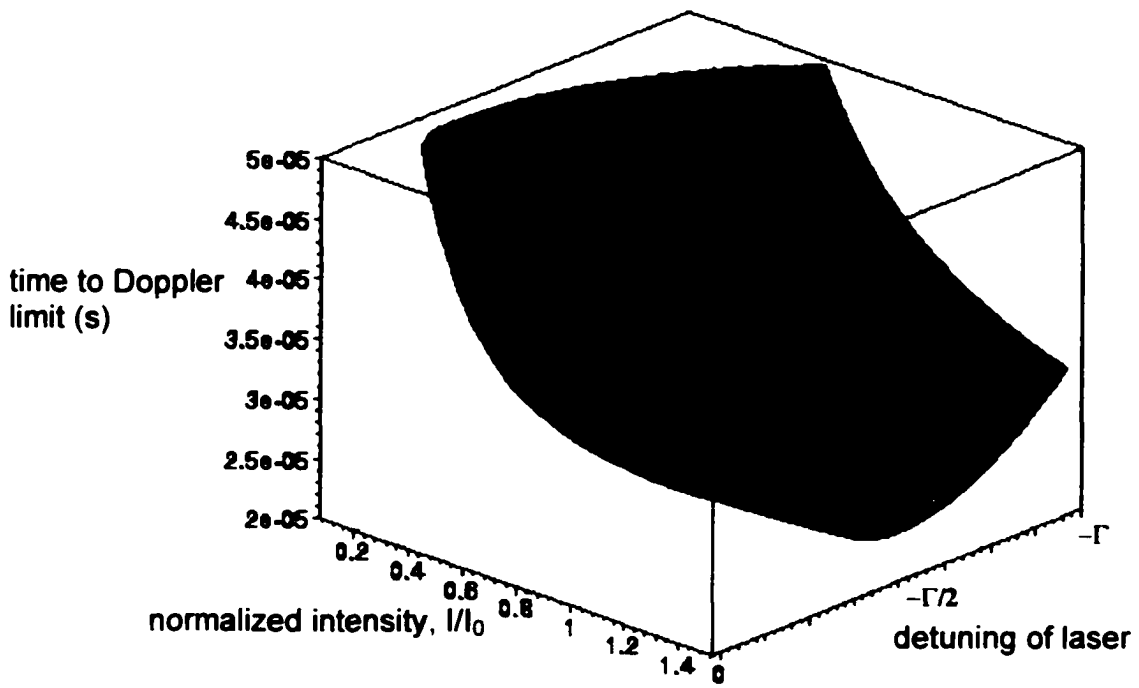

Figure 2.5 The time required for an atom in a Doppler molasses to cool to the Doppler limit as a function of the normalized intensity and laser detuning.

It is clear that the shortest cooling times occur for a detuning of $\Delta = -\Gamma/2$ and a high value of I/I_0. However for values of $I/I_0 \geqq 1$, saturation effects can disrupt the cooling process

and this graph is not valid. With appropriately chosen parameters, this graph implies that it would take an atom approximately 25 msec to reach the Doppler limit. For an atom travelling at 600 m/s (typical of atom velocities in the beams we will be discussing) this tells us a laser/atom interaction region of 1.5 cm is required to give the atom time to cool completely to the Doppler limit.

2.5 Polarization Gradient Cooling

As mentioned in Chapter one, in 1988 three groups almost simultaneously observed cooling of atoms well below the theoretical limit, T_{min}, derived above.[3,4,5] The explanation for this sub-Doppler cooling was the presence of an additional cooling force originating from the Zeeman sublevels of the atoms and the shifting of these sublevels due to gradients in the polarization of the cooling lasers. In the theory of Doppler cooling as explained above, nothing whatsoever was said about the polarization of the laser beams and the atom was modeled as a two level system. We must now amend this simplistic theory to account for the experimental realization of the sub-Doppler cooling.[6]

There are three important considerations that account for sub-Doppler cooling. (1) The laser beams that comprise the Doppler molasses exert an additional force on a moving atom due to non-adiabatic changes in the internal state of the atom caused by spatial variations in the laser field. (2) For atoms that have several Zeeman sublevels in the ground state, there is a characteristic time, the optical pumping time, that is different than $\tau = 1/\Gamma$ as described above. The optical pumping time is the time it takes for an atom to be transferred from one sublevel to another by absorption/emission cycles. This time is $\tau_p = 1/\Gamma'$ where Γ' can be considered to be the width of the ground state. (3) The additional frictional force is only relevant if the internal state of the atom depends

strongly on the position of the atom in the laser field. If this is true, then when the atom moves through the laser there are large changes in the internal state of the atom and large non-adiabatic effects leading to a large frictional force.

Spatial variations in the laser field can result in the strong dependence of the atom's internal state with position. Such strong spatial variations can be created by polarization gradients in the laser field. For a one-dimensional Doppler molasses, there are two types of polarization gradients that can be created. In the first type, the two counter propagating lasers have opposite circular polarizations (σ^+ and σ^-). This is commonly called a "corkscrew" gradient. In this gradient scheme the polarization of the light rotates along the direction of the laser beam, but it maintains its ellipticity. In the second polarization gradient configuration the two counter propagating laser beams have orthogonal linear polarizations. This is commonly called the "lin $\perp$ lin" configuration. These two polarization gradient schemes operate on different mechanisms for cooling. Since the lin $\perp$ lin configuration is the one most commonly used in laser cooling experiments and is the one intended for use in this study of Ga, the discussion on sub-Doppler cooling will be limited to it alone.

2.6 Lin $\perp$ Lin Polarization Gradient Cooling

In lin $\perp$ lin polarization gradient cooling the laser beam's polarization varies in space on a length scale of λ, the wavelength of the laser light. This situation is show in Figure 2.6. The counter-propagating laser beams have orthogonal polarizations: beam 1 propagating in the +z direction has a polarization ε_x and beam 2 propagating in the –z direction has a polarization ε_y. At z=0 the resulting polarization is linear (ε_1). At $\lambda/8$, it is circular (σ^-). At $\lambda/4$, it is linear again (ε_2). At $3\lambda/8$, it is circular (σ^+). At $\lambda/2$ it is

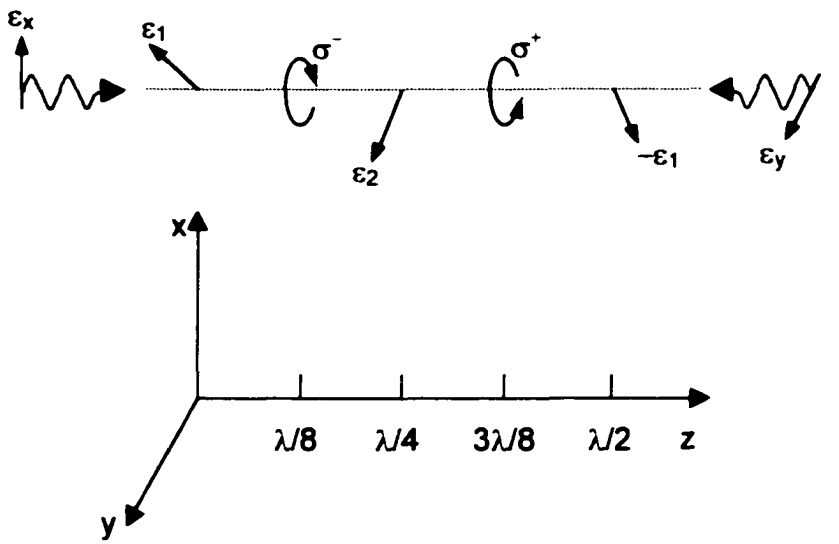

Figure 2.6 Polarization in a standing wave created by two opposing waves of orthogonal linear polarization (lin ⊥ lin).

linear ($-\varepsilon_1$). In between the positions of pure linear and pure circular polarization the polarization is elliptical. With regards to polarization, this gradient is periodic with a period $\lambda/2$, but is truly periodic in λ when the phase is considered.

Into this polarization gradient let us place a two level atom where the lower level is a J=1/2 ground state with two Zeeman sublevels $m_J = +1/2$ and -1/2 and the upper level is a J=3/2 state with four Zeeman sublevels, $m_J = +3/2, +1/2, -1/2$, and $-3/2$. A diagram of this atomic energy level scheme and the relevant Clebsch-Gordon coefficients for transitions between Zeeman sublevels is shown in Figure 2.7. Assuming red detuned laser light in the polarization gradient, this atom will experience splitting of the ground and excited levels due to the a.c. Stark shift. The amount of splitting is determined by the polarization and intensity of the laser light. Figure 2.8 shows the Stark shifting and allowed transitions under linearly polarized light, σ^+ circularly polarized light, and σ^-

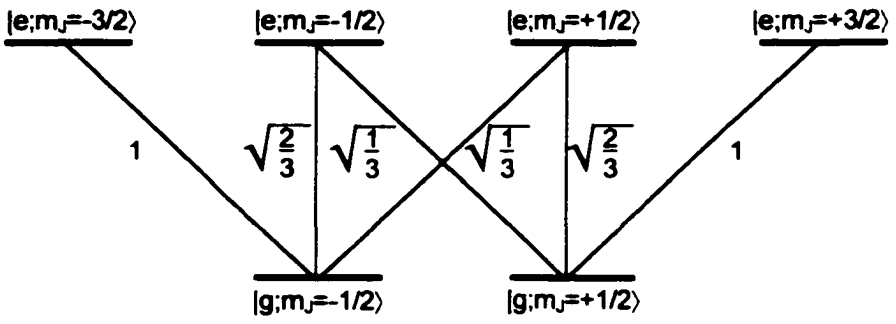

Figure 2.7 Clebsch-Gordon coefficients for a J=1/2 → J=3/2 transition.

circularly polarized light. The dashed line indicates the energy levels in the absence of any laser field. With σ^+ light, the largest positive m_J sublevels experience the largest Stark shift. For σ^- light, it is the largest negative m_J sublevels which experience the largest shift. With linearly polarized light the Stark shift is equal for the $m_J=\pm 1/2$ sublevels.

This a.c. Stark shifting is position dependent because the polarization varies in space across the polarization gradient. If the atom has any velocity along the axis of the laser beams, it rapidly moves through regions of alternating polarization and experiences shifting Zeeman sublevels. As the atom shifts sublevels, it is constantly gaining or losing potential energy and must, by conservation of energy, be gaining or losing a corresponding amount of kinetic energy. Thus, the atom's kinetic energy can be removed by gaining atomic potential energy. Consider an atom moving along the polarization gradient, as shown in Figure 2.9. Assume the atom starts at $\lambda/8$ in a region of σ^- light and is in a potential energy valley of the $m_J = -1/2$ state. Remember that the time it takes for this atom to be pumped to a different m_J level is given by the pumping time, τ_p, as

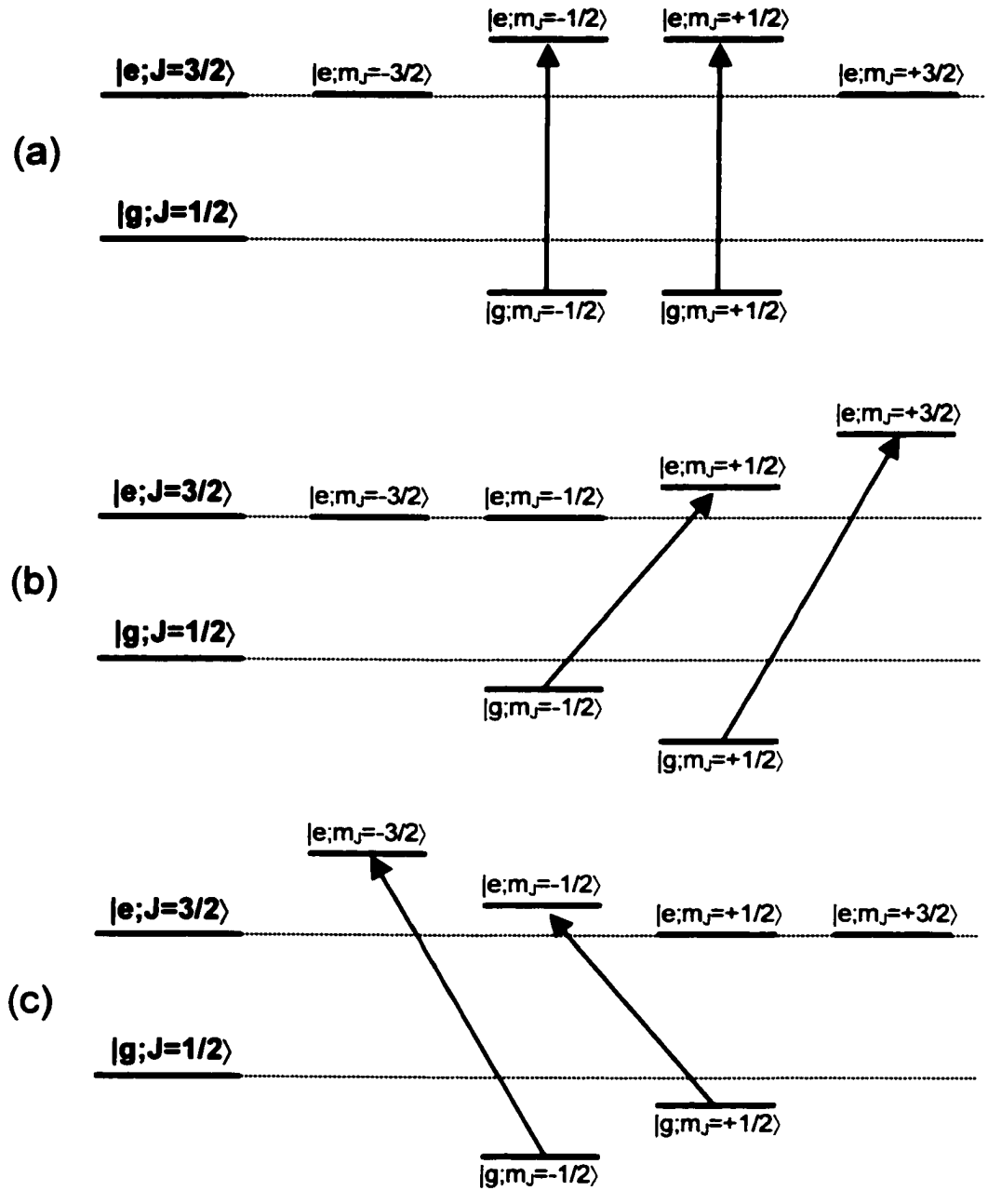

Figure 2.8 Energy level diagram for a J=1/2 → J=3/2 transition exhibiting polarization dependent a.c. Stark shifting. (a) Transition induced by linear polarized light. (b) Transition induced by σ^+ circularly polarized light. (c) Transition induced by σ^- circularly polarized light.

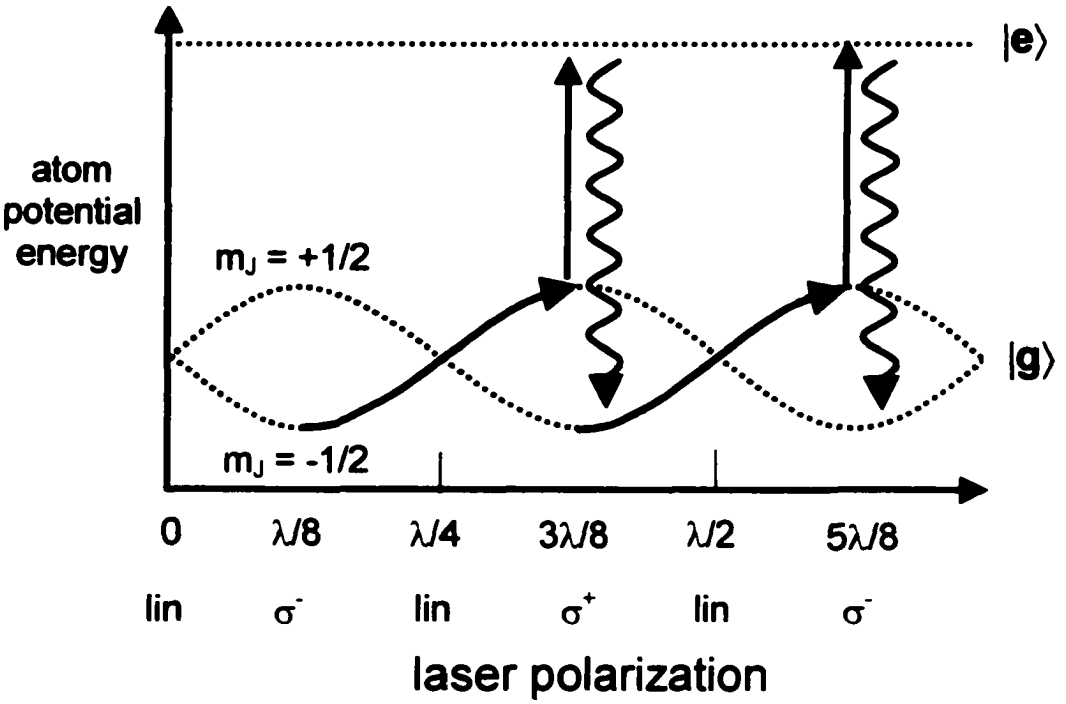

Figure 2.9 Sisyphus cooling due to a standing wave laser in the lin ⊥ lin configuration.

defined above. If the velocity of the atom is such that it travels a distance of $\lambda/4$ during this time τ_p, then on average the atom will remain in the same sublevel while climbing the potential hill due to the changing polarization before it is optically pumped to the other sublevel, m_J =+1/2 which is now lower in potential energy. In the presence of red-detuned laser light, the atom will preferentially populate the lowest shifted energy level. The atom will repeat this process over and over, losing kinetic energy every time it climbs a potential hill before being pumped away. This continues until the atom does not have enough kinetic energy to climb the potential hill any more. Because this atom effectively toils like Sisyphus, the mythic Greek character who was doomed to repeatedly

push a rock to the top of a hill, this cooling mechanism has been dubbed the Sisyphus effect.

This Sisyphus cooling is much more effective than the Doppler molasses but acts on atoms with a smaller velocity. Specifically, the Sisyphus cooling is most effective when the atom travels a distance $\lambda/4$ in the time τ_p. This puts a fundamental limit on the initial velocity the atom may have along the direction of the laser beam before the Sisyphus force can cool the atom. This velocity is called the critical velocity and is denoted v_c. In practice, the two cooling mechanisms are used at the same time, with the same laser beam. Initially the fast atoms (several m/s) are slowed by the Doppler force to much lower velocities at which time the Sisyphus force becomes effective and very quickly cools the atoms to their ultimate limit. Figure 2.10 shows the force exerted by the Doppler molasses, the force exerted by the Sisyphus cooling, and the net force on a Ga atom. The detuning is $\Delta = -\Gamma$ and the normalized intensity is $I/I_0 = 0.1$. The Sisyphus force is characterized by a new damping coefficient α

$$\alpha = -\frac{3}{2}\hbar k^2 \frac{2\Delta}{\Gamma} \tag{2.5}$$

which gives rise to a new force

$$F = -\frac{\alpha}{2\pi} \frac{v}{1 + v^2/v_c^2} \tag{2.6}$$

where the critical velocity is given by

$$v_c = \Gamma \frac{I}{I_0} \frac{(\Gamma/2\Delta)^2}{k} \tag{2.7}$$

In the case of Ga to be discussed later, $v_c \approx 0.18$ m/s.

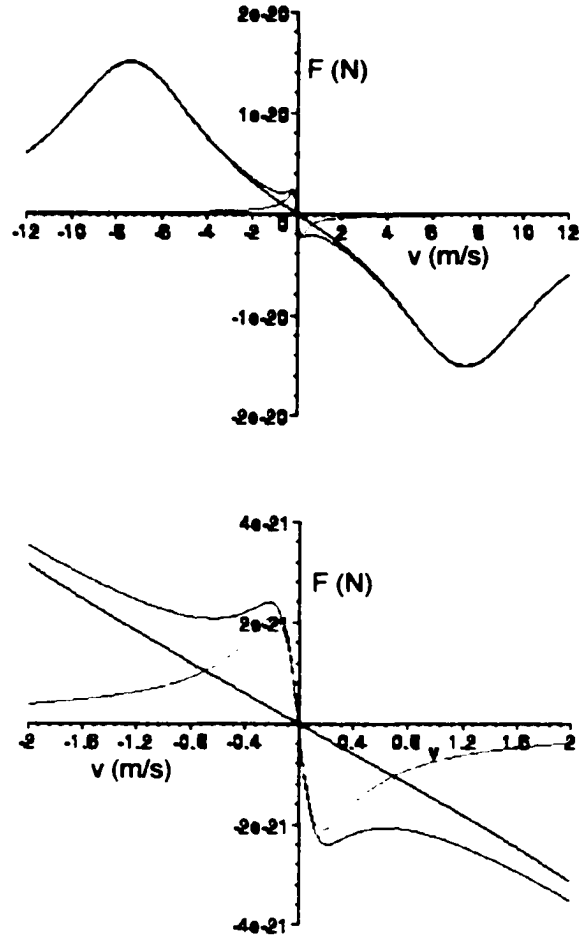

Figure 2.10 (a) The total force (brown) on an atom in a lin ⊥ lin polarization gradient as a function of the atomic velocity in the direction of the laser. The Doppler force is shown in black. The Sisyphus force is shown in green. (b) Same graph as (a), detailing the region around the origin.

In Figure 2.10, the Sisyphus force is also linear near the origin, although over a much smaller region – specifically for $v < v_c$. The slope is much higher however, indicating a much stronger damping force. Although this strong damping regime is not encountered until the atom velocity falls below the critical velocity, if we look at the total force exerted on the atom, it is easy to see that even when the velocity has fallen to five

times v_c it is already experiencing a stronger force than it would due to the Doppler molasses alone. In this way, the atomic velocity in the lin ⊥ lin beam is very quickly damped to near zero.

The ultimate limit achievable by laser cooling can be no lower than the amount of energy imparted by a single photon impact. This is called the "recoil limit". This energy limit can be obtained by setting the thermal energy of atom in one dimension (1/2 $k_B T$) equal to the kinetic energy imparted to the atom by one photon. This limit is then

$$k_B T_R = \frac{(\hbar k)^2}{m} \tag{2.8}$$

where T_R is the recoil temperature. In practice, the experimental lower cooling limit is typically several times T_R.

2.7 The Dipole Force

The force utilized for standing wave focusing of neutral atoms is fundamentally different from the spontaneous force used for cooling that was described in Section 2.1. Near resonant light illuminating a neutral atom can also exert another force on the atom. This force is due to an induced dipole moment in the atom. Although the intrinsic dipole moment of an atom is zero, the oscillating electric field in the laser can induce an electric dipole moment, which will then experience a force if a gradient in laser intensity is present. For this reason, this force is also called the gradient force.

To understand the dipole force, we can write the potential energy of an atom with an induced dipole moment **p** as $U = -\mathbf{p} \bullet \mathbf{E}$. The direction of **p** in relation to **E** can be understood if we recognize that this system is analogous to a driven simple harmonic oscillator. In such a driven system, if the driving frequency is below the natural resonance frequency of the system, the oscillation of the system is in phase with the

driver. If the driving frequency is greater than the natural resonance, then the oscillation and the driver are π out of phase. In the same way, if the resonant frequency of the laser ω is smaller than the atomic resonance ω_0 ($\omega < \omega_0$) then **p** and **E** are parallel, or in phase, and $U = -pE$. If $\omega > \omega_0$, then **p** and **E** will be anti-parallel, or π out of phase with each other, and $U = pE$. This potential will then give rise to a force if there is any gradient in the oscillating field, $\mathbf{F} = -\nabla U$. Thus the larger the gradient, the larger the resulting force.

The simplest way to maximize the gradient of the oscillating electric field in a propagating laser is to create a standing wave. In such a wave, the intensity changes from zero at the nodes to a maximum at the anti-nodes over a distance $\lambda/4$. The direction of the force is determined by the laser detuning. If the laser is red detuned ($\omega < \omega_0$), the atoms will experience a potential energy minimum at the anti-nodes where E is maximum. The atoms are said to be "strong field seeking", since the force acts to push them into the standing wave anti-nodes. Conversely, if the laser is blue detuned ($\omega > \omega_0$), the atom's potential energy minimum is at the standing wave nodes. The atoms are called "weak field seeking" since the force acts to push them into the nodes.

Unlike the spontaneous force, the dipole force is a conservative force and is mediated by absorption and stimulated emission. This process conserves momentum. In fact, the efficiency will be degraded if spontaneous emission does occur, so steps must be taken to prevent this. In particular the laser detuning and intensity must be chosen to minimize the occurrence of spontaneous emission. For this reason, although both blue and red detuning are capable of focusing atoms via the dipole force, it is commonly accepted now that using a blue detuning is preferable since the atoms are being pushed

into regions of small field intensity where the probability of spontaneous emission is smaller.

The theory of the dipole force was examined in detail in 1980 by Gordon and Ashkin.[7] Building on this theoretical foundation, in 1985 Dalibard and Cohen-Tannoudji developed an approach which provided a quantitative understanding of the dipole force based on the dressed atom picture of laser/atom interaction.[8] In the dressed atom approach, the atom wave function and laser mode are coupled. If the Hamiltonian of the coupled system (atomic internal energy, laser mode energy, and atom-laser mode coupling) is diagonalized, the eigenstates are the so called "dressed states". This approach can yield a more natural development of the evolution of the system. In the dressed atom picture, the atom projects into one of the two dressed states when it enters the laser. The optical potential felt by the atom in this state is just the energy of the dressed state and is given by[9]

$$U = \frac{\hbar\Delta}{2}\sqrt{1 + 2p} \tag{2.9}$$

where p is the saturation parameter and is given by

$$p = \frac{I}{I_0}\frac{1}{(1 + 4\Delta^2/\Gamma^2)} \tag{2.10}$$

This focusing theory assumes a perfectly collimated, monochromatic beam of atoms. That is, all atoms enter the standing wave with equal velocity. If this is true, and assuming the potential wells to be harmonic, then each atom that enters the standing wave begins an oscillation about its minimum of potential (the node or anti-node depending on laser detuning) with an amplitude independent period T. At time T/4, all the atoms are together at the potential minimum, and the atoms are perfectly focused. As long as the

atoms stay within the harmonic potential well, they will oscillate through the potential minimum and be focused every T/2. This condition is shown in Figure 2.11. Because this force is conservative, the atoms do not dissipate energy while oscillating in the wells. The atoms undergo adiabatic exchange of potential and kinetic energy through absorption and stimulated emission into the laser mode.

Typically, due to experimental conditions, it is impossible to eliminate all occurrences of spontaneous emission. When this occurs, the force is non-conservative and the average force exerted on the atom may be derived from the gradient of a pseudopotential given by[10]

$$U = \frac{\hbar\Delta}{2} \ln(1 + 2p) \tag{2.11}$$

This pseudopotential may be generalized to remain valid in the regime of saturation which can occur at high laser powers or small detunings if two assumptions about the atom/laser interaction are made. It must be assumed that the atom moves slowly enough through the laser such that the atom's internal state and the laser field are always in equilibrium. Also the number of spontaneous emissions may be non-zero, but must be small enough such that photon recoil will not significantly alter the atom trajectory.[11] Typically, the pseudopotential in Eq. 2.11 is used rather than the potential in Eq. 2.9 to calculate the focusing capabilities of the standing wave.

2.8 Experimental Focusing Regimes

The standing wave laser acts like a periodic array of cylindrical atom lenses. To be useful for direct write optical lithography (DWOL) nanofabrication, the atoms must be

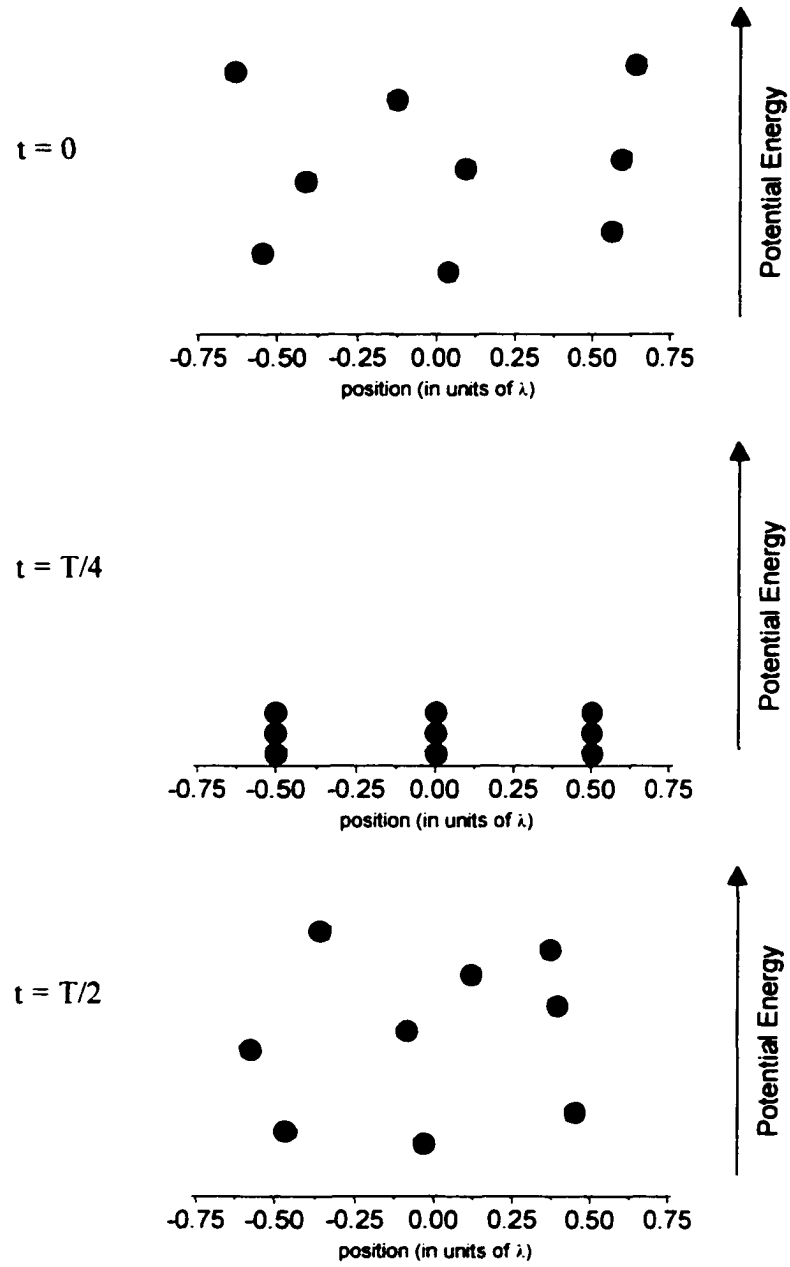

Figure 2.11 Atomic potential energy vs. position in a standing wave. The atoms oscillate about the potential minimum with a period T.

caught by a substrate when they are focused by the standing wave. If the substrate is placed a short distance from a tightly focused standing wave laser, the atom lens is said to be operating in the "thin lens" regime, by analogy with geometric optics. More traditionally, the substrate is actually placed at the center of a focused laser beam (waist ≈100 μm), by allowing the substrate to clip the standing wave and blocking half its power. In this case, the atoms are collected while still experiencing the force of the focusing laser. The standing wave is acting in the "thick lens" regime or as an immersion lens. This has been the preferred regime for DWOL up to this date. A third alternative has been demonstrated called the "channeling regime". In this regime a focused standing wave laser with a thick waist (~2 mm) is used and the atoms are not exactly focused. The atoms in the blue-detuned channeling laser oscillate through the nodes with a decreasing amplitude as they travel through the laser toward the center where the intensity of the laser, and thus the force the atoms feel, is strongest. As in the thick lens regime, the substrate is placed to clip the laser beam in half, the difference being that in the channeling regime, no true focal plane can be defined.

2.9 Focusing Aberrations

In the theory described in Section 2.7, the ultimate achievable deposited linewidth feature would seem to be on the order of the size of an atom, assuming all atoms are focused at the same time into the same place. There are aberrations in atom optics, however, just as there are in light optics. The aberrations preclude the focusing and deposition of atoms to arbitrarily small features. These aberrations, along with surface effects which will be discussed later, have limited the final atom deposition feature sizes to the order of tens of nanometers. The smallest feature linewidth achieved by one-

dimensional standing wave focusing for four different atomic species is given in Table 2.1.

Given the simplicity of the focusing theory, the aberrations, which have a quite complicated influence on atom trajectory, are typically modeled as perturbations to the laser focusing force. The resulting deposition lineshapes due to the perturbed atom trajectories are computed in Monte Carlo simulations and compared to experimental results for validation.

Table 2.1: Minimum feature size obtained by laser focusing for four elements

Element	Feature Size (nm)
sodium[12]	20
chromium[13]	29
chromium[14]	50
aluminum[15]	70
cesium[16]	120

A significant amount of work has been done previously to model these aberrations (e.g. atom diffraction, spherical aberration, and chromatic aberration)[9,11,17] and the influence of the focusing laser beam's Gaussian profile.[11,18] Diffraction is due to the atom's de Broglie wavelength (λ_{dB}). As in light optics, the full width half-maximum (FWHM) diffraction limited feature for a one-dimensionally focused atom beam is

$$d = 0.88 \frac{f \lambda_{dB}}{x_0} \qquad (2.12)$$

Let us assume f, the focal length of the system, is the Gaussian beam $1/e^2$ radius (typically ~50 μm). The de Broglie wavelength corresponding to thermal atoms is ~10 pm. x_0 is the full width of the atom lens which we can assume to be half the wavelength

of the laser ($\lambda/2$) in the first approximation. A typical value for x_0 is 150 nm. Using these parameters, a diffraction limited feature size FWHM of 3 nm is obtained. Even though this calculation is extremely simple and not particularly valid in the presence of other aberrations, given the feature widths presented in Table 2.1 it is clear that diffraction is not the principal source of aberration.

Spherical aberration is the result of higher order terms in the full equation of motion for an atom in the light field. It is caused by atoms entering the lens far from the potential minimum (the node or anti-node) feeling a weaker force than is necessary to bring them into focus. In light optics, techniques to minimize spherical aberration are to use lenses with aberration correcting surface shapes (an asphere), to use two lenses cemented in optical contact with each other to balance each others aberration (a doublet), or to limit the aperture to retain only paraxial (close to the optical axis) light rays. In atom optics, currently no method exists for creating such complicated atom lenses. Although the group currently pursuing iron focusing is attempting to eliminate the spherical aberration by only utilizing the paraxial atoms for focusing,[19] most experimental demonstrations of standing wave focusing did not address this aberration.

Chromatic aberration refers to the variation in focal length for light of different wavelength or color. In atom optics it refers to the variation in focusing due to atoms entering the lens with different kinetic energies. Because the beams used in atom focusing are typically produced by thermal sources and can have a wide longitudinal velocity spread (the full width of the velocity distribution is roughly equal to the velocity - typically several hundred meters per second) the chromatic aberration can be quite significant. Methods for compensating the chromatic aberration include using a velocity

selective source, utilizing a supersonic expansion, or performing longitudinal laser cooling. In practice these methods are not employed and will not be discussed further.

However well compensated the optical aberrations are, there is evidence that it is the surface motion of the atoms after encountering the substrate that ultimately limits the deposition feature size. It has been observed previously that surface conditions are critical and that on certain surfaces the mobility of the atoms limits the contrast (height to width ratio) of any deposited feature to 1:1.[20] A more careful theoretical examination of the surface dynamics of the deposited atoms concludes that during deposition the adatoms move primarily as a result of collisions with incident atoms.[21] In this theory, any deposited feature will smooth and broaden with increasing deposition time (film thickness). No matter how well focused the incident atom flux, the steady state surface corrugations formed by focused deposition will have a FWHM that is greater than 45% of the peak to peak distance. This fundamental limit on feature size can only be overcome by depositing a relatively thin surface film, i.e. utilizing short deposition times.

2.10 Laser Cooling and Focusing of Gallium

We can now address the particular experimental parameters required for one-dimensional laser cooling and focusing of Ga atoms. The choice of lasers is determined by the energy level structure of the Ga atom. Figure 2.12 shows the lower lying energy levels of Ga. We have identified a closed, or cycling, hyperfine transition suitable for laser cooling: the $4p^2P_{3/2}(F=3) \rightarrow 4d^2D_{5/2}(F=4)$ transition at 294.45 nm. A laser cooling transition must be cycling because a large number (>100) of absorptions and spontaneous emissions are required for the cooling to be effective. If the atom can decay via spontaneous emission to any other state than that from which it started, it is not a cycling

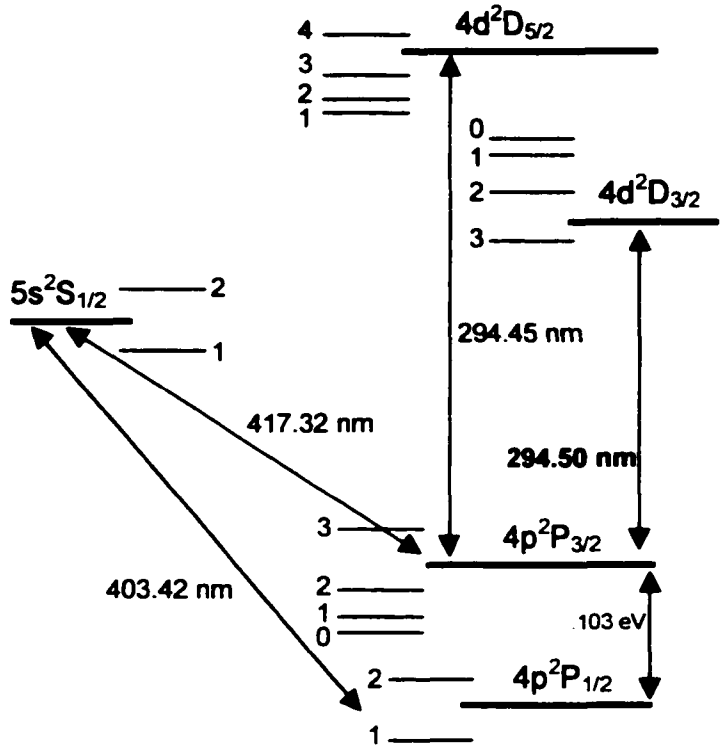

Figure 2.12 The lower lying energy levels in gallium.

transition. The atom will be pumped into the other states and no further cooling of the atom can occur. These loss channels via optical pumping can be stopped by using repumping lasers to repopulate the ground state of the cooling transition, but obtaining several frequency stabilized lasers at the wavelengths required in Ga is experimentally difficult. It is for this reason that we wish to cool on the UV transition given above. Atoms excited to the F=4 state can only decay back to the F=3 state due to the dipole selection rules. Utilizing this scheme, only one UV laser will be required for laser cooling. The lower state of the transition, $4p^2P_{3/2}(F=3)$, is not the true ground state, but lies only 0.103 eV above the ground state. This level will be statistically populated in a

thermal atomic beam and will provide enough atoms in the correct state for cooling and focusing.

Using the theory for one-dimensional laser cooling developed in Sections 2.1 – 2.6, the theoretical cooling limits for Ga can be calculated. Table 2.2 shows all the relevant cooling parameters for gallium,[22] as well as for aluminum, chromium and sodium, three of the other atoms which have been previously cooled. The cooling parameters for three other atoms of interest (cesium, indium, and iron) are given in Appendix two.

Table 2.2: Cooling parameters for gallium, aluminum, chromium, and sodium

	Gallium	**Aluminum**	**Chromium**	**Sodium**
Atomic Number	31	13	24	11
Atomic Mass (a.u.)	70	27	52	23
Stable Isotopes	^{69}Ga: 60.1% ^{71}Ga: 39.9%	^{27}Al: 100%	^{50}Cr: 4% ^{52}Cr: 84% ^{53}Cr: 10% ^{54}Cr: 2%	^{23}Na: 100%
I (nuclear spin)	3/2	5/2	0	3/2
Cooling Transition	$4p^2P_{3/2}(F=3) \rightarrow 4d^2D_{5/2}(F=4)$	$3p^2P_{3/2}(F=4) \rightarrow 3d^2D_{5/2}(F=5)$	$4s^7S_3 \rightarrow 4p^7P_4$	$3s^2P_{1/2}(F=2) \rightarrow 3p^2P_{3/2}(F=3)$
Vacuum wavelength (nm)	294.5	309.4	425.6	589.0
Photon momentum $\hbar k$ (kg m/s)	2.25×10^{-27}	2.14×10^{-27}	1.56×10^{-27}	1.12×10^{-27}
Saturation intensity I_0 (mW/cm^2)	115	57	8.5	6
Natural linewidth $\Gamma/2\pi$ (MHz)	25	13	5	10
Doppler Limits T_D, v_D	596 μK, 0.27 m/s	314 μK, 0.31 m/s	120 μK, 0.14 m/s	240 μK, 0.30 m/s
Recoil Limits T_R, v_R	3.2 μK, 0.019 m/s	7.5 μK, 0.048 m/s	2 μK, 0.018 m/s	2.4 μK, 0.03 m/s

The biggest obstacles to laser cooling Ga are its high saturation intensity, which will necessitate a high UV laser power, the large natural linewidth of the cooling transition, and the isotopic composition. The Ga saturation intensity given is for the F=3

$\rightarrow$ F=4 transition only and is actually the value for the transition between magnetic sublevels, $m_F=3 \rightarrow m_F=4$, an allowed transition with circularly polarized light. The saturation intensities for transitions between other m_F sublevels extend up to 3226 mW/cm^2. When excited by linearly polarized light, the saturation intensity for transitions between the various m_F components ranges from 222 mW/cm^2 to 508 mW/cm^2. Since both linear and circularly polarized light are present in the cooling laser, it is difficult to define a single value for the saturation intensity, but it is believed that the atoms eventually wind up being pumped to the "furthest pumped" m_F transition, so that value is reported.

Aluminum, which has a ground state energy level structure very similar to Ga, is the only other group III atom to be cooled and focused. In that experiment around 8 mW of laser power at 309 nm was required to cool on a transition with a saturation intensity roughly half of that in Ga and a natural linewidth also half that of Ga.[23] We therefore expect that we will need at least four times as much power - at least 30 mW of laser power at 294.5 nm - to laser cool the Ga atoms.

To focus the cooled Ga atoms using the dipole force, it is necessary to utilize a transition that has the $4p^2P_{3/2}$ (F=3) as its lower state. Because the dipole force is conservative, a cycling transition is not required. From Figure 2.12 it can be seen that either the same laser at 294.45 nm or a second laser at 417.32 nm may be utilized for focusing. In order to reserve all the UV laser power for cooling, we decided to obtain a tunable 417 nm laser to focus on the $4p^2P_{3/2}(F=3) \rightarrow 5s^2S_{1/2}(F=2)$ hyperfine transition. To focus aluminum, around 15 mW of 309 nm laser power was utilized. To focus Ga

efficiently should require no more than this amount, which is a much more modest requirement than for cooling.

Using the known characteristics of our focusing laser (λ = 417 nm, P = 11 mW) we can calculate the focusing potential energy of the standing wave. Figure 2.13 shows the potential well depth in the atom lens as a function of blue detuning. This graph was

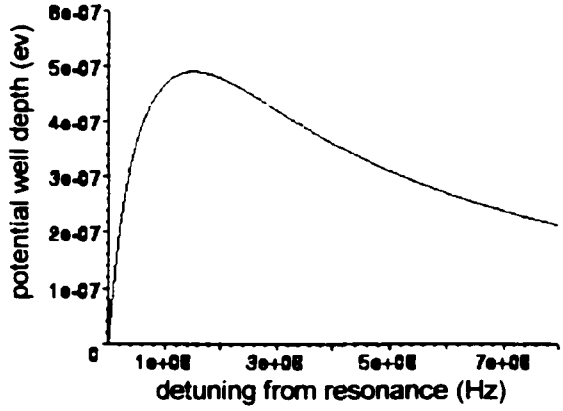

Figure 2.13 The depth of the potential well in the standing wave atom lens as a function of detuning from resonance.

calculated using the pseudopotential given in Eq. 2.11. This laser was focused to an elliptical cross section with $1/e^2$ radii given by w_{0x} = 98 μm and w_{0y} = 155 μm. Linear polarization was assumed, I_0 = 329 mW/cm^2. The maximum focusing force occurs when $\Delta \cong +150$ MHz, where the potential well depth is 500 neV. To be focused, an atom must have a one-dimensional kinetic energy less than this value or else the atom will not oscillate in the potential well, but will skip over the top. Using the Doppler and recoil limits given in Table 2.2, we can see that the Doppler limit T_D = 596 μK corresponds to 26 neV and the recoil limit temperature, T_R = 3.2 μK corresponds to 0.1 neV. Therefore

even with just Doppler cooling alone we should be able to focus the atoms with the power available to us. Given this energy surplus, it is advantageous to detune the laser even further from resonance to decrease the possibility of spontaneous emission (detunings on the order of 10Γ or greater are common). Figure 2.14 shows the potential well depth and shape of the atom lens as a function of the position in the standing wave for three different blue detunings: +300 MHz, +400 MHz, and +500 MHz. Because the shape and

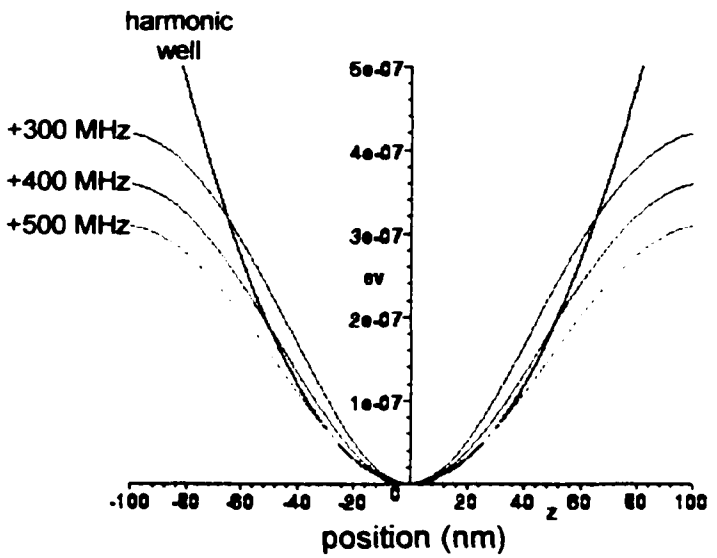

Figure 2.14 Potential well depth and shape for three different laser detunings.

not just the depth of the well changes as a function of detuning (and power) a harmonic well is shown for comparison. The more closely the potential well resembles a pure harmonic well, the better the focusing will be. The further from resonance the laser is detuned, the more nearly harmonic the well becomes. Decreasing the laser intensity also creates a shallower, but more harmonic shape.

A summary list of the relevant anticipated experimental parameters required for laser cooling and focusing of Ga is given in Table 2.3.

Table 2.3: Gallium cooling and focusing anticipated experimental parameters

identified cooling transition	$4p^2P_{3/2}$ (F=3) → $4d^2D_{5/2}$ (F=4) 294.45 nm
power required for laser cooling	> 30 mW
detuning of cooling laser from resonance	-12.5 MHz
minimum Ga atom energy/velocity after cooling (anticipated)	2 neV, 50 μK, 8 cm/s
maximum atom energy/velocity allowed for focusing	500 neV, 12 mK, 1.2 m/s
identified focusing transition	$4p^2P_{3/2}$ (F=3) → $5s^2S_{1/2}$ (F=2) 417.32 nm
power required for laser focusing	12 mW
detuning of focusing laser from resonance	+ 300 MHz
anticipated focused Ga feature size	50 - 100 nm

2.11 Conclusions

In this chapter I have presented the theories of laser cooling and laser focusing. Using these theories, I have explained how the laser cooling and laser focusing techniques may be applied to manipulate Ga atoms and calculated the effectiveness of the techniques given our experimental parameters.

To experimentally demonstrate one-dimensional laser cooling and standing wave laser focusing we will need to develop a source of Ga atoms that can generate a continuous beam of atoms for at least 10 hours before refilling is required. We will need a UV laser at 295 nm of sufficient power (at least 30 mW) and frequency stability to cool the atomic beam in one-dimension. The transverse kinetic energy of the atoms in the cooled atomic beam must at a very minimum be below 500 neV, which corresponds to 12 mK or atoms moving at 1.2 m/s. Once the atom beam is collimated we will need to develop a method for measuring the efficiency of cooling and its dependence on laser detuning, power, and size.

We will need a laser at 417 nm with sufficient power (at least 10 mW) and frequency stability to focus the cooled Ga atoms. We will need a substrate mount that is capable of introducing the substrate into the focused standing wave laser beam so that we can operate in the "thick lens" focusing regime. Finally, we will need to measure the efficiency of laser focusing by observing and measuring the size and periodicity of the one-dimensional nanostructures created.

The remainder of this thesis will detail my efforts to produce these apparati and utilize them in the laser manipulation experiments.

REFERENCES

[1] P.D. Lett, W.D. Phillips, S. L. Rolston, C.E. Tanner, R.N. Watts, and C.I. Westbrook, "Optical molasses," J. Opt. Soc. Am. B **6**, 2084 (1989)

[2] R. Loudon, *The Quantum Theory of Light*, (Oxford Science, Oxford, 1983)

[3] P.D. Lett, R.N. Watts, C.I. Westbrook, W.D. Phillips, P.L. Gould, and H.J. Metcalf, "Observation of atoms laser cooled below the Doppler limit," Phys. Rev. Lett. **61**, 169 (1988)

[4] J. Dalibard, C. Salomon, A. Aspect., E. Arimondo, R. Kaiser, N. Vansteenkiste, and C. Cohen-Tannoudji, "New schemes in laser cooling," in *Atomic Physics 11*, S. Haroche, J.C. Gay , and G. Grynberg, eds. (World Scientific, Singapore, 1989), p. 199

[5] S. Chu, Y. Shevy, D. Weiss, and P. Ungar, "Laser cooling due to atomic dipole orientation," in *Atomic Physics 11*, S. Haroche, J.C. Gay , and G. Grynberg, eds. (World Scientific, Singapore, 1989), p. 636

[6] A complete overview of the theory for sub-Doppler cooling may be found in J. Dalibard and C. Cohen-Tannoudji, "Laser cooling below the Doppler limit by polarization gradients: simple theoretical models," J. Opt. Soc. Am. B **6**, 2023 (1989)

[7] J. P. Gordon and A. Ashkin, "Motion of atoms in a radiation trap," Phys. Rev. A **21**, 1606 (1980)

[8] J. Dalibard and C. Cohen-Tannoudji, "Dressed–atom approach to atomic motion in laser light: the dipole force revisited," J. Opt. Soc. Am. B **2**, 1707 (1985)

[9] V. Natarajan, R.E. Behringer, D.M. Tennant, and G.M. Timp, "Nanolithography using a laser focused neutral atom beam," J. Vac. Technol. B **13**, 2823 (1995)

[10] G. Timp, R.E. Behringer, D.M. Tennant, and J.E. Cunningham, "Using light as a lens for submicron, neutral-atom lithography," Phys. Rev. Lett. **69**, 1636 (1992)

[11] J.J. McClelland, "Atom-optical properties of a standing-wave light field," J. Opt. Soc. Am. B **12**, 1761 (1995)

[12] V. Natarajan, R.E. Behringer, and G. Timp, "High-contrast, high-resolution focusing of neutral atoms using light forces," Phys. Rev. A **53**, 4381 (1996)

[13] W.R. Anderson, C.C. Bradley, J.J. McClelland, and R.J. Celotta, "Minimizing feature width in atom optically fabricated chromium nanostructures," Phys. Rev. A **59**, 2476 (1999)

[14] Th. Schulze, B. Brezger, R. Mertens. M. Pivak, T. Pfau, J. Mlynek, "Writing a superlattice with light forces," Appl. Phys. B **70**, 671 (2000)

[15] R.W. McGowan, D.M. Giltner, and S.A. Lee, "Light force cooling, focusing, and nanometer-scale deposition of aluminum atoms," Opt. Lett. **20**, 2535 (1995)

[16] F. Lison, H. –J. Adams, D. Haubrich, M. Kries. S. Nowak, D. Meschede, "Nanoscale atomic lithography with a cesium atomic beam," Appl. Phys. B **65**, 419 (1997)

[17] K.K. Berggren, M. Prentiss, G.L. Timp, and R.E. Behringer, "Calculation of atomic positions in nanometer-scale direct-write optical lithography with an optical standing wave," J. Opt. Soc. Am. B. **11**, 1166 (1994)

[18] R.E. Behringer, V. Natarajan, and G. Timp, "Optical profile for a Gaussian standing-wave atom-optical lens", Opt. Lett. **22**, 114 (1997)

[19] R. Bosch, *Ferromagnetic Nanostructures by Laser Manipulation*, Ph.D. Thesis (Eindhoven University of Technology, Eindhoven, Germany 2002)

[20] R.E. Behringer, V. Natarajan, G. Timp, "Surface diffusion limitation in laser focused atomic deposition," Appl. Surf. Sci. **104/105**, 291 (1996)

[21] R.M. Bradley, A. Eschmann, and S.A. Lee, "Theory of feature broadening in direct-write optical lithography," J. Appl. Phys. **88**, 3316 (2000)

[22] S.J. Rehse, R.W. McGowan and S.A. Lee, "Optical manipulation of group III atoms," Appl. Phys. B **70**, 657 (2000)

[23] R.W. McGowan, D.M. Giltner, and S.A. Lee, "Light force cooling, focusing, and nanometer-scale deposition of aluminum atoms," Opt. Lett. **20**, 2535 (1995)

CHAPTER 3

A Thermal Atomic Gallium Beam Source

The demonstration of light force manipulation of gallium required an atomic beam source that provided an adequate flux for deposition and optical measurement, did not require frequent refilling with Ga, had pointing stability and reproducibility, was relatively inexpensive and was easy to maintain and modify if necessary. This chapter describes the development of a Ga atomic beam source that satisfied all these criteria. The thermal properties of the source and atomic beam are described, as is the vacuum system associated with the source.

The atomic beam source utilized in the Ga manipulation experiments was originally developed for use in an aluminum manipulation experiment.[1] Ga and Al are both group III elements (metals) and have similar physical and chemical properties. Therefore the source developed for the Al experiment was adapted to work with Ga.

3.1 High-Temperature Oven

The source used is a resistively heated oven with a small exit aperture. Although Ga melts at 30° C and is a liquid at room temperature, it has a relatively low vapor pressure. Figure 3.1 shows the vapor pressure curve of Ga as a function of temperature.[2]

To generate a sufficient flux of atoms from the oven, a vapor pressure around 0.1 Torr was required. Therefore an oven that could heat up to at least 1500 K was needed.

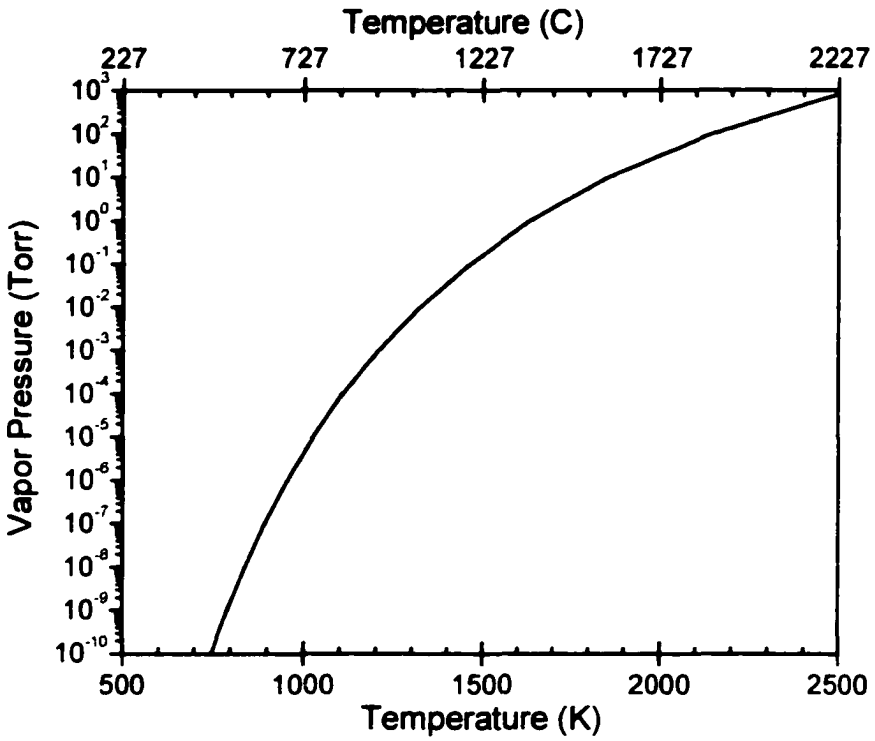

Figure 3.1 Vapor pressure of gallium as a function of temperature.

To withstand the high temperatures, an oven was constructed out of an intermetallic composite (IMC) material. This was a composite of titanium diboride, boron nitride, and aluminum nitride (TiB_2-BN-AlN) manufactured by Advanced Ceramics Corporation in a hot press process. This material was easily machinable into a suitable oven shape. The oven design is shown in Figure 3.2(a). It was comprised of two separate pieces, a body and a cap. Around 5 g of Ga fit in the cap which was on the bottom of the oven. The body and cap were machined to high tolerances so that they could be press fit together to provide a tight seal. A molybdenum clip was used to further

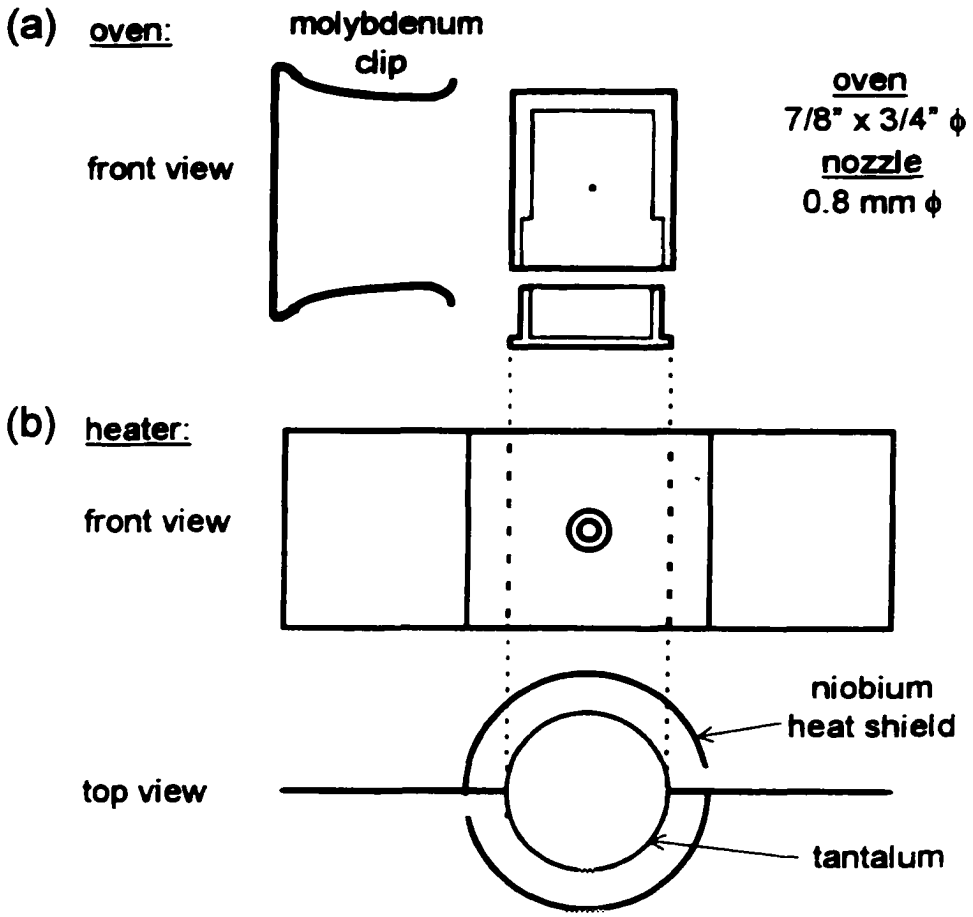

Figure 3.2 The oven (a) and heater (b) utilized to produce an effusive atomic gallium beam.

press the cap into the body. Additionally, a variety of high-temperature ceramic adhesives from Aremco Products, Inc. were used on the lip of the cap to provide a tight seal during operation. It was found that all of these adhesives degraded during the multiple heating/cooling cycles the oven was subjected to. Also removal and replacement of the adhesive was required after each refilling of the oven. Ultimately it was decided that no adhesive was required for the oven to operate adequately.

A round hole drilled in the body of the oven ($\phi \approx 0.8$ mm) was the source aperture of the atomic beam. The diameter and depth of this exit nozzle, along with the mean free path of the atoms in the oven, determined the atomic beam characteristics. The mean free path, Λ, of the Ga atoms is a function of the temperature (T), vapor pressure (P), and collisional cross section (σ). The mean free path is given by[3]

$$\Lambda = \frac{1}{n\sigma\sqrt{2}} = \frac{7.321\text{x}10^{-20}\ T}{P\ \sigma} \tag{3.1}$$

where the temperature is in K, the pressure in Torr, and the collisional cross section in cm^2. With $\sigma_{Ga} = 5.72\text{x}10^{-16}$ cm^2 and T and P related by Figure 3.1, we can plot the mean free path as a function of the oven temperature. This is shown in Figure 3.3. Also shown

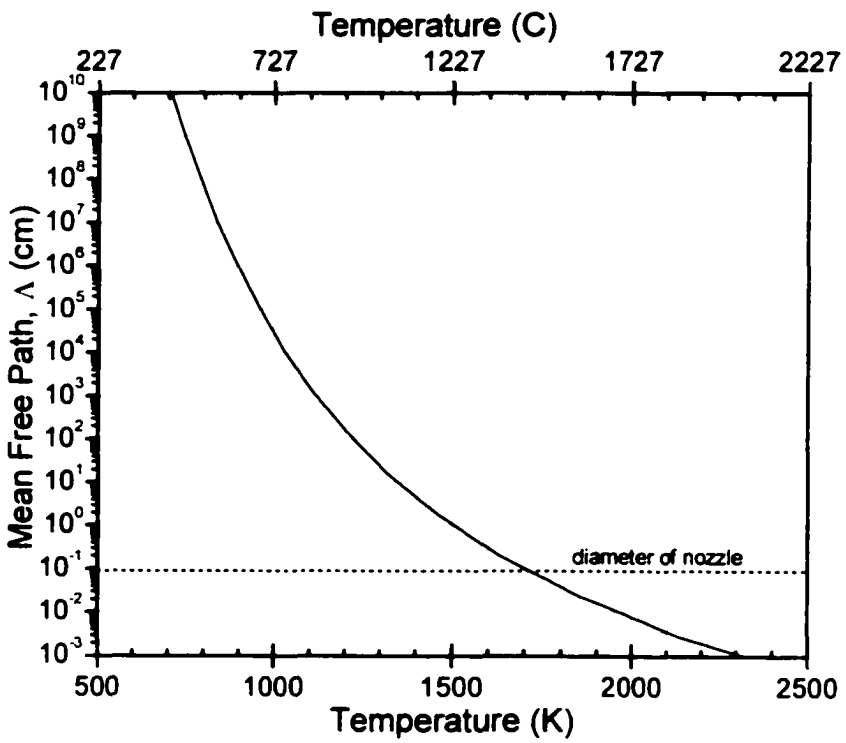

Figure 3.3 Mean free path of gallium atoms as a function of temperature.

in Figure 3.3 is the nozzle diameter ϕ. The Knudsen number (K_n) is defined to be the ratio of the mean free path to the diameter of the aperture:

$$K_n \equiv \Lambda/\phi \tag{3.2}$$

If $K_n > 1$, the mean free path is greater then the diameter of the aperture and the nozzle acts as an effusive source.[3] This means the atoms leave the nozzle as a free molecular flow. If $K_n < 1$, the nozzle is in a regime of hydrodynamic flow with the result being a turbulent gas jet rather than an effusive source. This is undesirable, so we must restrict the temperature of the oven to $T < 1700$ K to remain in the effusive regime.

Also of importance was the length, l, of the nozzle. For a hole drilled through the wall of the oven body, this was just the wall thickness. For collisions inside the nozzle to be negligible, we required $\Lambda > l$. Typically, when operated in the effusive regime, we would impose the additional restriction that $l/\phi < 1$. In our oven, this was accomplished by first drilling the hole through the oven wall, then grinding out the wall on the inside of the oven to make l as small as possible.

In the molecular effusion regime the angular dependence of the forward beam intensity varied as $\cos\theta$, where θ was the angle relative to the beam axis of propagation. This $\cos\theta$ dependence allowed a less stringent pointing requirement for the source. At this point it should be noted that a commercially purchased molecular beam epitaxy (MBE) effusion cell could have adequately functioned as a Ga atomic beam source. The characteristics and practicality of a typical MBE cell are discussed in Appendix three.

3.2 Thermal Beam Characteristics

We can calculate the velocity with which atoms left the oven. The most probable velocity inside the source is given by

$$\alpha = \sqrt{(2k_B T/m)} \tag{3.3}$$

where k_B is the Boltzmann constant, T is the temperature of the oven and m is the mass of the atom. The most probable velocity in the atomic beam is

$$v_{pB} = \sqrt{(3/2)}\,\alpha \tag{3.4}$$

A graph of the most probable velocity in our Ga beam as a function of oven temperature is given in Figure 3.4. Typical oven operating temperatures were around 1400 K, which produced a beam with $\alpha \approx 577$ m/s and $v_{pB} \approx 700$ m/s.

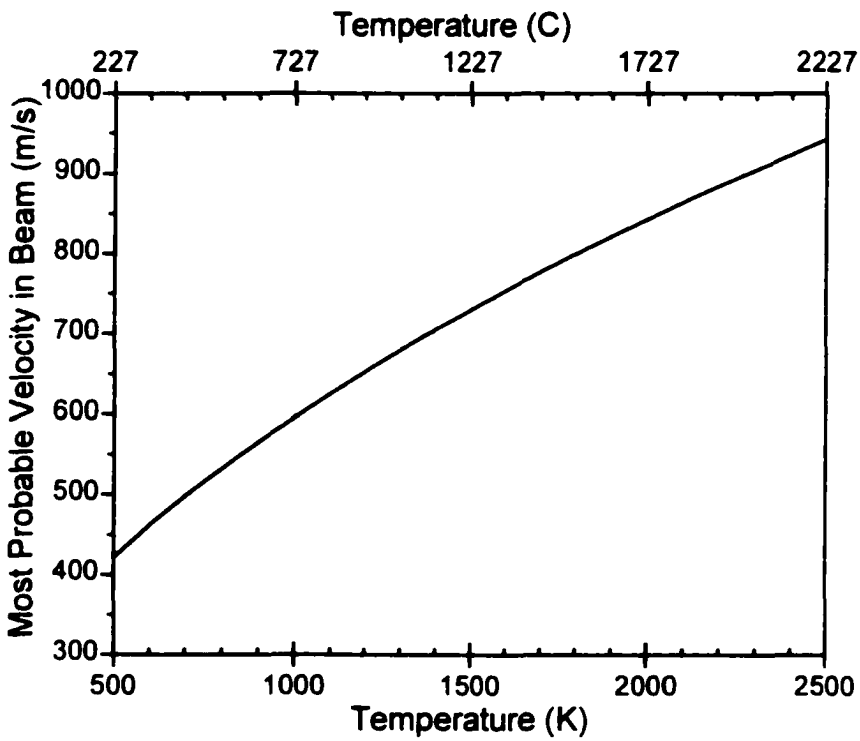

Figure 3.4 Most probable velocity in a gallium atomic beam as a function of oven temperature.

The atoms emerging from the effusive source were not monoenergetic. The velocity distribution emerging from the nozzle can be characterized by

$$I(v) = \frac{2I_0}{\alpha^4} v^3 \exp(-v^2/\alpha^2) \tag{3.5}$$

where I_0 is the full-beam intensity. Assuming an oven temperature of 1400 K, a graph of this forward velocity distribution is given in Figure 3.5. Note that the spread of the velocity distribution is roughly equal to the most probable velocity ($\Delta v \approx v_{pB}$). This is characteristic of effusive sources.

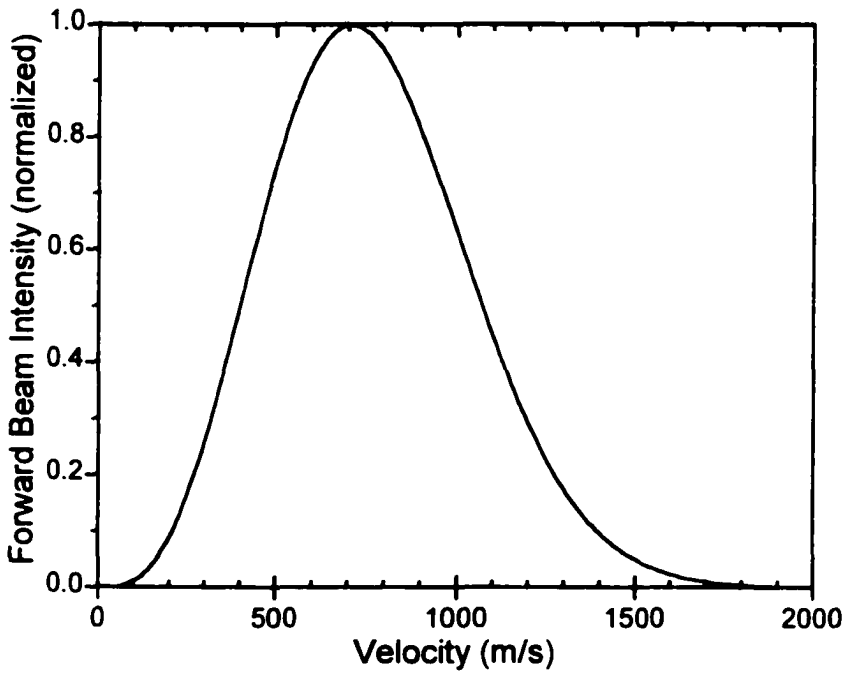

Figure 3.5 Velocity distribution in a gallium atomic beam for an oven T = 1400 K.

The distribution of atoms among the quantum states was also determined by the temperature of the oven. The laser cooling and focusing techniques were performed on atoms in the $4p^2P_{3/2}(F=3)$ state. Figure 3.6 shows the total percentage of atoms in the beam that are ^{69}Ga in the $4p^2P_{3/2}(F=3)$ state as a function of oven temperature. The

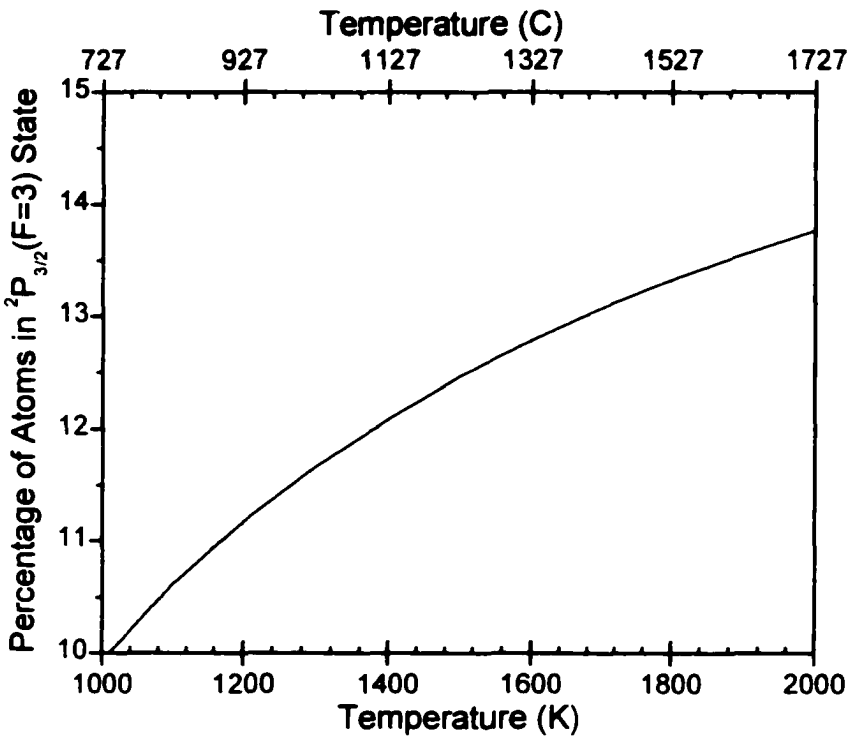

Figure 3.6 Percentage of atoms in the atomic beam that are in the correct ground state for cooling as a function of oven temperature.

isotopic ratio of Ga is taken into consideration in this Figure. It can be seen that in the temperature range for the experiment, we only had around 12% to 13% of the correct isotope in the correct state. These are the atoms that could be manipulated with the laser light. All the other atoms acted as background.

3.3 Heating the Oven

To heat our oven to ~1400 K, custom heaters built for vacuum evaporative sources were purchased from R. D. Mathis. The heater and how it fits together with the oven is shown in Figure 3.2(b). The oven was machined to fit snugly inside the circular heater element which was made out of tantalum. The bottom of the tantalum heater was crimped in slightly to support the oven. The heaters had niobium heat shields to reduce excess radiant heat from the front and back. The heaters were at times run with and without the niobium heat shields, which had a tendency to fall off after many heating/cooling cycles. No appreciable difference in operation was ever noted due to the presence or absence of the niobium heat shields. These heaters were quite robust and were reusable for many heating/cooling cycles.

The resistive heater was held in a custom made water-cooled assembly attached to a 4.5" Conflat flange. This is shown in Figure 3.7. On the outside of the flange were two copper feed-through electrodes for carrying the current into the vacuum system. Cooling water was run through these two electrodes, which attached to opposite sides of the heater. With the heater firmly held in the water cooled copper assembly, the 4.5" flange was bolted to a 6" Conflat "cross" with the heater assembly inside. This is shown in Figure 3.8. Attached to the inside of this cross was a copper water-cooled shroud which completely enclosed the heater assembly, except for a 1 cm diameter hole which allowed the Ga beam to emerge. The water-cooled shroud reduced radiative heating of the walls of the vacuum system.

Refilling the Ga oven or replacing the heater required the removal of the 4.5" mounting flange for the heater and oven. If the heater was not disturbed, the pointing

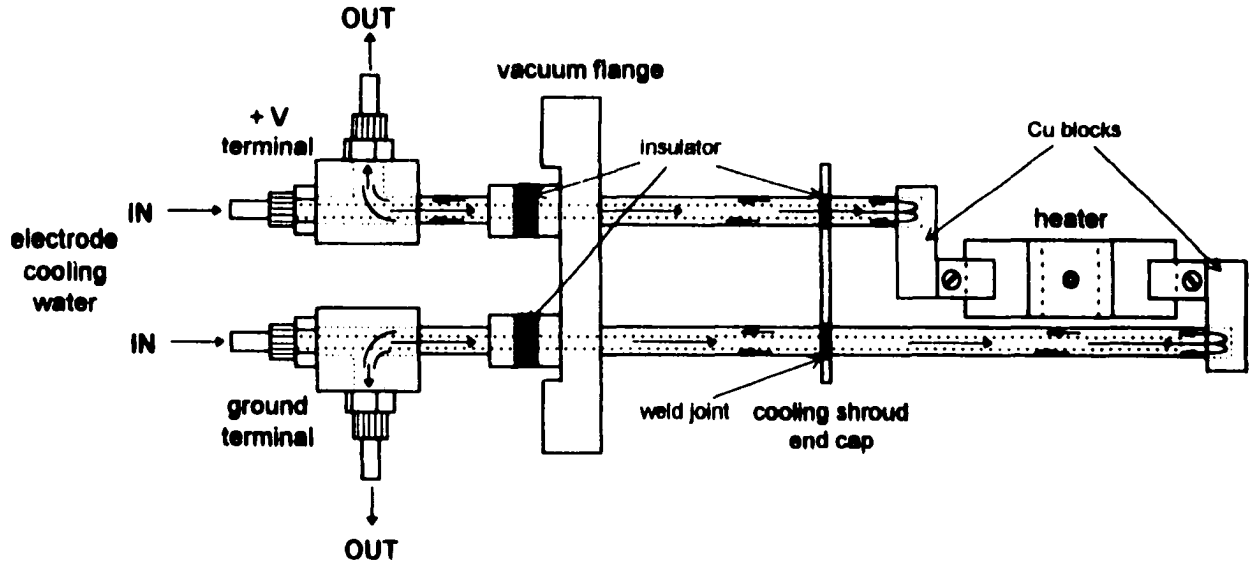

Figure 3.7 The gallium source assembly for producing the atomic beam.

reproducibility of the oven nozzle when the flange was re-bolted to the vacuum system was excellent. The heater occasionally required replacement after many heating/cooling cycles, usually at every other or every third oven refilling. When a new heater was

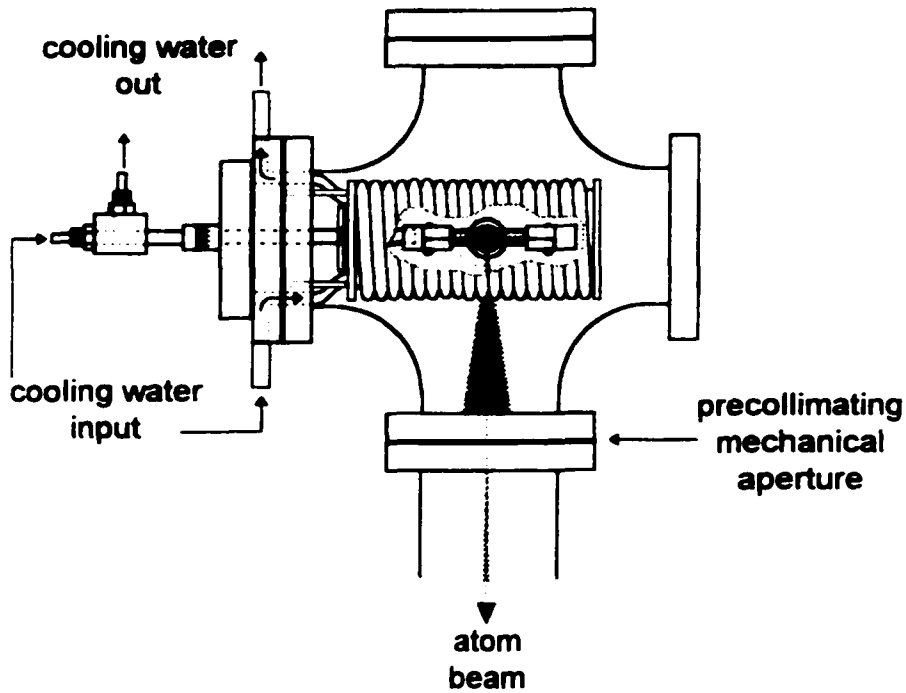

Figure 3.8 The gallium source assembly inside the vacuum chamber.

installed, the pointing of the atomic beam was always different. To check the pointing, a Ga deposition was made on a glass microscope slide or on the glass end window. If the atomic beam was pointed far from the center axis of the vacuum system, the heater was repositioned by opening the vacuum and manually adjusting its placement. It typically took several iterations until the beam was as close to the center axis of the vacuum as possible.

An aperture was placed inside the arm of the cross downstream from the Ga oven. This rectangular aperture was 0.8 mm wide by 1 mm tall, and served to pre-collimate the

atomic beam. The divergence of the Ga beam was determined by the geometry of the oven nozzle and the aperture to be 6.2 mrad (full-angle) in the horizontal plane. Since all the light-force manipulation experiments were intended to be one-dimensional, the vertical plane was not considered.

This oven chamber was pumped by a liquid nitrogen trapped 6" "Mexican-hat" style diffusion pump, which could pump down to pressures in the 10^{-7} Torr range. A vacuum hose from the side of the oven chamber was connected to the rest of the system. This was necessary because the mechanical aperture, held by a plug that sat in the oven chamber, restricted pumping of the vacuum system located downstream from it. The specific configurations of the vacuum system used for cooling and focusing of the Ga atomic beam are described in more detail in Chapters six and seven.

3.4 Oven Operation

To run the heater a 6 V, 600 A d.c. power supply was used. This power supply was run in a current limited mode, where the temperature of the oven was varied by increasing the current supplied to the heater. As the current was increased, the voltage increased as well. The temperature of the oven was measured with an optical pyrometer through an end window. The amount of Ga being produced in the atomic beam was inferred by observing the heater current and voltage and the pressure in the oven chamber. A typical graph of the heater voltage and oven chamber pressure as a function of applied current is shown in Figure 3.9. An appreciable beam was produced only after turning the power supply to 300 A or greater. The oven was typically run at an oven chamber pressure of 1×10^{-6} Torr. At this pressure, over 80 hours of operation were achieved with one charge of Ga.

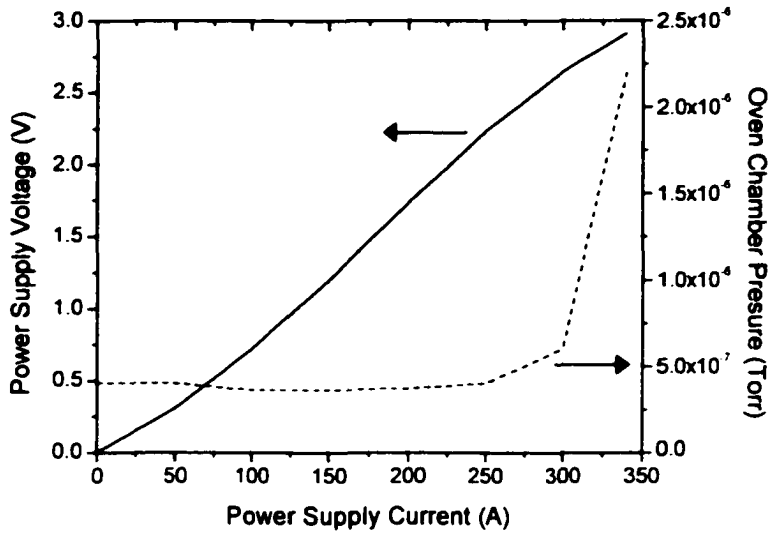

Figure 3.9 Power supply voltage and oven chamber pressure as a function of applied current to the heater.

When running at this average flux, the oven deposited a 310 nm layer of Ga in 237 minutes, corresponding to a deposition rate of 13.1Å/min. This rate was measured by depositing onto a glass slide and measuring the deposition thickness with a Telcor Instruments Alpha-Step profilometer. This rate was sufficient to deposit a measurable (by atomic force microscope) amount of Ga in a reasonable quantity of time: around 10-20 minutes. To arrive at how many atoms this is, the intensity of the atomic beam can be calculated.

$$I = 1.118\text{x}10^{22}\,\frac{P\,A_s\,A_d}{l_0\,\sqrt{(MT)}}\text{atoms/s} \qquad (3.6)$$

where P is the source pressure in Torr, M is the molecular weight, T is the absolute temperature in Kelvin, A_s is the source area in cm^2, A_d is the detector area in cm^2, and l_0 is the length from the source to the detector.[3] If we ignore the A_d term we arrive at a flux

which is more useful than an intensity. Typical distances to the deposition surface in our apparatus was 37 cm and the nozzle aperture area was 5.4×10^{-3} cm^2. Assuming an oven operating at 1400 K with a corresponding source vapor pressure of 0.04 Torr yields an on-axis flux of 5×10^{12} atoms cm^{-2} s^{-1}.

3.5 Conclusion

An efficient Ga atomic beam source was developed that allowed many hours of continuous beam operation under very stable, reproducible conditions. Over 80 hours of operation were achieved with one 5 g charge of Ga in the oven. The source was self-contained in a vacuum system that could be connected to other vacuum components in multiple configurations for use in the laser cooling and laser focusing experiments. The source was capable of providing a sufficient flux for the Ga deposition experiments and for adequate signal to noise in laser-induced fluorescence experiments.

REFERENCES

[1] R. McGowan, *Light Force Cooling, Manipulation, and Nanometer-Scale Deposition of Neutral Aluminum Atoms*, Ph.D. Thesis (Colorado State University, Fort Collins, Colorado, 1996)

[2] R.E. Honig and D.A. Kramer, "Vapor pressure data for the solid and liquid elements," RCA Review **30**, 285 (1969)

[3] N.F. Ramsey, *Molecular Beams*, (Oxford University Press, London, 1956)

CHAPTER 4

Generation of Tunable Continuous-Wave Laser Radiation at 295 nm and 417 nm

This chapter describes the generation of tunable continuous-wave (cw) laser radiation at 295 nm and 417 nm with sufficient power and frequency stability for one-dimensional laser cooling and laser focusing of Ga.

The UV laser light at 295 nm was produced by frequency doubling a tunable dye laser in a nonlinear optical crystal via second harmonic generation in an external power enhancement cavity. In this chapter I will discuss the theory of second harmonic generation in nonlinear optical crystals and the design and construction of external power enhancement cavities for use in frequency doubling. I will also describe the frequency stabilization of the fundamental dye laser used for second harmonic generation.

The 417 nm laser light was produced by a commercial gallium-nitride (GaN) diode laser which utilized grating feedback to narrow the frequency linewidth. In this chapter I will describe the technique of grating feedback for use in semiconductor diode lasers and the difficulties encountered implementing this type of laser into our experiment.

4.1 Second Harmonic Generation

To produce tunable cw laser light in the UV or violet (<400 nm) regime, second harmonic generation (SHG) or higher order harmonic generation has been the technique of choice for many years. In this technique light of a lower frequency, ω, is converted to light at a higher frequency, ω', inside a nonlinear optical crystal. In the case of SHG, $\omega' = 2\omega$, thus this is referred to as "frequency doubling".

In general, the frequency conversion of light in a nonlinear crystal is due to a field dependent index of refraction, n. Within the crystal, a polarization **P** is related to the strength of the electric field vector **E** by the matter equation.[1]

$$\mathbf{P}(\mathbf{E}) = \kappa(\mathbf{E})\mathbf{E} = \kappa_0\mathbf{E} + \chi^{(2)}\mathbf{E}^2 + \chi^{(3)}\mathbf{E}^3 + \ldots \tag{4.1}$$

where κ is the dielectric susceptibility (and is equal to κ_0 in the absence of any electric field) and $\chi^{(2)}$ and $\chi^{(3)}$ are the nonlinear dielectric susceptibility coefficients. In an anisotropic material like a nonlinear optical crystal, $\chi^{(2)}$ and $\chi^{(3)}$ are tensors of rank two and three, respectively. The square nonlinearity is present only in crystals without an inversion symmetry (acentric crystal) but the cubic nonlinearity is present in all crystalline materials. However, because the cubic nonlinearity is weaker ($\chi^{(3)} << \chi^{(2)}$) we shall only consider crystals that possess the square nonlinearity.

In crystals with $\chi^{(2)}$, the propagation of two light waves with frequencies ω_1 and ω_2 will give rise to new light waves with the sum and difference frequencies ω_3 and ω_4 given by

$$\omega_{3,4} = \omega_2 \pm \omega_1 \tag{4.2}$$

SHG is one special case of this interaction when $\omega_1 = \omega_2$ and $\omega_3 = 2\omega_1$. For the propagation of the two lasers, we can define a wavevector difference Δk

$$\Delta k \equiv k_3 - 2k_1 = k^{2\omega} - 2k^{\omega} \tag{4.3}$$

Noticeable nonlinear effects can be observed only when $\Delta k=0$, or when $k^{2\omega}=2k^{\omega}$. If $\Delta k\neq 0$, then the second harmonic power generated at one plane in a crystal will be out of phase with the second harmonic light generated at another plane.[2] In this case the second harmonic waves are not adding coherently in the crystal on a macroscopic scale and very little power is generated.

4.2 Phase Matching

To ensure that the phase-matching condition ($\Delta k=0$) is satisfied and a sufficient amount of second harmonic power can be generated, we can make use of the natural birefringence of an anisotropic crystal. When a wave propagates in a crystal, birefringence occurs when the index of refraction of the crystal, and thus the wave's phase velocity, is dependant on the polarization of the wave. To satisfy the phase-matching condition we must find a propagation direction within the crystal for which the fundamental wave and the second harmonic wave propagate with equal phase velocities.

In an anisotropic medium the index of refraction that a propagating wave experiences is polarization dependent. However, there are certain directions of propagation within the crystal for which the index of refraction does not depend on polarization. When this happens, orthogonally polarized waves propagating along this direction travel at the same phase velocity. This direction is referred to as an optic axis.[2]

We will limit our discussion to uniaxial crystals, i.e. crystals in which two of the three principal axes have the same index of refraction. The Z axis is taken to be the optic axis. Let us consider a light wave propagating through such a crystal. The plane containing the Z axis and the wave vector k is called the principal plane. If the

polarization of the light wave is normal to the principal plane, it is called an ordinary wave, or o-wave. If the polarization of the light wave is within the principal plane, it is called an extraordinary wave, or e-wave. This is illustrated in Figure 4.1. In this Figure, θ is the angle between the (optic) Z axis and the direction of propagation. For the o-

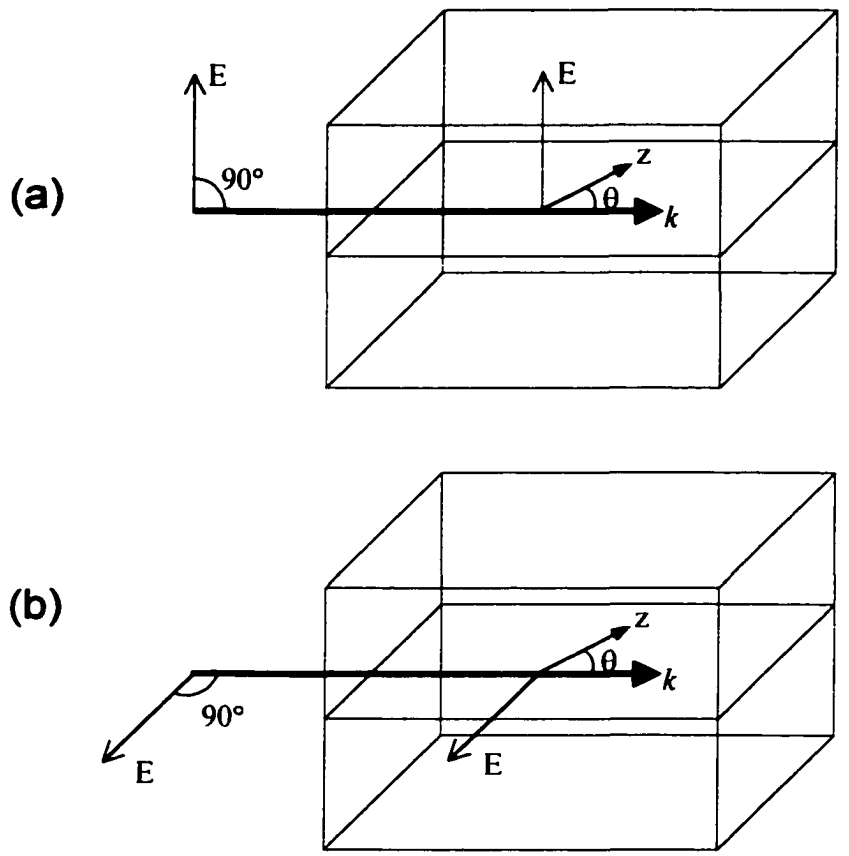

Figure 4.1 Principal plane of a crystal (the plane containing both *k* and Z) and a wave propagating as (a) an ordinary wave and (b) an extraordinary wave.

wave, the index of refraction is independent of θ, or $n_o(\theta)=n_o$. For the e-wave, the index of refraction is dependent upon θ: $n_e=n_e(\theta)$, where

$$\frac{1}{(n_e(\theta))^2} = \frac{\cos^2\theta}{(n_o)^2} + \frac{\sin^2\theta}{(n_e)^2} \qquad (4.4)$$

By our definition of the optic axis, if the e-wave propagates along the optic axis then $n_e(0)=n_o$. If $n_e>n_o$ the crystal is positive uniaxial and if $n_e<n_o$ it is negative uniaxial.

Satisfying the phase-matching condition requires that $n^{2\omega}=n^{\omega}$. There are two types of phase-matching. In Type 1 phase-matching the two polarizations of the fundamental beams are parallel and the second harmonic is orthogonal to these two waves. In Type 2 phase-matching, the polarizations of the fundamental beams are orthogonal and the polarization of the second harmonic is parallel to one of these. In SHG, both fundamental beams are usually supplied by a single laser, so that Type 1 phase-matching is much more common.

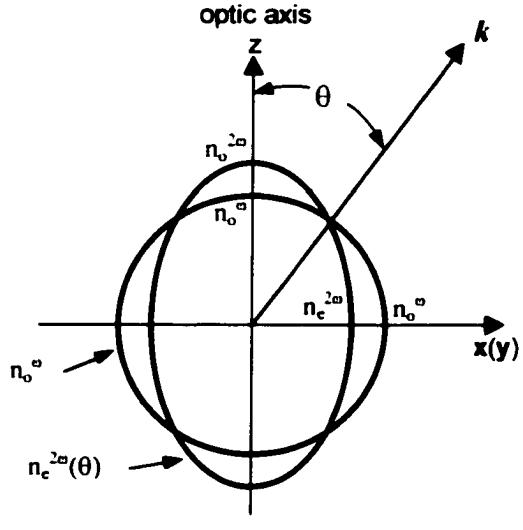

Figure 4.2 Indices of refraction for the fundamental wave propagating as an o-wave (n_o^{ω}) and the second harmonic wave propagating as an e-wave ($n_e^{2\omega}$). The intersection point gives the phase-matching angle.

In normally dispersive media the index of refraction of the o-wave or the e-wave along a give direction increases with ω. Figure 4.2 shows the typical index relationship

for a negative uniaxial crystal. For Type 1 phase-matching, the fundamental beam with frequency ω should propagate as an o-wave and the second harmonic with frequency 2ω should propagate as an e-wave. To satisfy the phase-matching condition $n^{2\omega}=n^{\omega}$, the waves must propagate at an angle θ_m to the optic axis that makes $n_e^{2\omega}(\theta)=n_o^{\omega}$. This is called "angle-tuning". At this phase-matching angle there will be no phase slippage between the fundamental beam and the second harmonic, and appreciable power can be built up due to macroscopic coherent addition of all the second harmonic power.

4.3 Second Harmonic Generation Efficiency

The amount of second harmonic power produced cannot be increased indefinitely by allowing the crystal length to go to infinity. When a plane wave propagates in a uniaxial crystal there is a rotation between the direction of propagation of the second harmonic and the fundamental by a walk-off angle, $\rho(\theta)$. This walk-off angle limits the amount of overlap between the two beams and thus the effective interaction length over which the second harmonic power adds coherently. The walk-off angle is given by

$$\rho(\theta) = \pm\arctan[(n_o/n_e)^2\tan\theta] \mp \theta \qquad (4.5)$$

where the upper signs are for negative uniaxial crystals and the bottom signs are for positive uniaxial crystals.

If θ_m is equal to 0° or 90°, then there is no walk-off and this is called 90° non-critical phase matching. In this case, the wavelength tunability of the crystal is achieved by controlling the temperature of the crystal. Typically the index of refraction of the extraordinary axis is more temperature dependent that that of the ordinary axis. Thus, the phase matching condition for a particular wavelength can be satisfied by heating or

cooling the entire crystal until the indices of the two waves are equal. This is referred to as temperature-tuned phase-matching.

To calculate how much second harmonic power one can expect from a given input fundamental power, one can use a preliminary theory developed to describe resonant optical second harmonic generation.[3] This theory assumes illumination of a nonlinear crystal of length l by light with a fundamental frequency ω_1. This light is focused to a waist w_0, where w_0 is the 1/e radius. Given the walk-off between the fundamental and the second harmonic beams, it is useful to define an efficient interaction length, l_a, called the aperture length.

$$\frac{l_a}{w_0} = \frac{\sqrt{\pi}}{\rho} \tag{4.6}$$

It is also necessary to define b, the confocal parameter.

$$b = k_1 w_0^2 \tag{4.7}$$

where $k_1 = n_1\omega_1/c$. A third length scale is called the effective length of a focused beam, l_f, and it is given by

$$l_f = \frac{\pi}{2} b \tag{4.8}$$

If $l_a << l_f$ then the second harmonic power, P_2, produced by illumination of a crystal with a fundamental power P_1 is given by

$$P_2 = K (P_1)^2 l_a l_f / w_0^2 \tag{4.9}$$

where

$$K = \frac{128 \pi^2 \omega_1^3}{(n_1 c)^3} d_{eff}^2 \tag{4.10}$$

and d_{eff} is the effective crystal nonlinear coefficient.

If $l_a << l_f$ does not hold, it is possible to replace Eq. 4.9 with

$$P_2 = K (P_1)^2 l^2 / w_0^2 \qquad (4.11)$$

In both Eqs. 4.9 and 4.11, the output power depends on the square of the input power. This is valid for SHG until very high input powers are used and saturation is reached. At that point, the dependence becomes linear.

We now know enough to calculate the expected power from the two SHG schemes describe later in this chapter. Both were constructed to double 589 nm light to obtain 294.5 nm UV light. The first utilized a 90° non-critically phase-matched temperature-tuned ADA (ammonium dihydrogen arsenate) crystal and the second utilized an angle-tuned BBO (β-barium borate) crystal. Table 4.1 lists the crystal characteristics and beam parameters that were used in the final experiments.

Table 4.1 Experimental parameters for SHG in two crystals

	BBO	ADA
crystal length, l	5 mm	20 mm
fundamental frequency, ω_1	3.199×10^{15} rad/s	3.199×10^{15} rad/s
fundamental waist, w_0	23 μm	52 μm
phase-matching angle, θ_m	41.465°	90°
walk-off angle, ρ	4.746°	0°
aperture length, l_a	4.9×10^{-4} m	N/A
index of refraction, n_0	1.66985	1.574617
wavevector, k_1	1.781×10^7/m	1.680×10^7/m
confocal parameter, b	9.4 mm	45.4 mm
effective length, l_f	14.8 mm	71.3 mm
d_{eff}	1.6 pm / V	0.45 pm / V
K	1.5×10^{-8}	1.4×10^{-9}
P_2 (W/W^2)	2.06×10^{-4} *	2.07×10^{-4} **

* calculated with Eq. 4.9
** calculated with Eq. 4.11

A further refinement of the theory of SHG was made by Boyd and Kleinman.[4] It took into account the interaction of the nonlinear crystal with a focused Gaussian light beam. To use this more complete theory, several new parameters must be defined. First is the focusing parameter, ξ.

$$\xi = l / b \tag{4.12}$$

For a given walk off angle, ρ, there is an optimum focusing parameter ξ_m. This in turn determines the optimum waist size. Knowing this *a priori* is advantageous, as a frequency doubling cavity can then be constructed which will yield this optimal waist size at the center of the nonlinear crystal.

Also introduced in this theory is a parameter B, which accounts for double refraction.

$$B = \rho(l k_1)^{1/2}/2 \tag{4.13}$$

When the walk-off angle is zero, B=0 and ξ_m=2.8. As B gets large, ξ_m asymptotically approaches the value of 1.39. If B and ξ are known then a final parameter $h_m(B,\xi)$ can be defined.

$$h_m(B,\xi) = \frac{\sqrt{\pi}}{2B\sqrt{\xi}} \tan^{-1}(\xi) \tag{4.14}$$

Figure 4.3 shows a graph of $h_m(B,\xi)$ as a function of ξ for one particular B value. $h_m(B,\xi)$ takes on its maximum value at ξ=1.39.

Using these parameters, a new expression for the generated second harmonic power can be stated:

$$P_2 = K (P_1)^2 l k_1 h_m e^{-\alpha l} \tag{4.15}$$

Eq. 4.15 is similar to the previous expressions for second harmonic power, with the addition of h_m and a term that accounts for loss in the nonlinear crystal due to absorption, $e^{-\alpha l}$. In this term, α is the crystal absorption per unit length and l is the crystal length.

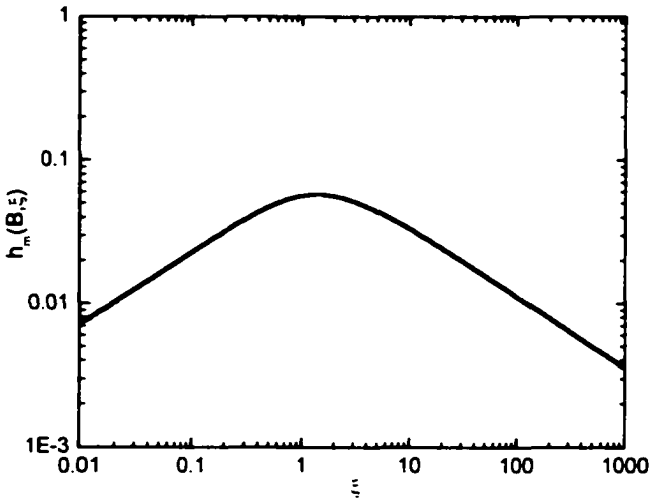

Figure 4.3 SHG power represented by the function $h_m(B,\xi)$ as a function of the focusing paramter $\xi = l/b$. In this graph B=12.4.

Using the BBO crystal from above as an example, we can calculate the SHG efficiency for the case of optimized h_m and also for the real parameters we had in the experiment. With a walk-off angle ρ=0.082 rad. and a 5 mm crystal, B=12.4. The optimal ξ is 1.39 and this gives a beam waist of 14.2 μm. As noted in Table 4.1. the waist in our crystal (due to experimental constraints) was 23 μm. This corresponded to a ξ of 0.53. The calculated values of h_m and P_2 for both the optimized case (w_0=14 μm) and the actual experimental case (w_0=23 μm) are given in Table 4.2. For BBO, the

absorption coefficient at the wavelengths being discussed was α=0.001 cm^{-1}. Therefore $e^{-\alpha l} \sim 1$ for a 5 mm crystal.

Table 4.2 SHG Power and Calculated Parameters For Doubling in BBO

	optimized case	experimental case
waist, w_0	14 μm	23 μm
focusing parameter, ξ	1.39	0.53
$h_m(B,\xi)$	0.057	0.048
SH power, P_2	7.6×10^{-5} W/W^2	6.4×10^{-5} W/W^2

From Table 4.2 we can see that not having the optimized waist size does not significantly decrease the second harmonic power, as h_m is only softly dependent on ξ in the vicinity of the maximum.

As stated in Chapter two, we need at least 30 mW of power at 295 nm to laser cool Ga. Using the experimental case given in Table 4.2

$$0.030 \text{ W} = 6.4 \times 10^{-5} \text{ W/W}^2 \times (P_1)^2 \qquad (4.16)$$

and solving for P_1 gives P_1 = 21.7 W at 590 nm. This is more than our dye laser could produce, therefore we were required to increase this fundamental power in an external power enhancement cavity. Two computer programs were used to design the doubling cavity. A complete description of these programs is given in Appendix four.

4.4 An External Power Enhancement Cavity for SHG with ADA

For the first attempt to produce 295 nm UV laser light via SHG, we utilized a Brewster cut ADA crystal in an external frequency doubling cavity. In hindsight, ADA was a poor choice because it was easily damaged by the UV and could only produce a few mW of UV reliably.

The fundamental laser beam at 590 nm was produced by a Coherent 699-21 tunable dye laser pumped by a 5.5 W Spectra-Physics Millennia 532 nm solid-state pump laser. The dye used was Rhodamine 6G. The output from the dye laser, ~500 mW of vertically linearly polarized laser light, was put through a periscope assembly to rotate the polarization to horizontal, then passed through a polarizing beamsplitter to remove any residual vertical polarization component. This beam was then passed through an f=75 cm lens and entered the power enhancement cavity, hereafter called the frequency doubling cavity.

The frequency doubling cavity was a confocal bowtie configuration cavity, shown in Figure 4.4 The cavity had two flat mirrors and two spherical concave mirrors. The astigmatism introduced by the off axis reflection at the surface of the curved mirrors in the cavity was compensated for by the astigmatism caused by the Brewster interface of the crystal, as suggested by Kogelnik et al.[5] Confocal cavities such as this have two

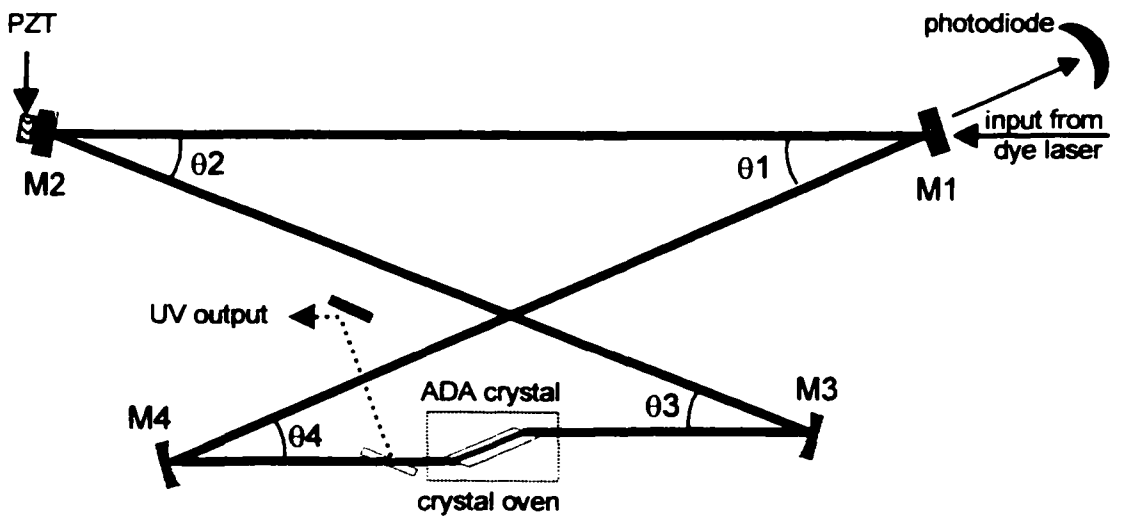

Figure 4.4 A schematic of the bowtie cavity used to frequency double 590 nm light in an ADA crystal.

waists within the cavity. The primary waist was 52 μm and was located between the curved mirrors. The secondary waist was several times larger than this and was located between the flat mirrors. The cavity had three high reflectivity mirrors, purchased from VLOC with R> 99.9% @ 589 nm @ 13° angle of incidence, p-polarization. The input coupler had R=97.4%, and was a spare output coupler from a Coherent 699 DCM dye optic set. A dichroic beamsplitter coated for high reflectivity in the UV and high transmission at the visible wavelengths was inserted in the cavity at Brewster's angle. The dichroic beamsplitter was a standard Coherent intra-cavity doubling optic. This beamsplitter was used to couple the UV laser light out of the cavity for use in the experiment while retaining appreciable power build-up in the cavity. All the specifications of the cavity design and components are summarized in Table 4.3.

Fundamental laser light reflecting off the flat input coupler was monitored by a photodiode to observe the cavity Fabry-Perot fringes as the length of the cavity was slowly modulated at 10 Hz by a mirror mounted on a piezo-electric crystal stack. When the cavity was on resonance, the reflected light was a minimum due to maximum coupling into the cavity. Additionally, a 30 kHz modulation frequency was applied to the piezo-electric crystal and was used to lock the cavity on resonance. The motion of the piezo-mirror was controlled by a PZT driver. The PZT driver supplied all the voltages to the PZT, including the high voltage and both the slow and fast frequency modulation. The cavity locking was done with an NBS lock-in servo amplifier which provided feed-back to the PZT driver to keep the cavity on resonance.

Table 4.3 ADA cavity design and component specifications

input coupler, M1	ROC (radius of curvature) = ∞ R (reflectivity) = 97.4 %
piezo-mirror, M2	ROC = ∞ R > 99.9%
curved mirror, M3	ROC = 15 cm R > 99.9%
curved mirror, M4	ROC = 30 cm R > 99.9%
θ1	13°
θ2	29°
θ3	29°
θ4	13°
distance M1-M2	22.9 cm
distance M2-M3	16.3 cm
distance M3-crystal face	8.5 cm
distance crystal face-M4	18.0 cm
distance M4-M1	37.8 cm
ADA crystal	5 mm x 5 mm x 2 cm
waist at crystal center, w_0	52 μm
free spectral range	284 MHz

The crystal was a 5 mm x 5 mm x 2 cm 90° non-critically phase-matched temperature-tuned ADA crystal from Quantum Technology. It had Brewster cut faces and was Z-cut for doubling at 590 nm. The crystal was positioned between the curved mirror so that the primary waist was at the center of the crystal. The crystal came from the manufacturer in an aluminum housing shown in Figure 4.5. The housing had two holes drilled through it. A thermistor was coated with heat conducting paste and inserted into the housing through one of these holes. This thermistor (Wavelength Electronics Model TCS650 50 kΩ) was used to monitor the temperature of the crystal.

To heat the crystal to the phase-matching temperature, an oven was built around the crystal housing. Figure 4.6 shows the oven design - an Al cylinder with end caps that allowed the laser to pass through. This oven was wrapped in heater tape (Minco 10.8 Ω

resistance) capable of heating the oven with around 20 W. The oven was insulated with Al foil, then wrapped in several layers of self-adhering elastic tape.

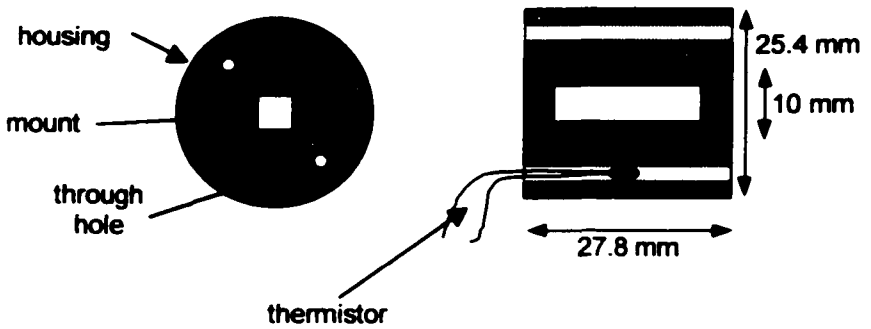

Figure 4.5 End-on and side view of the cylindrical ADA crystal housing showing the Al housing (gray), the crystal mount (black), the crystal (white), and the holes through the mount used for temperature monitoring.

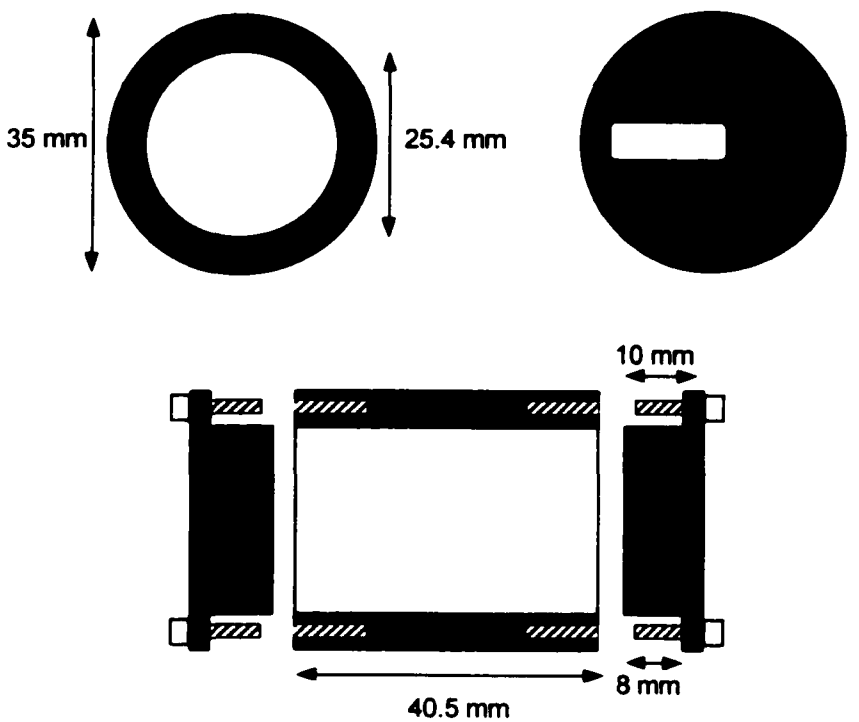

Figure 4.6 End-on and side view of the cylindrical ADA crystal oven constructed to allow temperature tuning of the crystal.

To control and maintain the oven temperature a Wavelength Electronics RHM-4000 PID temperature controller was used. To ensure proper phase-matching, the oven needed to hold the temperature of the crystal to better than 0.2° C. The RHM-4000 was adequate for this requirement.

Using this cavity and oven configuration, we could reliably produce from 1-5 mW of UV laser power at 295 nm with 400 – 500 mW of fundamental power. This was enough power to perform the UV laser spectroscopy of the hyperfine transitions described in Chapter five. This was not enough power to attempt laser cooling. Although SHG utilizing ADA nonlinear crystals to produce >20 mW of UV has been described previously,[6,7] our experience is that it is only useful for producing ~10 mW of cw UV. More UV power creates cavity mode instabilities due to localized heating effects, such as thermally induced lensing, in the crystal. When we observed circulating powers in the cavity exceeding 10 W, the thermal lensing was evidenced by the cavity rapidly blinking in and out of lock. It was also observed on occasion that our crystal could produce over 10 mW of power, but only for a short time (on the order of 1-5 minutes). After performing the UV Ga spectroscopy, we found a more suitable nonlinear optical crystal for use in the production of 295 nm laser light.

4.5 An External Power Enhancement Cavity for SHG with BBO

Other than ADA, several other types of crystals have been utilized for SHG at 295 nm. These include ADP,[8] KDP,[9] $LiIO_3$, LBO,[10,11,12] BBO,[13] and others. Of these, beta barium borate (β-BBO referred to as just BBO) is an excellent choice at this wavelength due to its low UV absorption, relatively low hygroscopy, high damage threshold, and

good nonlinear doubling coefficient. BBO is a negative uniaxial crystal and the phase matching is Type I.

A UV grade BBO crystal was purchased from Cleveland Crystal, Inc. The crystal was 5 mm long, 3 mm x 3 mm in cross section, and the faces were Brewster cut for the fundamental wavelength of 590 nm. The BBO crystal was placed at the primary waist of a confocal bowtie configuration cavity. This cavity was different from that used with ADA in two respects. First, the cavity resonance was locked with light transmitted through one of the curved high-reflector mirrors. It was observed that using the reflected light from the input coupler for locking caused the photodiode to saturate, making cavity performance comparisons difficult. Second, enough UV power was produced in this cavity that the small amount not reflected out of the cavity by the dichroic beamsplitter passed through the other curved end mirror and could be used as a probe beam in the laser cooling experiment. Thus, this cavity produced two useful UV laser beams which

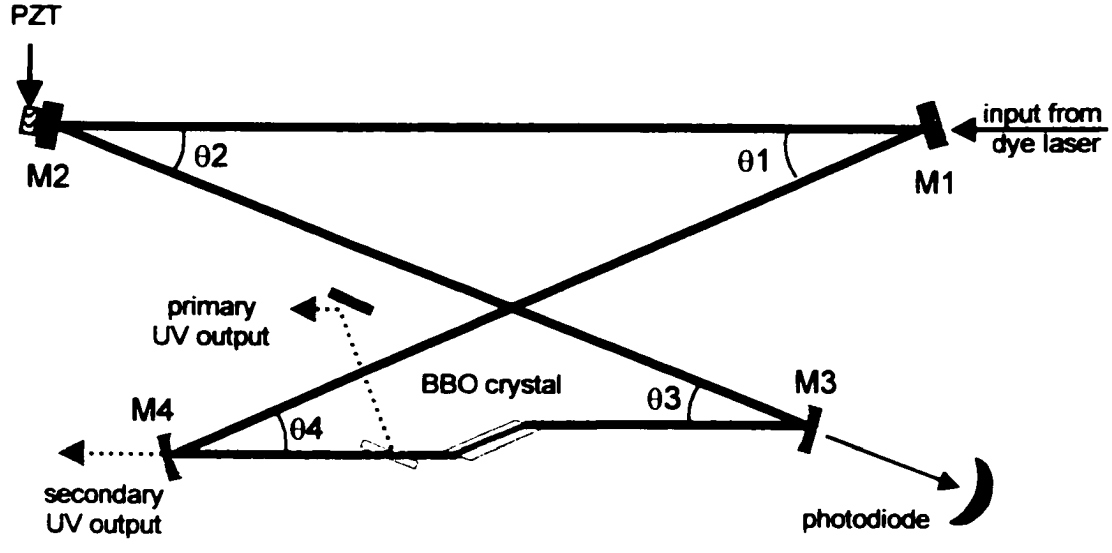

Figure 4.7 A schematic of the bowtie cavity used to frequency double 590 nm light in an BBO crystal.

were always tuned to the same frequency. The BBO cavity is shown in Figure 4.7. The cavity design and component specifications are given in Table 4.4.

Table 4.4 BBO cavity design and component specifications

input coupler, M1	ROC (radius of curvature) = ∞ R (reflectivity) = 97.4 %
piezo-mirror, M2	ROC = ∞ R > 99.9%
curved mirror, M3	ROC = 10 cm R > 99.9%
curved mirror, M4	ROC = 10 cm R > 99.9%
θ1	23°
θ2	11.5°
θ3	11.5°
θ4	23°
distance M1-M2	43.4 cm
distance M2-M3	37 cm
distance M3-crystal face	5.1 cm
distance crystal face-M4	5.1 cm
distance M4-M1	19.7 cm
BBO crystal	3 mm x 3 mm x 5 mm
waist at crystal center, w_0	23 μm
free spectral range	271 MHz

In this cavity the primary waist was 23 μm and was located symmetrically between the two 10 cm radius of curvature mirrors. The waist size was as close as practical to the calculated 14 μm optimum waist size. The secondary waist of this cavity was 200 μm and was located between the flat mirrors. Significant care was taken to mode match the dye laser to this waist with one aspheric lens (focal length = 70 cm) mounted in an x-y-z translation stage located 82 cm in front of the cavity input coupler. The UV laser beam reflected out of the cavity by the dichroic beamsplitter was highly divergent and elliptical in shape. It was collimated with an f=50 cm cylindrical lens and an f=106 cm spherical lens to a 1 mm x 5.5 mm spot. Not all the UV light was reflected

out of the cavity by the dichroic beamsplitter. The remaining UV light passed through one curved cavity mirror which transmitted approximately 70%.

The BBO crystal was angle-tuned to achieve phase-matching with a mount designed to allow rotation around the three axes of the crystal. These are is shown in Figure 4.8. Horizontally polarized light (parallel to the surface of the table and the plane

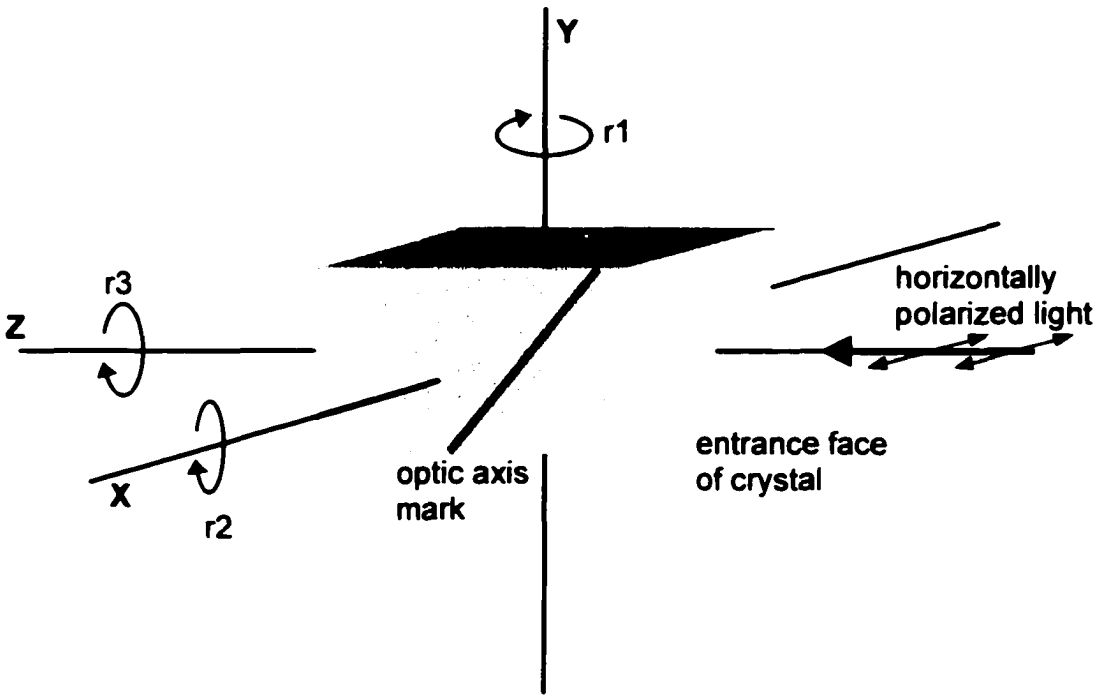

Figure 4.8 The three geometric axes of the BBO doubling crystal and the rotations about those axes.

containing the cavity) entered the crystal through the entrance face along the Z-axis. The first rotation (r1) around the Y-axis was performed to minimize the Brewster reflection. This was a critical rotation for significant power build up in the cavity. The optic axis of the crystal was denoted by a small pencil mark on the side of the crystal. The phase-matching angle was achieved by rotating the crystal around the X-axis (r2). When the crystal was close to the phase-matching angle, twin spots of second harmonic were

visible. One spot moved with r2, and one did not. When the crystal was at the phase-matching angle, these spots overlapped and the total second harmonic power was significantly increased. Finally, rotation about the Z-axis was performed to maximize the SHG and minimize loss from the Brewster face.

When generating UV, the immediate vicinity of the crystal was purged with a slow flow of ultra-pure oxygen. It has been observed that over time the production of UV from a small intense waist in an enhancement cavity is capable of generating color centers within the crystal, possibly due to interaction of the generated UV and the atomic oxygen within the BBO crystal. The slow flow of oxygen over the crystal is thought to reduce this interaction significantly and slow the rate at which the UV damages the crystal.[14] The entire enhancement cavity sat on a small optical breadboard floating on compact self-leveling pneumatic isolation legs (Newport, CM-225). The breadboard and optics were enclosed in a Plexiglas box held at a positive over-pressure by a purge of clean dry nitrogen to prevent crystal face degradation.

The power enhancement cavity had a typical buildup factor of 75. The output UV power varied quadratically with the dye laser input. This is shown in Figure 4.9. The maximum UV output obtained was 94 mW, with a dye laser input of 820 mW. The actual UV generated in the crystal was 125 mW, when the reflectivity of the dichroic beamsplitter (97%) and the Fresnel loss (22%) at the face of the crystal were accounted for. The doubling efficiency in this case was 3.3×10^{-5} W/W^2, typical of values obtained over eight months of operation of the crystal. This doubling efficiency implied an effective non-linear coefficient d_{eff}=1.15 pm/V at 295 nm. The overall cavity efficiency, defined as the total UV power generated divided by the fundamental input power, was

15%. Generating up to 90 mW of UV power, this frequency doubling cavity was used in the laser manipulation experiments described in Chapters six and seven.

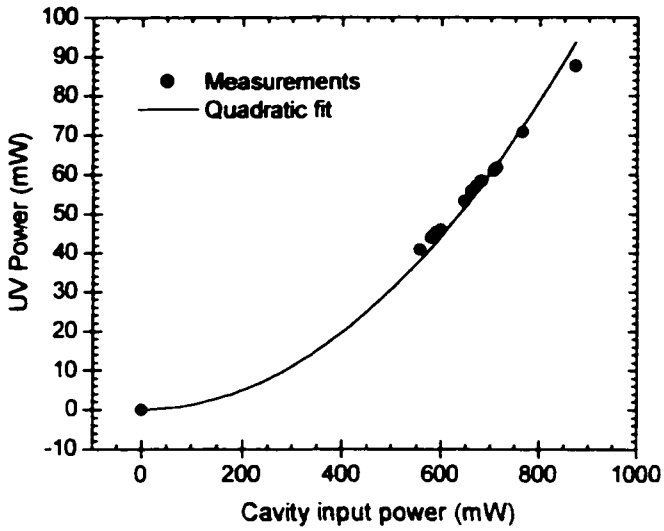

Figure 4.9 Measured UV output power vs. input 590 nm fundamental power. The line is a quadratic fit to the data forced to go through the origin.

It should be noted that the Fresnel loss at the exit face of the crystal was not really a loss, since the beam reflected internally from the exit face and then struck the side of the doubling crystal. In a subsequent setup, we used a crystal with a polished side so a significant portion of the Fresnel reflection was coupled out of the cavity. In this way, a cavity could be made to generate at least three beams with enough power to make them useful experimentally.

4.6 Frequency Stabilization of the Fundamental Dye Laser

Generation of high UV power with the BBO crystal required an increase in the available fundamental power at 590 nm. To achieve this we pumped the Coherent 699-21 tunable dye laser with an 8W Coherent Verdi solid-state laser operating at 532 nm.

Typical pump powers ranged from 5 W to 7 W depending on the dye laser power required. The Coherent 699-21 had a temperature stabilized Fabry-Perot reference cavity to ensure single frequency operation. During typical operation of this dye laser, a drift of 1-2 MHz every 10 minutes was observed. This drift was unacceptably large for the laser manipulation experiments. The desired drift rate was <1 MHz / 15 minutes. To achieve this kind of frequency stability, the dye laser was locked to an iodine hyperfine transition using the technique of saturated absorption. Figure 4.10 shows the Ga hyperfine spectrum of the $4p^2P_{3/2} \rightarrow 4d^2D_{5/2}$ transition at 295 nm,[15] expressed in terms of the

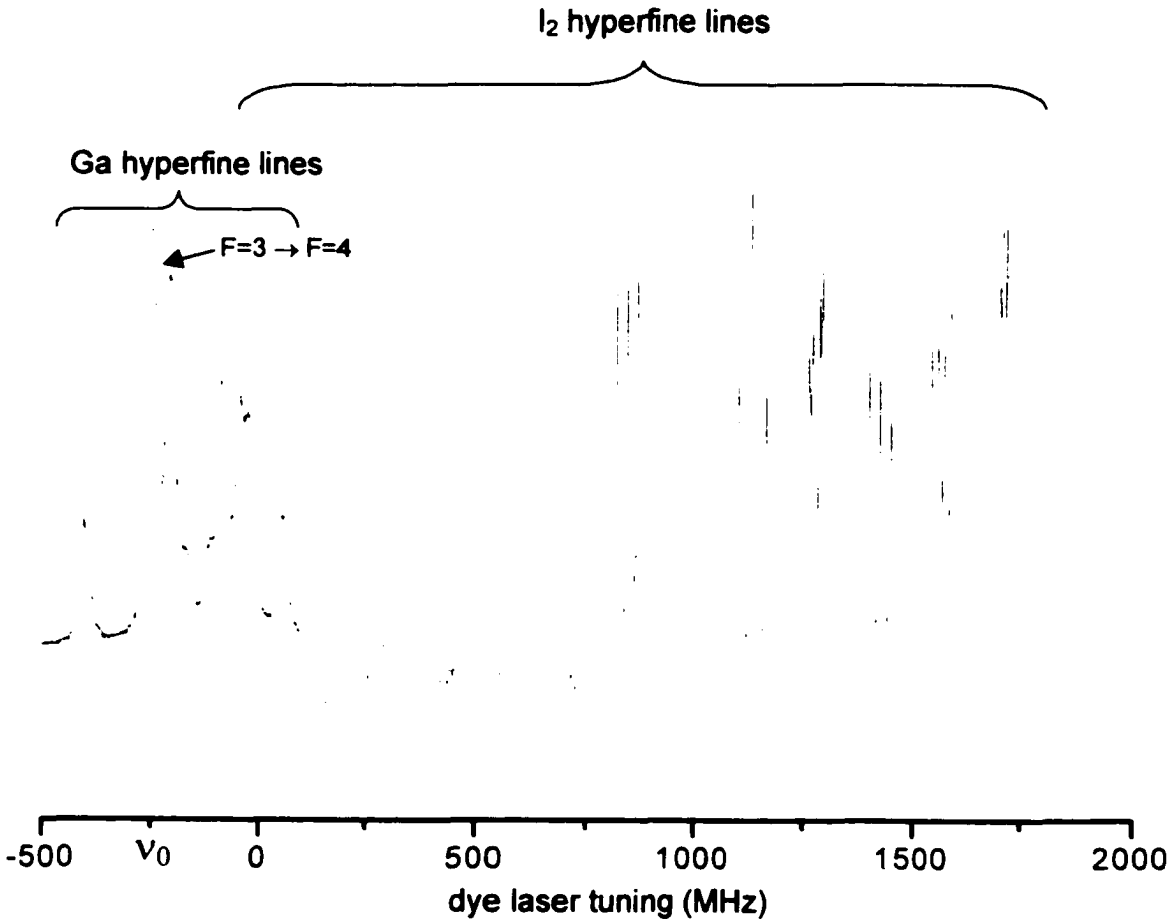

Figure 4.10 The hyperfine lines of the Ga $4p^2P_{3/2} \rightarrow 4d^2D_{5/2}$ transition and the hyperfine components of the iodine transitions P(97)16-2 and P(73)20-4 obtained by scanning the fundamental laser (vacuum wavelength = 588.90 nm).

fundamental dye laser frequency, and the two nearest I_2 lines obtained by saturated absorption. The large peaks in the I_2 spectrum are the hyperfine components of the P(97)16-2 transition at 588.898 nm (identified as line 262 in the CNRS I_2 spectral atlas).[16] The small peaks are the hyperfine components of the P(73)20-4 transition at 588.899 nm (unobservable in the CNRS atlas). The small hyperfine peak centered at 0 MHz is the peak the laser was eventually locked to. While laser cooling Ga, the UV laser was detuned slightly to the red of the ^{69}Ga F=3 $\rightarrow$ F=4 hyperfine resonance and this was where the dye laser frequency ν_0 was parked. The iodine locking peak was shifted to a lower frequency by ~250 MHz to overlap ν_0. To do this, we used a double passed acousto-optic modulator (AOM) with a variable shifting frequency of 110±25 MHz. The double pass arrangement also allowed frequency tuning without a change in the laser beam direction. By manually setting the frequency shift of the double passed AOM, the fundamental laser remained tuned to ν_0 while the frequency that the iodine cell saw was shifted to the iodine hyperfine absorption.

A schematic of the I_2 locking apparatus is shown in Figure 4.11. A beamsplitter set near Brewster's angle allowed us to pick off about 15 mW from the main dye laser beam. The Faraday rotator rotated the linear polarization of the laser beam by 45°. The half-wave plate was needed to rotate the polarization back to vertical, in order to match the eigen-direction of the AOM. The retroreflected beam had twice the AOM frequency shift and upon passing through the Faraday rotator was polarized perpendicular to the incident beam and was picked off by a polarizing beamsplitter. At this point the laser power was about 5 mW and was sent to the saturation spectrometer. A second AOM served as the chopper for the saturating beam and was modulated at 30 kHz with TTL

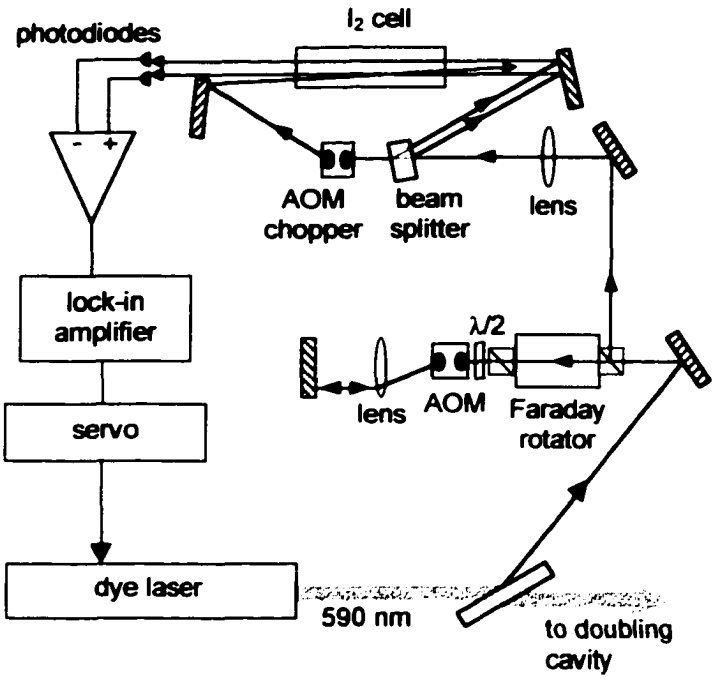

Figure 4.11 Schematic diagram showing the iodine saturated absorption experimental arrangement used to frequency stabilize a ring dye laser.

pulses. For the small I_2 peaks at least 1.3 mW average power was needed in the saturation beam in order to provide enough signal to noise for locking. Typical probe power was 0.3 mW per beam. The probe signal was demodulated and fed-back to the dye laser's locking circuitry by adding it to the reference cavity photo-signal. In this way the laser was offset locked to the half-max point on the red side of the desired hyperfine absorption peak. More details on the locking procedure will be given in Chapter six. Figure 4.12 shows the frequency drift of the dye laser for a time period of 13 minutes. In Figure 4.12(a), the laser was unlocked and drifted off the absorption curve altogether (~1 MHz). In Figure 4.12(b), the laser was locked. When locked, the dye laser short term jitter was less than 50 kHz and the long term drift was less than 1 MHz over many hours. As a result, the doubling cavity maintained its lock for many hours without mode

hopping. By manually tuning the double pass AOM frequency shift, the dye laser was shifted ±10 MHz while remaining locked to the iodine line. This allowed up to 40 MHz of UV tuning, one and a half times the Ga linewidth, which was enough for the laser cooling experiment described in Chapter six.

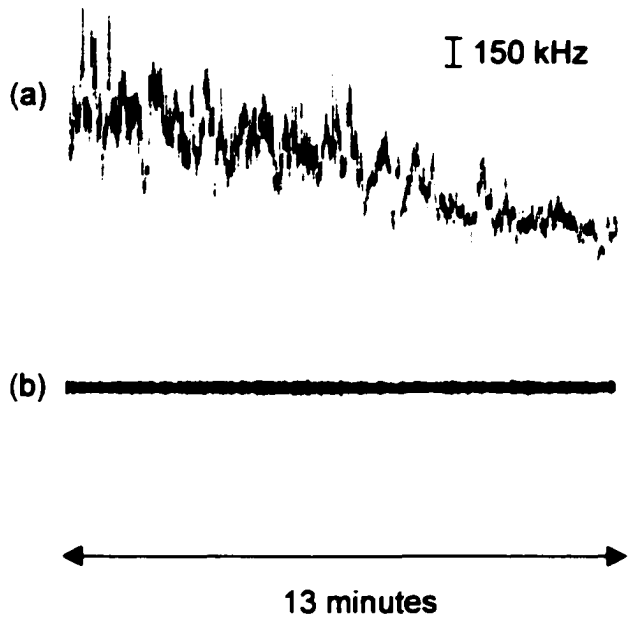

Figure 4.12 Saturated absorption signal from an iodine hyperfine transition over 13 minutes. (a) Unlocked laser placed at half-max of absorption peak and allowed to drift. (b) Servo engaged. Laser is off-set locked to the side of the hyperfine peak.

4.7 A Tunable Single-Frequency Diode Laser at 417 nm

As described in Chapter two, the laser focusing of the cooled Ga atomic beam can be performed with the 295 nm UV laser (suitably frequency shifted) or with a laser tuned to the $4p^2P_{3/2} \rightarrow 5s^2S_{1/2}$ transition at 417.32 nm. It was decided to preserve as much of the UV power as possible for laser cooling and attempt laser focusing on the 417 nm

transition. A tunable, single-frequency GaN diode laser DL100 was purchased from Toptica Photonics AG that could produce up to 15 mW of power at 417 nm.

Typically, free-running laser diodes have linewidths on the order of 100 MHz, which would be completely unacceptable for spectroscopy or laser focusing. To narrow the linewidth to < 1 MHz, the DL100 uses grating feedback. In this technique, the light emitted from the front facet of the diode laser is collimated by a multi-element lens with a very short focal length and then strikes a diffraction grating.[17,18] This is shown in Figure 4.13. This grating is adjusted such that the first diffraction order is reflected back toward the laser diode. This is called the "Littrow" configuration. The light passes through the collimator lens and is thus focused back into the laser diode. This feedback is considerably higher than the feedback from the diode front facet. This creates a new laser

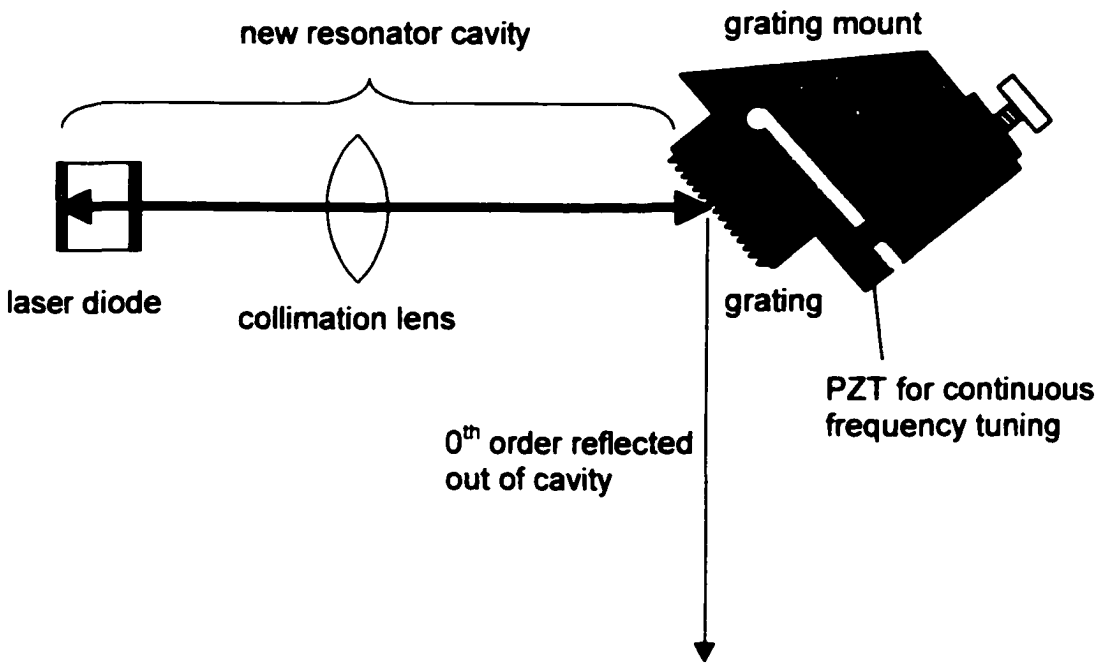

Figure 4.13 A free-running laser diode made to oscillate with narrow linewidth via grating feedback in the Littrow configuration.

resonator cavity, consisting of the rear of the laser diode and the grating. The free spectral range of this new resonator cavity is smaller that that of the laser diode, and thus the linewidth of the laser is substantially reduced.

Using this feedback, the DL100 produced 15 mW at 417 nm continuously tunable over a range of 20 GHz. The diode laser was extremely sensitive to feedback in the form of reflections from optical elements downstream. This was problematic for laser focusing, as in that technique the laser must be retroreflected back on itself as closely as possible to provide optimum focusing. In the infra-red, such feedback is reduced by using two Faraday isolators which provide a 60 dB isolation. In the blue region of the spectrum, there is no good Faraday isolator material. To minimize the feedback into the DL100, a polarizing beamsplitter and quarter-waveplate were positioned after the laser head. This reduced the power available for laser focusing to around 12 mW. It was observed that using a cube-type polarizing beamsplitter and a 0^{th} order waveplate for 417 nm did not reduce the feedback from the retroreflection enough to eliminate frequency disruption. Our commercial polarizing beamsplitter cube had an extinction ratio around 500:1. For isolation of the diode laser head, it may be preferable to switch to a more expensive polarizer such as a Glan Thompson, which can have an extinction ratio up to 10^5:1. Even then, the isolation system would be limited by the waveplate and other downstream optics.

The DL100 came with a current controller, temperature controller, and scan controller. The current controller and scan controller were adequate for tuning the laser diode to the desired frequency and holding it fixed after tuning. The scan controller allowed the laser frequency to be continuously scanned by applying a voltage to a piezo-

electric transducer (PZT) attached to the diffraction grating. Slight changes in the position of the diffraction grating resulted in changes of the cavity length, which allowed a continuous tuning of the resonant cavity frequency up to 20 GHz. This was found to be adequate for performing spectroscopy of the $4p^2P_{3/2} \rightarrow 5s^2S_{1/2}$ transition as described in Chapter five and to attempt laser focusing as described in Chapter seven.

4.8 Conclusions

We obtained tunable UV laser light from SHG in an ADA and a BBO crystal. Placed at the waist of a dye laser pumped power enhancement cavity, the ADA crystal provided up to 5 mW of power at 295 nm. To generate more UV laser power, the temperature-tuned ADA crystal was replaced by an angle-tuned BBO crystal. This crystal generated up to 90 mW of power and was a much better choice for UV production via SHG. A GaN laser diode operating with grating feedback in the Littrow configuration provided 15 mW of power at 417 nm. It had a narrow linewidth and was continuously tunable over 20 GHz. This laser was very sensitive to retroreflections from optical elements placed downstream from it. These lasers were used to perform the spectroscopy and light force manipulation described in the ensuing chapters of this thesis.

REFERENCES

[1] V. G. Dmitriev, G. G. Gurzadyan and D. N. Nikogosyan, *Handbook of Nonlinear Optical Crystals* (Springer, Berlin, 1997)

[2] A. Yariv, *Optical Electronics*, 3rd Ed. (Holt, Rinehart and Winston, New York, 1985)

[3] A. Ashkin, G.D. Boyd, and J. M. Dziedzic, "Resonant optical second harmonic generation and mixing," IEEE J. of Quant. Elec. **2**, 109-124 (1966)

[4] G. D. Boyd and D. A. Kleinman, "Parametric interaction of focused gaussian light beams," J. Appl. Phys. **39**, 3597-3639 (1968)

[5] H. W. Kogelnik, E. P. Ippen, A. Dienes, and C. V. Shank, "Astigmatically compensated cavities for cw dye lasers," IEEE Journ. Quant. Elec. **8**, 373-379 (1972)

[6] D. Froelich, L. Stein, H. W. Schroeder, and H. Welling, "Efficient frequency doubling of cw dye laser radiation," Appl. Phys. **11**, 97-101 (1976)

[7] A. I. Ferguson and M. H. Dunn, "A tunable, frequency-doubled, continuous-wave dye laser using ADA," Opt. Comm. **23**, 177-182 (1977)

[8] A. I. Ferguson, M. H. Dunn and A. Maitland, "Tunable, continuous wave, ultra-violet radiation around 300 nm by frequency doubling a Rhodamine 6G dye laser," Opt. Comm. **19**, 10-13, (1976)

[9] J. S. Nielsen, "Generation of 90-mW continuous-wave tunable laser light at 280 nm by frequency doubling in a KDP crystal," Opt. Lett. **20**, 840-842 (1995)

[10] D. Woll, B. Beier, K.-J. Boller, R. Wallenstein, M. Hagberg, and S. O'Brien, "1 W of blue 465-nm radiation generated by frequency doubling of the output of a high-power diode laser in critically phase matched LiB_3O_5," Opt. Lett. **24**, 691-693 (1999)

[11] C.S. Adams and A.I. Ferguson, "Tunable narrow linewidth ultra-violet light generation by frequency doubling of a ring Ti:sapphire laser using lithium tri-borate in an external enhancement cavity," Opt. Comm. **90**, 89-94 (1992)

[12] T. Kaing, and M. Houssin, "Ring cavity enhanced second harmonic generation of a diode laser using LBO crystal," Opt. Comm. **157**, 155-160 (1998)

[13] B. Beier, D. Woll, M. Scheidt, K.-J. Boller, and R. Wallenstein, "Second harmonic generation of the output of an AlGaAs diode oscillator amplifier system in critically phase matched LiB_3O_5 and β-BaB_2O_4," Appl. Phys. Lett. **71**, 315-317 (1997)

[14] James Bergquist, National Institute of Standards and Technology, (personal communication)

[15] S. J. Rehse, W. M. Fairbank, Jr., and S. A. Lee, "Measurement of the hyperfine structure of the $4d^2D_{3/2,5/2}$ levels and isotope shifts of the $4p^2P_{3/2} \rightarrow 4d^2D_{3/2}$ and $4p^2P_{3/2} \rightarrow 4d^2D_{5/2}$ transitions in gallium 69 and 71," J. Opt. Soc. Am. B **18**, 855 (2001)

[16] S. Gerstenkorn and P. Luc, *Atlas du Spectre d'Absorption de la Molecule D'Iode 15600 cm^{-1} – 17600 cm^{-1}* (Editions CNRS, Paris, 1977)

[17] C.E. Wieman and L. Hollberg, "Using diode lasers for atomic physics," Rev. Sci. Instrum. **62**, 1 (1991)

[18] K.B. MacAdam, A. Steinbach, and C. Wieman, "A narrow-band tunable diode laser system with grating feedback, and a saturated absorption spectrometer for Cs and Rb," Am. J. Phys. **60**, 1098 (1992)

CHAPTER 5

Gallium Hyperfine Spectroscopy at 295 nm and 417 nm

In gallium, both the laser cooling and laser focusing techniques operate on specific hyperfine transitions between lower lying energy levels. Therefore any attempt to manipulate an atom via these techniques requires a thorough knowledge of the hyperfine structure of the levels involved. In this chapter, I will describe the optical hyperfine spectroscopy performed on Ga. Specifically, the $4p^2P_{3/2} \rightarrow 4d^2D_{3/2}$ (294.50 nm), $4p^2P_{3/2} \rightarrow 4d^2D_{5/2}$ (294.45 nm), and $4p^2P_{3/2} \rightarrow 5s^2S_{1/2}$ (417.32 nm) transitions were studied by laser-induced fluorescence in our atomic Ga beam.

The hyperfine constants for the 4^2D states were measured previously,[1] but our preliminary experiments indicated these constants might be incorrect. Therefore, a very careful spectroscopy was performed on the two UV transitions in order to determine the constants accurately.[2]

The hyperfine constants for both the 4^2P and 5^2S levels were known, therefore a detailed spectroscopy of the 417 nm transition was not warranted. Our spectroscopic results confirmed previously published values and allowed us to propose an effective laser focusing scheme utilizing this transition. The previously reported hyperfine constants are given in Table 5.1.[3]

Table 5.1 Ga hyperfine constants

Level	Hyperfine constant (MHz)	^{69}Ga	^{71}Ga
$4p^2P_{1/2}$	A	1338.994	1701.347
$4p^2P_{3/2}$	A	190.794	242.434
	B	62.523	39.399
	C	8.7e-6	11.4e-6
$5s^2S_{1/2}$	A	1070	1359

5.1 Hyperfine Interaction

Hyperfine energy level splitting is a result of the interaction between valence electrons and the nucleus. The total angular momentum **F** of an atom is obtained from the coupling between the total electronic angular momentum operator **J** and the nuclear angular momentum operator **I**. Specifically,

$$\mathbf{F} = \mathbf{J} + \mathbf{I} \tag{5.1}$$

The quantum number J of the state is due to the fine structure splitting, or the interaction between the valence electron spin operator **S** and the angular momentum **L** (**J** = **L** + **S**). Thus each fine structure level (or J level) will have its degeneracy lifted by an interaction with the nucleus – the hyperfine splitting – and each of these new hyperfine levels will have a quantum number F. According to the rules for adding angular momenta, F will have values that range from J + I to |J - I| in integer steps.

The nuclear–atomic interaction is usually calculated by constructing a Hamiltonian composed of two series expansion multipoles: one for the nuclear moment and one for the electronic moment.[4] By parity considerations, only even electric multipoles and odd magnetic multipoles of the nucleus are allowed. The first non-zero

term involves the nuclear magnetic dipole moment, μ_I, and the magnetic field $\mathbf{B}_{el}$ produced by the electron cloud at the nucleus. We write this Hamiltonian as

$$H = -\mu_I \bullet \mathbf{B}_{el} \tag{5.2}$$

This interaction can be characterized by a parameter A, called the magnetic dipole hyperfine structure constant, by writing

$$H = A\,(\mathbf{I}\bullet\mathbf{J}) \tag{5.3}$$

The second non-zero term in the expansion involves the nuclear electric quadrupole moment, Q. This interaction is characterized by a parameter B, called the quadrupole hyperfine structure constant. B is proportional to Q and $\langle \partial^2 V_e/\partial z^2 \rangle$ which is the average gradient of the electric field at the nucleus due to the electrons. The multipole expansion terms continue on with the magnetic octupole moment (characterized by a constant C) and so on, with each successive term getting rapidly smaller. In this work, the data were only well defined enough to resolve the first two interactions, so we will limit our discussion to just the A and B hyperfine structure constants.

If I and J are non-zero, each fine structure level will split into hyperfine structure components shifted from the unperturbed level by an amount

$$\Delta E = \frac{A}{2}\,[F(F+1) - J(J+1) - I(I+1)] + \frac{B}{4}\,\frac{[\,\frac{3}{2}K(K+1) - 2J(J+1)I(I+1)]}{J(2J-1)I(2I-1)} \tag{5.4}$$

In Eq. 5.4, J is the total electronic angular momentum and $K = [F(F+1) - J(J+1) - I(I+1)]$. Hyperfine spectroscopy is done by measuring the energy difference between hyperfine

transitions and from that energy difference determining a value for A and B, assuming that the correct values for F have been assigned to each transition.

Also of importance in hyperfine spectroscopy is the isotope shift. This is an energy shift in the entire hyperfine spectrum (a shift in the spectrum's center of mass) due to mass differences between the isotopes. The usual convention is to describe an isotope shift as positive when the line frequency is greater for the heavier isotope. Because isotopes may not have the same nuclear spin or hyperfine structure constants, the spectra may be very complicated, particularly when the transitions from many different isotopes overlap. Because Ga has two stable isotopes with an unfortunate isotopic ratio (^{69}Ga at 60.4% and ^{71}Ga at 39.6%) our spectroscopy had to measure the isotope shift of the transition and the hyperfine structure constants for both isotopes.

5.2 Spectroscopy of the Ga UV Transitions at 295 nm

Let us first concern ourselves with the two ultraviolet wavelength transitions: $4p^2P_{3/2} \rightarrow 4d^2D_{3/2}$ (294.50 nm) and $4p^2P_{3/2} \rightarrow 4d^2D_{5/2}$ (294.45 nm). Both Ga isotopes have I = 3/2. The hyperfine splitting of the upper and lower states in both transitions, as well as the allowed hyperfine transitions and their calculated relative intensities, are shown in Figure 5.1. There are nine allowed transitions, giving a total of 18 transitions in each spectrum from the two isotopes.

Spectroscopy of the two hyperfine transitions required a tunable UV laser source near 294.5 nm. The UV laser light was generated by frequency doubling a dye laser in an external cavity utilizing an ADA crystal as described in Chapter four. A portion of the dye laser beam was picked off before the frequency doubling cavity and used for frequency determination and frequency scan calibration. The wavelength of the

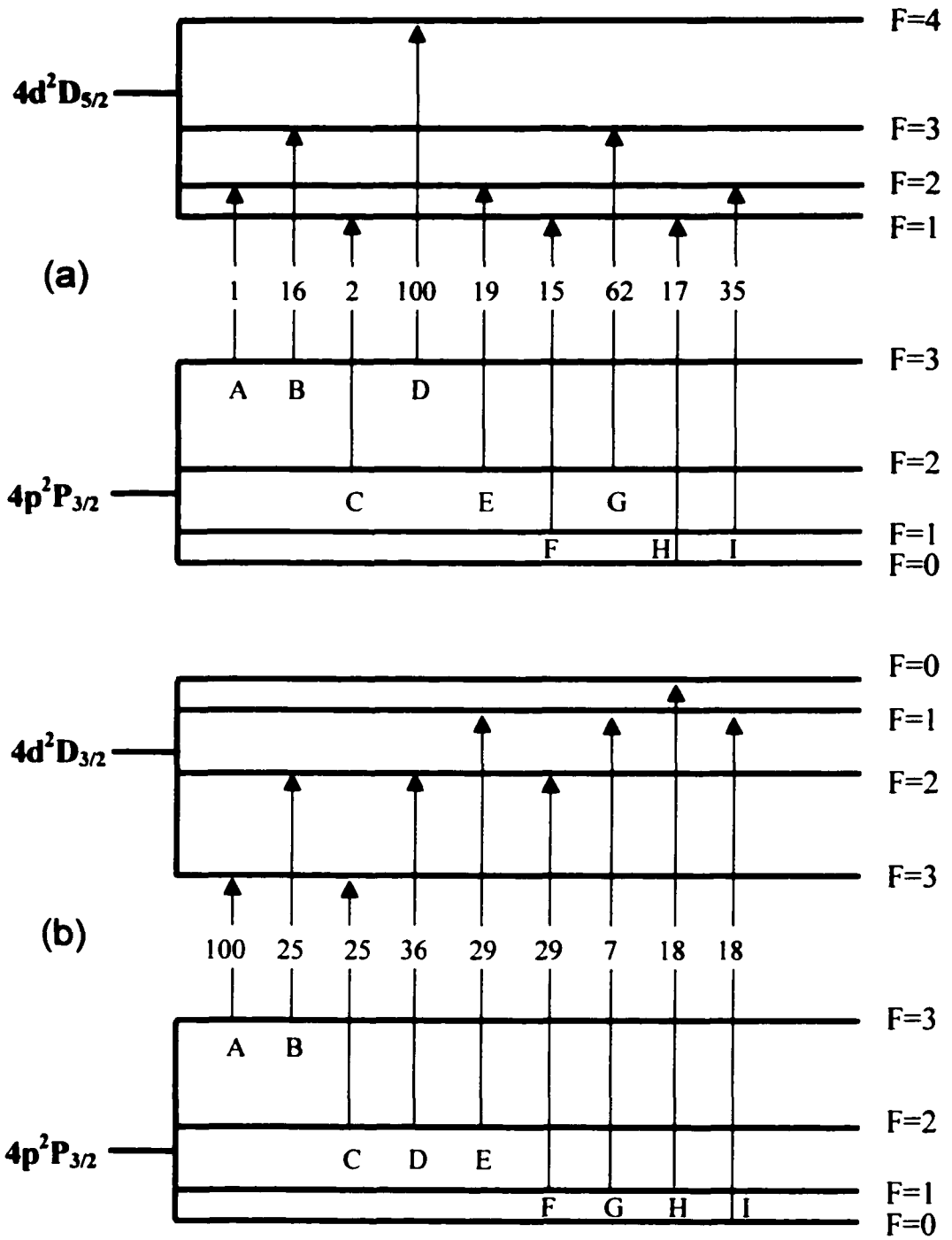

Figure 5.1 Diagrams of the upper and lower levels of the two UV transitions studied: (a) the $4p^2P_{3/2} \rightarrow 4d^2D_{5/2}$ transition and (b) the $4p^2P_{3/2} \rightarrow 4d^2D_{3/2}$ transition. The letters (A, B, C, ...) identify particular transitions allowed by using linearly polarized laser excitation. The numbers indicate the relative theoretical intensities of the transitions.

fundamental laser was determined by the lambda meter: a traveling Michelson interferometer with a frequency stabilized helium neon reference laser.[5] As the dye laser was tuned, the frequency interval was monitored using a temperature stabilized 1m confocal Fabry-Perot cavity. The free spectral range of this cavity was calibrated against I_2 reference lines and determined to be 74.227(36) MHz.[6] A schematic of the laser system utilized in this experiments is given in Figure 5.2. The majority of the fundamental beam, typically between 300 and 400 mW, went into the frequency doubling

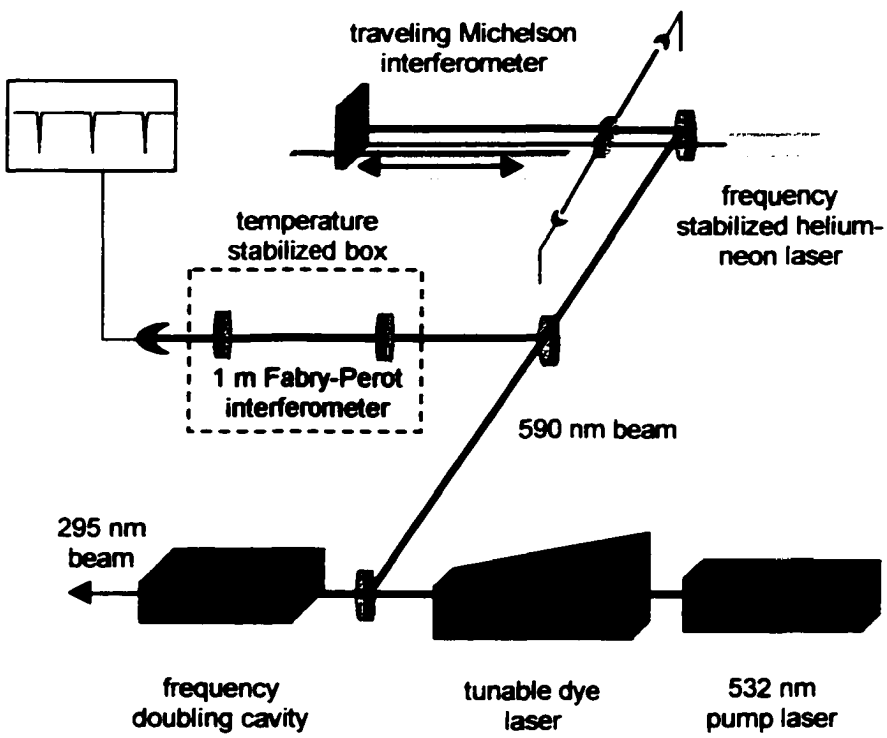

Figure 5.2 A schematic of the lasers used in the spectroscopy of the 4^2D levels of gallium.

cavity. Typical UV powers used in this spectroscopy were 1–3 mW, giving an intensity in the laser/atom interaction region just above the saturation intensity for most of the m_F components of the hyperfine levels.[7]

A beam of thermal Ga atoms was generated by a resistively heated effusive oven source with a 0.8 mm diameter nozzle hole as described in Chapter three. The oven was operated at approximately 1200° C, as determined by an optical pyrometer. A 0.7 mm x 1.0 mm aperture slit was placed in the Ga beam 15 cm from the oven to collimate it. The UV laser was introduced into the vacuum system through quartz Brewster windows and passed perpendicular to the Ga beam at a distance of approximately 15 cm from the collimating slit. A photomultiplier tube (PMT) located above the interaction region was used to detect the fluorescence as the UV laser was scanned through the transition. A schematic of the Ga beam source and interaction region is given in Figure 5.3.

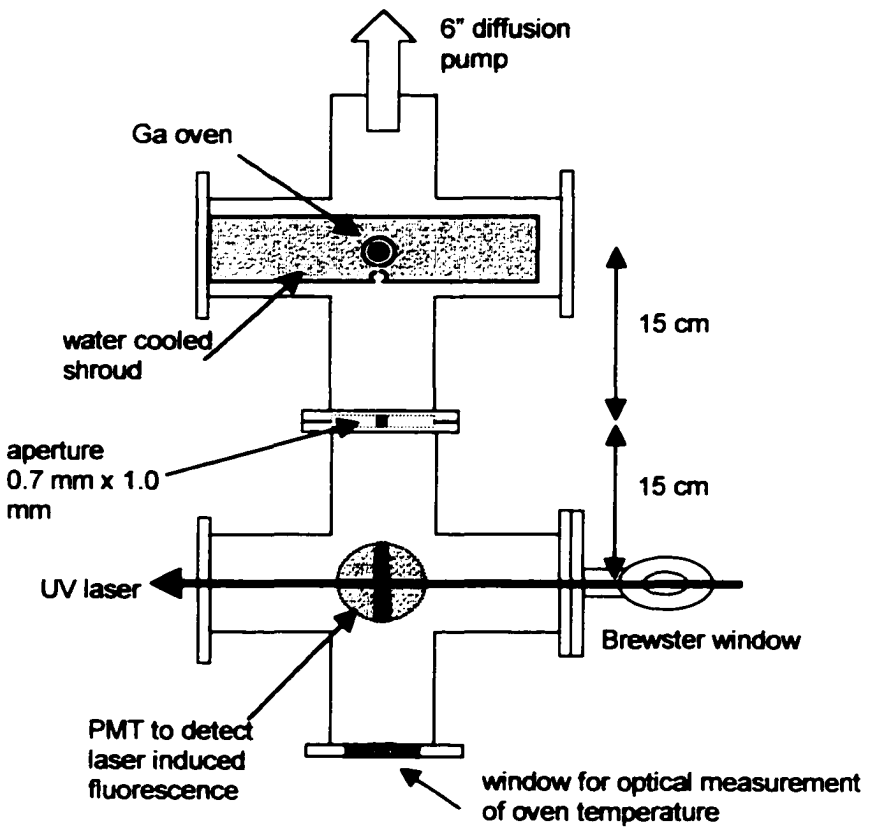

Figure 5.3 A schematic of the Ga atomic-beam apparatus.

The fluorescence spectra from the PMT as well as the fringe output from the 1m calibration cavity were collected simultaneously by two chart recorders. These data were digitized and the Fabry-Perot cavity fringe scans were used to calibrate the fluorescence spectra and check for small scan nonlinearities. Multiple spectra were taken for each transition. Typical spectra from the Ga fluorescence and the Fabry-Perot fringes are shown in Figure 5.4. In both transitions, the 18 different hyperfine components from the two Ga isotopes are not all resolved. In the case of the $4p^2P_{3/2} \rightarrow 4d^2D_{3/2}$ transition, the locking range of the doubling cavity was not sufficiently broad to obtain a complete fluorescence spectrum in one continuous scan. Hence, two scans were made.

5.3 Analysis of the 4^2D Spectroscopy

Qualitatively, the spectra obtained for these transitions did not agree with the spectra obtained by calculation of the linecenter positions using previously published values of the hyperfine structure constants.[1] This discrepancy and a lack of a suitable explanation for it prompted us to perform a careful spectroscopy and obtain our own values for the hyperfine structure constants.

The hyperfine A and B constants of the 4^2D levels and the isotope shifts were determined by fitting the spectra with these constants as fitting parameters. The fitting was done with a Fortran program and subroutines written specifically for this experiment. The Fortran program utilized a non-linear least squares procedure as discussed in Numerical Recipes.[8]

The fitting procedure was as follows. The hyperfine structure constants for the $^2P_{3/2}$ lower level of the two transitions were very well known (see Table 5.1), so in the fitting routine they were fixed. An initial set of five parameters, the A and B coefficients

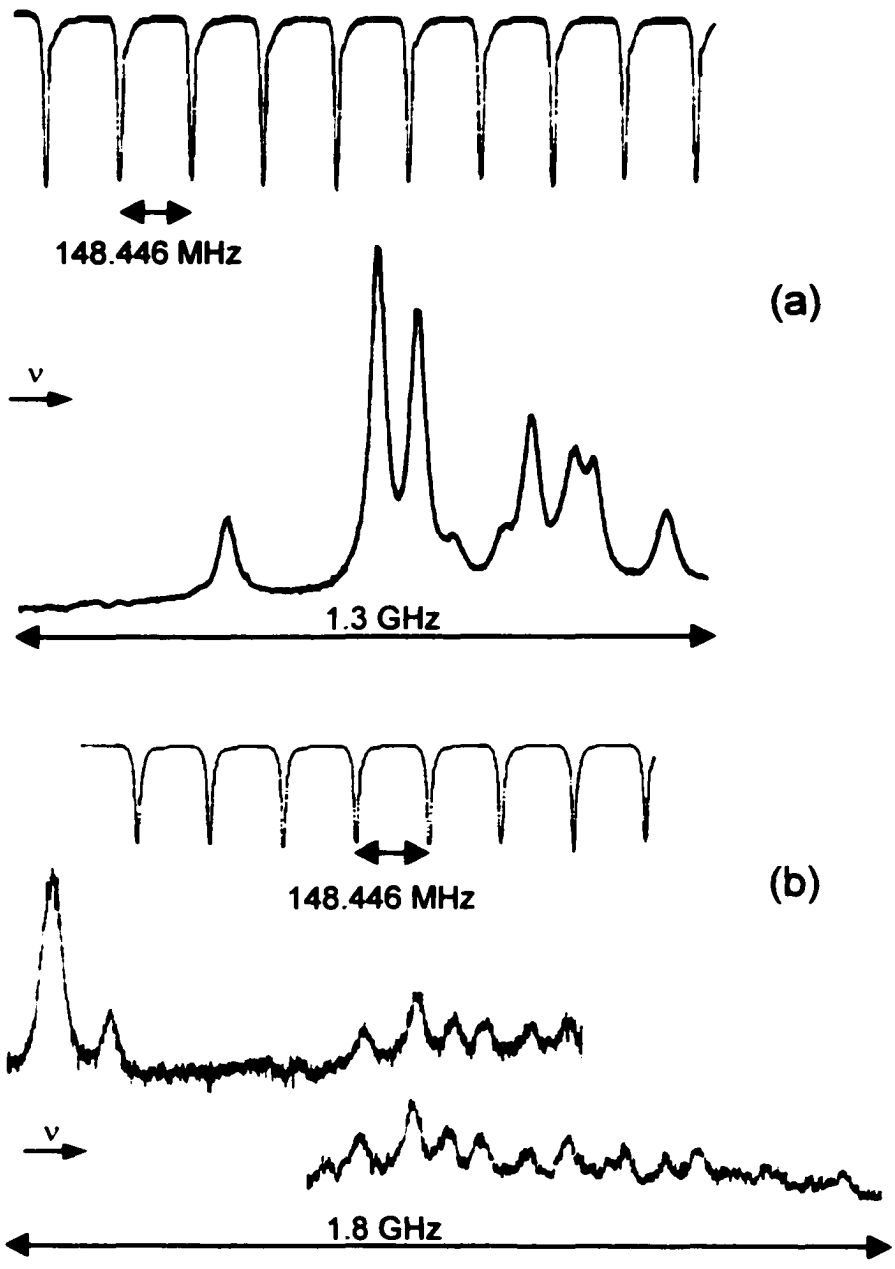

Figure 5.4 Laser induced fluorescence spectra and Fabry-Perot cavity fringes. (a) The $4p^2P_{3/2} \rightarrow 4d^2D_{5/2}$ transition. (b) The $4p^2P_{3/2} \rightarrow 4d^2D_{3/2}$ transition.

for each Ga isotope and the isotope shift, were used to compute the linecenter positions of the 18 allowed transitions. All the transitions were assumed to have the same width and

lineshape. The overall intensity and in some cases individual peak heights were additional fitting parameters. The Fortran fitting program calculated the total lineshape and compared this to the experimental fluorescence spectrum. The χ^2 of the fit was computed and changes were made to the fitting parameters in order to minimize the χ^2, which was a measure of the difference between the experimental fluorescence spectrum and the calculated spectrum. All fitting calculation and program compilation was performed on the CSU UNIX server. The Fortran program and subroutines created for this fitting are presented in Appendix five.

This program was flexible in being able to change the number of fitting parameters. It was possible to start fitting with only an A constant, then when the fitting agreement was good, add a B constant to the calculation to refine it. In the final fitting procedure, the hyperfine A coefficients for both ^{69}Ga and ^{71}Ga, the B coefficient for ^{69}Ga, and the isotope shift were used as fitting parameters. The spectra did not have sufficient resolution to allow a separate B coefficient for ^{71}Ga to be determined independently. Therefore its value was fixed to the value for ^{69}Ga by the relation $B(^{71}Ga) = 0.630 \times B(^{69}Ga)$, where the factor 0.630(1) was the ratio of the nuclear electric quadrupole moments determined previously.[9]

Graphical results of the fitting for both transitions are shown in Figure 5.5, where the fitted spectra are shown as solid black curves and the fluorescence spectra are shown as dashed red lines. The relative intensities of the peaks were fixed to the theoretical line strength ratios (shown in Figure 5.1) and the isotopic abundance ratio. A 42(8) MHz linewidth was used for fitting the $4p^2P_{3/2} \rightarrow 4d^2D_{5/2}$ transition and a 32(11) MHz linewidth was used for fitting the $4p^2P_{3/2} \rightarrow 4d^2D_{3/2}$ transition (3σ errors). The natural

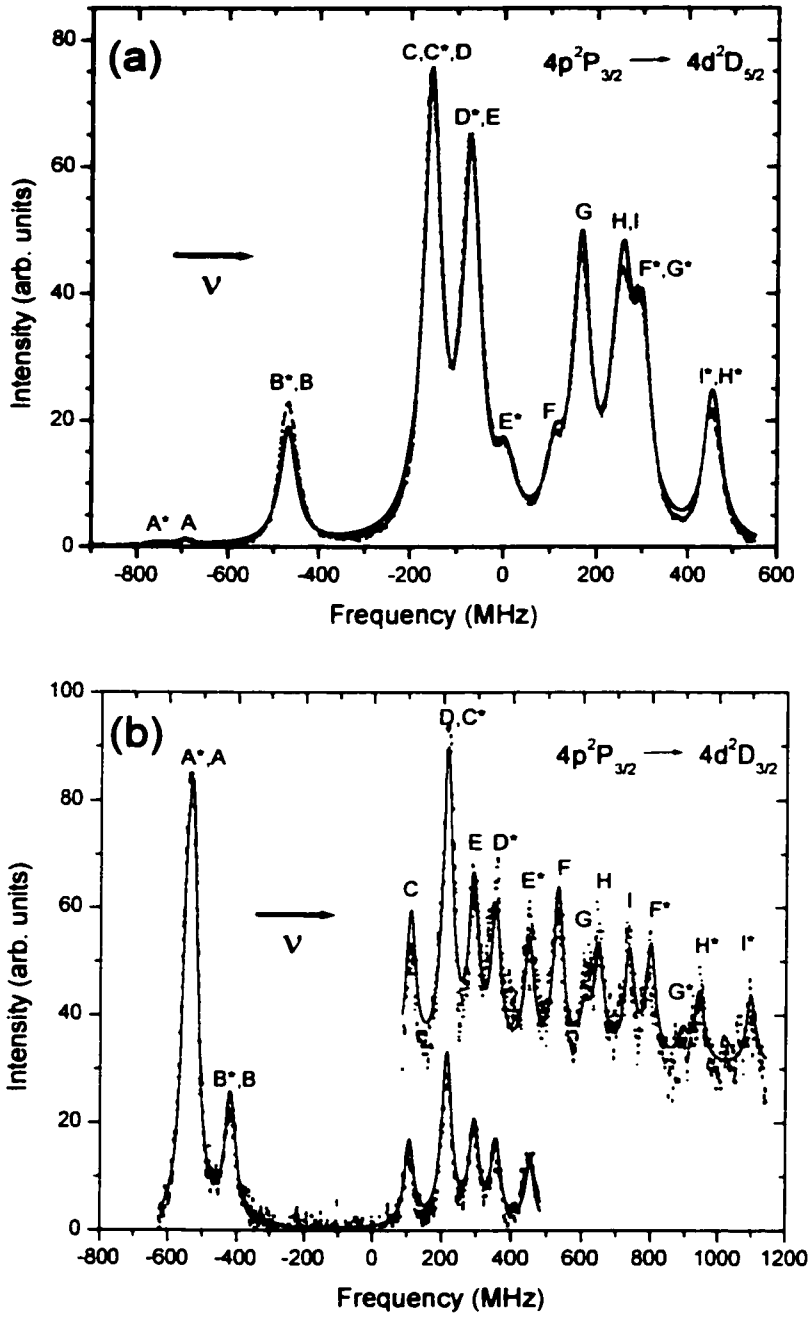

Figure 5.5 Laser-induced fluorescence spectrum (red dotted line) and the fitted spectrum (black solid line) for the (a) $4p^2P_{3/2} \rightarrow 4d^2D_{5/2}$ and (b) $4p^2P_{3/2} \rightarrow 4d^2D_{3/2}$ transitions. Frequency 0 denotes the center-of-mass of the ^{69}Ga transition. Specific hyperfine transitions designated with a letter (A, B, C, ...) are identified in Figure 5.1. Transitions designated with an asterisk (*) are from the isotope ^{71}Ga. In several instances one or more peaks overlap and are indistinguishable. In (b) the vertical scale of the blue end of the spectrum has been magnified.

linewidth of the transition is 25 MHz. The residual Doppler width was less than 6 MHz and could be neglected. The difference between the natural and the fitted linewidths can be attributed to power broadening. The laser saturation parameter (I/I_0) was 1.5 to 2.0 for the $4p^2P_{3/2} \rightarrow 4d^2D_{5/2}$ fluorescence spectrum and was 0.5 to 1.0 for the $4p^2P_{3/2} \rightarrow 4d^2D_{3/2}$ spectrum. Using these values of the saturation parameter, our fitted values for the linewidths agreed well with the estimated power broadened linewidths. Different lineshapes were investigated for the fitting, including Lorentzian, Gaussian and the Voigt profile. The choice of the lineshape did not affect the outcome for the hyperfine constants, although the Lorentzians provided the best χ^2 value.

Other fitting procedures were also investigated. The peak intensities of some of the strongest lines were allowed to vary independently. A lower χ^2 was obtained, but the hyperfine constant results did not change significantly using these additional parameters. Fitting was also attempted without locking the ratio of the B constants, however no meaningful value for $B(^{71}Ga)$ could be determined. These other procedures were not used to determine the final results.

There were commercial peak fitting programs that could have been utilized for fitting and one such program, Origin, was tried. It was found that this program was not successful at fitting all 18 peaks, particularly the small peaks that overlapped larger peaks in the spectrum. Origin was good at finding the location of individual larger peaks, but it could not determine the relationships between the positions, i.e. the A and B coefficients or the isotope shift. By contrast, our program determined these parameters directly.

5.4 Fitting Results

The three hyperfine structure constants, determined by averaging over seven scans of the $4p^2P_{3/2} \rightarrow 4d^2D_{5/2}$ transition and three pairs of scans of the $4p^2P_{3/2} \rightarrow 4d^2D_{3/2}$ transition, are given in Table 5.2. The isotope shifts are given in Table 5.3. In both tables, previously published results are given for comparison.

Table 5.2 Experimental values of the hyperfine structure constants

		^{69}Ga		^{71}Ga	
Level	Source	A(MHz)	B(MHz)	A(MHz)	B(MHz)
$4d^2D_{3/2}$	This work	-36.3(2.2)	+4.6(4.2)	-46.2(3.8)	a
	Weber et al.[1]	+36(2)	-	+46(3)	-
$4d^2D_{5/2}$	This work	+77.3(0.9)	+5.3(4.1)	+97.9(0.7)	a
	Weber et al.[1]	-78(3)	-	-98(4)	-

[a] $B(^{71}Ga) = 0.630 \times B(^{69}Ga)$

Table 5.3 Experimental values of the isotope shifts

Transition	Source	Isotope Shift (MHz)
$4p^2P_{3/2} \rightarrow 4d^2D_{3/2}$	This work	+114(8)
	Weber et al.[1]	+121(10)
$4p^2P_{3/2} \rightarrow 4d^2D_{5/2}$	This work	+115(7)
	Weber et al.[1]	+117(9)

Our agreement with the absolute value of the published A values was excellent. The difference in sign, but not in magnitude, of the A coefficients between our investigation and [1] required further investigation. The laser scan direction was checked carefully using the lambda-meter and verified against known iodine transitions. Furthermore, having an A coefficient with the opposite sign in the 4^2D state would not simply reverse the positions of the spectral lines. It would completely change the locations of the components because the hyperfine structure of the ground state remains

unchanged. This effect is shown in Figure 5.6 for the $4p^2P_{3/2} \rightarrow 4d^2D_{5/2}$ transition. As can be seen in Figure 5.6(c), an opposite sign in A cannot fit the laser-induced fluorescence spectrum obtained in this study.

To explain the discrepancy in sign, it became necessary to examine the previous experiment in more detail. In [1] the Ga hyperfine structure was obtained using resonant Doppler-free two-photon spectroscopy, with the 4^2D state being the intermediate state. Two lasers were used to obtain resonance, one fixed and one tunable, and both counterpropagating and copropagating spectra were taken to determine the intermediate-state structure. Thus the experiment had more variables than our simple laser-induced fluorescence technique. We were able to fit the spectra in [1] using our hyperfine constants. In all cases the peak location agreed to better than 10 MHz. At the same time, we tried the opposite signs on the A coefficients, i.e., using the results of [1]. We found that there was no agreement between the calculated and their measured peak positions. The misfit was similar to the type shown in Figure 5.6. Thus the signs of the A coefficients reported by Weber et al. in [1] are incorrect.

This spectroscopy provided a significant improvement in the accuracy of the hyperfine structure constants and corrected sign errors in the previous determination of the A constants. The ratios of $A(^{71}Ga)/A(^{69}Ga)$ were 1.27(2) and 1.27(13) for the $4d^2D_{5/2}$ and $4d^2D_{3/2}$ levels, respectively. These numbers agreed well with the ratio of the nuclear magnetic dipole moments, 1.2700(8).[9] No other measurement of the B constants had been made prior to this work. The measured isotope shifts all fell within the errors of the previously published values.

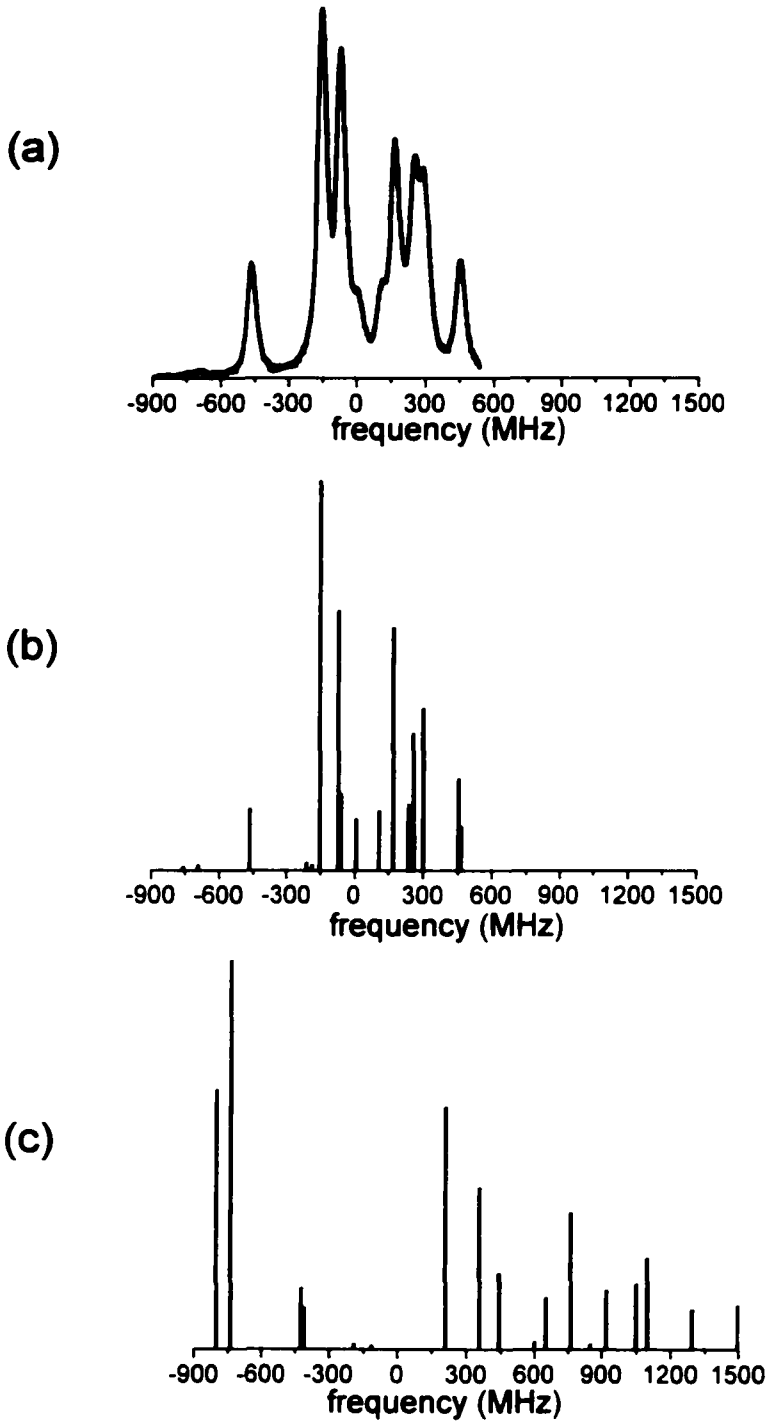

Figure 5.6 (a) Laser-induced fluorescence spectrum for the $4p^2P_{3/2} \rightarrow 4d^2D_{5/2}$ transition obtained in the present work. (b) Calculated peak locations using the hyperfine constants reported in this work. (c) Calculated peak locations using the hyperfine constants reported by Weber et al.[1]

The uncertainties reported with our parameter values were 3σ deviations from the mean. The dominant error in the data was due to the noise of the laser-induced fluorescence signal, particularly in the $4p^2P_{3/2} \rightarrow 4d^2D_{3/2}$ transition, which had a much smaller signal. Systematic errors, e.g. frequency scan nonlinearities, UV laser power variations, and optical pumping effects, (all of which were investigated) were small by comparison.

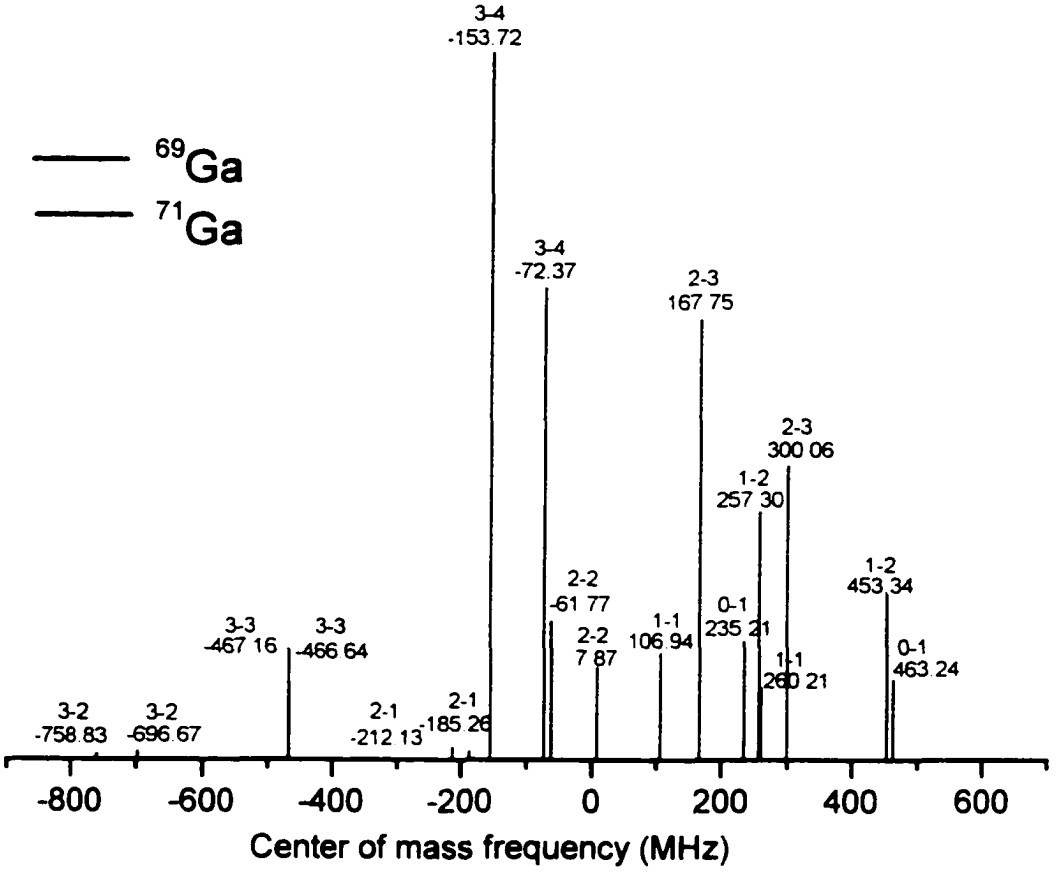

Figure 5.7 Calculated linecenter positions, relative theoretical intensities and hyperfine transition identification for the $4p^2P_{3/2} \rightarrow 4d^2D_{5/2}$ transition.

Finally, using the numerical results obtained by this spectroscopy, the linecenter position of each hyperfine transition was calculated. A "stick figure" spectrum for the $4p^2P_{3/2} \rightarrow 4d^2D_{5/2}$ is given in Figure 5.7. Figure 5.8 is a stick figure diagram for the $4p^2P_{3/2} \rightarrow 4d^2D_{3/2}$ transition. From Figure 5.7 we note that the hyperfine transition intended for laser cooling, the ^{69}Ga F=3 → F=4, is located at −154 MHz. To Doppler cool we must detune the laser slightly (~13 MHz) to the red, or low frequency side, of

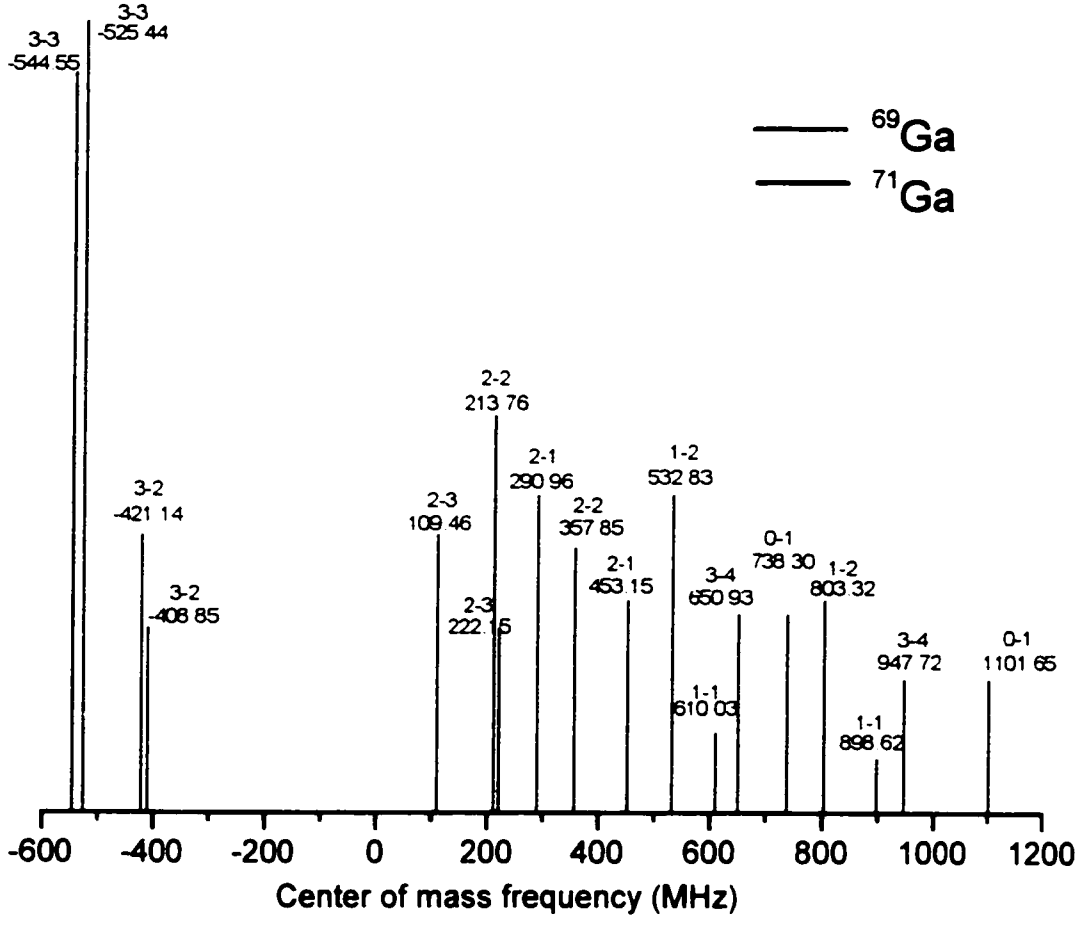

Figure 5.8 Calculated linecenter positions, relative theoretical intensities and hyperfine transition identification for the $4p^2P_{3/2} \rightarrow 4d^2D_{3/2}$ transition.

this transition. This detuning will bring the laser close to resonance with both of the F=2 → F=1 transitions (at –212 MHz and –185 MHz). This will result in optical pumping of the F=2 state, but should not affect the laser cooling. The only transition that can provide a way for cold atoms to decay to the incorrect ground state (so that the cooling transition is no longer cycling) is the F=3 → F=3 transition at –467 MHz. This transition is ~10Γ to the red of the cooling transition, which may be off-resonantly excited if the atom spends enough time in the laser.

5.5 Spectroscopy of the Ga $4p^2P_{3/2} \rightarrow 5s^2S_{1/2}$ Transition at 417 nm

A careful spectroscopy of the $4p^2P_{3/2} \rightarrow 5s^2S_{1/2}$ transition was not performed. It was our intention only to confirm the previously published results, as given in Table 5.1.[10] The hyperfine splitting of the upper and lower states of this transition, as well as the allowed hyperfine transitions and their calculated relative intensities, are shown in Figure 5.9. For the $4p^2P_{3/2} \rightarrow 5s^2S_{1/2}$ transition the isotope shift was –38.96 MHz.[3] This transition had six allowed hyperfine transitions per isotope. The splitting of the $5s^2S_{1/2}$ level was quite a bit larger than in either the ^2P or ^2D levels, and had a wider frequency spectrum and less overlap of the hyperfine components, making them easier to resolve.

For this spectroscopy, the same apparatus from Figure 5.3 was used, however the UV laser was replaced with a tunable single-frequency diode laser at 417 nm. This diode laser could be scanned up to 25 GHz which was enough to cover the entire transition. The diode laser power was reduced with neutral density filters to less than 1 mW in an elliptical beam (1.5 mm and 3.3 mm $1/e^2$ diameters). At powers above 1 mW, the hyperfine peaks were power broadened and overlapped each other. A laser-induced fluorescence spectrum of this transition is shown in Figure 5.10. A stick figure diagram

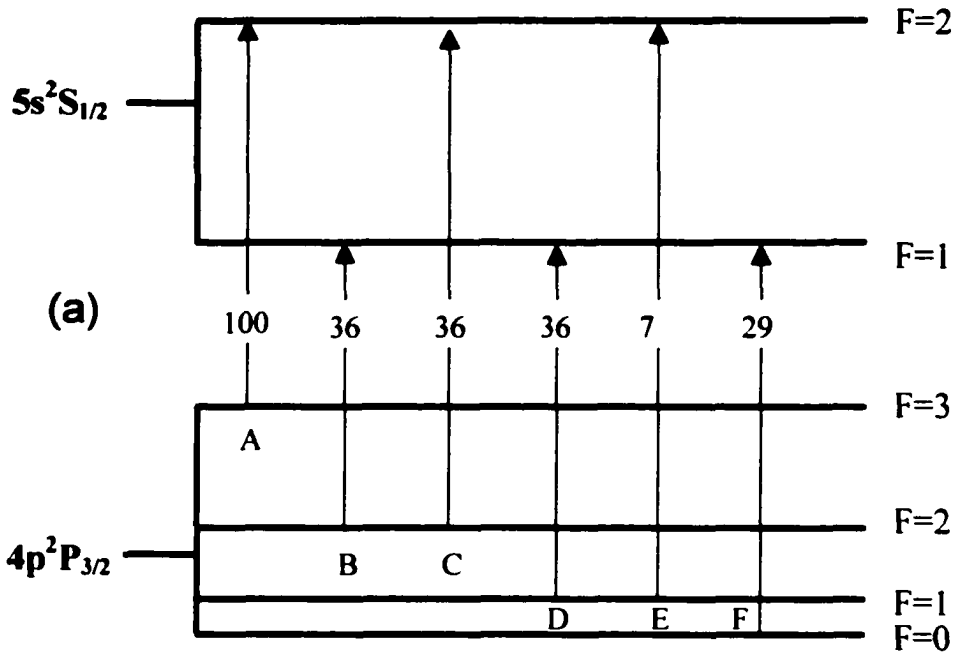

Figure 5.9 Diagram of the upper and lower levels of the $4p^2P_{3/2} \rightarrow 5s^2S_{1/2}$ transition. The letters (A, B, C, ...) identify particular transitions allowed by using linearly polarized laser excitation. The numbers indicate the relative theoretical intensities of the transitions.

with each hyperfine transition identified and its calculated linecenter is shown in Figure 5.11. The agreement between the experimental spectrum and the calculated spectrum was excellent. The tallest peak at 357 MHz was the F=3 → F=2 transition of ^{69}Ga. This was the laser focusing transition. In focusing, the laser is usually detuned to the blue of the appropriate transition. We see that the nearest transition was the F=3 → F=2 transition of ^{71}Ga, 68 MHz to the blue. Since we intended to detune approximately 300 to 400 MHz, the presence of this transition was not problematic. In fact, we see that in the region where we intended to detune (~700 MHz from the center of mass frequency) there

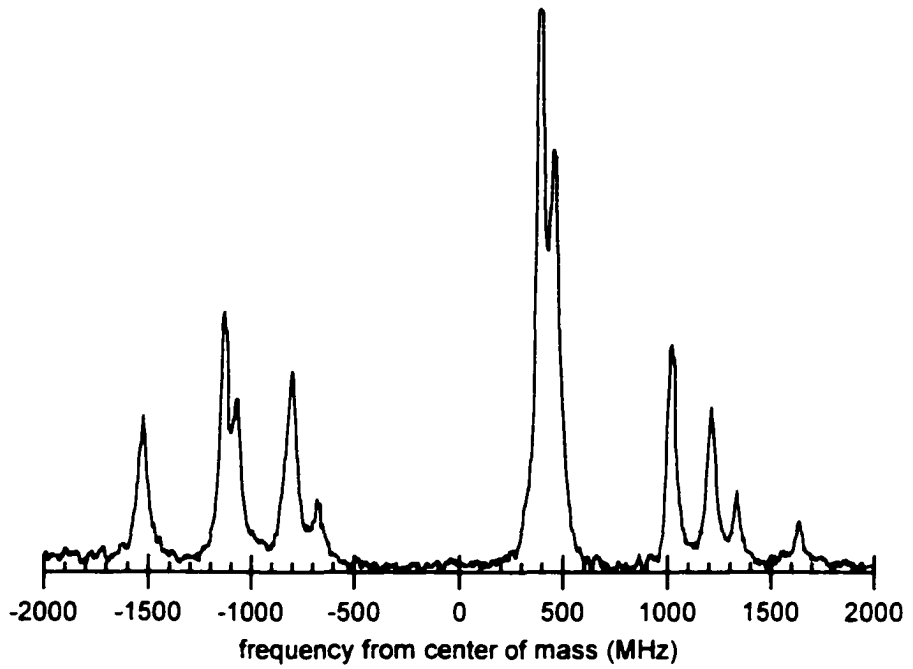

Figure 5.10 Laser-induced fluorescence spectrum of the $4p^2P_{3/2} \rightarrow 5s^2S_{1/2}$ transition.

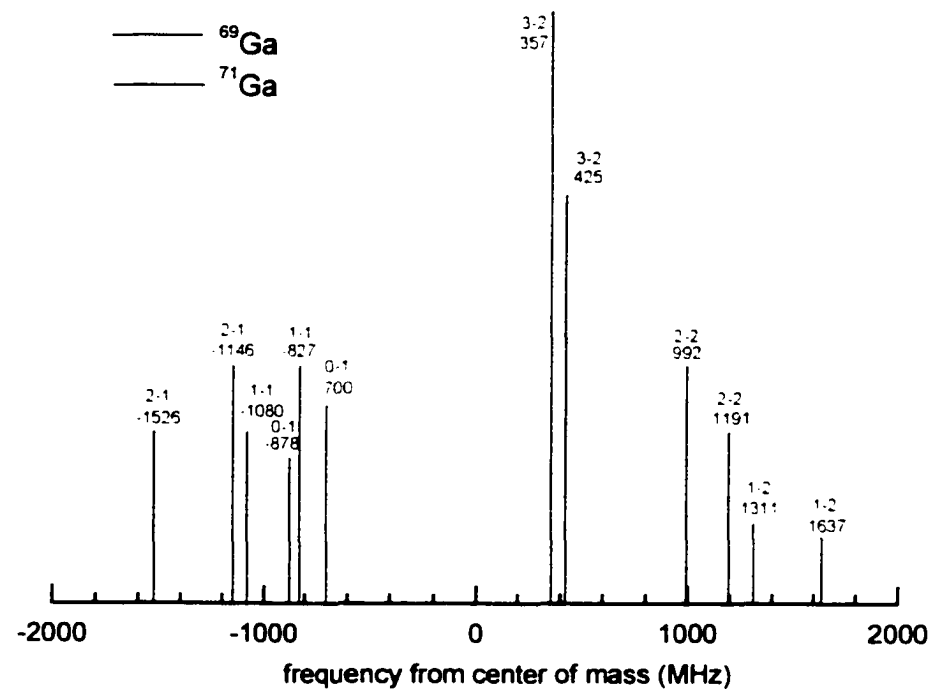

Figure 5.11 Calculated linecenter positions, relative theoretical intensities, and hyperfine transition identification for the $4p^2P_{3/2} \rightarrow 5s^2S_{1/2}$ transition.

were no hyperfine transitions at all. This was a very convenient hyperfine structure for laser focusing.

5.6 Conclusions

We have performed optical spectroscopy on three transitions in Ga 69 and 71: $4p^2P_{3/2} \rightarrow 4d^2D_{3/2}$ (294.50 nm), $4p^2P_{3/2} \rightarrow 4d^2D_{5/2}$ (294.45 nm), and $4p^2P_{3/2} \rightarrow 5s^2S_{1/2}$ (417.32 nm). A careful determination of the hyperfine A and B constants for the UV transitions revealed a discrepancy with published values, resulting in a newer and more accurate measurement. The hyperfine A constant measured for the $4d^2D_{5/2}$ level was 77.3±0.9 MHz for ^{69}Ga and 97.9±0.7 MHz for ^{71}Ga (3σ errors). The A constant measured for the $4d^2D_{3/2}$ level was –36.3±2.2 MHz for ^{69}Ga and –46.2±3.8 MHz for ^{71}Ga. These measurements corrected sign errors in the previous determination of these constants. For ^{69}Ga, the hyperfine B constants measured for the $4d^2D_{5/2}$ and $4d^2D_{3/2}$ levels were 5.3±4.1 MHz and 4.6±4.2 MHz, respectively. This was a first ever measurement of this constant. The isotope shift was determined to be 114±8 MHz for the $4p^2P_{3/2} \rightarrow 4d^2D_{3/2}$ transition and 115±7 MHz for the $4p^2P_{3/2} \rightarrow 4d^2D_{5/2}$ transition. This was in agreement with previous measurement. The $4p^2P_{3/2}(F=3) \rightarrow 4d^2D_{5/2}(F=4)$ transition, intended for laser cooling, was identified in the fluorescence spectrum.

The spectroscopy of the $4p^2P_{3/2} \rightarrow 5s^2S_{1/2}$ transition at 417 nm was in agreement with the previously obtained values for the hyperfine constants. In this spectrum, we identified the intended laser focusing transition, the hyperfine F=3 → F=2 transition of ^{69}Ga. A detuning of the laser ~300 MHz to the blue of this hyperfine peak will resulted in the laser being in a relatively empty section of the spectrum.

REFERENCES

[1] K.H. Weber, J. Lawrenz, A. Obrebski, and K. Niemax, "High-resolution laser spectroscopy of aluminium, gallium, and thallium," Phys. Scr. **35**, 309 (1987)

[2] S.J. Rehse, W.M. Fairbank, and S.A. Lee, "Measurement of the hyperfine structure of the $4d^2D_{3/2,5/2}$ levels and isotope shifts of the $4p^2P_{3/2} \rightarrow 4d^2D_{3/2}$ and $4p^2P_{3/2} \rightarrow 4d^2D_{5/2}$ transitions in gallium 69 and 71," J. Opt. Soc. Am. B **18**, 855 (2001)

[3] E.B. Saloman, "A resonance ionization spectroscopy/resonance ionization mass spectrometry data service. V – Data sheets for Ga, Mn, Sc and Tl," Spec. Acta **49B**, 251 (1994) and references therein.

[4] A brief introduction to the topic of hyperfine structure and its relevance is given in G. T. Emery, "Hyperfine structure", in *Atomic, Molecular, and Optical Physics Handbook*, Ed. G.W.F. Drake (American Institute of Physics, Woodbury, NY, 1996) p. 198

[5] J.L. Hall and S.A. Lee, "Interferometric real-time display of cw dye laser wavelength with sub-Doppler accuracy," Appl. Phys. Lett. **29**, 367 (1976)

[6] L. Hlousek, S.A. Lee, and W.M. Fairbank, Jr., "Precision wavelength measurements and new experimental lamb shifts in helium," Phys. Rev. Lett. **50**, 328 (1983)

[7] Since the tunable UV laser was linearly polarized, the selection rules for $m_F \rightarrow m_F'$ transitions include $\Delta m_F = 0$ only. Saturation intensities calculated for the transitions between m_F levels of the F=3 → F=4 transition are: $m_F=0 \rightarrow m_F'=0$, 202 mW/cm^2; $m_F=1 \rightarrow m_F'=1$, 215 mW/cm^2; $m_F=2 \rightarrow m_F'=2$, 269 mW/cm^2; $m_F=3 \rightarrow m_F'=3$, 464 mW/cm^2. These values are typical of the other transitions as well.

[8] W.H. Press, S.A. Teukolsky, W.T. Vetterling, and B.P. Flannery, *Numerical Recipes in Fortran*, 2nd Ed. (Cambridge University Press, Cambridge, 1992)

[9] G.H. Fuller, "Nuclear spins and moments," J. Phys. Chem. Ref. Data **5**, 835 (1976)

[10] J.H.M. Neijzen and A. Donszelmann, "Hyperfine structure and isotope shift measurements in neutral gallium and indium with a pulsed dye laser," Physica **98C**, 235 (1980)

CHAPTER 6

Light Force Cooling of an Atomic Gallium Beam

This chapter describes the first experimental realization of the laser cooling of a gallium atomic beam in one dimension using the polarization gradient technique. I will describe the procedure for accomplishing the laser cooling and the analysis of the cooling results. The dependence of the cooling efficiency on the laser detuning, power, and interaction length will be discussed.

Optical pumping of Ga atoms out of the cooled hyperfine state due to the presence of the cooling laser was observed. This chapter describes the measurement of the optical pumping and the implementation of repumping schemes.

6.1 Experimental Apparatus

A schematic of the Ga atomic beam apparatus and laser system utilized in the laser cooling experiment is shown in Figure 6.1. The Ga beam apparatus is detailed in Figure 6.2 and was described more fully in Chapter three. A beam of Ga atoms was generated by a resistively heated effusive oven source operating near 1300° C. An aperture 0.8 mm x 1.0 mm precollimated the beam to a full-angle divergence of 6.2 mrad. The Ga atoms were collimated by the cooling laser and traveled 34 cm until they were illuminated by a weak probe laser to measure the amount of collimation. The generation

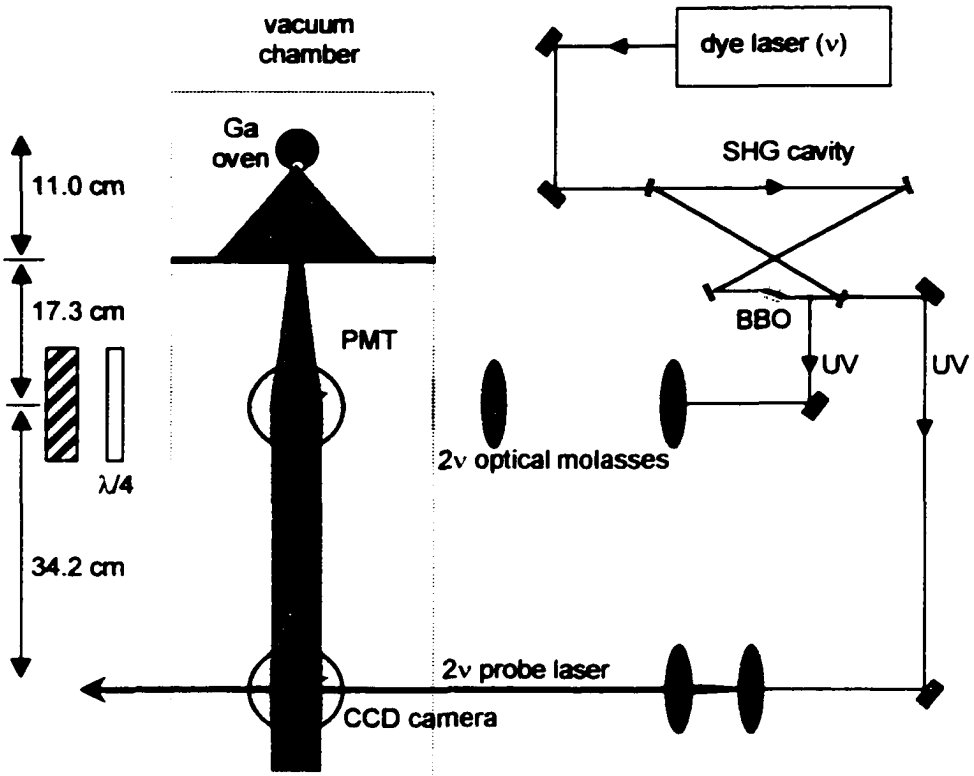

Figure 6.1 A schematic of the Ga atomic beam apparatus and laser system utilized in the laser cooling experiment.

of the UV light (the cooling beam and the probe beam) was described in Chapter four. To ensure full overlap with the atoms in the beam and a sufficiently long interaction time, the cooling laser had an elliptical cross-section: 1 mm x 5.5 mm, $1/e^2$ full-widths, and was Gaussian along both the major and minor axes of the ellipse. The cooling laser beam was linearly polarized vertically and passed through a quarter-wave plate on the far side of the interaction region prior to retroreflection generating a lin $\perp$ lin polarization gradient. Typical powers in the cooling laser during the collimation experiments ranged from 50 mW to 90 mW. The probe laser, also linearly polarized, was circular in cross section with a radius of approximately 0.8 mm at the interaction region and contained 10's to

100's of μW of power. This beam was passed through a telescope and an iris to bring it to a soft focus in the vacuum region. The laser-induced fluorescence from the interaction of this probe laser and the Ga atoms was imaged from above by a liquid nitrogen cooled UV sensitive CCD camera.

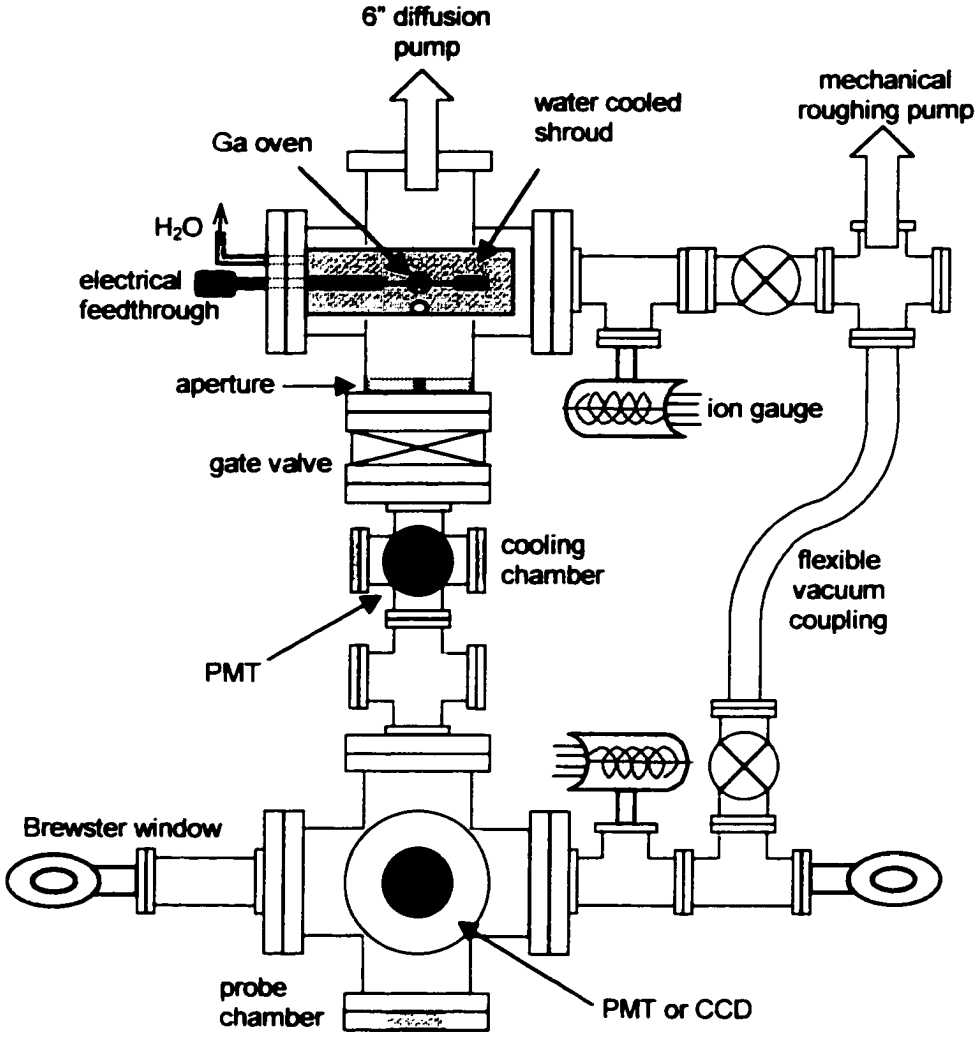

Figure 6.2 A detail of the vacuum system used in the Ga cooling experiment.

The CCD camera was a Princeton Instruments, Inc. liquid nitrogen (LN_2) cooled CCD, ideal for ultra-low light level experiments that require very long integration times.[1] The camera system consisted of a camera head, controller, and computer control package. The camera head contained a mechanical shutter housing, a UV sensitive back illuminated CCD chip, and a vacuum insulated LN_2 dewar. The CCD chip consisted of an array of 1100 x 310 pixels. Each pixel was 24 μm x 24 μm. The LN_2 dewar maintained the temperature of the CCD chip at –80° C for over 16 hours between refills. With the chip cooled to operating temperatures we estimated the sensitivity of the chip to be 10 photons per pixel "count". The controller controlled the opening and closing of the shutter, the temperature of the chip, and the readout of the CCD array through a PC interface. The software interface was a program called Winspec that controlled camera operation and data acquisition.

The CCD chip had to be kept vertical because of the LN_2 dewar, so the laser-induced fluorescence from the interaction of the Ga atomic beam and the probe laser was imaged onto the surface of the chip by means of an imaging lens and a relay periscope. To do this a light tight imaging/periscope system was constructed. A schematic of the periscope and camera is shown in Figure 6.3. The lens was a 1.5" diameter f = 76 mm plano-convex fused silica lens, AR coated for 248 – 355 nm. It sat atop a quartz window which was recessed into the vacuum system. Above this lens was the periscope assembly which consisted of a 2" enhanced UV aluminum coated mirror mounted on a mirror mount. The optics were enclosed in a light tight Al box. All surfaces of the box and the lens/mirror mounts were painted black to reduce scattered light. Great care was taken to minimize the amount of background light that illuminated the CCD array. A UV filter

was placed between the vacuum window and the lens to reduce light from the vacuum system. The entire apparatus - periscope and camera - was wrapped in many layers of heavy black cloth to block ambient light. This optical system had a magnification factor of 2.5. In the camera's fluorescence images each 24 μm pixel corresponded to 9.6 μm in the atomic beam.

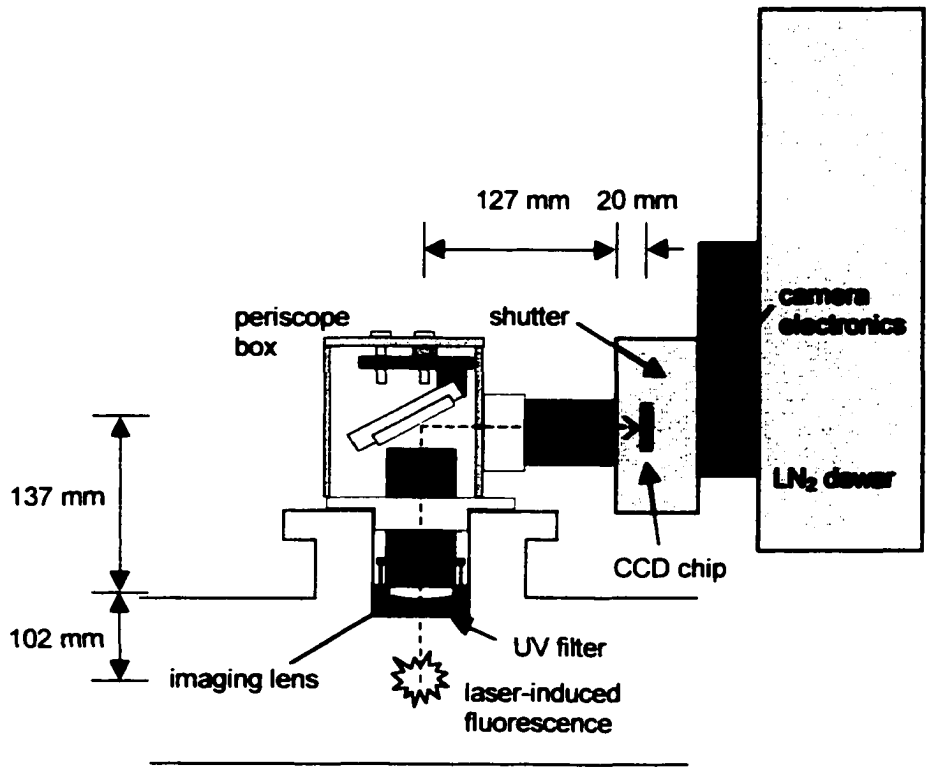

Fig. 6.3 A schematic of the apparatus used to detect the Ga laser-induced fluorescence.

6.2 Laser Cooling Procedure

The procedure for measuring the collimation due to laser cooling typically took around 8-12 hours from the time the experiment was begun. It was observed that both the atomic beam and the laser systems benefited from operating later at night due to reduced thermal fluctuation in the laboratory and reduced acoustic and vibrational noise from the

rest of the building. Initially the Ga atomic beam was slowly brought up to its operating temperature. The final oven conditions during laser cooling were typically achieved by heating with 800-900 W of power (at least 300 A d.c. from the current generator). A pressure of at least 1.0 $x10^{-6}$ Torr was required in the oven vacuum chamber during operation to insure a sufficient number of atoms for good imaging, although a pressure around 2.0 $x10^{-6}$ Torr was preferable.

While the oven was being heated up, the CCD camera was cooled down to its operating temperature. After LN_2 was added to the dewar, the camera was set to read out data with a small repetition rate (one image every few seconds) with short shutter opening times (no more than 0.1 sec). It was important to take this data during the cool-down process to ensure that excessive charge did not build up on the CCD array. As the temperature decreased, the measured intensity on the chip would begin to fall until finally the background was reached. The background was very reproducible at around 470 counts per pixel. If this level could not be reached, the black cloth around the periscope assembly was adjusted until the light leakage was eliminated. When the acceptable light background was reached, the thermal regulation was activated on the camera. This was a small heater that raised the temperature of the CCD array to -80° C and kept it very stable during operation. This stabilization took about one-half hour. The camera could operate at lower temperatures, down to −120° C, but lowering the temperature would not significantly alter the dark count readout.

During this stabilization, the laser was peaked for maximum power and the wavelength was checked. Typical powers from the Coherent 699 tunable dye laser were around 600 or 700 mW. The laser wavelength was checked with the lambda meter. To

be on resonance with the correct Ga transition, the dye laser was tuned until a lambda meter reading of 0.930343 was obtained. At this point, the laser frequency after the double pass AOM apparatus was close to the iodine hyperfine resonances. Both the lambda meter and the iodine apparatus are described in Chapter four.

Before locking to the iodine hyperfine peak, the saturating beam was blocked and the intensity balance in the two probe beams was checked. The saturating beam was then unblocked and its overlap with one of the probe beams confirmed. The laser was then tuned and the fluorescence from the iodine cell was observed by eye. Referring to Figure 4.10, the large hyperfine peaks to the blue of the locking peak fluoresced orange and the small hyperfine peaks fluoresced green-yellow, making them easy to distinguish. When the green peaks were seen in the iodine cell, the saturated absorption signal from the lock-in amplifier was observed. The frequency of the laser was stepped until the correct hyperfine peak (the locking peak) was observed and centered in the lowest 699 scan width setting (0.01 GHz). With the locking peak at the center of the frequency scan, the zero offset of the lock-in amplifier was adjusted to set the half-max point of the hyperfine peak at zero voltage. The fundamental dye laser was now ready for frequency locking.

At this point the doubling cavity was locked and UV laser light was produced and sent into the vacuum system. The Ga hyperfine fluorescence peak was always observed prior to frequency locking the dye laser. To do this, the UV beam power was attenuated and high voltage was applied to the photomultiplier tube (PMT) located above the cooling region. Typically around –750 V was applied to this PMT (EMI 9558QB) and its output was read out on a Keithley 610C electrometer. Typical readings on the electrometer for the F=3 $\rightarrow$ F=4 fluorescence peak ranged from 10^{-7} to 10^{-8} A.

The orthogonality of the cooling laser beam and the atomic beam was checked while observing this PMT signal. The cooling laser was passed through a small hole (about 2 mm square) located roughly 1 meter prior to the vacuum system. The retroreflected spot was adjusted until it also passed through the small hole. The retroreflection was then blocked and a frequency scan was done across the cooling transition while recording the fluorescence spectrum. This was a "single-pass" scan. The retroreflection beam was then unblocked and a second frequency scan was taken. This was a "double-pass" scan. The retroreflection beam was again blocked, and a third scan was taken. This whole procedure took about three minutes. If the laser and the Ga beam were orthogonal, the double-pass scan was twice as tall as the single-pass scans, but all three scans were equally narrow and centered at the same frequency. If the laser and Ga beam were not orthogonal, a two-peaked signal was seen on the double-pass scan. In this case the mirror that directed the cooling laser into the vacuum was adjusted, as was the retroreflection mirror, and the sequence of three fluorescence scans was repeated. This procedure was repeated until the UV laser and Ga beam were orthogonal. Three sequences of scans with the Ga beam and cooling laser becoming progressively more orthogonal are shown in Figure 6.4. The reason for taking two single pass scans, one before and one after the double-pass scan, was to observe any frequency drift or scan irregularities in the dye laser. If a drift was present, none of the three peaks lined up, but the change in the center position was consistent.

Once the cooling laser was orthogonal to the atomic beam, the probe laser was made parallel to the cooling laser. This was done by measuring the separation between the centers of the laser beams on the input side of the vacuum system and then again on

the output side of the vacuum system. With this method, the two beams were made parallel to better than 1 mm over a 2 m distance. This corresponds to a < 0.5 mrad deviation between the two beams.

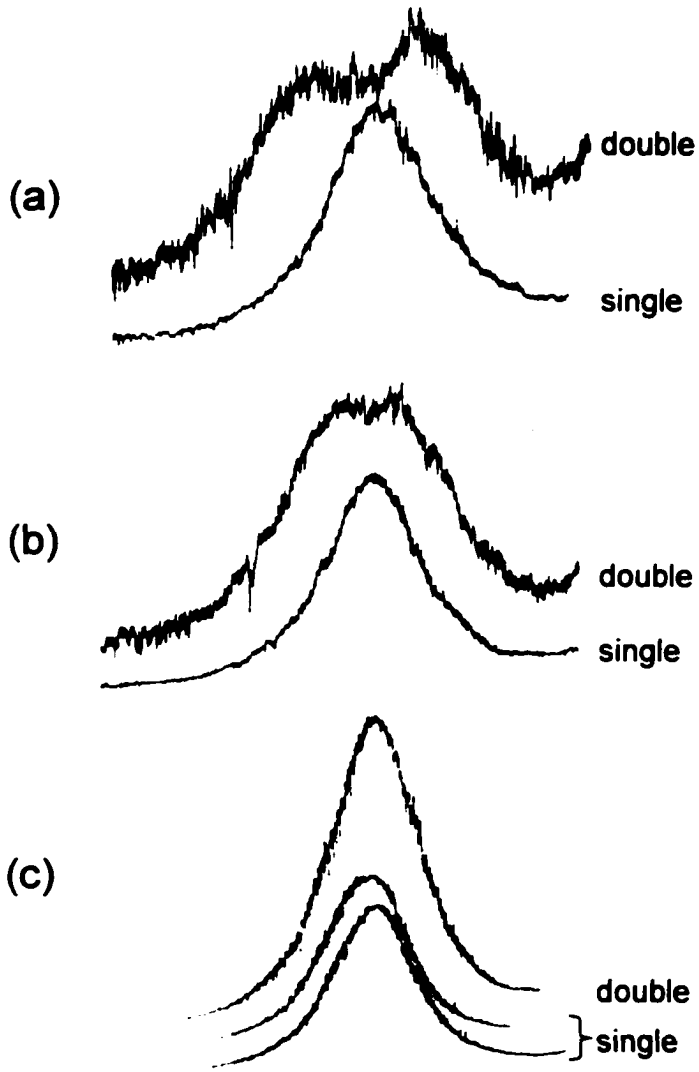

Figure 6.4 Laser-induced fluorescence peaks from the F=3 → F=4 transition taken during single-pass and double-pass frequency scans. The scans from (a) to (c) were taken with a laser increasingly orthogonal to the atomic beam. In (c), the two smaller peaks at the bottom were single-pass scans taken before and after the double-pass scan.

With the cooling and probe lasers parallel, the fluorescence from the probe laser/Ga beam interaction was observed. The dye laser was manually tuned to the resonance peak by observing the PMT signal, and the AOM in the saturated absorption apparatus was adjusted until the half-max point of the iodine hyperfine line was crossing zero. At this point the locking servo in the dye laser feedback chain was activated, and the dye laser was locked to the resonance peak of the cooling F=3 → F=4 transition.

With the laser tuned to resonance, the fluorescence was usually easy to observe with the CCD camera. Taking full two-dimensional images of the illuminated Ga beam (utilizing the entire 1100 x 310 pixel array on the CCD chip) required a shutter opening time of at least one second. Typical shutter exposure times were anywhere from 1 s to 45 s. When the camera was initially used, the dye laser frequency locking system was not yet operational, and the maximum exposure time was around 10 s. If the shutter was open any longer, the laser would drift in frequency during that time and the measurement could not be considered accurate. With the laser frequency locked, data were taken with very long (45 s) exposure times to provide excellent signal to noise. When aligning and centering the fluorescence image on the CCD array - not taking data - typical exposure times were 1 s to 5 s.

Centering the image on the pixel array was done in two ways. Some horizontal centering could be done by small rotations of the entire periscope assembly. Gross horizontal and vertical misalignments necessitated taking the back cover off the light-tight periscope box and manipulating the mirror mount. Care was taken to not allow the shutter to be open while the back cover of the box was off, even if all the room lights were off. This much background swamped the Ga fluorescence signal. To prevent this, a

hand was inserted into the box to manipulate the mirror mount, and then the box, hand, and camera were covered with the black cloth. Only in this way could the mount be manipulated while observing the fluorescence image moving across the CCD face. This procedure allowed the image to be well centered in the pixel array. With the fluorescence image centered, the cooling and collimation of the Ga atomic beam could be investigated.

6.3 Cooling Results

The physical dimensions of the Ga atomic beam at the cooling region and at the probe region were obtained by direct deposition onto a glass substrate and subsequent measurement with an optical microscope. In the horizontal dimension, the beam was 1.77 mm in diameter at the center of the cooling laser interaction region and 3.86 mm in diameter 342 mm away at the center of the probe laser interaction region. This corresponded to a half-angle divergence of 3.1 mrad and a nominal transverse velocity of 2.3 m/s. This result was in full agreement with the divergence calculated from the geometry of the atomic beam oven and mechanical slit configuration, as discussed in Section 3.3.

The effect of laser cooling is presented in Figure 6.5. Two CCD images of the atom beam illuminated by the probe laser are shown. This cooling was done with 68.4 mW of power (I/I_0 = 13.7) in the cooling laser and a detuning of –12.2 MHz. In the fluorescence images, the atoms were travelling from top to bottom and the laser was illuminating from left to right. This geometry of the fluorescence measurement is shown in Figure 6.5(c). Thus the width of the fluorescence spot is a real measurement of the spatial distribution of the atoms in the beam. In 6.5(a) the cooling laser was on and the atom beam was collimated, while in 6.5(b) the cooling laser was off and the beam was

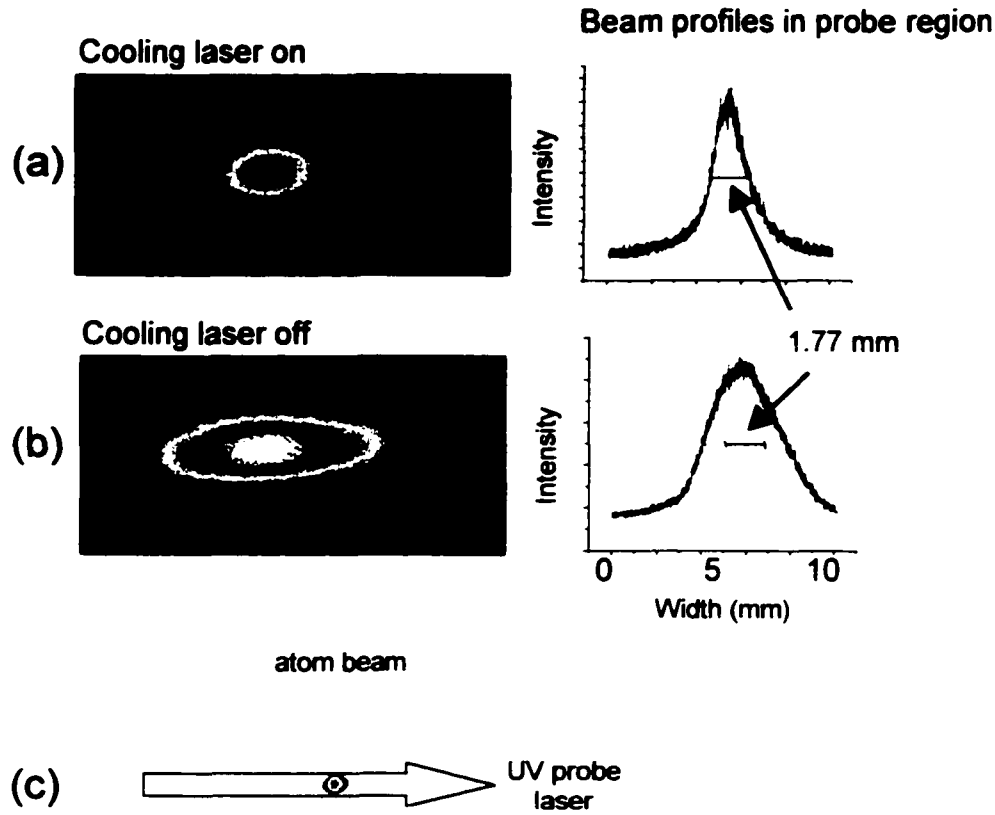

Figure 6.5 Laser-induced fluorescence images of the illuminated gallium atomic beam with the cooling laser turned on (a) and off (b). The beam profiles are horizontal intensity slices taken through the center of the fluorescence image. In these images, Δ = -12.2 MHz and I/I_0 = 13.7 (P= 68.4 mW). (c) The geometry of the fluorescence measurement.

uncollimated. To the right of the CCD images is a line scan taken through the middle of the fluorescence. The FWHM of the fluorescence image was determined by these intensity profiles. The FWHM of the fluorescence image of the cooled beam was 1.77 mm and the FWHM of the fluorescence image of the uncooled beam was 3.86 mm. The fluorescence image in the probe zone confirms the measurement of the Ga deposition

made with the optical microscope. Recall that 1.77 mm was the atom beam's horizontal dimension at the center of the cooling region – the smallest size a fully collimated atom beam could be. This size is indicated in Figure 6.5. This graph indicates no measurable divergence of the beam occurred over the 342 mm flight path from the cooling region to the probe regions. The noise in the CCD image limited our measurement of the full-width to ±15 CCD pixels. The corresponding limit in the atom beam size was ±145 μm. This was a conservative estimate of the measurement resolution. If the full measurement uncertainty was ascribed to the divergence of the cooled atom beam, then the beam had a maximum residual divergence of 0.2 mrad (half-angle) or a maximum transverse velocity of 14 cm/s. A velocity of <14 cm/s corresponded to a one-dimensional temperature T <165 μK. For Ga, the Doppler limited velocity and temperature were v_D = 27 cm/s and T_D = 596 μK. Thus we have demonstrated sub-Doppler cooling of the Ga atoms. The one-dimensional kinetic energy of the atoms was <7.11 neV. This was sufficient for the laser focusing experiment.

The cooling efficiency as a function of detuning was investigated. The detuning of the laser was accomplished by manually changing the drive frequency of the double pass AOM in the saturated absorption apparatus. A change of 1.0 V applied to the driver resulted in a tuning of 20 MHz in the UV laser. It is worth noting again that the probe beam and the cooling beam were produced by the same frequency doubling cavity and always had the same frequency. As the cooling laser was detuned the probe laser was also detuned. This was always taken into consideration when interpreting the observed results.

CCD images were obtained with the cooling laser blocked and unblocked as the laser frequency was changed. The results of this are shown in Figure 6.6. The collimation resulting from the laser cooling was dependent on the cooling laser detuning down to approximately -Γ/2, or -12.5 MHz. At higher detunings, the collimation was relatively independent of the detuning. As discussed in Chapter two, a larger red detuning cooled atoms with a faster initial velocity more effectively, although a longer interaction or more laser power was required to cool all the atoms.

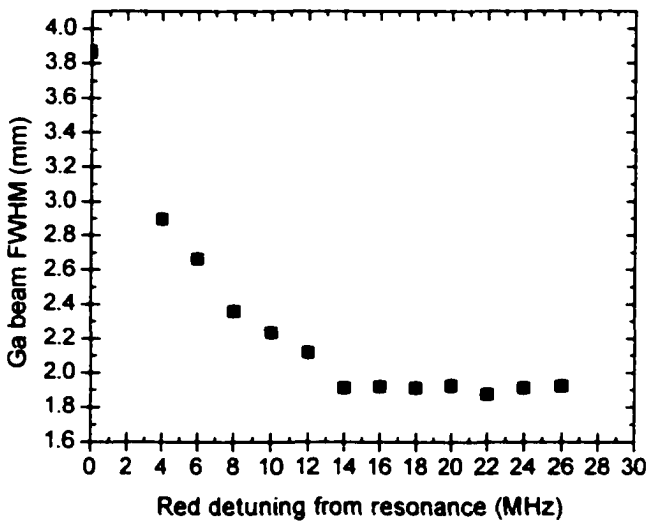

Figure 6.6 Collimation of the Ga atomic beam as a function of the cooling laser detuning from resonance. The cooling laser $I/I_0 = 13.7$. The natural linewidth of the transition is $\Gamma/2\pi = 25$ MHz.

The cooling efficiency as a function of interaction distance was investigated next. CCD images were obtained with the cooling laser blocked and unblocked as a razor blade was translated through the cooling laser. Figure 6.7(a) shows the results for two different detunings. Because the cooling laser was Gaussian in intensity, moving the razor 1 mm

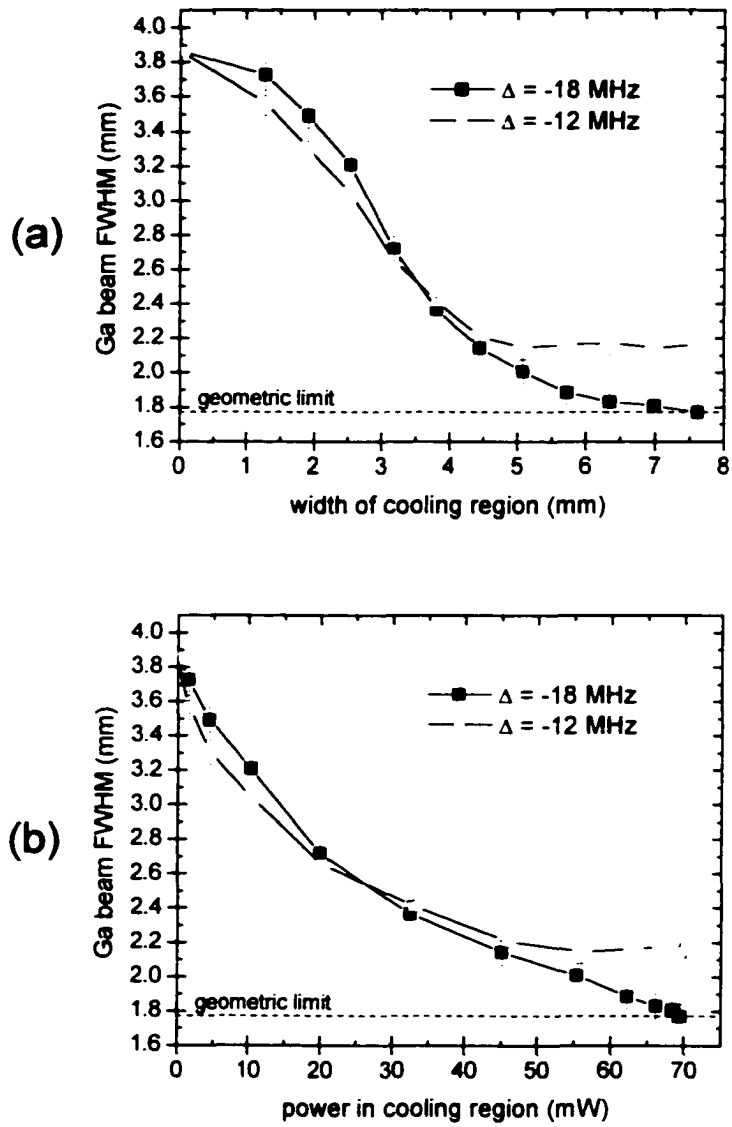

Figure 6.7 Collimation of the Ga atomic beam as a function of (a) width of the cooling region and (b) power in the cooling region.

at the edge of the beam had less effect than moving it 1 mm at the center of the beam. Thus this graph actually contains information about the cooling dependence on the laser power. The cooling efficiency as a function of the total power in the truncated laser beam is shown in Figure 6.7(b). For the smaller detuning (-12 MHz) only ~50 mW was needed before the collimation of the beam ceased at a beam FWHM of 2.15 mm. For a larger detuning (-18 MHz) it required at least 70 mW to cool the atoms all the way to their absolute minimum (1.77 mm diameter). This is in agreement with the theory described earlier. From Figure 6.6, it can be seen that a detuning of −14 MHz was the minimum detuning that collimated the atom beam to its minimum size. Figure 6.7 proves that larger detunings can also collimate the atom beam to this limit, but require more power or a longer interaction region to do so. A compromise between detuning and power was reached by detuning the laser to −14 MHz and requiring at least 60 mW in the incoming cooling laser beam.

The effect of the polarization gradient cooling was investigated by removing the quarter-waveplate from the retroreflected laser beam. Figure 6.8 shows three CCD images of the atom beam 342 mm downstream from the laser collimation region and intensity profiles taken through the center of the fluorescence images. The top image, Figure 6.8(a), shows the uncollimated, normally diverging atom beam with a FWHM = 3.86 mm. Figure 6.8(b) shows the atom beam with the cooling laser on, but the quarter-waveplate removed with a FWHM = 2.39 mm. This cooling was from the Doppler molasses only. Figure 6.8(c) shows the atom beam with the cooling laser on and the waveplate in place with a FWHM = 2.01 mm. In all of these images, the cooling laser power was 52 mW (I/I_0 = 10.5) and the Δ = -10.4 MHz. The atom beam cooled with the

lin ⊥ lin polarization gradient was more collimated and brighter on axis than the Doppler molasses cooled beam. This was direct evidence of the polarization gradient extending the cooling limit into the sub-Doppler regime.

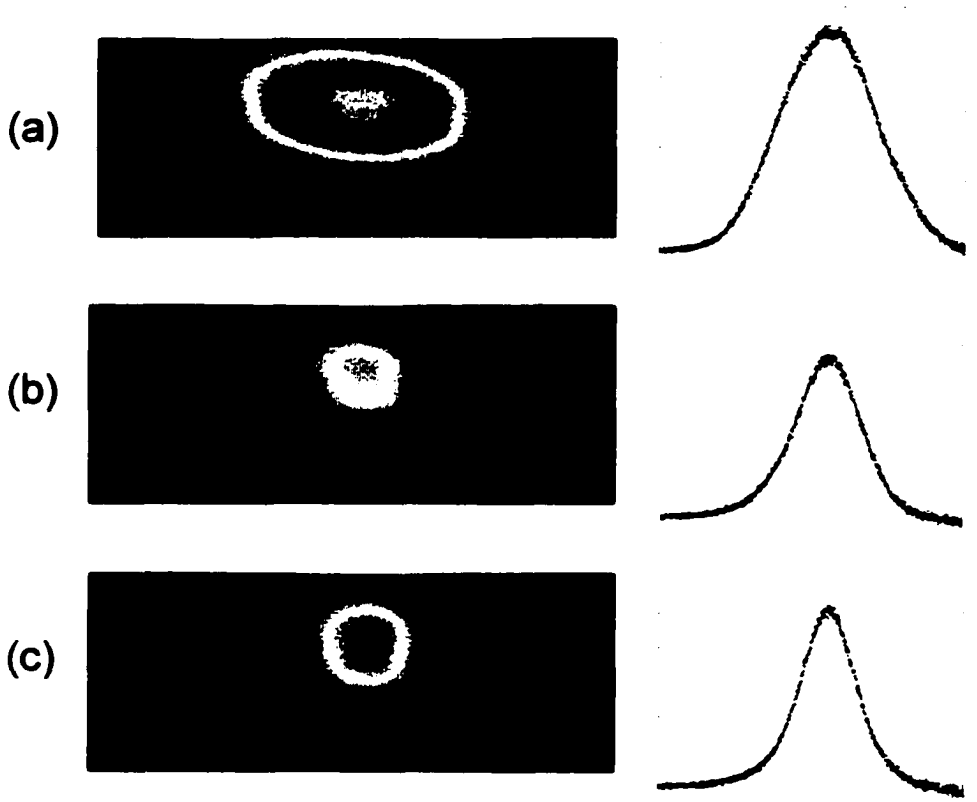

Figure 6.8. CCD Images of laser-induced fluorescence from an atomic gallium beam illuminated 342 mm downstream from the cooling laser. Cooling laser $I/I_0 = 10.5$, $\Delta = -10.4$ MHz.
(a) No laser cooling.
FWHM = 3.86 mm
(b) Cooling laser on, optical molasses only.
FWHM = 2.39 mm
(c) Cooling laser on, lin-⊥-lin polarization gradient.
FWHM = 2.01 mm

6.4 Optical Pumping

In Figures 6.5 and 6.8 it was apparent that the on-axis intensity of the cooled beam was never greater than it was in the uncooled beam. Because the same number of atoms was being illuminated in both pictures, the intensity, which was directly proportional to the number of illuminated atoms, should be greater on axis in the cooled atomic beam. The total integrated fluorescence intensity of the image however (the total number of pixel counts) should remain constant. Figure 6.9 shows a graph of the total fluorescence intensity on the face of the CCD as a function of cooling laser interaction width. The cooling laser detuning was Δ = -18 MHz. During the course of the

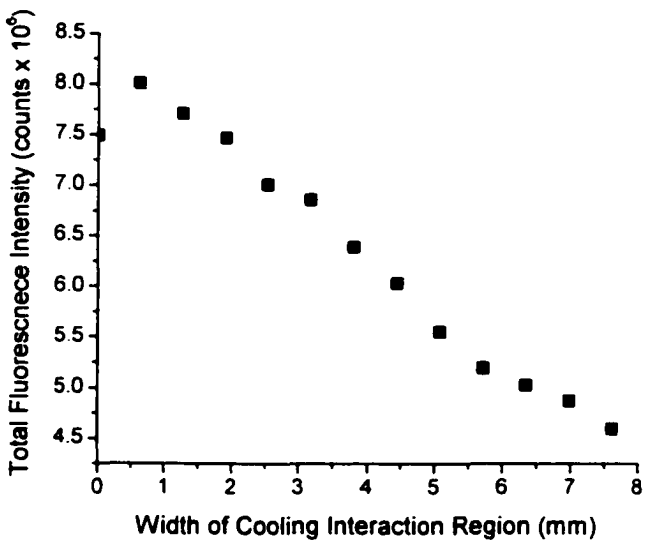

Figure 6.9 The total integrated fluorescence intensity on the CCD array as a function of the cooling interaction width. Cooling laser Δ = -18 MHz.

measurement, the power in the cooling laser decreased from 79 mW to 68 mW. As the interaction region got longer, the total fluorescence intensity decreased in a linear fashion. The intensity decrease was due to the loss of cooled atoms from the F=3 state due to

optical pumping by the cooling laser. After the atoms had traversed the full width of the cooling region, the total fluorescence intensity had decreased by 43%.

We have previously performed optical spectroscopy of the $4p^2P_{3/2} \rightarrow 4d^2D_{5/2}$ transition - as detailed in Chapter five - and determined that the proximity of the 18 hyperfine components could make the undesirable optical pumping of atoms out of the $4p^2P_{3/2}(F=3)$ state possible. The optical pumping scheme that could result in a loss of atoms from the F=3 state was off-resonant excitation of the F=3 → F=3 transition by the cooling laser and a subsequent decay to the F=2 ground state. Given a large enough number of absorption/spontaneous emission cycles, a certain percentage of atoms would be lost from the F=3 state due to this process.

In the $4p^2P_{3/2} \rightarrow 4d^2D_{5/2}$ spectrum, Figure 5.7, the F=3 → F=3 transition lies 12.5Γ to the red of the F=3 → F=4 cooling transition. The relative oscillator strengths of the two transitions are shown in Figure 6.10(a). Not all atoms that get excited to the F=3 state will be lost from the cooling transition. The spontaneous emission branching ratios for the F=3 excited state are shown in Figure 6.10(b). While 80% of the atoms excited to the F=3 state are lost via spontaneous emission to the F=2 state, 20% will remain in the cooled F=3 state.

The probability that an atom will be pumped to the uncooled F=2 state as a function of the laser detuning can be estimated. The probability that an atom will absorb a photon from a laser detuned by an amount Δ from the resonance of a transition with a natural linewidth Γ is

$$P_a \propto \frac{1}{(\Delta/\Gamma)^2 + 1/4} \qquad (6.1)$$

where the Doppler effect and saturation have been ignored. The relative probability of absorbing into one particular transition or another can be calculated by multiplying the

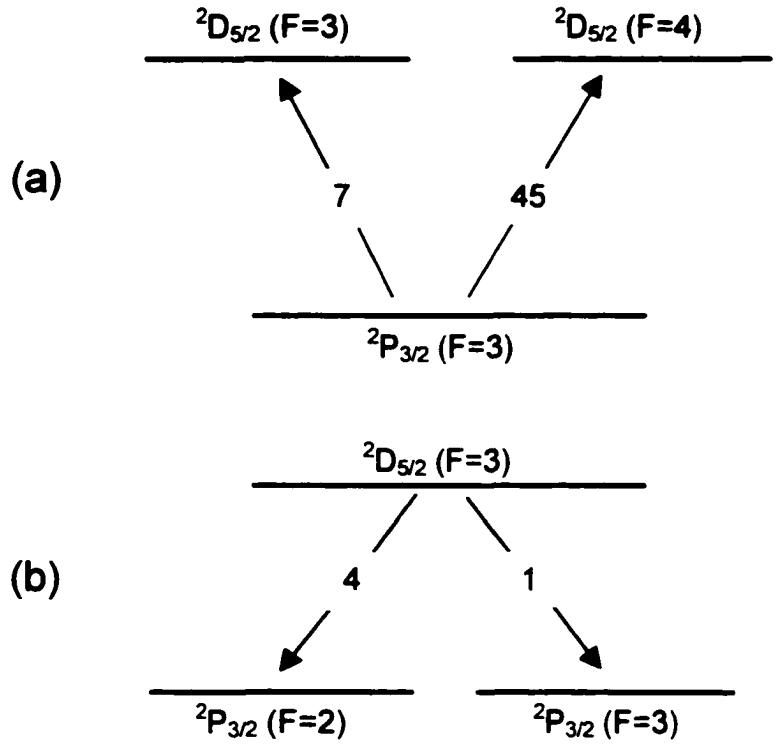

Figure 6.10 (a) Relative oscillator strengths for the F=3→F=3 and F=3→F=4 transitions. (b) Branching ratios for spontaneous emission from the $^2D_{5/2}$(F=3) to the $^2P_{3/2}$ (F=3) and (F=2) states.

probability P_a by the oscillator strength given in Figure 6.10. Assuming a typical Doppler molasses red detuning of -Γ/2, or -12.5 MHz, for each absorption and spontaneous emission cycle there is a 3.7×10^{-4} probability that a Ga atom will be pumped out of the F=3 state into the F=2 state and be unavailable for further cooling. Each absorption/emission cycle takes 12.7 ns in the saturated regime. If the atoms in our beam have a mean longitudinal velocity around 700 m/s and the cooling region width is 5.5 mm

(typical in our experiment), we can expect 80% of the atoms initially in the F=3 state to remain in that state during cooling. If the detuning is increased to -Γ, or –25 MHz, the probability increases to 1.1×10^{-3} per cycle and 50% of the initial F=3 atoms will remain after traversing the cooling region. This rather simple calculation neglects saturation effects which complicate the pumping probabilities, but it nonetheless adequately describes the loss of atoms from the cooled F=3 state via the off-resonant excitation of the F=3 → F=3 transition. This cooling laser-induced optical pumping puts a limitation on the number of cold atoms available.

To study this pumping, the CCD camera was replaced by a photomultiplier tube (EMI 9839 B) and the UV probe laser was replaced by the tunable 417 nm diode laser tuned to the $4p^2P_{3/2} \rightarrow 5s^2S_{1/2}$ transition. This was a better transition for studying the effects of optical pumping because there were fewer hyperfine peaks and they overlapped less. Figure 6.11 shows the laser-induced fluorescence spectrum obtained by 417 nm excitation of the Ga atoms with the cooling laser upstream turned on and off. The power in the 417 nm beam was 0.6 mW and the power in the UV cooling beam was 45 mW. Figure 6.11(b) is a calculated spectrum for both isotopes to assist in identifying the transitions. The loss of atoms from the $4p^2P_{3/2}(F=3)$ state was observed by the decrease in peak intensity of the F=3 → F=2 transition. A repumping laser tuned to the $4p^2P_{3/2}(F=2) \rightarrow 4d^2D_{5/2}(F=3)$ transition could repopulate the $^2P_{3/2}(F=3)$ state and stop this loss channel.

To demonstrate this, a portion of the cooling laser was picked off, frequency shifted, and overlapped with the cooling laser. This is shown in Figure 6.12. Two acousto-optic modulators (IntraAction Models ASM-2002-8 and ASM-2002B8-1) were

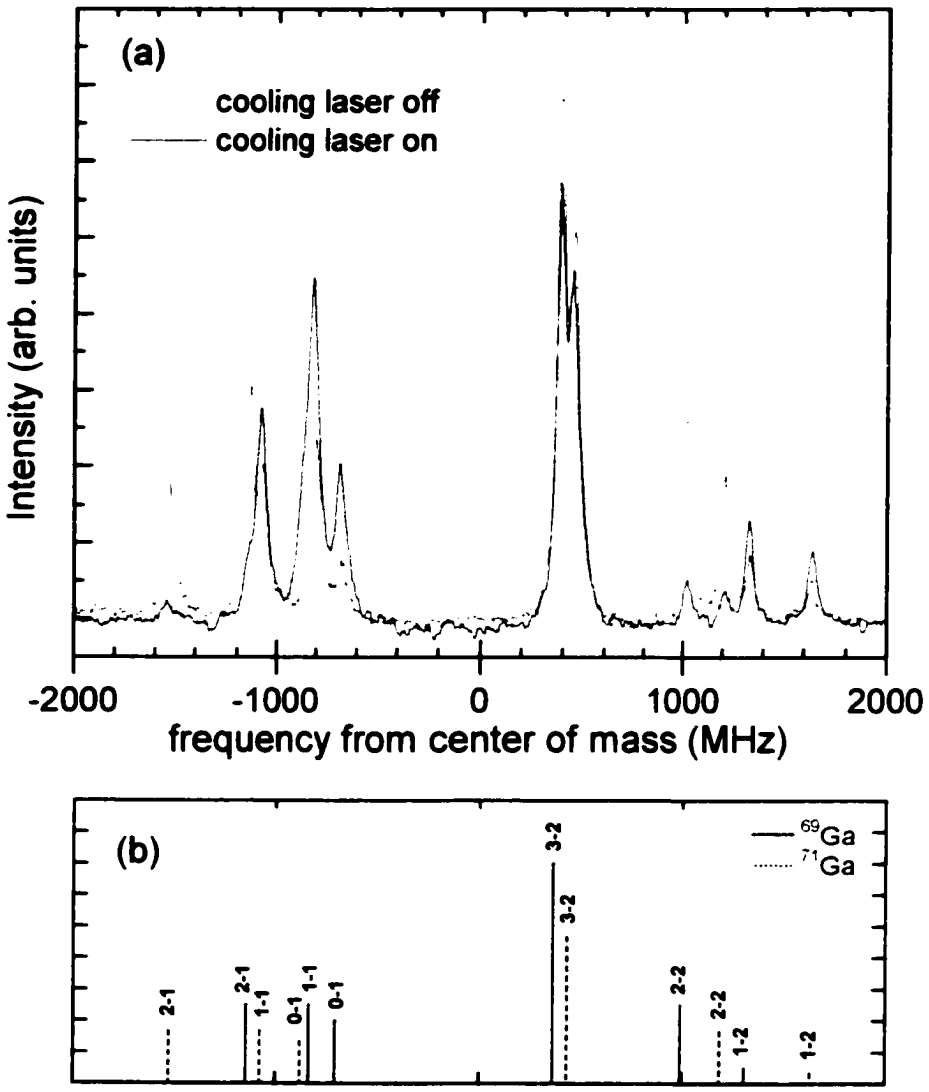

Figure 6.11 (a) The laser-induced fluorescence spectrum obtained by 417 nm excitation with the cooling laser on (black line) and off (red line). (b) The calculated line spectrum of the hyperfine transitions for both isotopes of Ga.

each driven with 2 W at 167 MHz. The cooling beam passed through both AOMs unshifted. The repump beam was frequency shifted by both AOMs a total of +334 MHz, placing it on resonance with the $4p^2P_{3/2}(F=2) \rightarrow 4d^2D_{5/2}(F=3)$ transition of ^{69}Ga. The

repump beam's polarization was rotated to horizontal by a half-waveplate and the cooling beam and repump beam were overlapped in a polarizing beamsplitter. Both beams were retroreflected and were in the lin ⊥ lin configuration. Laser induced-fluorescence spectra

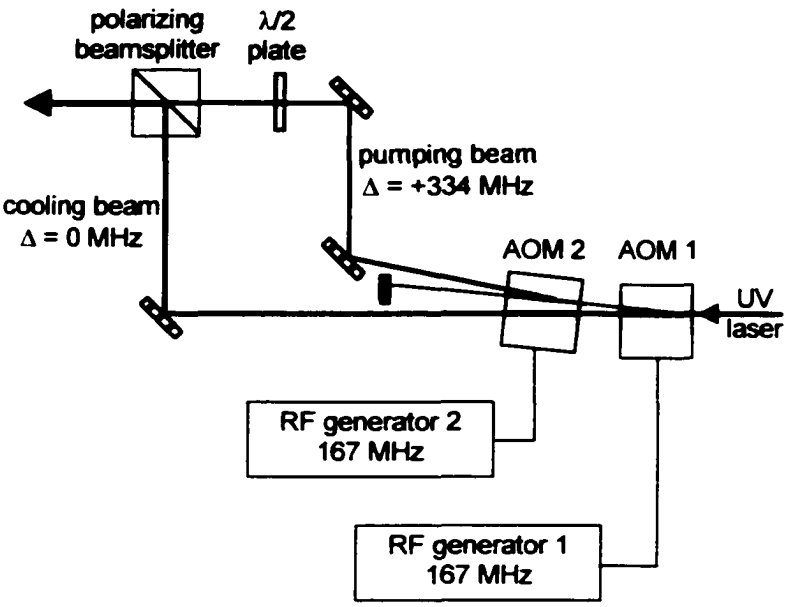

Figure 6.12 Laser arrangement for cooling and pumping of Ga beam.

were taken downstream with the 417 nm laser operating at 0.4 mW. Figure 6.13 shows four laser-induced fluorescence spectra taken at 417 nm. 6.13(a) was taken with both the cooling and repump lasers off; 6.13(b) with only the cooling laser turned on; 6.13(c) with both the cooling and repump lasers on; and 6.13(d) with only the repump laser on. The cooing laser was detuned by –14 MHz and had 20.2 mW. The repump laser power was 4.5 mW. It can be seen that the presence of the repump laser in 6.13 (c) and (d) effectively pumped atoms into the F=3 state, as indicated by the increase in the F=3 → F=2 peak height. The cooling laser redistributed atoms among the other F states, but did not decrease the population of the F=3 state with the repump laser on.

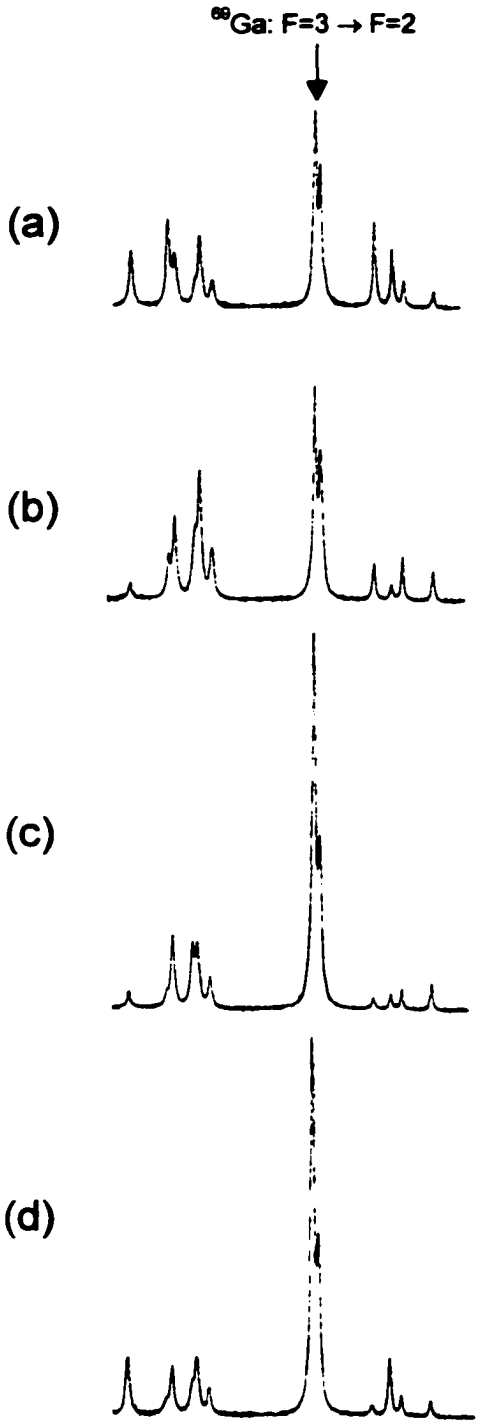

Figure 6.13 417 nm laser-induced fluorescence spectra taken with (a) cooling and repump laser off; (b) only cooling laser on; (c) cooling and repump laser on; (d) only repump laser on. Repump laser Δ = +334 MHz, P = 4.5 mW.

The repumping efficiency dependence on power was studied. Figure 6.14 shows the increase in height of the F=3 → F=2 peak as a function of power in the repump beam. All the data points in Figure 6.14, except for the one at 8.3 mW, were taken with the 20 mW cooling laser on and detuned by –14 MHz. Around 5 mW of repump power were needed to almost completely empty the F=2 state and pump the atoms to the F=3 state. Figure 6.14 shows that even very low repump powers (<1 mW) were capable of putting a significant number of atoms into the F=3 state.

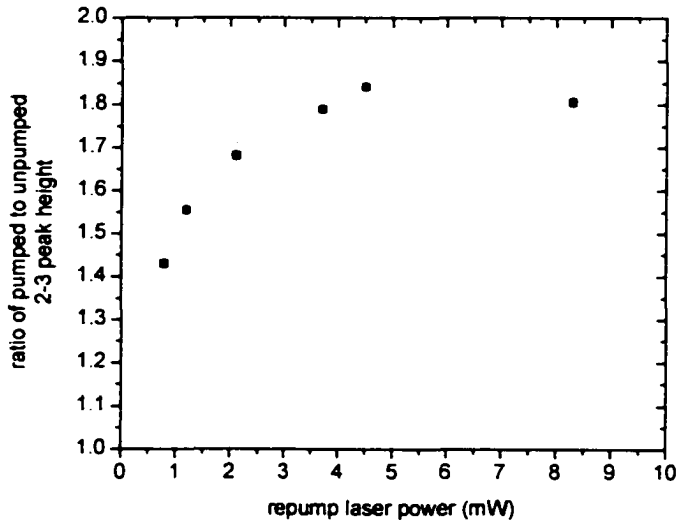

Figure 6.14 Repumping efficiency as a function of power in the repump laser beam. Repump laser Δ = +334 MHz.

Figure 6.11 shows that the $4p^2P_{3/2}(F=2)$ state was almost completely emptied by the cooling laser due to the $4p^2P_{3/2}(F=2) \rightarrow 4d^2D_{5/2}(F=1)$ transition which was only 58 MHz to the red of the cooling transition (see Figure 5.7). Any atom which decayed to the $4p^2P_{3/2}(F=2)$ state was almost immediately pumped into the $4p^2P_{3/2}$ (F=1) or (F=0) states as could be seen in Figure 6.11 by the increase in the fluorescence intensity of those peaks. In the presence of a very powerful cooling beam, this depopulation of the F=2

state during cooling might disrupt our repumping. We therefore investigated an alternate repumping scheme.

AOM 1 was set to +200 MHz and AOM 2 was set at several different frequencies around +200 MHz. This created a repump beam ~400 MHz to the blue of the cooling transition. This detuning allowed pumping on both the F=0 → F=1 and F=1 → F=2 transitions (separated by only 20 MHz) in ^{69}Ga. Figure 6.15 shows the 417 nm spectrum again with (a) cooling and repump laser off; (b) only the cooling laser on; (c) cooling and repump laser on; and (d) only the repump laser on. The cooling laser was detuned −14 MHz and had 19.1 mW of power. The repump laser was detuned +410 MHz and had 6.1 mW of power. From 6.15 (c) and (d) it can be seen that this repumping scheme was able to increase the population of the $^2P_{3/2}$(F=3) state. This was due to atoms decaying from the $^2D_{5/2}$(F=2) state to the $^2P_{3/2}$(F=3) state. However, this indirect repumping was not as effective as the previous scheme.

Several repump beam detunings were investigated, including +380, +390, +400, +410, and +420 MHz. All of these detunings were effective at increasing the population of the $^2P_{3/2}$(F=3) state. The populations of the other states, F= 1 and F=0, were different. Since the populations of these state were of little importance, all of these detunings acted as an effective repump.

6.5 Conclusions

Using the cycling $4p^2P_{3/2}$(F=3) → $4d^2D_{5/2}$(F=4) hyperfine transition at 294.45 nm, a Ga atomic beam was collimated to better than < 0.4 mrad (full-angle). The cooling laser was operated in the lin ⊥ lin polarization gradient configuration with at least 60 mW of power and a detuning between −12 and −18 MHz. The transverse velocity of the

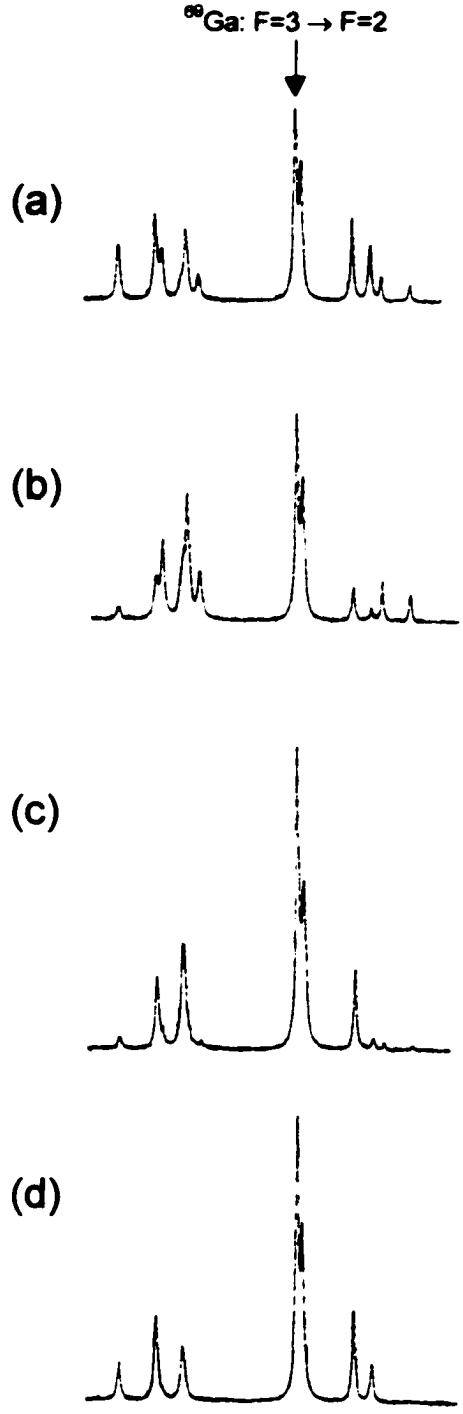

Figure 6.15 417 nm laser-induced fluorescence spectra taken with (a) cooling and repump laser off; (b) only cooling laser on; (c) cooling and repump laser on; (d) only repump laser on. Repump laser Δ = +410 MHz, P = 6.1 mW.

atoms was reduced to <14 cm/s, equivalent to a one-dimensional temperature of <165 μK. This was about one-fourth the Doppler cooling limit temperature.

The dependence on the cooling laser detuning and interaction length was studied and the pumping of the cooled atoms out of the desired $^2P_{3/2}(F=3)$ state by the cooling laser was observed. To address this depopulation, two repumping schemes utilizing an additional frequency shifted laser beam at 295 nm were investigated. Repump beams detuned +334 MHz and +410 MHz from the cooling laser frequency were found to be effective at increasing the population of the $^2P_{3/2}(F=3)$ state in the presence of the cooling laser.

REFERENCES

[1] The CCD camera was on loan from the research group of Professor Carmen Menoni, Department of Electrical and Computer Engineering, Colorado State University.

CHAPTER 7

An Attempt to Demonstrate Standing Wave Light Force Focusing of Gallium

This chapter describes our attempt to demonstrate one-dimensional laser focusing of gallium utilizing a 417 nm single frequency diode laser. The focusing experiment was inconclusive due to self-organized islanding of the Ga atoms on the substrates during deposition. It was observed that this islanding – the formation of small Ga droplets on the surface – occurred on different substrate materials (Si, GaAs, and fused silica).

In this chapter I will describe the apparatus and procedure used during the laser focusing experiments. I will then present the results of the focusing experiments in the form of atomic force microscope images of the depositions. I will discuss the islanding phenomenon we observed and comment on the behavior of the Ga islands deposited on the substrates.

7.1 Experimental Apparatus

A schematic of the laser focusing experiment is shown in Figure 7.1. The vacuum system was modified from the cooling experiment. A detail is shown in Figure 7.2. It was important that the standing wave nodes were fixed in space with respect to the

substrate during the laser focusing. With this in mind, a custom-made mirror mount and substrate holder, shown in Figure 7.3, was used in the vacuum chamber. Details of the design criteria, the construction and the operation of this mount may be found in the thesis of Roger McGowan.[1]

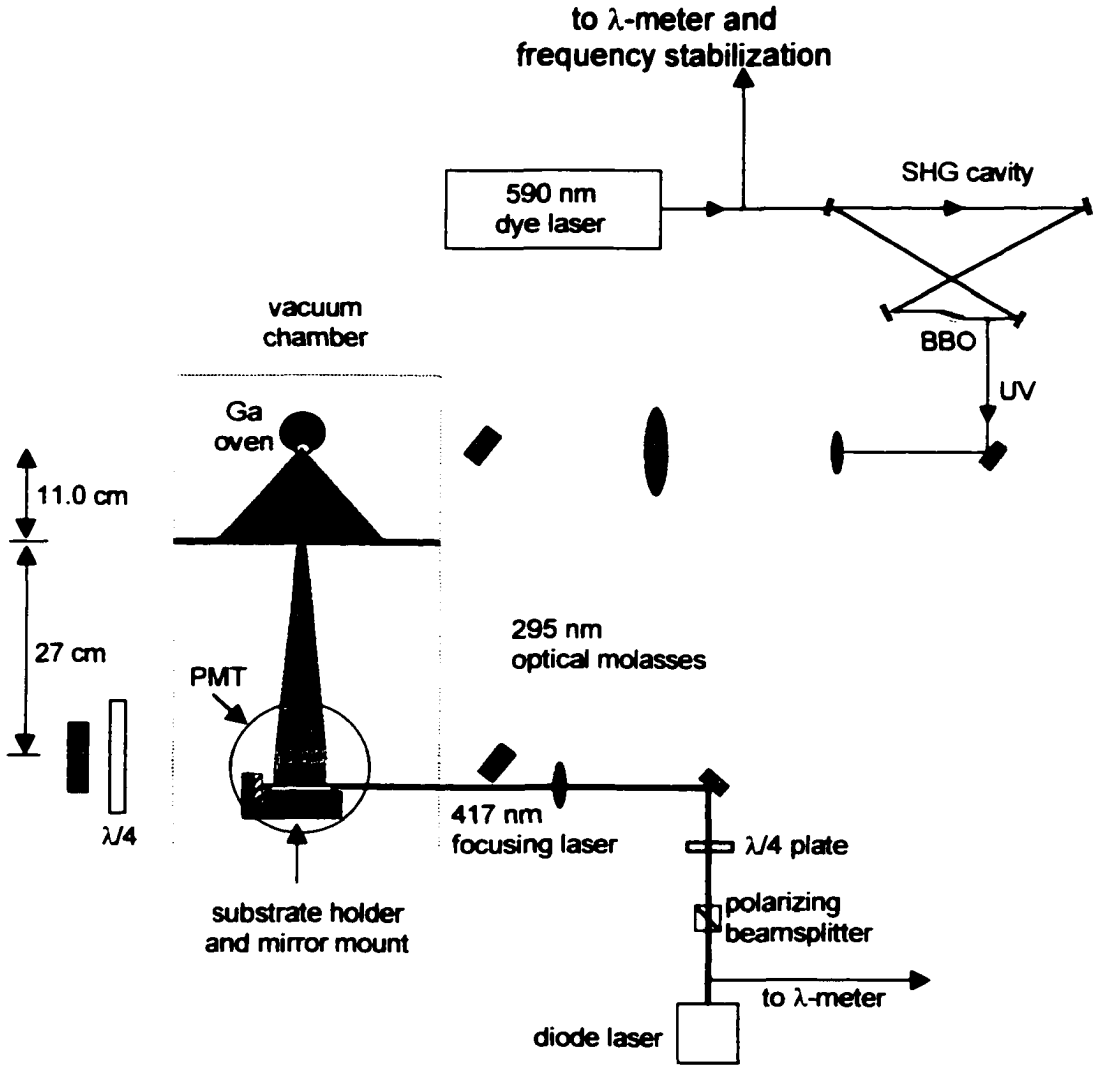

Figure 7.1 A schematic of the laser focusing experiment.

The substrate holder consisted of a flat surface with springy clips for firmly holding the substrate in place. The substrate, ~1 cm^2 in size, was positioned normal to

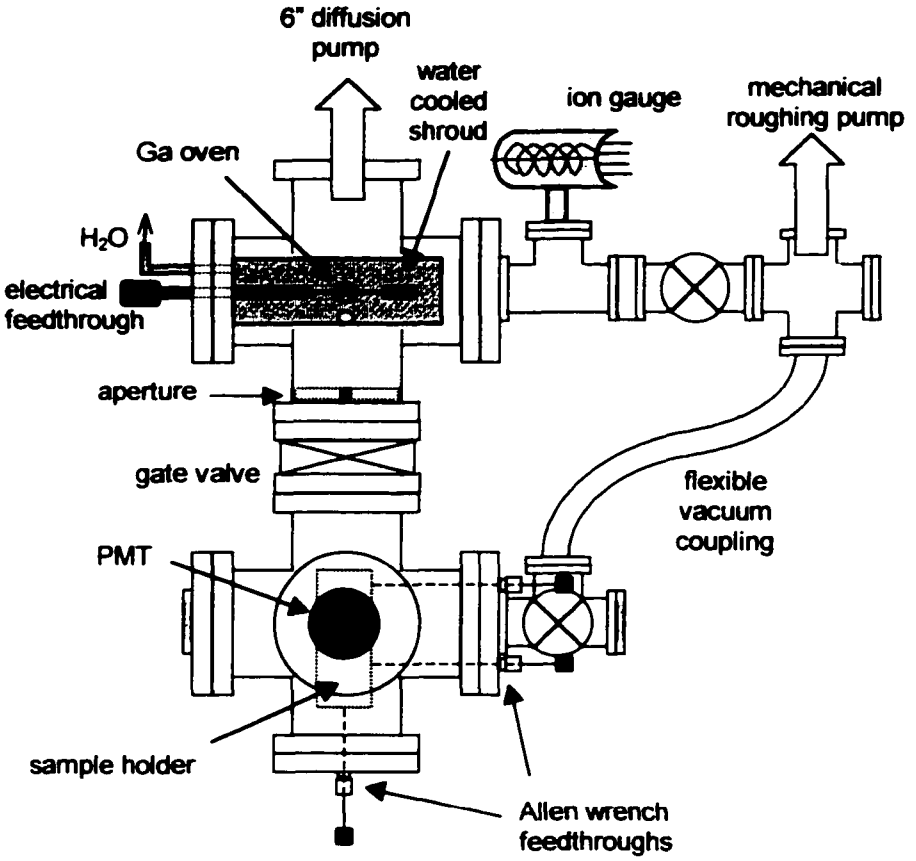

Figure 7.2 A detail of the vacuum system used in the Ga focusing experiment.

the direction of propagation of the cooled atom beam. This is the +x direction in Figure 7.3 This substrate holder was machined out of a single piece of Invar. Attached to it was the standing wave mirror for the focusing laser. The mirror was glued to the substrate holder with a vacuum compatible epoxy. The substrate holder was machined very precisely such that the surface of the substrate and the surface of the mirror were highly perpendicular. In the focusing experiment, a node of the focusing standing wave was always located at the mirror. Any relative motion between the mirror and the substrate would result in a "washing out" of the focused features. The Invar holder ensured that

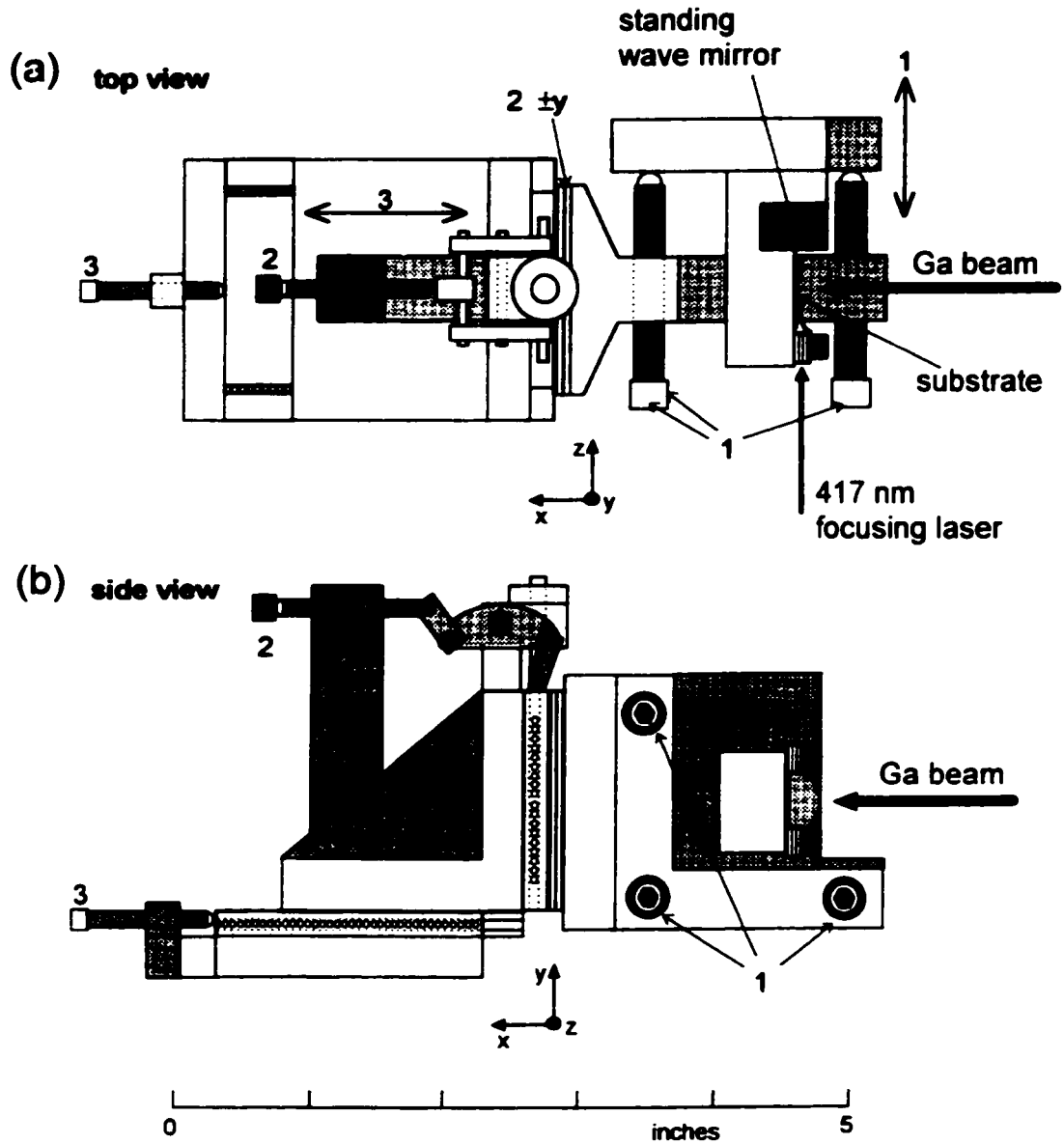

Figure 7.3 The substrate holder and mirror mount for standing-wave focusing. (a) Top view and (b) side view.

there was very little variation in the spacing of the substrate and the mirror due to thermal fluctuations. Also, any mechanical vibrations would move both pieces together resulting in no relative motion between the two.

The mirror mount had three 80-pitch screws for adjusting the tilt of the mirror/substrate holder and translating the substrate in the ±z direction. These screws are identified by the #1 in Figure 7.3. The screws were turned from outside the vacuum system by Allen wrenches that passed through a custom vacuum flange in such a way that the mirror could be manipulated while maintaining the integrity of the vacuum. The substrate holder also had two additional screws that provided translation. Identified in Figure 7.3, screw #2 controlled the vertical translation (±y) of the substrate and screw #3 controlled the horizontal translation in the ±x direction. These screws were manipulated from outside the vacuum system by Allen wrenches that passed through a second custom flange. This entire mirror mount and substrate holder assembly was bolted to a brass support that was clamped to the inside of the vacuum system.

The lasers used in the focusing experiment were described in Chapter four. The frequency stabilized dye laser was used to pump a second harmonic generation cavity with a BBO crystal to generate the requisite laser cooling power at 295 nm. A 417 nm single-frequency diode laser operating at around 12 mW was used to create the standing wave focusing beam. The characteristics of the cooling laser beam were the same as were used in the cooling experiment described in Chapter six. The 1 mm x 5.5 mm elliptical beam passed through the vacuum system as closely as possible to the focusing laser standing wave mirror without clipping it and was then retroreflected on the far side

of the vacuum system after passing through a quarter-waveplate to generate a polarization gradient.

The focusing laser and the cooling laser entered the vacuum chamber through the same 2.75" Conflat flange. Prior to entering the chamber, the focusing beam passed through a 50 cm focal length lens, which focused the beam to a waist located at the surface of the standing wave mirror. The waist size was 98 μm x 155 μm with the bigger dimension located along the vertical axis. The confocal parameter, the distance over which the beam spread out by a factor of $\sqrt{2}$, was 7 cm. This relatively soft focus ensured that the beam size did not change appreciably over the surface of the substrate. The laser had propagated 6 m through the laboratory prior to reaching the lens and had diverged to a vertical elliptical shape with $1/e^2$ radius waists 0.76 mm x 1.63 mm.

To minimize optical feedback to the diode laser head from the retroreflection, an AR coated polarizing beamsplitter and a 417 nm 0^{th} order quarter-waveplate were used to circularly polarize the focusing beam (see Figure 7.1). The retroreflected beam became orthogonally polarized after passing though the waveplate and was blocked by the beamsplitter. The use of a circularly polarized standing wave for laser focusing in conjunction with a lin ⊥ lin polarization gradient cooling scheme is common, and may be preferred due to optical pumping of the cooled atoms to the highest (or lowest) magnetic sublevel by the polarization gradient.[2]

7.2 Standing Wave Laser Focusing Procedure

The procedure for bringing the oven up to its final operating temperature and for optimizing the saturated absorption frequency stabilization system were the same as in the laser cooling experiment described in Chapter six. Initially the substrate mount was

retracted to the rear of the vacuum system as far away from the oven source as possible via a translation in the +x direction (using screw #3 in Figure 7.3). This allowed both the 295 nm cooling laser beam and the 417 nm focusing laser beam to propagate all the way through the vacuum system and emerge on the other side. This was done to check the parallelness of the two beams. As in the cooling experiment, the cooling laser was initially aligned perpendicular to the atom beam by observing the laser-induced fluorescence from a single pass and a retroreflected double pass. After the cooling laser was perpendicular to the atomic beam, the focusing laser was made parallel to it.

This was accomplished by observing the two beams far away from the focusing chamber. The distance between the centers of the two beams was measured before entering the vacuum system. The beams emerging from the vacuum system were reflected off a glass slide and allowed to propagate a distance of 9 m. The separation of the two beams was again measured. Any difference in the separation of the beam centers was corrected by making adjustments to the mirror that reflected the focusing laser into the system. The cooling laser alignment was determined by the atomic beam, thus only the focusing laser could be changed. Using this method, the two beams were aligned parallel to within 1 mm over a distance of 9 m. This corresponded to an angular deviation of 0.1 mrad. When the two laser beams were parallel, the retroreflecting mirror and waveplate for the cooling laser were reinserted outside the vacuum system. The substrate mount was then translated forward in the -x direction until the standing wave mirror intercepted and retroreflected the focusing laser.

The focusing laser was retroreflected back on itself except for an intentional slight vertical misalignment. This vertical misalignment allowed the retroreflected power to be

measured with a power meter. While observing this power, the substrate mount was then translated forward in the -x direction again until the substrate clipped the focusing laser. Typically this translation was stopped when the power in the retroreflected laser beam was 50% of its initial unobstructed value. When this power was reached the vertical misalignment was corrected. In this way the surface of the substrate was brought into the maximum of the Gaussian profile of the focusing standing wave, the so-called "thick lens" focusing regime (see Section 2.8).

At this point the lasers were aligned for standing wave direct write optical lithography. The cooling laser was locked with the saturated absorption apparatus and then detuned for cooling. To set the frequency of the 417 nm laser, a spectrum was taken for the $4p^2P_{3/2} \rightarrow 5s^2S_{1/2}$ transition to ensure that the diode laser was operating in the correct mode. The scan was disabled, and the laser frequency was set to the line center of the F=3 $\rightarrow$ F=2 transition by changing the PZT voltage on the diode laser grating mount. The frequency was measured with the lambda meter with a precision of ±60 MHz. The laser was detuned by adjusting the PZT voltage and the detuning was then checked with the lambda meter. This was a somewhat crude way of determining the detuning. We wished to investigate focusing detunings ranging from 200 MHz to 500 MHz, so the uncertainty in the knowledge of the detuning was acceptable. Ideally this focusing laser would also be locked to its own saturated absorption apparatus, but this was not done during the focusing experiment.

The procedure for preparing the lasers and the Ga oven for the focusing experiment typically took four to six hours. With this completed, the system was ready to attempt Ga focusing. With the beams parallel and detuned from resonance by the desired

amount, the substrate was translated to provide a fresh surface for the laser-focused deposition. Horizontal translation of the substrate was accomplished by turning all three mirror mounts screws (#1 in Figure 7.3) equal amounts. Typically four 360° rotations of these screws provided enough spacing between deposition pads to eliminate any overlap. Vertical translation of the substrate was accomplished by turning screw #2 in Figure 7.3 six turns. Using these translations, two rows of depositions with four or five depositions per row could be made on a ~1 cm^2 substrate. The total deposition time for a pad was determined from when the translation to a new deposition spot was completed to the time the substrate was translated to a new spot. Typical deposition times ranged from as short as two minutes up to 45 minutes.

During the laser-focused deposition, all that was required of the operator was to observe the locking of the cooling laser. If the cooling laser jumped out of lock (almost always due to excessive drift of the frequency that the servo could not keep up with), the servo was unlocked and placed on "acquire" which provided a soft feedback. The laser frequency was manually tuned until the locking signal was reacquired and the servo was reengaged. All of this took no longer then 5 seconds. The rate of this unlocking was dependent on environmental conditions in the laboratory. At times, the system ran for hours without unlocking. Sometimes, it would unlock every five to ten minutes.

For the longer deposition times (> 30 minutes) the detuning of the focusing laser had to be checked during the deposition because its frequency was not stabilized. This was done by blocking the retroreflection and observing the reading of the lambda-meter. If some frequency drift had occurred, the intended detuning was reachieved by slightly changing the voltage applied to the diffraction grating in the diode laser head. No current

or temperature tuning was required. Typically this check of the detuning and any correction took no longer than a minute or two. For shorter deposition times, lambda-meter readings were always taken immediately prior to and after a deposition.

Laser-focused depositions were made using many different experimental conditions. Three different substrate materials were utilized: single crystal silicon (Si), single crystal gallium-arsenide (GaAs), and fused silica. The detuning of the cooling laser was varied from –12 MHz to –18 MHz. The detuning of the focusing laser was varied. Blue detunings from +200 MHz to +500 MHz were used as were red detunings from -200 MHz to -500 MHz. As already mentioned, deposition times ranged from two minutes to 45 minutes. As all the power generated by the lasers was deemed necessary for the experiment (~50 mW in the cooling laser and ~12 mW in the focusing laser) no attempt was made to study the effect of changing the laser power.

7.3 AFM Results of Standing Wave Laser-Focused Depositions

The results of the standing wave focusing were observed by using an atomic force microscope (AFM) to image small areas within the deposition pad. Typically, AFM measurements were performed several days after the depositions were made. Since Ga was a soft material, we believed it was best to allow time for an oxide layer to grow on top of the Ga deposition pad. Also, as the AFM was located in another building, removal from the vacuum system and oxidation were unavoidable. After removal from the vacuum, the substrate samples were typically cleaved to a smaller size with the depositions in the center to facilitate measurement with the AFM.

The AFM used in these measurements was a Nanoscope III from Digital Instruments run in tapping mode.[3] The AFM works by utilizing a small (~10 nm) Si

probe suspended at the end of a 125 μm cantilever arm. The cantilever is driven near its natural resonance frequency and is brought near a surface. Van der Waals interactions between the small Si tip and the atoms on the surface of the deposition cause a damping of the vibration of the cantilever. A voltage is applied to a PZT which moves the cantilever up from the surface to eliminate the damping. This applied voltage is measured and then converted to a distance from the surface. As the cantilever arm is translated over the surface, a map of the surface elevation is made with at least 1 nm accuracy (assuming no sharp features are being measured). Typical two-dimensional AFM surface scans are shown in Figures 7.4-7.6. Figure 7.4 shows AFM images of two Ga deposition pads on a Si substrate. The two pads were exposed to the standing wave focusing laser for 22 minutes in 7.4(a) and 45 minutes in 7.4(b). Both 1 μm^2 and 500 nm^2 scans are shown as are side-angle views to provide a better feature contrast. The region where the standing wave laser illuminated the substrate was much smaller than the deposition pad itself, so the entire surface of the pad was measured with the AFM. These images are representative of surface conditions over the whole pad. The Ga, rather than being focused into one-dimensional parallel lines by the standing wave laser, formed small droplets across the deposition pad. On the 22 minute deposition, these droplets were approximately 30 nm to 50 nm in diameter and around 50 nm tall. On the 45 minute deposition, the droplets were approximately 80 nm to 100 nm in diameter and around 100 nm tall. In both cases the size distribution of the droplets was fairly uniform, and the coverage was quite dense, with no empty space between dots other than that expected when packing spherical objets.

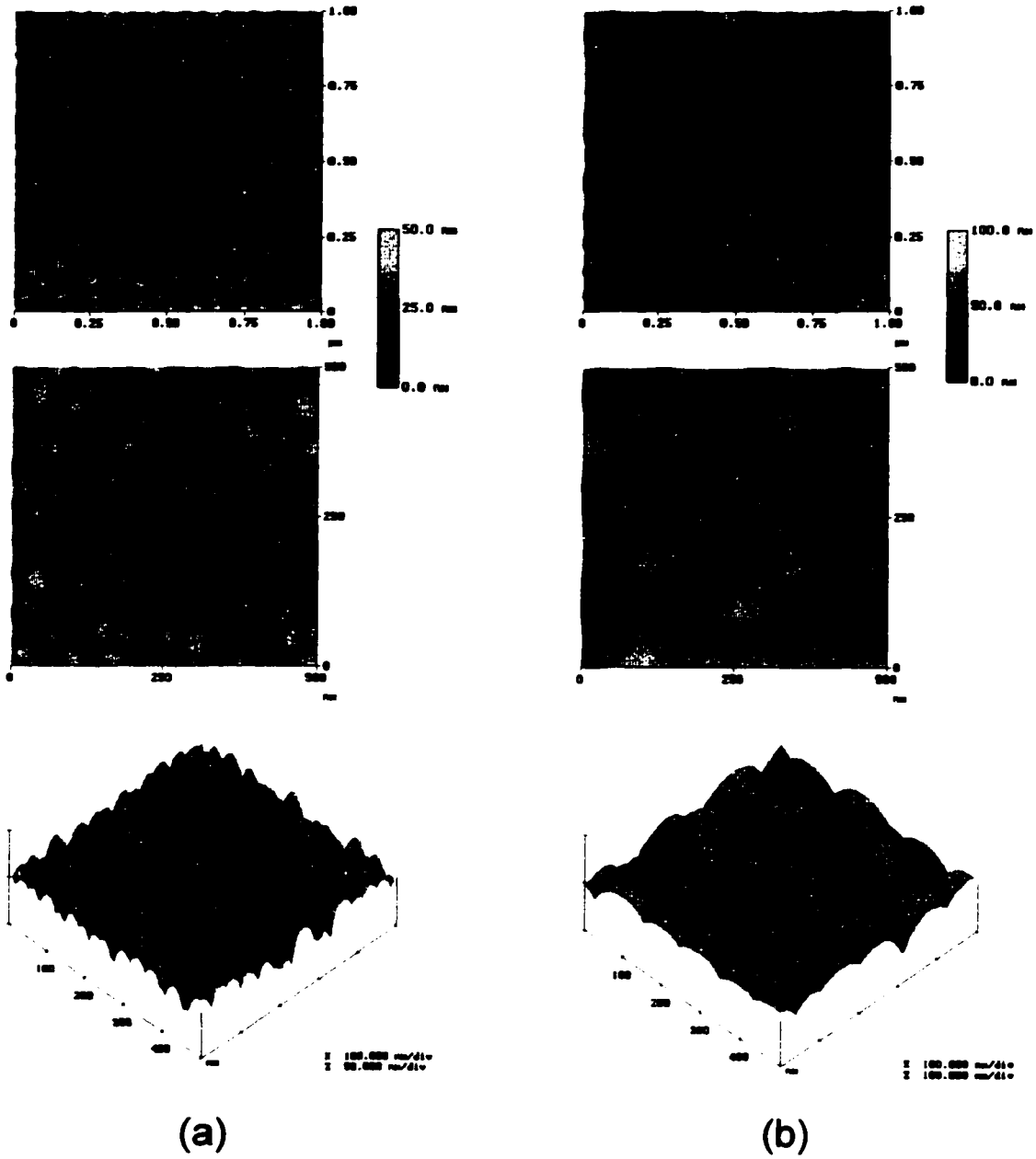

Figure 7.4 AFM images of Ga deposited on Si: 1 μm and 500 nm scales. (a) 22 min deposition. (b) 45 min deposition.

It was determined that the size of these droplets was too large to allow imaging of any laser-focused features which would at best be only 5 nm in height. It was hoped that the standing wave laser might provide regions of low potential energy on the surface where these islands would preferentially cluster, but no evidence of this type of behavior was observed.

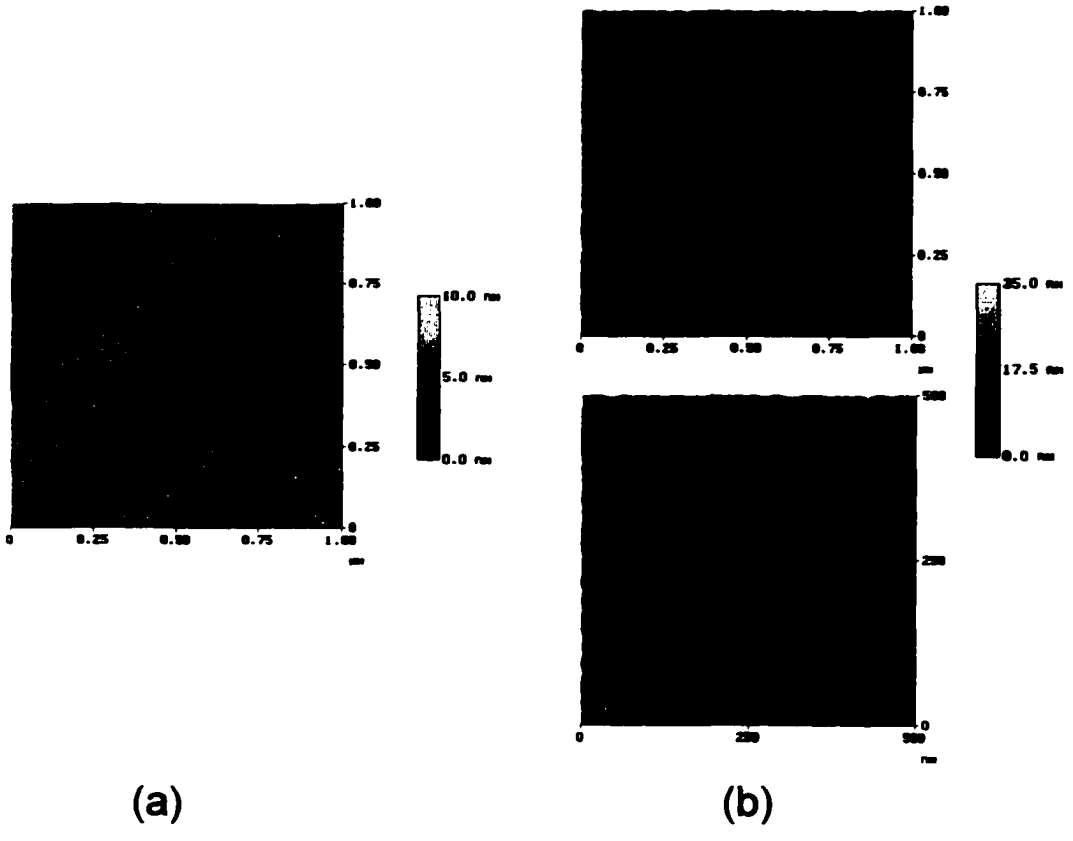

Figure 7.5 AFM images of Ga deposited on GaAs: 1 μm and 500 nm scales. (a) No Ga. (b) 15 min deposition time.

The same behavior was also observed for Ga deposition on a GaAs substrate. Figure 7.5(a) shows an AFM image of the GaAs substrate without Ga and 7.5(b) shows the substrate after 15 minutes of laser-focused Ga deposition. In 7.5(b), the images are also of areas 1 μm^2 and 500 nm^2. Again the Ga droplets were observed although they

were smaller this time: approximately 10-20 nm in diameter and around 20 nm in height. The uncovered substrate was quite smooth, with height fluctuations no taller than 1 or 2 nm. Thus it was not likely that any surface irregularity was responsible for the formation of the Ga droplets. The Si substrates were even smoother than the GaAs.

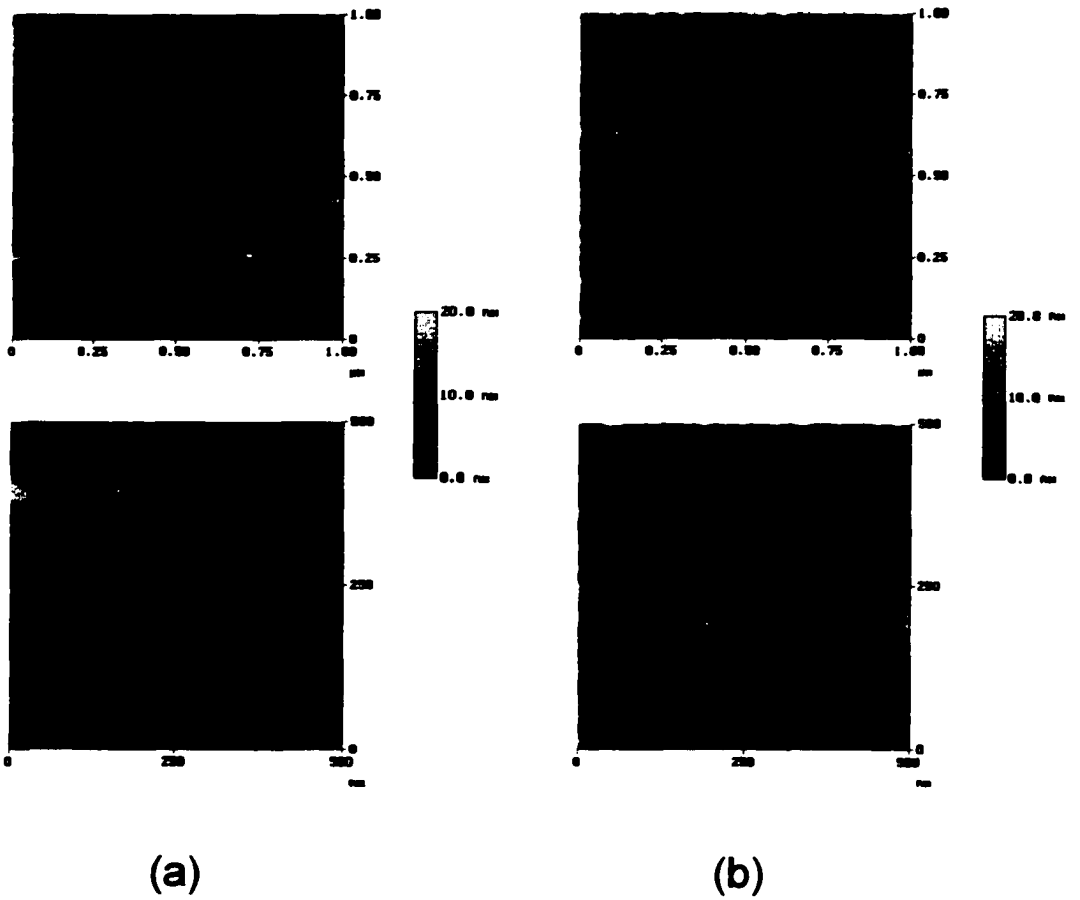

Figure 7.6 AFM images of Ga deposited on fused silica: 1 μm and 500 nm scales. (a) No Ga. (b) One hour deposition.

Figure 7.6(a) shows AFM images of the fused silica substrate without Ga and 7.6(b) shows the substrate after one hour of Ga deposition with the standing wave focusing laser turned off. The image sizes are again 1 μm^2 and 500 nm^2. The quartz

substrate had far more surface flaws and defects as can be seen in Figure 7.6(a). These features were at least 10 nm deep and located randomly across the surface of the substrate. The Ga droplets in the one hour exposure were small, approximately 10 - 20 nm in diameter and around 20 nm in height.

The AFM images in Figures 7.4 to 7.6 are typical of all the AFM images taken of Ga depositions. The Ga droplets always formed on the substrates. Depositions were made with the cooling laser on and off. No difference was observed. Deposition were made with the focusing laser on and off. No difference was observed. The only difference ever observed was related to deposition time. From Figures 7.4 and 7.5 and from other depositions made with varying times on Si and GaAs, it was apparent the droplets grew larger with longer exposure to the Ga atom beam flux. The increase in size (both diameter and height) was fairly uniform with deposition time corresponding to the additional Ga impinging on the surface being incorporated into existing droplets. On the quartz substrate the size of the droplets after one hour of exposure was nearly the same as the droplets on the GaAs substrate after only 15 minutes of exposure. It is fairly obvious that the surface conditions had a major influence on the specific growth behavior of these droplets.

During all deposition conditions, the Ga on the surface grew in the form of these islands which were always larger than the features expected from laser-focused deposition. For example, during laser focused deposition of aluminum, the focused Al lines were only 2.7 nm tall yet were formed on a very smooth (<1 nm height deviation) Al background.[4] It is apparent that if any laser-focusing was occurring, the formation of the droplets would preclude the imaging of focused features. Most likely the laser

focused deposition was occurring, but because at least 90% of the atoms were not being focused, their growth in the form of these droplets destroyed the periodic deposition of the laser cooled atoms by absorbing them into the ever expanding droplets.

It should be mentioned that the inability to observe the periodic laser-focused deposition of nanofeatures due to the self-organized islanding of the Ga in our apparatus in no way implies an inability to accomplish it during MBE growth. The MBE growth procedures for GaAs provide conditions that promote uniform thin film growth without islanding. It is still anticipated that the standing wave laser-focusing technique will preferentially influence the deposition of the Ga atoms during these procedures.

7.4 Self-Organized Islanding

The formation of nanosize droplets during thin-film growth on a substrate has been observed previously in Ga and other systems.[5,6,7] These droplets are often referred to as self-organized or self-assembled nanoparticles (islands).

The formation of nanosize Ga islands is related to growth in the liquid growth mode. This mode is based on the deposit of a material on a substrate in partial wetting or partial drying conditions. The conditions for growing these islands are dependent on the surface energy balance between the interfaces involved in the process.[5] The wetting of a substrate by a liquid nanosize droplet is shown in Figure 7.7. Partial wetting, as shown in Figures 7.7(a) and 7.7(b), refers to droplets whose liquid/vapor interface makes some contact angle, θ, with the substrate.[8] Complete wetting occurs when $\theta = 0$, Figure 7.7(c). All of these interface effects are very sensitive to surface conditions and properties.

The wetting-dependent liquid droplet formation is also temperature dependent.[9] There is some temperature T_D above which the nanoparticle formation is by a liquid

growth mode and below which the formation is by a solid/crystal growth mode. This temperature can be substantially lower than the bulk melting temperature. Since Ga is a liquid near room temperature, this suggests that the substrate must be cooled before the atoms are deposited in the solid growth mode.

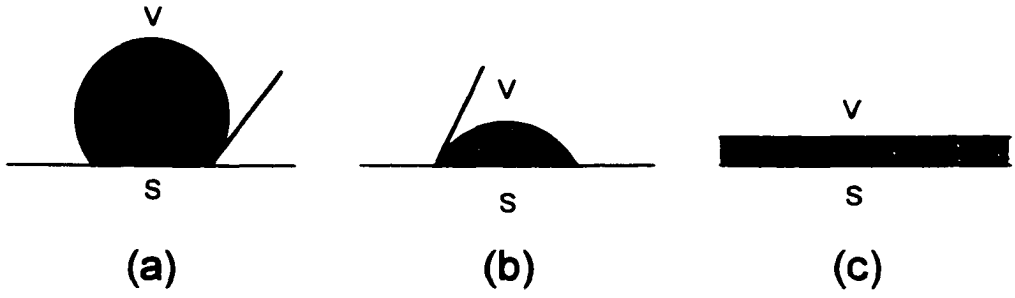

Figure 7.7 A nanoparticle liquid (L) droplet in equilibrium with a vapor (V) and a solid (S) substrate. (a) and (b) correspond to partial wetting. The wetting is stronger in (b). (c) corresponds to complete wetting ($\theta = 0$).

Deposition of Ga on the tip of a LN_2 cooled optical fiber was investigated in [7]. Deposition of non-islanded Ga was observed on both the uncooled and LN_2 cooled substrate. However the formation of self-organized Ga islands was observed when pulsed laser light illuminated the fiber core. This experiment suggests that the growth mode of Ga during deposition is very sensitive to surface conditions including temperature. A study of the island formation parameters (density, size, etc.) as a function of substrate temperature in our system would be the logical next step. Determination of a transition point, or critical temperature T_D, between the solid growth and liquid growth modes would be of great interest and potential usefulness.

7.5 Conclusions

Standing wave laser-focused deposition of one-dimensionally cooled Ga atoms was attempted on three substrates. For all combinations of experimental parameters, Ga

nanoparticles – self-organized islands – were grown on the substrates which precluded any observation of periodic nanostructures created by the standing wave laser focusing. The appearance of these islands was attributed to a liquid growth mode. Further study of island formation parameters and their temperature dependence is of interest.

REFERENCES

[1] R. McGowan, *Light Force Cooling, Manipulation, and Nanometer-Scale Deposition of Neutral Aluminum Atoms*, Ph.D. Thesis (Colorado State University, Fort Collins, Colorado, 1996)

[2] J.J. McClelland, R.E. Scholten, E.C. Palm, and R.J. Celotta, "Laser-focused atomic deposition," Science **262**, 877 (1993)

[3] The AFM was from the group of Professor Bruce Parkinson of the Department of Chemistry, Colorado State University.

[4] R.W. McGowan, D.M. Giltner, and S.A. Lee, "Light force cooling, focusing, and nanometer-scale deposition of aluminum atoms," Opt. Lett. **20**, 2535 (1995)

[5] E. Sondergard, R. Kofman, P. Cheyssac, and A. Stella, "Production of nanostructures by self-organization of liquid Volmer-Weber films," Surf. Sci. **364**, 467 (1996)

[6] M. Nisoli, S. Stagira, S. De Silvestri, A. Stella, P. Tognini, P. Cheyssac, and R. Kofman, "Ultrafast electronic dynamics in solid and liquid gallium nanoparticles," Phys. Rev. Lett. **78**, 3575 (1997)

[7] K.F. MacDonald, V.A. Fedotov, S. Pochon, K.J. Ross, G.C. Stevens, N.I. Zheludev, W.S. Brocklesby, and V.I. Emel'yanov, "Optical control of gallium nanoparticle growth," Appl. Phys. Lett. **80**, 1643 (2002)

[8] P.G. de Gennes, "Wetting: statics and dynamics," Rev. Mod. Phys. **57**, 827 (1985)

[9] N.T. Gladkikh, S.P. Chizhik, V.I. Larin, L.K. Grigor'yeva, and V.N. Sukhov, "Supercooling during crystallisation of islet-like films," Russ. Metal. **5**, 159 (1982)

CHAPTER 8

Conclusions

8.1 Summary of Results

This thesis describes the first laser manipulation of an atomic gallium beam. The $^{69}Ga\ 4p^2P_{3/2}(F=3) \rightarrow 4d^2D_{5/2}(F=4)$ transition at 294.45 nm was identified as a cycling transition suitable for laser cooling. A resistively heated Ga oven was used as an effusive source to generate an atomic Ga beam. The ground state of the cooling transition was thermally populated in the Ga beam.

An external frequency doubling cavity utilizing a 2 cm long temperature-tuned ADA nonlinear crystal was built to produce UV laser light at 295 nm by second harmonic generation of a 590 nm dye laser. This cavity generated up to 5 mW of UV power and was used to perform a careful spectroscopy of the cooling transition. This spectroscopy corrected an error in the existing literature for the Ga hyperfine constants.

A second external frequency doubling cavity was constructed which utilized a 5 mm long angle-tuned BBO nonlinear crystal to generate over 90 mW of UV power. The UV laser was frequency stabilized by locking the fundamental laser frequency with an iodine hyperfine saturated absorption apparatus. When locked to the iodine line the laser was stable for hours at a time and did not drift. This also greatly improved the stability of the frequency doubling cavity. This laser was used to demonstrate the first one-

dimensional laser cooling of an atomic Ga beam. Utilizing a UV-sensitive CCD camera, the collimation of the Ga beam by laser cooling was observed and measured directly. The transverse velocity of the Ga beam along the direction of the cooling laser was reduced from >2 m/s to <14 cm/s. This collimation was good enough to attempt direct write optical lithography (DWOL) via standing wave laser focusing. The cooling required at least 60 mW of power in a 5.5 mm diameter beam, with a red detuning of at least 13 MHz from resonance.

A 417 nm single-frequency diode laser capable of generating 14 mW of power was selected for laser focusing on the $4p^2P_{3/2}(F=3) \rightarrow 5s^2S_{1/2}(F=2)$ transition. This allowed all the available UV power to be used for laser cooling. Standing wave laser focusing was attempted on three different substrates (GaAs, Si, and fused silica) with a variety of experimental parameters. The results of the focusing were analyzed with an atomic force microscope (AFM) to look for the periodic focused depositions. Due to self-organized islanding of the Ga on all three surfaces, no evidence of standing wave laser focusing was observed. Instead, the Ga was deposited in nanosize (10's to 100's of nm) islands on each substrate. This precluded any observation of an atom focusing effect.

8.2 Improvements

There were certain areas of the experiment that could be improved. An atomic beam source whose pointing or orientation could be adjusted *in situ* would be highly advantageous and time saving. One possibility is to mount the oven on a flange that can be tilted slightly while bolted to the rest of the vacuum. Another possibility is to relocate the vacuum pump on our system and mount the oven on an end flange, rather than a side

flange as was done in our experiment. The end flange could be constructed to allow x-y translation of the oven on the order of several millimeters. Such a flange was used on our metastable beam apparatus.

A redesign of the substrate holder/standing wave mirror mount is another time saving improvement. The substrate was loaded and unloaded from the mount through a 6" flange located directly above it. The limited access to the mount made the loading/unloading difficult and removing the flange each time was time consuming.

The greatest improvement in the laser system could be made by replacing the 417 nm diode laser with a frequency doubled Ti:sapphire laser. We are currently in the process of constructing a second external frequency doubling cavity utilizing a BBO crystal. This cavity will double a Coherent 899 Ti:sapphire laser operating at 834 nm. With non-optimized cavity optics, we have already generated as much single-frequency power at 417 nm as the diode laser can produce. It is anticipated that more power is possible. There are several advantages in using a doubled Ti:sapphire laser. It is much easier to control the frequency settings and scanning of the Coherent 899 than the diode laser. Selecting the appropriate detuning from resonance for standing wave focusing could be accomplished much more easily. Also, the ring cavity design of the 899 and the doubling cavity is insensitive to feedback from the standing wave laser retroreflecting mirror. This feedback is always a concern when using the diode laser. It is expected that more power can be obtained from the BBO cavity than the diode laser and as much power as possible is always required in a standing wave focusing experiment. Lastly, the useful operation lifetime of the doubled Ti:sapphire is much greater than the anticipated 2000 hours before the laser diode will need to be replaced.

To improve the standing wave laser focusing, the 417 nm laser, whether the doubled Ti:sapphire or the diode laser, must be locked to a frequency reference. This essential step will provide long-term frequency stability and an accurate determination of the frequency detuning. The locking of the focusing laser can be done utilizing a Ga hollow-cathode tube. Such tubes provide a Ga discharge in a background environment of neon or another inert gas with excellent optical access. The discharge provides Ga atoms which can be used in a saturated absorption type locking scheme. A Ga hollow cathode tube with quartz end windows has already been purchased from Hamamatsu (L2783-31NE-GA). The implementation of this locking scheme is essential for the next generation of Ga manipulation experiments.

The most significant experimental improvement would be to increase the number of cooled F=3 state atoms during the laser cooling/focusing. Future versions of this experiment should utilize one of the repumping schemes demonstrated in Chapter six to prevent the depopulation of the F=3 state by the cooling laser. In addition, state pre-preparation is also possible. In this technique, the atoms would be illuminated by a pumping laser prior to cooling. This laser would pump the atoms from the other $4p^2P_{3/2}$ hyperfine states into the F=3 state, freeing us from the limit of statistical population of the state.

Another option for increasing the number of cooled atoms is to manipulate both isotopes of Ga. In this thesis, all the light force manipulation was performed only on ^{69}Ga – only 60% of the atoms in the beam. With the addition of frequency shifted lasers, it may be possible to manipulate the 71Ga atoms as well. This effectively doubles the number of atoms available for cooling and focusing.

8.3 Future Work

The laser manipulation techniques investigated in this work can be extended to the MBE growth of III-V semiconductor heterostructures. To this end, an MBE growth chamber was designed with these light-force experiments in mind. The chamber was constructed by APX Scientific Instruments. Technical drawings of the final MBE chamber are given in Figures 8.1 through 8.3. The chamber utilizes a turbo-pumped load/lock chamber to place sample substrates on the heated substrate mount. The chamber has an ion pump and LN_2 cryopanels for reducing the background pressure to better than $1x10^{-10}$ Torr. Three MBE effusion sources were obtained from EPI MBE

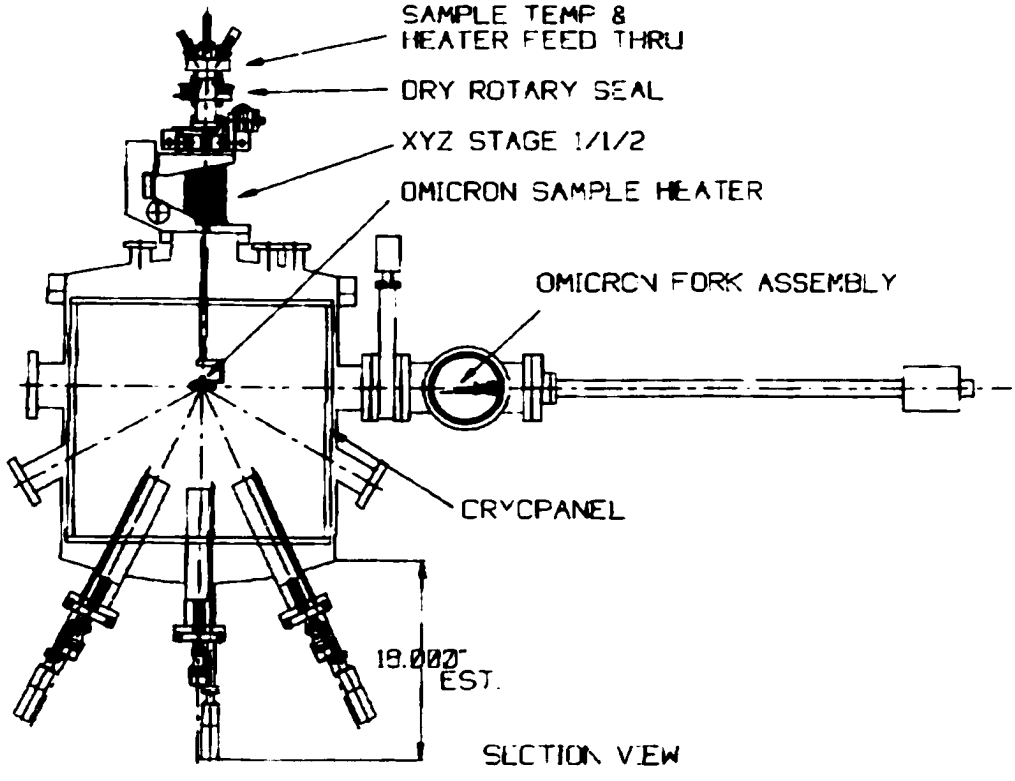

Figure 8.1 A section view of the MBE growth chamber designed for use in the light force manipulation experiments.

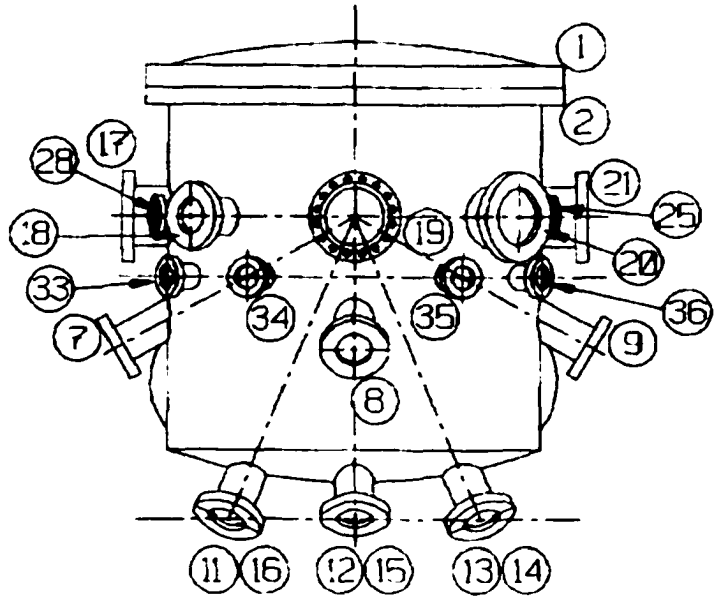

FRONT VIEW

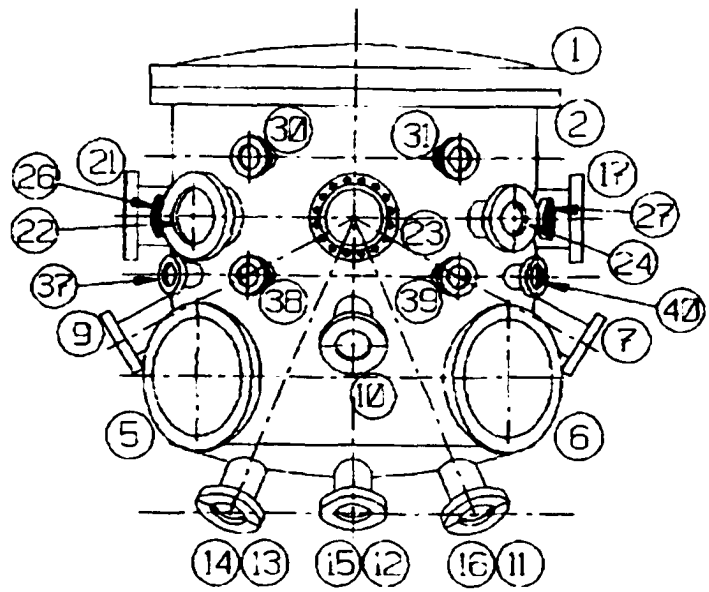

REAR VIEW

Figure 8.2 Front and rear side views of the MBE growth chamber designed for use in the light force manipulation experiments.

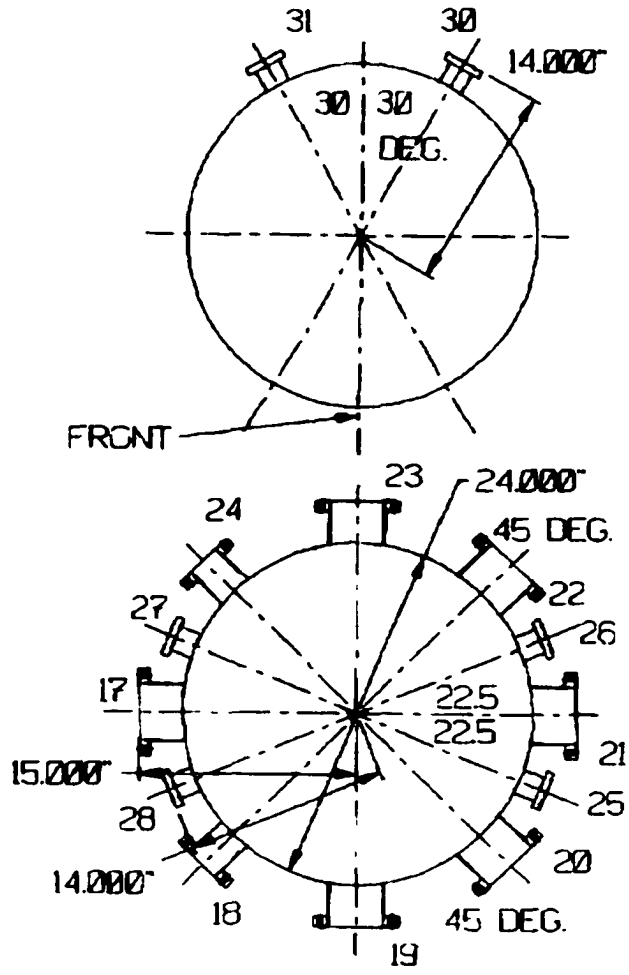

Figure 8.3 Two top views of the MBE growth chamber designed for use in the light force manipulation experiments.

Products Group. The sources are described more thoroughly in appendix three. A two-filament group III source is located at the bottom of the chamber, pointing straight up vertically. This will be the Ga source. Two additional sources were obtained for arsenic and aluminum. In this way GaAs or AlGaAs samples can be grown. The As and Al sources point upward at an angle as is typical with MBE growth chambers. The main difference between our chamber and a traditional MBE system is the large number of

ports for optical access to the substrate. In Figure 8.3, ports 17,19, 21, and 23 are 6" ports with quartz windows to allow two-dimensional laser cooling and focusing with UV or visible laser wavelengths. The other ports are for growth or chamber diagnostics.

8.4 Conclusions

The work described in this thesis demonstrated the ability to manipulate Ga atoms with light-force techniques. The described experiment and apparatus provided a flexible test platform for determination of the experimental parameters required for optimal light-force manipulation. Having proven the viability of laser cooling Ga atoms in a "bench-top" system, it remains now to attempt to reproduce these experiments in the MBE growth chamber. The techniques developed for manipulating Ga revealed the experimental challenges particular to Ga, but can also be more broadly applied to all the group III elements during MBE growth. This may open the way for the fabrication of many types of new and novel semiconductor materials in the years to come.

APPENDIX 1

Nanolithography With Metastable Neon Atoms

A1.1 Introduction

There has been increased interest recently in using neutral atomic beams as the lithographic source for the fabrication of nanostructures. Atoms have small de Broglie wavelengths, typically of the order 10 pm for thermal atomic beams, thus diffraction effects are negligible and resolution of a few nanometers is potentially possible. Atom beams have large cross sections, thereby allowing large areas to be patterned simultaneously. One potential advantage of atom lithography over e-beam or x-ray lithography is that atoms have internal energy levels which provide a mechanism for manipulation with laser light.[1] The wavelength of the manipulating laser maintains excellent long range spatial-phase coherence that is difficult to achieve with e-beam lithography. One important area in atom lithography is investigating the use of atoms to expose or to deposit resist materials that have high resolution and can withstand etching.[2,3,4,5] In this regard metastable rare gas atoms are particularly attractive as the source for lithography.[4,5] The atoms are inert and do not bind to the substrates. The internal energy of the atoms is delivered directly to the resist, and the atoms may be easily manipulated by lasers for future applications. For these techniques to become practical, it is important to have a short resist exposure time and to quantify the resist

formation rate and etching performance. Thus far quantitative results are lacking.

This appendix describes our use of metastable neon (Ne*) atoms to deposit contamination resist on a GaAs substrate and the subsequent anisotropic etching of the resist and GaAs by chemically assisted ion beam etching (CAIBE) to form nanostructures.[6] The resist formation rate was almost an order of magnitude increase over previous results.[4] This technique offered excellent control over both the resist formation and etching process, provided a high degree of selectivity, and allowed the characteristics of the lithographic process to be quantified. The fabrication of sharply defined 50 nm diameter pillars with an aspect ratio greater than 2:1 in GaAs is discussed. These were the best resolution and highest aspect ratio that had ever been achieved with metastable atom nanolithography. Measurements of the resist formation rate as a function of time and as a function of internal metastable energy were made, as were measurements on the etch rates of GaAs and the resist, and the etch selectivity as a function of the ion beam voltage.

A1.2 Resist Formation Mechanism

In a diffusion pumped vacuum system, background pump oil vapor molecules tend to adsorb on the inner surfaces of the system. A layer of carbon atoms was formed when a surface with adsorbed pump oil molecules was impinged by a beam of Ne* atoms. Previously, electron beams[7] and metastable argon (Ar*) atoms[4] had been shown also to deposit this "contamination resist". In the case of Ne*, the physical mechanism responsible for resist formation was well defined. A schematic of the resist formation process is shown in Figure A1.1. The large metastable energy of Ne*, 16.6 eV per atom, ensured that the dominant de-excitation process of Ne* in collisions with the surface was

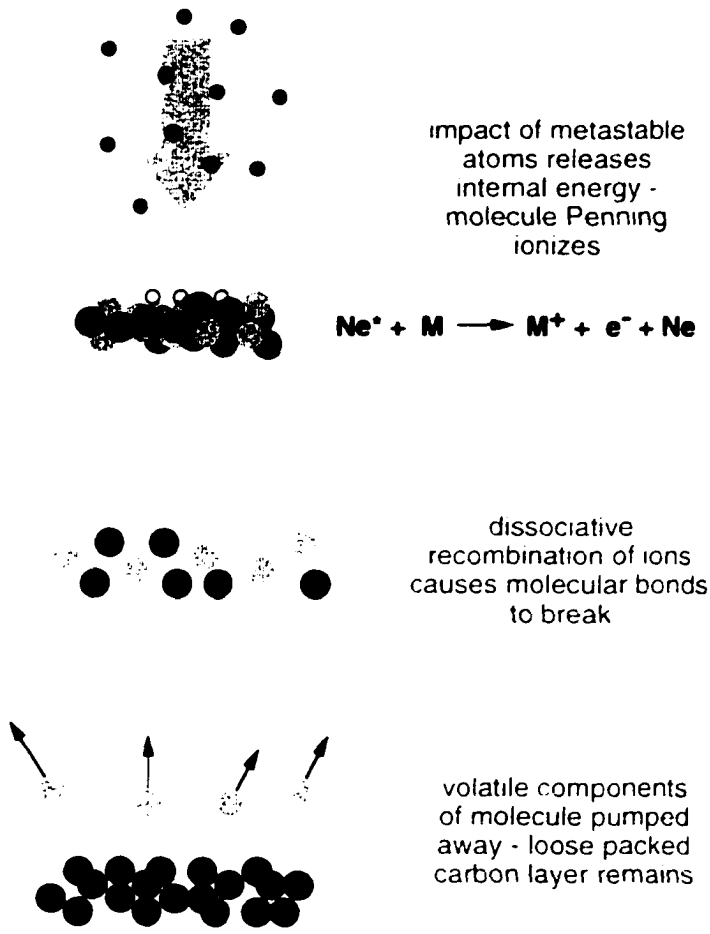

Figure A1.1 Contamination resist formation process due to impact by neutral metastable atoms.

through Penning ionization of the absorbed hydrocarbon molecules.[8] Recombination of the molecular ions with electrons followed rapidly on the surface, resulting in the dissociation of the molecules.[9] The volatile fragments were pumped away, leaving carbon atoms on the surface. The Penning ionization by Ne* was only weakly dependent on the adsorbate and the underlying substrate. In contrast, Ar* has low metastable energy (~12 eV) and its de-excitation mechanism efficiency was strongly dependent on the exact nature of the adsorbate since the typical ionization energy for hydrocarbons is 10-15 eV.

Large uncertainties also existed for the determination of the metastable Ar* beam flux;[8] thus reliable quantitative results for Ar* nanolithography were difficult to attain. Our experiment allowed us to reliably control the resist formation by the use of Ne*.

The rate of resist formation was studied for four metastable atoms: Kr* (9.9 eV), Ar* (11.5 eV), Ne* (16.7 eV), and He* (19.8 eV). The amount of resist formed per atom as a function of its metastable energy is shown in Figure A1.2. The non-linearity of the resist formation rate dependence on metastable energy suggested the existence of some threshold energy value between 11.5 eV and 16.7 eV. This corresponds to the typical ionization energy for hydrocarbons mentioned above. No additional data points were available between these two energies to probe that region further.

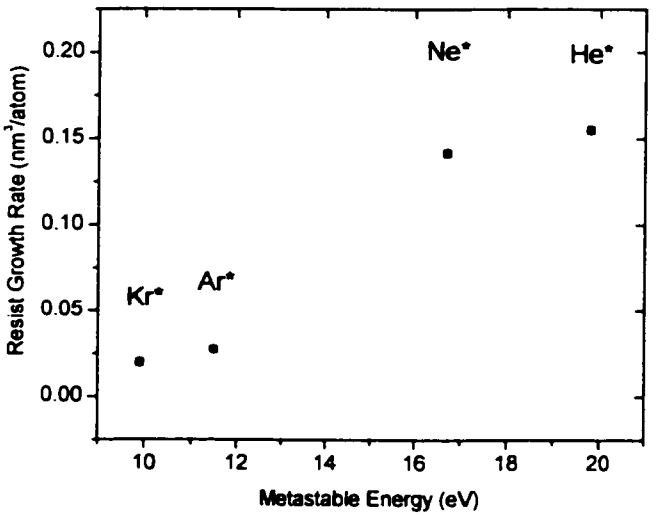

Figure A1.2 Contamination resist formation rate as a function of metastable energy.

The resist formation rate as a function of time was also investigated. Figure A1.3 shows the measured resist height as a function of the exposure time to the metastable beam for two different atoms: He* and Ne*. It is apparent that the resist formation

process progressed linearly for both metastable species for resist depths up to 300 nm and exposure times up to 72 hours. No leveling off or saturation of the resist formation process was observed.

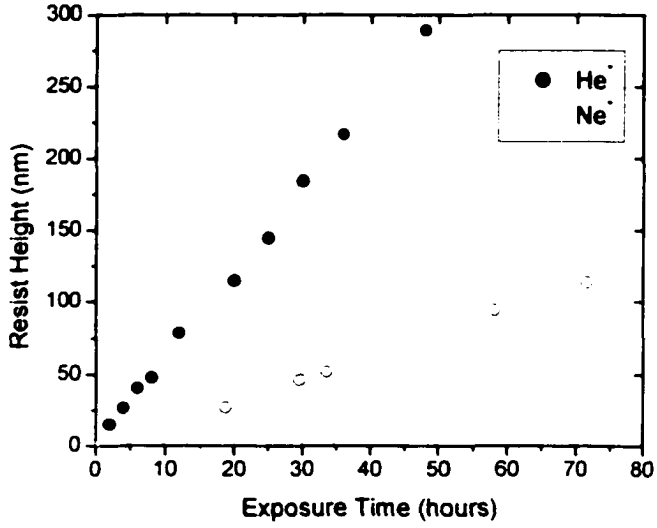

Figure A1.3 Contamination resist formation rate as a function of exposure time to the metastable beam for two different atoms: He* and Ne*.

As can be seen in Figures A1.2 and A1.3, He* was the most efficient atom for producing the resist. Prior to making these measurements, Ne* was the preferred metastable species due to its highly stable beam properties. All of the nanostructures in the experiments below were fabricated by exposure to the Ne* beam.

A1.3 Metastable Atom Lithography

The experimental arrangement for the deposition of contamination resist is shown in Figure A1.4. A beam of neon atoms was produced by a supersonic nozzle source.[10] The atoms were excited to the metastable $3s[3/2]^0_{J=2}$ and $3s'[1/2]^0_{J=0}$ levels by a dc discharge operating between a sharp needle and a cone-shaped skimmer electrode. The atoms passed through the 1-mm diameter skimmer hole and entered a deposition

chamber. The average velocity of the atoms was 1000 m/s±10%. The electrons and ions contained in the beam were steered away by a set of deflection plates. The Ne* flux was ~4.6 x 10^{11} atoms cm^{-2} s^{-1}. The vacuum system was pumped with diffusion pumps[11] that were cold trapped with liquid nitrogen. The background pressure in the deposition chamber was 1x10^{-7} Torr with the neon beam off, and 2x10^{-6} Torr when the beam was on.

The metastable atom lithography process is shown schematically in Figure A1.5. The lithography consisted of three steps: exposure of a substrate to the patterning beam, resist formation on the surface of the substrate, and transfer of the pattern to the substrate by etching. The substrates were mounted on a micrometer stage 40 cm downstream from

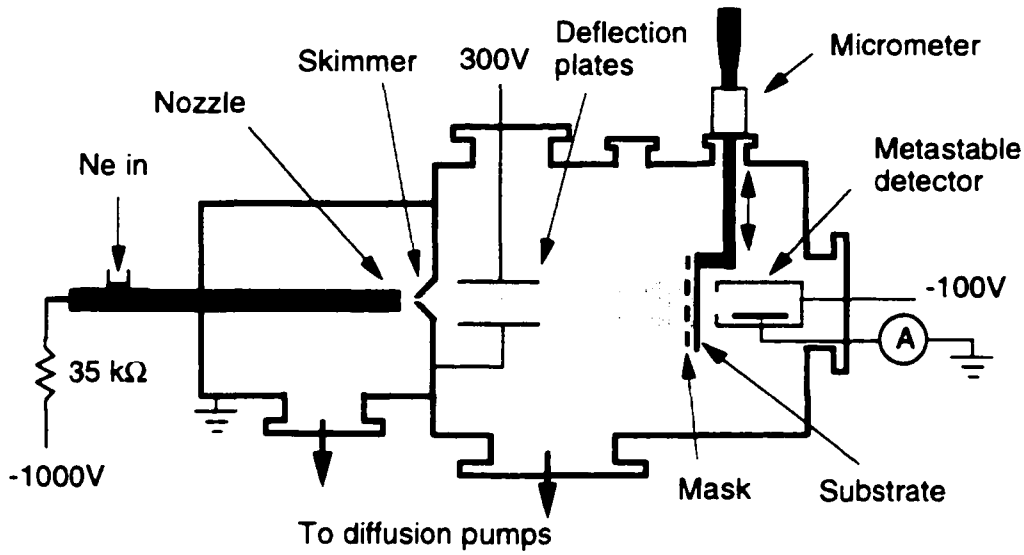

Figure A1.4 Schematic of the neon metastable beam apparatus for the deposition of contamination resist.

the skimmer and could be translated to intercept the metastable beam. The <100> *p*-doped GaAs wafers were exposed to the Ne* beam patterned by physical masks mounted on the substrate surface. Two different types of masks were used. E-beam fabricated

masks,[12] which consisted of a 50 nm thick, 100 μm x 100 μm Si_3N_4 membrane with nanoscale perforations supported on Si, were used to pattern nanometer scale features on the substrates. These were referred to as nanomasks. Transmission electron microscopy

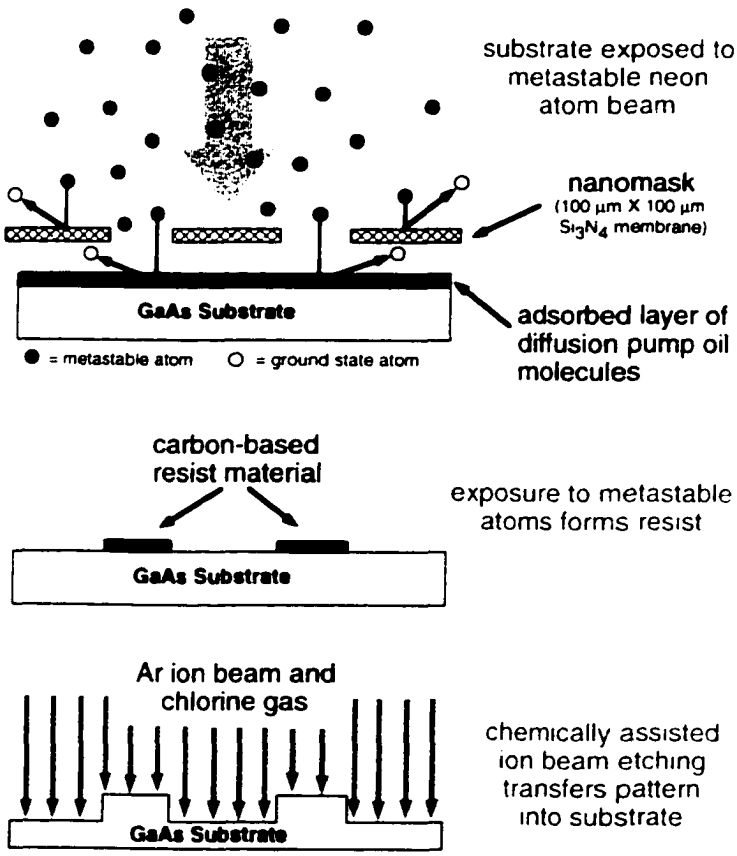

Figure A1.5 Schematic of the metastable atom lithography process.

(TEM) grids with μm-scale openings were used in studies pertaining to deposition and etching rates. The metastable beam diameter was approximately 3 cm in the substrate region, allowing simultaneous exposure of several samples. Exposure times ranged from 2 to 36 h. The thickness of the contamination resist was measured with an atomic force microscope (AFM). The resist height for a 24 h exposure through the TEM grids was found to be 40±3 nm. For comparison, the previous experiment[4] with Ar* had a resist

height of 6±2 nm. Thus the use of Ne* increased the resist depth by a factor of seven.

A1.4 Chemically Assisted Ion Beam Etching

The patterns of the contamination resist were transferred to the GaAs substrates using CAIBE.[13] CAIBE was performed using chlorine as the reactive gas together with an Ar ion beam produced from an Ion Tech Model 3-1500-150 ion source. A schematic of the CAIBE apparatus is shown in Figure A1.6. Typical etching conditions were as follows: 200-350 V Ar ion beam voltages, 0.25 mA/cm^2 ion beam current density, 5 sccm Cl_2 flow, and 2 mTorr pressure in the etching chamber.

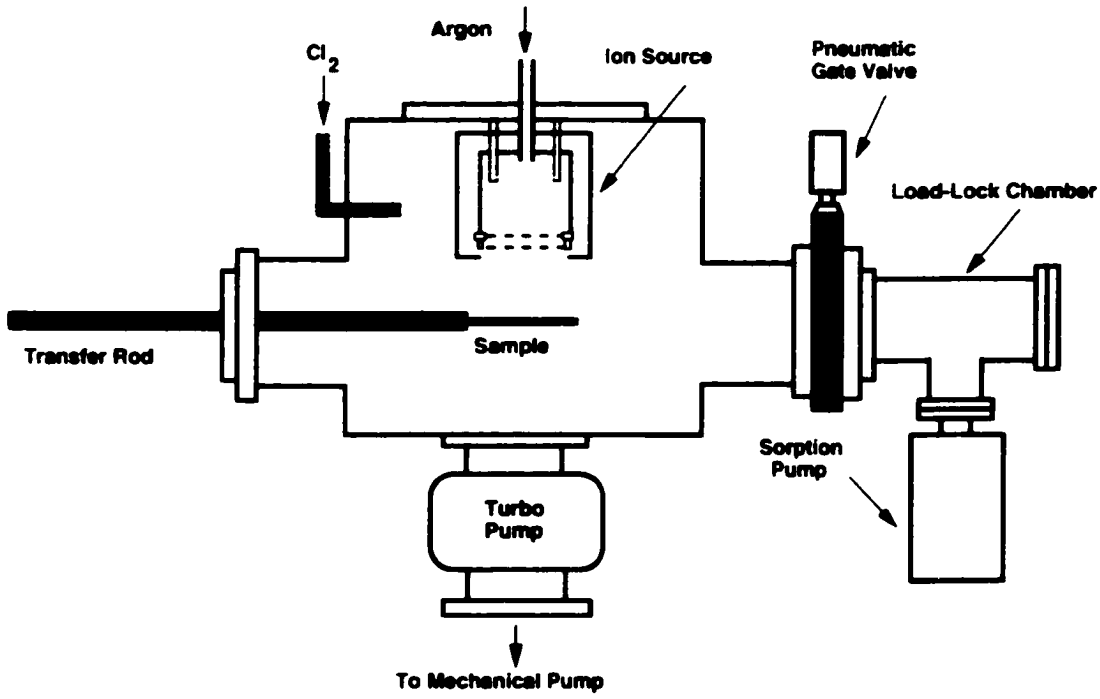

Figure A1.6 Schematic of the CAIBE apparatus.

We investigated the dependence of the etch rates of GaAs and the contamination resist on the ion beam voltage. The results are shown in Figure A1.7. For these studies, clean GaAs substrates were exposed to the Ne* beam through TEM grids for 24 h. Auger electron analysis showed that greater than 98% of the resist was composed of carbon.

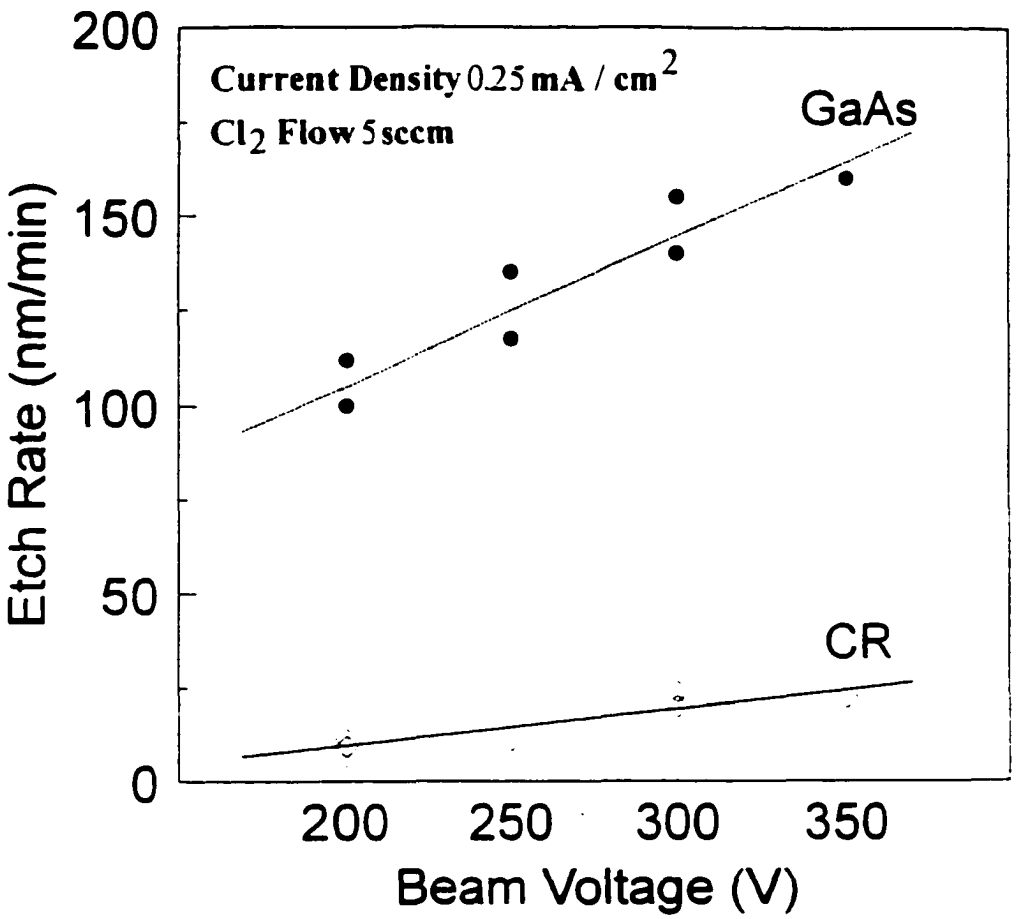

Figure A1.7 The etch rates of GaAs and of the contamination resist (CR) as a function of Ar ion beam voltage.

The contamination layer performed well as a resist, as shown by the results of Figure A1.7. The selectivity, defined as the ratio of the etch rates for GaAs and the contamination resist, varied from 7.3 at 300 V to 11 at 200 V. We also measured the

etching rate of GaAs and the contamination resist when no chlorine gas was present. The sputtering rate at 200 V and 0.25 mA/cm^2 argon ions was found to be 12 nm/min for GaAs and 2.5 nm/min for the resist. Thus CAIBE improved the selectivity while increasing the etching rate for GaAs and the contamination resist.

A1.5 CAIBE Results

Figure A1.8 shows scanning electron microscope (SEM) images of the structures etched into <100> *p*-doped GaAs. The exposure time to the Ne* beam was 15 h for Figures (a)-(c) and 36 h for Figures (d) and (e). The samples were etched for 2 min [Figures (a)-(c)] and 6 min [Figures (d) and (e)] at an ion beam voltage of 200 V. The nanomask consisted of arrays of 500 nm square holes and 50 nm round holes. This pattern was transferred to GaAs [Figure A1.8(a)]. Figure A1.8(b) is an image of the 50 nm features viewed at a 60° angle. The pillars are ~130 nm tall, giving an aspect ratio of better than 2:1. At the time, these were the highest aspect ratio nanostructures ever created using neutral atom lithography. Figure A1.8(c) shows the 50 nm round pillars viewed from above (0° angle). They have well-defined edges, indicating that even smaller features may be fabricated with this technique. Figures A1.8(d) and A1.8(e) show the 500 nm square posts. The feature height is ~500 nm. The 50 nm diameter pillars, however, did not survive the 6 minute etch due to undercutting in the sidewalls. The undercutting was most likely due to the divergence of our ion beam. This may be improved by optimizing the ion beam focusing conditions and by increasing the source to substrate distance.[14] With modifications to the CAIBE setup, it is not unreasonable to expect that an aspect ratio greater than 5:1 is possible for the 50 nm pillars.

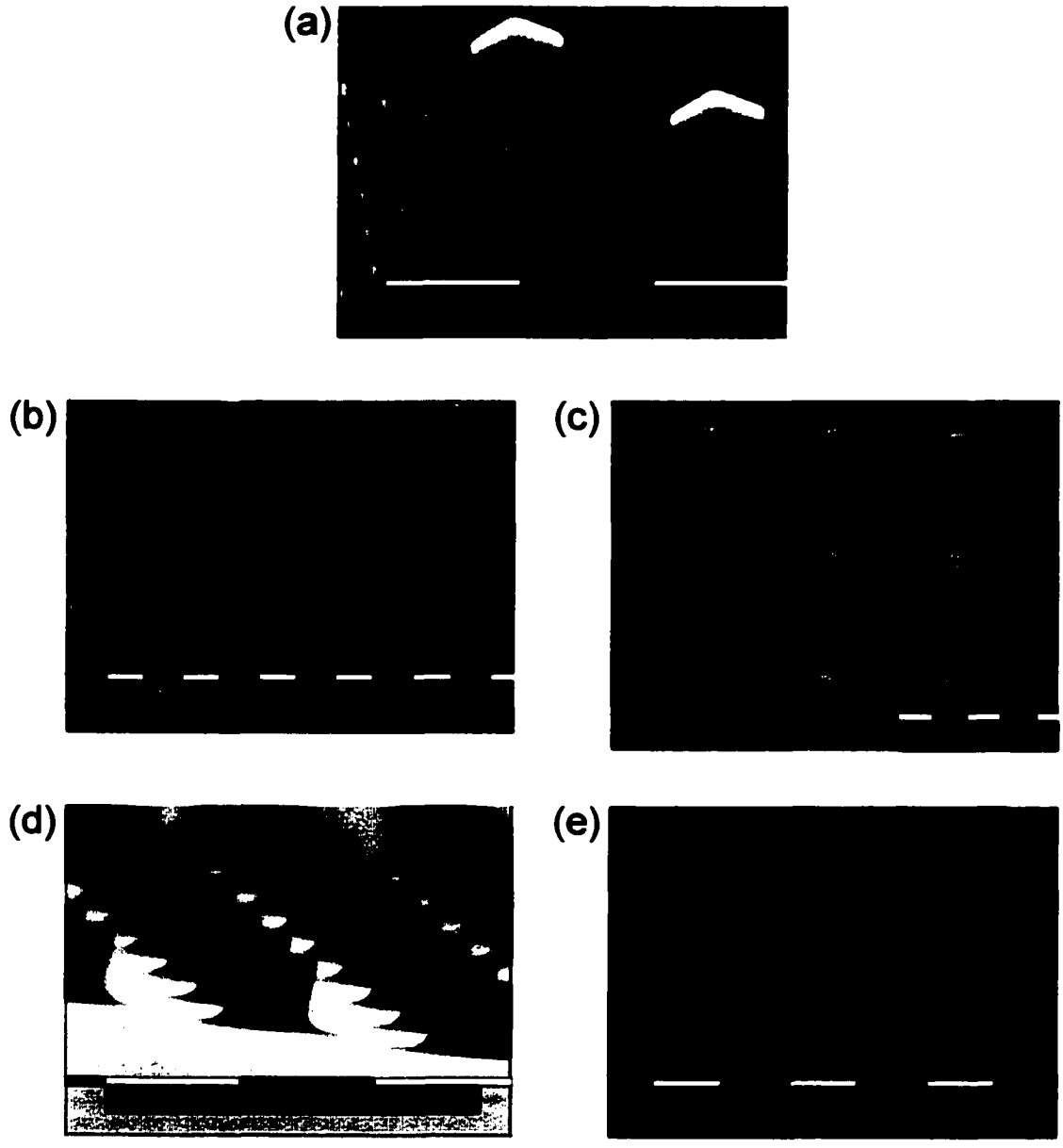

Figure A1.8 SEM images of nanostructures in GaAs. (a) The structures contain 500 nm square posts and 50 nm round posts. (b) A magnified view of the 50 nm diameter pillars. The SEM view angle is 60°. (c) Same as (b) but viewed at 0°. (d), (e) The 500 nm squares views at 90° and at 60° respectively.

A1.6 Conclusions

Using metastable neon atoms to deposit contamination resist and the standard CAIBE technique, we achieved significant improvements in the resist formation rate, etch anisotropy, etch rates, and selectivity for fabricating nanoscale structures in GaAs. The resolution obtained in this Ne* experiment was quite comparable to that of e-beam lithography. The ability to manipulate atoms with laser light provides additional possibilities.[1,15] In addition, enhancement in the metastable beam flux by more than a factor of 10 may be obtained with laser cooling.[16] With these improvements, the atom lithographic technique demonstrated here may become attractive for practical applications.

REFERENCES

[1] G. Timp, R.E. Behringer, D.M. Tennant, J.E. Cunningham, M. Prentiss, and K.K. Berggren, Phys. Rev. Left. **69**, 1636 (1992); J.J. McClelland, R.E. Scholten, E.C. Palm, and R.J. Celotta, Science **262**, 877 (1993); R.W. McGowan, D.M. Giltner, and S.A. Lee, Opt. Lett. **20**, 2535 (1995); U. Drodofsky, J. Stuhler, B. Brezger, T. Schulze, M. Drewsen, T. Pfau and J. Mlynek, Microelectron. Eng. **35**, 285 (1997)

[2] K.K. Berggren, A. Bard, J.L. Wilbur, J.D. Gillaspy, A.G. Helg, J.J. McClelland, S.L. Rolston, W.D. Phillips, M. Prentiss, and G.M. Whitesides, Science **269**, 1255 (1995)

[3] See, for example, M. Kreis, F. Lison, D. Haubrich, D. Meschede, S. Nowak, T. Pfau, and J. Mlynek, Appl. Phys. B **63**, 649 (1996); see also K.K. Berggren, R. Younkin, E. Cheung, M. Prentiss, A.J. Black, G.M. Whitesides, D.C. Ralph, C.T. Black, and M. Tinkham, Adv. Mater. **9**, 52 (1997)

[4] K.S. Johnson, K.K. Berggren, A. Black, C.T. Black, A.P. Chu, N.H. Dekker, D.C. Ralph, J.H. Thywissen, R. Younkin, M. Tinkham, M. Prentiss, and G.M. Whitesides, Appl. Phys. Lett. **69**, 2773 (1996)

[5] S. Nowak, T. Pfau and J. Mlynek, Appl. Phys. B **63**, 203 (1996)

[6] S.J. Rehse, A.D. Glueck, S.A. Lee, A.B. Goulakov, C.S. Menoni, D.C. Ralph, K.S. Johnson, and M. Prentiss, Appl. Phys. Lett. **71**, 1427 (1997)

[7] W.W. Molzen, A.N. Broers, J.J. Cuomo, J.M.E. Harper, and R.B Laibowitz, J. Vac. Sci. Technol. **16**, 269 (1979); see also A.N. Broers, Philos. Trans. R Soc. London, Ser. A **353**, 291 (1995)

[8] H. Hotop, in *Experimental Methods in the Physical Sciences*, edited by F.B. Dunning and R.G. Hulet (Academic, San Diego, 1996), Vol. 29B, pp 191-215

[9] See, for example, D.R. Bates, in *Dissociative Recombination: Theory, Experiment, and Applications*, edited by B.R. Rowe, J.B.A. Mitchell and A. Canosa (Plenum, New York, 1993), and references therein.

[10] Our metastable beam source is similar to the one described by D.W. Fahey, W.F. Parks, and L.D. Schearer, J. Phys. E **13**, 381 (1980)

[11] The diffusion pump oil used was Neovac SY (alkyldiphenylether) from Varian Vacuum Products.

[12] K.S. Ralls, R.A. Buhrman, and R.C. Tiberio, Appl. Phys. Lett. **55**, 2459 (1989)

[13] M.W. Geis, G.A. Lincoln, N. Efremow, and W. J. Piacentini, J. Vac. Sci. Technol. **19**, 1390 (1981)

[14] G.A. Lincoln, M.W. Geis, S. Pang, and N.N. Efremow, J. Vac. Sci. Technol. B **1**, 1043 (1983)

[15] A.P. Chu, K.K. Berggren, K.S. Johnson, and M. Prentiss, Quantum Opt. **8**, 521 (1996)

[16] F. Shimizu, K. Shimizu, and K. Takuma, Chem. Phys. **145**, 327 (1990); M.D. Hoogerland, J.P.J. Driessen, E.J.D. Vredenbregt, H.J.L. Megens, M.P. Schuwer, H.C.W. Beijerinck and K.A.H. van Leeuwen, Appl. Phys. B **62**, 323 (1996)

APPENDIX 2

Cooling Parameters For Additional Elements of Interest

Three other elements of interest for laser manipulation are cesium, indium, and iron. Indium is a group III element with unusual properties of self-organized islanding during III-V heterostructure growth. cesium is an easily manipulated group I element, and iron is of interest for its ferromagnetic properties. Table A2.1 lists all the relevant cooling parameters for these three elements.

Table A2.1: Cooling parameters for indium,[1] iron,[2] and cesium[3]

	Indium	**Iron**	**Cesium**
Atomic Number	49	26	55
Atomic Mass (a.u.)	115	56	133
Stable isotopes	^{115}In: 96% ^{113}In: 4%	^{56}Fe: 92% ^{54}Fe: 6% ^{57}Fe: 2%	^{133}Cs: 100%
I (nuclear spin)	9/2	0	7/2
Cooling Transition	$5p^2P_{3/2}(F=6) \rightarrow 5d^2D_{5/2}(F=7)$	$4s^5D_4 \rightarrow 4p^5F_5$	$6s^2S_{1/2}(F=4) \rightarrow 6p^2P_{3/2}(F=5)$
Vacuum wavelength (nm)	325.7	372	852.1
Photon momentum $\hbar k$ (kg m/s)	2.03×10^{-27}	1.78×10^{-27}	0.78×10^{-27}
Saturation intensity I_0 (mW/cm^2)	78	6.2	1.1
Natural linewidth $\Gamma/2\pi$ (MHz)	21	16.2	5.22
Doppler Limits T_D, v_D	504 μK, 0.19 m/s	240 μK, 0.31 m/s	125 μK, 0.088 m/s
Recoil Limits T_R, v_R	1.6 μK, 0.011 m/s	2.5 μK, 0.019 m/s	0.2 μK, 0.003 m/s

REFERENCES

[1] S.J. Rehse, R.W. McGowan and S.A. Lee, "Optical manipulation of group III atoms," Appl. Phys. B **70**, 657 (2000)

[2] R. Bosch, *Ferromagnetic nanostructures by laser manipulation*, Ph.D. Thesis (Eindhoven University of Technology, Eindhoven, Germany 2002)

[3] F. Lison, H. –J. Adams, D. Haubrich, M. Kries, S. Nowak, D. Meschede, "Nanoscale atomic lithography with a cesium atomic beam," Appl. Phys. B **65**, 419 (1997)

APPENDIX 3

Molecular Beam Epitaxy Effusion Cells

An effusion cell designed for use in molecular beam epitaxy (MBE) can generate a large area uniform atomic beam. These cells are often called "Knudsen cells" even though a true Knudsen cell would have an aperture diameter of less than 1 mm. An example of a typical MBE cell manufactured by EPI MBE Products Group is shown in Figure A3.1. In this type of cell the material to form the beam, which could be Ga or any number of other materials, is deposited within the crucible (1). The crucible is heated by

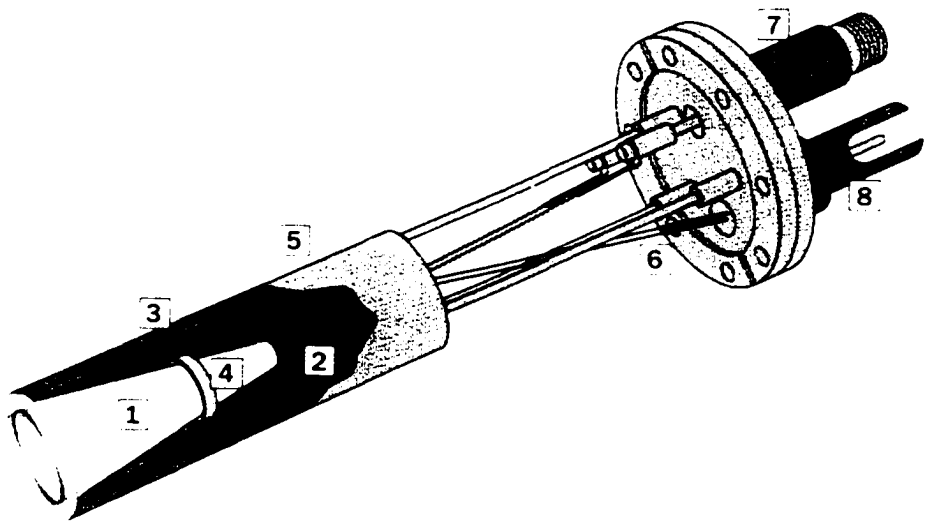

Figure A3.1 A commercially manufactured MBE effusion cell.

electron bombardment. The electron bombardment comes from passing current down the wire filaments (2) inside the source. The cell is mounted on a vacuum flange (6) with electrical feedthroughs (7), temperature monitoring feedthroughs (8), and water cooling connections (not shown).

A detailed look at the exit end of an effusion cell designed specifically for use with group III elements is shown in Figure A3.2. A twin filament heating scheme prevents the group III elements, all of which tend to condense on the coolest parts of the oven and then destroy oven material to some extent, from clogging up the exit aperture.

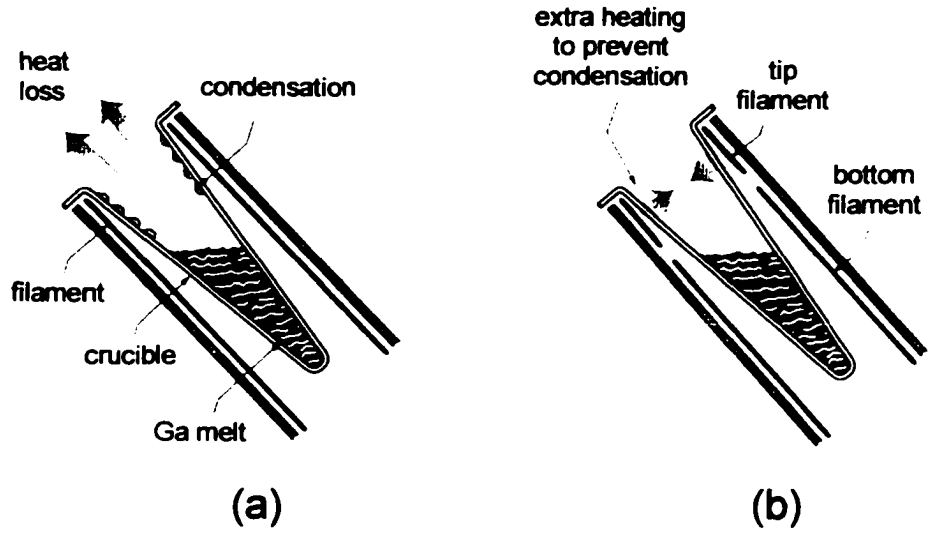

Figure A3.2 Detail of the exit aperture of a commercial MBE effusion cell. (a) The lip of the crucible tends to be colder than the rest of it, prompting Ga condensation. (b) A second filament is used specifically to heat the lip of the crucible.

From this figure it can be seen that the exit aperture is large, usually at least 1" in diameter or greater. It is this wide aperture that produces a large uniform beam, which is required for large diameter wafer growth. In our experiment a large beam was not required. In fact, a highly collimated beam with a small area was desired. Since extreme

aperturing of the beam produced by an MBE cell would be necessary, a large amount of Ga would have been wasted if used in our application.

In Figure A3.2 it is also clear that these cells cannot be used in a horizontal configuration. If positioned horizontally, the Ga would spill out of the crucible. In MBE operation, these cells are used in an almost vertical orientation, typically making a 10° angle with vertical. While there is nothing prohibitive about performing the laser cooling and focusing experiments in a vertical configuration, a complete redesign of the vacuum system and substrate mount would have been required.

Lastly, these MBE effusion cells are costly: around $10,000 to $20,000 apiece. This does not include the crucible or the cost of the two power supplies required to run one dual-filament cell. In comparison, our Ga heaters were quite inexpensive and we manufactured our ovens ourselves. Any change in oven design that was desired could be accomplished with about one day of machining.

In a commercial application where high uniformity large area beams are required and the vacuum system is opened very infrequently, this type of source would be very appropriate. In a horizontal bench-top apparatus where flexibility of use is desirable and very small deposition areas are required, this source design is not adequate.

APPENDIX 4

Cavity Stability Calculations

At various times in the design phase of the second harmonic generation (SHG) external power enhancement cavities (frequency doubling cavities) two software programs were used to determine stability conditions and cavity parameters (beam waist size, divergence, etc.). The first program was a Maple routine written specifically for designing these bowtie frequency doubling cavities. The second was a commercial program called "Paraxia-Plus ABCD" from Sciopt Enterprises and Stanford University. Both programs used the ABCD formalism for describing the propagation of a Gaussian beam through a series of optical elements. The ABCD software had the added benefit of including a graphical interface that performed ray tracing of the beam. The Maple routine had no graphical interface, but did calculate cavity stability curves which the ABCD program could not. This was useful because it provided the cavity designer with some idea of the precision with which the optical elements (particularly the curved mirrors) must be placed in the cavity. In the final design stages, cavities were designed and modeled using the Maple routine and the design was checked with the ABCD program. Both were useful for providing information about the performance of the cavity.

A4.1 The ABCD Technique

Ray tracing is modeling the behavior of light. It assumes that the light does not spread to any appreciable degree as it propagates through an optical system. If this is true, we can define a ray as the path that the center of a very slowly diverging electromagnetic beam takes as it goes through the system.[1] These rays move as straight lines through the optical system, so the complete behavior of the ray can be described by knowing, at any instant, the ray's position (in this case the distance away from the optical axis) and its slope relative to that optical axis. This does assume a paraxial (close to the optical axis) ray. Since only these two parameters need be known, we can describe the ray as a 1x2 array

$$\begin{pmatrix} r \\ r' \end{pmatrix} \tag{A4.1}$$

where r is the ray's distance from the optic axis and r′ is the ray's slope at that position. A ray's interaction with any simple geometric optical element, including lenses, mirrors, solids, free space, etc. can be described by the matrix equation

$$\begin{pmatrix} r_{out} \\ r'_{out} \end{pmatrix} = \begin{pmatrix} A & B \\ C & D \end{pmatrix} \begin{pmatrix} r_{in} \\ r'_{in} \end{pmatrix} \tag{A4.2}$$

where the array with r_{in} describes the incoming ray, the array with r_{out} describes the ray leaving the optical element, and the 2x2 matrix describes the optical element itself. This approach is valid because all the simple geometric optical elements act only to change the ray's position, slope, or some combination of the two.

Using the rules of linear algebra, any system of elements, such as our frequency doubling cavity, can be modeled as a 2x2 matrix which is the matrix product of every

element in the system. For example, in our frequency doubling cavity the fundamental laser beam entered through the input coupler, propagated through space to the first flat mirror, bounced off the mirror, propagated to the second mirror and so on. If every element (including the free space propagation) is assigned an appropriate 2x2 matrix and they are multiplied in the order in which the ray encounters them, the resulting 2x2 product matrix will contain all the information about the cavity. The ABCD software and Maple routine were essentially used just to calculate these 2x2 matrices.

A4.2 Cavity Stability

At the heart of both the ray tracing programs described here lies the issue of cavity stability. Simply put, will the ray eventually bounce out of the cavity after one or many round-trips (unstable) or can it complete multiple roundtrips and stay within the cavity (stable)? This question can be easily answered if the 2x2 matrix for one round-trip through the cavity is known. This is called the unit cell since many passes around the cavity just duplicate this matrix. If this unit cell matrix is known, then the condition for stability is simply

$$0 \leq \frac{A + D + 2}{4} \leq 1 \qquad \text{(A4.3)}$$

If this condition is satisfied, the cavity is stable the and value of this inequality tells us how close to the edge of stability the cavity is.

A4.3 Maple Calculations

Given below is the routine (run on Maple 6) used to calculate two parameters of the cavity: the primary waist size and the cavity stability in both the tangential and sagittal planes. The routine assumed that the waist was located at the center of the crystal. The input parameters of the cavity were: the radii of curvature of the mirrors, the angle of incidence on the mirrors, the length of the crystal, the indices of refraction, the fundamental wavelength, and the distances between all the optical elements included. To model different cavities, these parameters were changed for each permutation.

```
> with(plottools);
> with(plots);

> with(linalg);
```

Input Angle 1 (the half-angle off mirror 1 in degrees) => alpha
Input Angle 2 (the half-angle off mirror 2 in degrees) => beta
Input Z length (total distance from curved mirror to curved mirror in cm) => z
Input the radii of curvature of mirror 1 and mirror 2 in cm => ra and rb

```
> alpha := 11.5;
> beta := 5.7;
> z := 100;
> alpha:=alpha*Pi/180;
beta:=beta*Pi/180;
> ra:=10;
rb:=10;
```

Input n (the index of refraction of the crystal at 590 nm)
Input l (the perpendicular length of the crystal - not face to face distance)
Input c (the length of the dichroic beamsplitter)
Input nc (the index of refraction of the dichroic beamsplitter at 590 nm)

```
> n := 1.67;
l := .429;
c := 0.2;
nc := 1.48;

> dz := matrix( 2, 2,
[1, z, 0, 1] );
>
> cx := matrix( 2, 2,
[1, c*sqrt((nc^2+1))/nc^2, 0, 1] );
```

```
>
>cy := matrix( 2, 2,
[1, c*sqrt((nc^2+1))/nc^4, 0, 1] );
>
>ey1 := matrix( 2, 2,
[1, 0, (-2)/(ra*cos(alpha)), 1] );
>
>ex1 := matrix( 2, 2,
[1, 0, (-2*cos(alpha))/ra, 1] );
>
>ey2 := matrix( 2, 2,
[1, 0, (-2)/(rb*cos(beta)), 1] );
>
>ex2 := matrix( 2, 2,
[1, 0, (-2*cos(beta))/rb, 1] );
>
>bx1 := matrix( 2, 2,
[1, 1/2*sqrt((n^2+1))/n^2, 0, 1] );
>
>by1 := matrix( 2, 2,
[1, 1/2*sqrt((n^2+1))/n^4, 0, 1] );
>
>
>dx := matrix( 2, 2,
[1, x, 0, 1] );
>my := multiply(by1,cy,dx,ey1,dz,ey2,dx,by1);
>mx := multiply(bx1,cx,dx,ex1,dz,ex2,dx,bx1);
>


>sy := ((my[1,1]+my[2,2])/2)^2;
sx := ((mx[1,1]+mx[2,2])/2)^2;
uy := 1-((my[1,1]+my[2,2])/2)^2;
ux := 1-((mx[1,1]+mx[2,2])/2)^2;
wy := (sqrt(abs(5.90e-5*my[1,2]/(Pi*n*sqrt(uy)))));
wx := (sqrt(abs(5.90e-5*mx[1,2]/(Pi*n*sqrt(ux)))));


>
>plot
([sx*0.005,sy*0.005,wx*1.29,wy*1.29],x=4.9..5.35,waist=0..25
e-4,color=[blue,red,green,black],labels=["crystal/mirror
separation (cm)","waist diam.
(cm)"],labelfont=[HELVETICA,10],axesfont=[HELVETICA,10]);
```

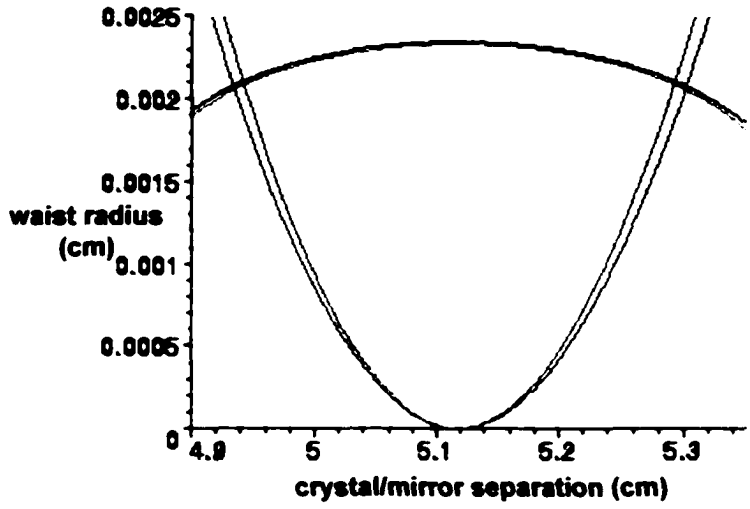

Figure A4.1 Output graph from Maple routine.

The output of the program is the graph at the bottom of the program. Figure A4.1. This graph shows the waist in the tangential and sagittal planes for different separations between the crystal and the curved mirrors. The waists are the green and black nearly horizontal lines crossing the graph. At a crystal/mirror separation of 5.12 cm, the waist in both planes was 23 μm. Also shown on this graph are the cavity stability curves for the tangential and sagittal planes, the red and blue parabolas. Solutions that lie above the stability curves are stable, while solutions that lie below the curves are unstable. In this case, crystal/mirror separations greater than 4.95 cm and less than 5.3 cm were stable. Many different combinations of parameters yielded stable cavities, but the ideal solutions had overlapping stability curves and waist sizes for both planes. Typically changing the angles of incidence on the curved mirrors changed the overlap of the beam waists and

stability curves, since these angles accounted for the astigmatic compensation with the Brewster interfaces. Changing the distances between elements changed the size of the waists.

The optimum waist size for maximum SHG was known before cavity modeling was begun (see Chapter four). Then the goal of using this program was to design a cavity that (1) approached this value as closely as possible (2) lie in the middle of the stability curve so there was some play in laying out the mirrors in the cavity and (3) had a soft waist curve so that slight misalignments of the cavity did not change the waist size appreciably. Figure A4.1 was a good solution and actually shows the BBO cavity described in Chapter four.

A4.4 ABCD Calculations

Figure A4.2 shows an output screen from the ABCD program. This is an example of the ray tracing output, showing all the optical elements in the cavity we have designed and the light beam propagating inside the cavity as both a tangential and sagittal ray (red and black lines). This graph shows one unit cell – or one round-trip pass – of the cavity. The cavity was modeled as a linear optical system and did not need to be shaped like the actual bowtie. ABCD was a very flexible program as cavity elements could be altered.

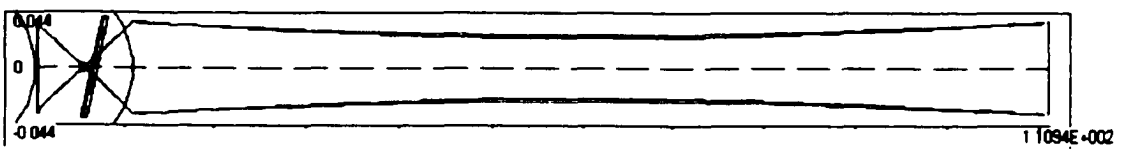

Figure A4.2 Output from the ABCD program. The cavity is mostly empty space, but all optical elements are represented.

added, or deleted with a very intuitive, graphic interface. As was mentioned earlier, this program was usually used after a cavity was designed using the Maple routine. Figure A4.2 shows the same cavity as was calculated by the Maple routine above. Using the ray tracing screen, the beam waist and diameter were known at every location. Of particular usefulness was the location and size of the secondary waist, which was clearly visible in the ray tracing screen. It should be noted that the flat mirrors did not appear in the calculation, since they did not change the ray propagation, and thus they are not visible in Figure A4.2.

REFERENCES

[1] J.T. Verdeyen, *Laser Electronics*, 3rd Ed. (Prentice-Hall, Inc., Englewood Cliffs, New Jersey, 1995)

APPENDIX 5

A Fluorescence Spectrum Fitting Program for Determining Hyperfine Structure Constants

A number of fitting programs were written in Fortran 77 to determine the hyperfine structure constants from laser-induced fluorescence spectra. All the programs in this appendix were written on the CSU lamar server using the PICO text editor. To utilize these programs, the fluorescence spectrum were reduced to two column x-y data (frequency vs. intensity).

Below I have given the code for one such fitting program, in this case entitled "fit56tb". The program read in the data (in this case from a file called "t1.prn"), and then asked for initial estimates for the parameters to be determined. The program called on several external subroutines and functions. "ran0" and "ran2" were random number generator functions which were also in the program directory. "mrqmin" and "mrqmin2" were programs obtained from Numerical Recipes in Fortran. The Numerical Recipes subroutines are not given here, as they may be found elsewhere,[1] but note that mrqmin and mrqmin2 both called several other subroutines which were required to be present in the directory for the program to run: "mrqcof", "gaussj", and "covsrt". The program that determined the mathematical form of the fitting (the program where all the real physics

was located) was the subroutine "lorz56". I have provided the code for "lorz56" below "fit56tb".

"fit56tb" used a least-squares fitting routine to arrive at the best fit to the data. The initial values for the fitting parameters were modified in user defined step sizes one parameter at a time until changing the parameter no longer lead to a decrease in the fitting χ^2. At that point another parameter was modified until it too no longer changed the χ^2. This was done iteratively until the χ^2 could not be changed by an amount greater than a user-specified value. At that point the fitting was complete and the program finished running. The time it took this program to run depended on several factors: the proximity of the initial guess to the final value, the parameter change step size, the final χ^2 limit desired, and the time of day (server usage by other users) being among them. Typically the first fitting of a spectrum took from 10 minutes to 30 minutes. As the parameter values for a spectrum came to be known more accurately and the initial guesses were made better, this time decreased, but that was often balanced by using decreasing step sizes, or a "tighter mesh" to find a more accurate parameter value.

Any changes made to the fitting routine (such as locking the peak height ratios, locking the ratio between B constants, etc.) were made in two places. The front end or fitting program (such as "fit56tb") was modified to provide the correct number of parameters and to export the results accordingly. The subroutine that described the physics - such as "lorz56" – was also modified. The other sub-routines did not require modification.

Two files were exported as the output of "fit56tb". "outputtb56" was a three column data file consisting of the x data points (frequency), y1 data points (the

experimental fluorescence data points read in from "t1.prn"), and y2 data points (the final fit to the data utilizing the best parameters). The output files such as "outputtb56" were FTP'ed to a desktop data analysis program (such as Origin) and a graph of the fluorescence spectrum and its fit was obtained. The other output file was called "paramtb56" and was a text file that summarized the results of the fitting: the values of the parameters that gave the best fit (the lowest χ^2) and the value of χ^2 ultimately obtained. This value allowed one to compare one fitting routine to another to determine which was most accurately fitting the data. An example of "paramtb56" is provided below "lorz56".

All the programs listed below are in their original Fortran format. Fortran convention is to use an asterisk (*) to denote a line that is a comment. The rest is executable code.

PROGRAM "fit56tb"

```
      PROGRAM fit56tb
************************************************************
*fit56tb fits all 10 peaks in the 3/2 to 3/2 spectrum by floating only
*A69,A71,B69,IS,gamma,c-of-g,and H33. The ratio of B69:B71
*is held fixed. Step size is 0.5
*This program will read in the experimental spectrum consisting
*of two columns of x and y data from a file.
*It will then call on subroutine mrqmin to vary the parameters
*specified to find the minimum chi squared value.
*The actual fitting function consisting of 10 Lorentzians is
*in subroutine lorz56.
************************************************************

      REAL xoffset,yoffset,num1,num2,alamda,chisq,iter,
     +     compare,test,limit,min,factor,mult,jump,
     +     yfit,range,finchi
      INTEGER i,j,k,l,m,n,ma,nca,ndata,size,idum
      EXTERNAL ran0,ran2
      PARAMETER(size=3187,ma=7,nca=7)
      REAL x(1:size),y(1:size),sig(1:size),a(1:ma),ia(1:ma),
     +     alpha(nca,nca),covar(nca,nca),low(1:ma),
     +     error(1:ma),coverr(1:ma)
```

```
      OPEN (UNIT =2, FILE="outputtb56", STATUS="UNKNOWN")
      OPEN (UNIT =1, FILE="t1.prn", STATUS="UNKNOWN")
      OPEN (UNIT =3, FILE="paramtb56", STATUS="UNKNOWN")

      idum=5
      i=1
10    CONTINUE

    READ (1,20, END = 30) num1,num2
      x(i)=num1
      y(i)=num2
      sig(i)=1.0
      i=i+1
20    FORMAT (F10.5,F10.5)
      GO TO 10

30    CONTINUE
      CLOSE (1)
      ndata=i-1
      PRINT *, 'the # of data points read from file is:',ndata

      PRINT *, 'The Levenberg-Marquardt Method'
      PRINT *, '----------'
      PRINT *
      PRINT *, 'Enter an initial guess for A'
            a(1)=-37.3
      PRINT *, 'Enter an initial guess for B'
            a(4)= 6.8
      PRINT *, 'Enter an initial guess for the isotope shift'
            a(5)=113.3
      PRINT *, 'Enter an initial guess for the max peak height'
            a(6)= 63.2
      PRINT *, 'Enter an initial guess for the peak width, gamma'
            a(7)= 33.4
      PRINT *, 'Enter an initial guess for the xoffset'
            a(3)=517.5

            a(2)=-46.7

***Indicate which parameters should be fitted for (1 in array ia)
***and which should be held fixed at initial values (0 in array ia)
***the array positions and corresponding parameters are:
***a(1)=A69;a(2)=A71;a(4)=B69;a(5)=IS;a(6)=height;a(7)=gamma;a(3)=c-of-g
35          CONTINUE
            ia(1)=1
            ia(2)=1
            ia(3)=1
            ia(4)=1
            ia(5)=1
            ia(6)=1
            ia(7)=1

***Now we call on subroutine mrqmin which will utilize our initial
***guesses of the parameters stored in array a. Initially, alamda is
***set negative to initialize the program. This program returns the
```

```
***current best-fit parameters in a and the chi-squared in chisq

      min=10000000
      alamda=-10.0
      n=1
40    CONTINUE
      CALL mrqmin(x,y,sig,ndata,a,ia,ma,covar,alpha,nca,chisq,
     +           funcs,alamda,test)
      limit =  0.001

      IF (test .GE. limit .OR. test .LT. 0.0) THEN
            GO TO 40
      ELSE

      PRINT *,'tb56 chisq=',chisq

55    FORMAT(A31,/,A2,F6.2,/,A2,F6.2,/,A3,F7.2,/,A7,F6.2,/,A6,F6.2
     +  ,/,A8,F6.2)
      ENDIF

            DO 57 k=1,ma
                  low(k)=a(k)
57          CONTINUE

      finchi=chisq

100   CONTINUE
      alamda=0

      call mrqmin(x,y,sig,ndata,a,ia,ma,covar,alpha,nca,chisq,
     +           funcs,alamda,test)

      DO 70 i=1,ma,1

      coverr(i)=SQRT ( finchi * ABS(covar(i,i)) )
65    FORMAT(2X,6F6.3)
70    CONTINUE

*************************************************************************
***Now we must calculate the error ranges on all the parameters.  For
***a 3-sigma error range, we must find how much to vary the parameters
***such that the chi-squared changes by 9 (99.73% confidence).  Similarly
***we may find 2-sigma at delta=4 (95.4% confidence) or a 1-sigma at
***delta=1 (68.3% confidence)
*************************************************************************


      DO 400 i=1,ma
            ia(i)=0
400   CONTINUE

      alamda=-10.0
      DO 500 i=1,ma,1

        range = finchi + 9.0
        chisq = finchi
```

```
        DO WHILE (chisq .LT. range)
          CALL mrqmin2(x,y,sig,ndata,a,ia,ma,covar,alpha,nca,
     +          chisq,funcs,alamda,test)

                IF (chisq .LT. finchi) THEN
                  GO TO 35
                ELSE
                  alamda=-10.0
              a(i)=a(i) + 0.01
                ENDIF
        END DO

        error(i)=a(i)- 0.01
        a(i)=low(i)
500     CONTINUE


        alamda=-10.0
        DO 510 i=1,ma,1

          range = finchi + 9.0
          chisq = finchi

          DO WHILE (chisq .LT. range)
            CALL mrqmin2(x,y,sig,ndata,a,ia,ma,covar,alpha,nca,
     +          chisq,funcs,alamda,test)

                IF (chisq .LT. finchi) THEN
                  GO TO 35
                ELSE
                  alamda=-10.0
              a(i)=a(i) - 0.01
                ENDIF
        END DO


        error(i)=a(i) + 0.01
        a(i)=low(i)
510     CONTINUE

        DO 502 i=1,ma
          error(i)=error(i) - low(i)
502     CONTINUE


        PRINT *,'errors calculated by covariance'
        WRITE (3,*)
        WRITE (3,*)

        WRITE (3,505)'A69=',low(1),'plus/minus',coverr(1)
        WRITE (3,505)'A71=',low(2),'plus/minus',coverr(2)
        WRITE (3,505)'B=',low(4),'plus/minus',coverr(4)
        WRITE (3,505)'IS=',low(5),'plus/minus',coverr(5)
        WRITE (3,505)'height of 3-3=',low(6),'plus/minus',coverr(6)
        WRITE (3,505)'gamma=',low(7),'plus/minus',coverr(7)
```

```
      WRITE (3,505)'xoffset=',low(3),'plus/minus',coverr(3)
      WRITE (3,*)'final fit56tb chi-squared is',finchi
      WRITE (3,*)

505   FORMAT(A14,F9.4,1X,A10,F9.4)

*************************************************************************
***At this point the minimum chi squared has been calculated and stored
***in finchi, the parameters that give this value are stored in low(1:ma)
***the x and y data are in x(ndata) and y(ndata) respectively.  We now
***write out the y values of the fit to file output1
*************************************************************************
      DO 300 i=1,ndata,1

            CALL lorz56(x(i),low,yfit,dyda,ma)

            WRITE (2,'(1X,F10.4,2X,A1,2X,F10.4,2X,A1,2X,F10.4)')
     +            x(i)-low(3),',',y(i),',',yfit

300   CONTINUE


      END
```

SUBROUTINE "lorz56"

```
      SUBROUTINE lorz56(x,a,y,dyda,na)

      INTEGER na,i,j,num
      REAL x,y,xo,width,height,a(1:na),dyda(1:na),cg
      PARAMETER (num=10)
      REAL peak(num),alpha(num),beta(num),gamma(num),delta(num)
      REAL derv5(num)


*************************************************************************
***Compute the y value and the 5 derivatives at a particular x value.
***a(1)=A69;a(2)=A71;a(3)=cg;a(4)=B69;a(5)=IS;a(7)=gamma;a(6)=H33
*************************************************************************

      peak(1)= a(6)
      peak(2)= a(6) * (1.0/4.0)
      peak(3)= a(6) * (1.0/4.0)
      peak(4)= a(6) * (5.0/14.0)
      peak(5)= a(6) * (2.0/7.0)
      peak(6)= 2.0/3.0 * a(6)
      peak(7)= 2.0/3.0 * a(6) * (1.0/4.0)
      peak(8)= 2.0/3.0 * a(6) * (1.0/4.0)
      peak(9)= 2.0/3.0 * a(6) * (5.0/14.0)
      peak(10)= 2.0/3.0 * a(6) * (2.0/7.0)

      derv5(1)=1.0
```

```
      derv5(2)=1.0/4.0
      derv5(3)=1.0/4.0
      derv5(4)=5.0/14.0
      derv5(5)=2.0/7.0
      derv5(6)=2.0/3.0
      derv5(7)=2.0/3.0 * 1.0/4.0
      derv5(8)=2.0/3.0 * 1.0/4.0
      derv5(9)=2.0/3.0 * 5.0/14.0
      derv5(10)=2.0/3.0 * 2.0/7.0

***   Peak 1: 3 to 3 (69)
***   loc(1)= (a * (9.0/4.0) + b * (1.0/4.0)) - 444.929171
      alpha(1)= 9.0/4.0
      beta(1)= 1.0/4.0
      gamma(1)= -444.929171
      delta(1)= 0.0

***   Peak 2: 3 to 2 (69)
***   loc(2)= (a * (-3.0/4.0) + b * (-3.0/4.0)) - 444.929171
      alpha(2)= -3.0/4.0
      beta(2)= -3.0/4.0
      gamma(2)= -444.929171
      delta(2)= 0.0

***   Peak 3: 2 to 3 (69)
***   loc(3)= (a * (9.0/4.0) + b * (1.0/4.0)) + 189.992696
      alpha(3)= 9.0/4.0
      beta(3)= 1.0/4.0
      gamma(3)= 189.992696
      delta(3)= 0.0

***   Peak 4: 2 to 2 (69)
***   loc(4)= (a * (-3.0/4.0) + b * (-3.0/4.0)) + 189.992696
      alpha(4)= -3.0/4.0
      beta(4)= -3.0/4.0
      gamma(4)= 189.992696
      delta(4)= 0.0

***   Peak 5: 2 to 1 (69)
***   loc(5)= (a * (-11.0/4.0) + b * (1.0/4.0)) + 189.992696
      alpha(5)= -11.0/4.0
      beta(5)= 1.0/4.0
      gamma(5)= 189.992696
      delta(5)= 0.0

***   Peak 6: 3 to 3 (71)
***   loc(6)= (a * (9.0/4.0) + b * (1.0/4.0)) - 555.340105
      alpha(6)= 9.0/4.0
      beta(6)= (1.0/4.00) * 0.630
      gamma(6)= -555.340105
      delta(6)= 1.0

***   Peak 7: 3 to 2 (71)
***   loc(7)= (a * (-3.0/4.0) + b * (-3.0/4.0)) - 555.340105
      alpha(7)= -3.0/4.0
      beta(7)= (-3.0/4.0) * 0.630
```

```
      gamma(7)= -555.340105
      delta(7)= 1.0

***   Peak 8: 2 to 3 (71)
***   loc(8)= (a * (9.0/4.0) + b * (1.0/4.0)) + 211.380046
      alpha(8)= 9.0/4.0
      beta(8)= (1.0/4.0) * 0.630
      gamma(8)= 211.380046
      delta(8)= 1.0

***   Peak 9: 2 to 2 (71)
***   loc(9)= (a * (-3.0/4.0) + b * (-3.0/4.0)) + 211.380046
      alpha(9)= -3.0/4.0
      beta(9)= (-3.0/4.0) * 0.630
      gamma(9)= 211.380046
      delta(9)= 1.0

***   Peak 10: 2 to 1 (71)
***   loc(10)= (a * (-11.0/4.0) + b * (1.0/4.0))
***     + 211.380046 + is
      alpha(10)= -11.0/4.0
      beta(10)= (1.0/4.0) * 0.630
      gamma(10)= 211.380046
      delta(10)= 1.0

***calculate the value of y at x

      y=0
      DO 10 i=1,10,1

      IF (i .LE. 5) THEN
       xo=(alpha(i)*a(1) + beta(i)*a(4) + gamma(i) + delta(i)*a(5))
      ELSE
       xo=(alpha(i)*a(2) + beta(i)*a(4) + gamma(i) + delta(i)*a(5))
      END IF

       width= (a(7)**2.0)/4.0
       y=y +( peak(i) * width ) / ( ((x-a(3)) - xo)**2.0 + width )

10    CONTINUE

***calculate the 6 partial derivatives dy/da(na) at x
      DO 15 j=1,na,1
       dyda(j)=0.0
15    CONTINUE

      DO 20 i=1,10,1
       width= (a(7)**2.0)/4.0

      IF (i .LE. 5) THEN
       xo=(alpha(i)*a(1) + beta(i)*a(4) + gamma(i) + delta(i)*a(5))

       dyda(1) = dyda(1) +
     +          ( peak(i) * width * 2.0 * ((x-a(3)) - x0) * alpha(i) ) /
     +          ( (((x-a(3)) - xo)**2.0 + width)**2.0    )
```

```
          dyda(2) = dyda(2) + 0.0

        ELSE

          xo=(alpha(i)*a(2) + beta(i)*a(4) + gamma(i) + delta(i)*a(5))

          dyda(2) = dyda(2) +
     +          ( peak(i) * width * 2.0 * ((x-a(3)) - x0) * alpha(i) ) /
     +          ( (((x-a(3)) - xo)**2.0 + width)**2.0    )

          dyda(1) = dyda(1) + 0.0

        END IF

          dyda(3) = dyda(3) +
     +          ( peak(i) * width * 2.0 * ((x-a(3)) - x0) ) /
     +          ( (((x-a(3)) - xo)**2.0 + width)**2.0    )

          dyda(4) = dyda(4) +
     +          ( peak(i) * width * 2.0 * ((x-a(3)) - x0) * beta(i) ) /
     +          ( (((x-a(3)) - xo)**2.0 + width)**2.0    )

          dyda(5) = dyda(5) +
     +          ( peak(i) * width * 2.0 * ((x-a(3)) - x0) * delta(i) ) /
     +          ( (((x-a(3)) - xo)**2.0 + width)**2.0    )

          dyda(7) = dyda(7) +
     +       ( ( ((x-a(3)) - xo)**2.0 + width )*( peak(i) * a(7)/2.0 ) -
     +          ( peak(i) * width )*( a(7)/2.0 ) ) /
     +          ( (((x-a(3)) - xo)**2.0 + width)**2.0    )

          dyda(6) = dyda(6) +
     +          ( derv5(i) * width ) / ( ((x-a(3)) - xo)**2.0 + width )



20        CONTINUE

          RETURN
          END
```

OUTPUT FILE "paramtb56"

```
      A69= -37.3100 plus/minus   .0421
      A71= -46.7401 plus/minus   .0439
       B=   6.7596 plus/minus   .2074
      IS= 113.3299 plus/minus   .2706
height of 3-3=  63.2373 plus/minus  8.3005
     gamma=  33.4280 plus/minus  5.3521
   xoffset= 517.5300 plus/minus   .1591
final fit56tb chi-squared is 17042.81250
```

REFERENCES

[1] W.H. Press, S.A. Teukolsky, W.T. Vetterling, and B.P. Flannery, *Numerical Recipes in Fortran*, 2nd Ed. (Cambridge University Press, Cambridge, 1992)